cancers

Special Issue Reprint

Advances in Uveal Melanoma

Edited by
Takami Sato and Mizue Terai

mdpi.com/journal/cancers

MDPI

Advances in Uveal Melanoma

Advances in Uveal Melanoma

Guest Editors

Takami Sato
Mizue Terai

MDPI

Basel • Beijing • Wuhan • Barcelona • Belgrade • Novi Sad • Cluj • Manchester

Guest Editors

Takami Sato
Department of Medical Oncology
Thomas Jefferson University
Philadelphia, PA
USA

Mizue Terai
Department of Medical Oncology
Thomas Jefferson University
Philadelphia, PA
USA

Editorial Office
MDPI AG
Grosspeteranlage 5
4052 Basel, Switzerland

This is a reprint of the Special Issue, published open access by the journal *Cancers* (ISSN 2072-6694), freely accessible at: https://www.mdpi.com/journal/cancers/special_issues/RMD73406GL.

For citation purposes, cite each article independently as indicated on the article page online and as indicated below:

Lastname, A.A.; Lastname, B.B. Article Title. *Journal Name* **Year**, *Volume Number*, Page Range.

ISBN 978-3-7258-9049-1 (Hbk)
ISBN 978-3-7258-9050-7 (PDF)
https://doi.org/10.3390/books978-3-7258-9050-7

Cover image courtesy of Mizue Terai

© 2026 by the authors. Articles in this reprint are Open Access and distributed under the Creative Commons Attribution (CC BY) license. The reprint as a whole is distributed by MDPI under the terms and conditions of the Creative Commons Attribution-NonCommercial-NoDerivs (CC BY-NC-ND) license (https://creativecommons.org/licenses/by-nc-nd/4.0/).

Contents

Emily Marcotte, Alicia Goyeneche, Mohamed Abdouh, Julia Valdemarin Burnier and Miguel Noel Burnier, Jr.
The Phenotypical Characterization of Dual-Nature Hybrid Cells in Uveal Melanoma
Reprinted from: *Cancers* **2024**, *16*, 3231, https://doi.org/10.3390/cancers16183231 . . . . . **1**

Justyna Pilch, Jakub Mizera, Maciej Tota and Piotr Donizy
GNAQ/GNA11-Related Benign and Malignant Entities—A Common Histoembriologic Origin or a Tissue-Dependent Coincidence
Reprinted from: *Cancers* **2024**, *16*, 3672, https://doi.org/10.3390/cancers16213672 . . . . . **20**

Hans Witzenhausen and Gustav Stalhammar
Survival Benefit of Primary Tumor Treatment in Uveal Melanoma: A Re-Analysis of the Collaborative Ocular Melanoma Study (COMS) and Natural History Study (NHS) Cohorts
Reprinted from: *Cancers* **2024**, *16*, 3839, https://doi.org/10.3390/cancers16223839 . . . . . **40**

Elsa Toumi, Luke B. Hesson, Vivian Lin, Dale Wright, Elektra Hajdu, Li-Anne S. Lim, et al.
Microdissection of Distinct Morphological Regions Within Uveal Melanomas Identifies Novel Drug Targets
Reprinted from: *Cancers* **2024**, *16*, 4152, https://doi.org/10.3390/cancers16244152 . . . . . **51**

Carly Zako, Arina Nisanova, Vivian Weinberg, Jessica Scholey, Carisa Swason, Armin R. Afshar, et al.
Long-Term Clinical Outcomes for Adolescent and Young-Adult Uveal Melanoma Patients Treated with Dedicated Particle-Beam Radiation
Reprinted from: *Cancers* **2025**, *17*, 2042, https://doi.org/10.3390/cancers17122042 . . . . . **69**

Laura Hawkins, Helen Kalirai, Karen Aughton, Rumana N. Hussain, Sarah E. Coupland and Jason L. Parsons
Understanding and Exacerbating the Biological Response of Uveal Melanoma to Proton Beam Therapy
Reprinted from: *Cancers* **2025**, *17*, 3104, https://doi.org/10.3390/cancers17193104 . . . . . **84**

Carolin M. Reiner, Martin A. Schneider, Hauke Weilert, Klara Welcker, Jochen Hoedtke, Andreas H. Mahnken, et al.
Survival Outcome After Percutaneous Hepatic Perfusion with High-Dose Melphalan for Liver-Dominant Metastatic Uveal Melanoma: A 10-Year Single-Center Experience
Reprinted from: *Cancers* **2025**, *17*, 3834, https://doi.org/10.3390/cancers17233834 . . . . . **102**

Simone Lubrano, Rodolfo Daniel Cervantes-Villagrana, Nadia Arang, Elena Sofia Cardenas-Alcoser, Kuniaki Sato, Gabriela Cuesta-Margolles, et al.
Unraveling Resistance Mechanisms to Gαq Pathway Inhibition in Uveal Melanoma: Insights from Signaling-Activation Library Screening
Reprinted from: *Cancers* **2026**, *18*, 74, https://doi.org/10.3390/cancers18010074 . . . . . **116**

Vitali Alexeev, Mizue Terai, Sergei Koshkin, Olga Igoucheva and Takami Sato
Cancer Vaccine Targeting Mutated GNAQ-Expressing Uveal Melanoma
Reprinted from: *Cancers* **2026**, *18*, 480, https://doi.org/10.3390/cancers18030480 . . . . . **135**

Domagoj Vlašić, Mira Knežić Zagorec, Antonia Jakovčević, Dina Lešin Gaćina, Marijana Ćorić and Tomislav Jukić
Clinicopathological Characteristics and BAP1 Expression in an Enucleation-Based Uveal Melanoma Cohort: A Single-Center Croatian Experience with Long-Term Follow-Up
Reprinted from: *Cancers* **2026**, *18*, 1211, https://doi.org/10.3390/cancers18081211 . . . . . **148**

Rino S. Seedor, Mizue Terai, Sergei Koshkin, Andrew E. Aplin, Marlana Orloff, Erin Sharpe-Mills, et al.
A Phase II Trial of Defactinib Combined with Avutometinib in Patients with Metastatic Uveal Melanoma
Reprinted from: *Cancers* **2026**, *18*, 2232, https://doi.org/10.3390/cancers18142232 . . . . . **165**

cancers

MDPI

Article

The Phenotypical Characterization of Dual-Nature Hybrid Cells in Uveal Melanoma

Emily Marcotte [1,2,*], Alicia Goyeneche [1,2], Mohamed Abdouh [1,2], Julia Valdemarin Burnier [1,3,4] and Miguel Noel Burnier, Jr. [1,2]

[1] Cancer Research Program, Research Institute of the McGill University Health Centre, Montreal, QC H4A 3J1, Canada; alicia.goyeneche@affiliate.mcgill.ca (A.G.); mohamed.abdouh@muhc.mcgill.ca (M.A.); julia.burnier@mcgill.ca (J.V.B.); miguel.burnier@mcgill.ca (M.N.B.J.)
[2] The MUHC–McGill University Ocular Pathology & Translational Research Laboratory, McGill University, Montreal, QC H4A 3J1, Canada
[3] Experimental Pathology Unit, Department of Pathology, McGill University, Montreal, QC H3A 2B4, Canada
[4] Gerald Bronfman Department of Oncology, McGill University, Montreal, QC H3A 3T2, Canada
* Correspondence: emily.marcotte@mail.mcgill.ca

Simple Summary: Uveal melanoma (UM) is a rare type of cancer of the eye that develops from a cell type called melanocytes, which are present in the uveal tract. These patients have a high risk of liver metastasis, usually many years after the initial diagnosis, which is life threatening. We discovered a population of cells in the primary tumor called dual-nature hybrid cells (DNCs) similar to previously discovered cells in the blood (i.e., circulating hybrid cells, CHCs) with shared characteristics of both cancer cells and white blood cells. In this paper, we determined the types of white blood cells capable of participating in the formation of a hybrid cell with a cancer cell, and we re-created these DNCs in a cell culture. The study of the cells of this tumor, particularly DNCs, is crucial to better understanding dissemination and uncovering a possible target for treatment of this systemic disease.

Abstract: Background: Metastasis, occurring years after primary diagnosis, represents a poor prognosis in uveal melanoma (UM)-affected individuals. The nature of cells involved in this process is under debate. Circulating hybrid cells that have combined tumor and immune cell features found in blood were predictive of metastasis and may correspond to dual-nature cells (DNC) in the primary tumor. Herein, we sought to determine the presence of DNCs in primary UM tumors, the cell types involved in their genesis, and their ability to be formed in vitro. Methods: UM lesions (n = 38) were immunolabeled with HMB45 in combination with immune-cell-specific antibodies. In parallel, we co-cultured UM cells and peripheral blood mononuclear cells (PBMCs) to analyze DNC formation. Results: $HMB45^+/CD45^+$ DNCs were present in 90% (26/29) of the tumors, $HMB45^+/CD8^+$ DNCs were present in 93% (26/28), and $HMB45^+/CD68^+$ DNCs were present in 71% (17/24). DNCs formed with $CD8^+$ and $CD68^+$ cells were positively correlated to the infiltration of their respective immune cells. Notably, UM cells were prone to hybridize with PBMCs in vitro. Conclusions: This phenotypical characterization of DNCs in UM demonstrates that $CD8^+$ T-cells and macrophages are capable of DNC formation, and they are important for better understanding metastatic dissemination, thus paving the path towards novel therapeutic avenues.

Keywords: uveal melanoma; dual-nature hybrid cells; circulating hybrid cells; primary tumors; immunophenotyping; cell co-culture; cell–cell fusion

1. Introduction

Uveal melanoma (UM) is classed as a rare disease, but it remains the most prevalent primary intraocular malignant tumor found amongst adults [1]. The incidence is approx-

imately 2–10 patients per million depending on the region, with the vast majority being light-skinned [1–3]. This malignancy typically presents in a unilateral manner and can be located within the choroid, ciliary body, or iris [4,5]. Treatments have improved as certain options, such as radiotherapy, have replaced enucleation in most cases, ultimately enhancing patients' quality of life through the preservation of the eye [6]. Despite this, survival has not improved, as metastasis still leads to death in over 40% of patients more than 15 years after the initial diagnosis [1,7–9]. These metastases are due to hematogenous dissemination occurring preferentially in the liver, which is affected in more than 90% of metastatic cases [10,11].

In order to stratify the prognosis of UM, clinical and histopathological prognostic factors, such as cell type, tumor size, the presence of vascular loops, mitotic figures, scleral invasion, and infiltrative inflammatory cells, have been established [12,13]. Patients with a predominantly epithelioid cell type, larger tumors, vascular loops, high mitotic counts, scleral invasion, and the presence of inflammatory cells have a worse prognosis (i.e., a higher incidence of metastasis and death). In contrast, patients with a predominantly spindle cell type, smaller tumors, decreased or no vascular involvement, lower or no mitotic counts, no scleral invasion, and no inflammatory cells have a better prognosis [12–23]. Moreover, the loss of the heterozygosity of chromosome 3 and the gain of the chromosome 8q arm were reported as the most relevant chromosomal abnormalities, and they are associated with poor prognosis [24].

The initiation and progression to metastatic disease in UM still raises many unanswered questions. The most common mutations in UM are in GNAQ or GNA11. Some research has pointed to initiation involving Hippo signaling through the YAP/TAZ pathway [25,26]. The inhibition of the Hippo tumor-suppressor pathway through YAP has been shown to be correlated to GNAQ/11 status as well as being important for tumor initiation in UM [25,26]. In fact, YAP inhibition with verteporfin has been shown to block tumorigenesis [26]. In addition, mitogen-activated protein kinase (MAPK), a potential downstream target in UM, has been demonstrated to have variable activation in tumors with GNAQ/11 mutation, contributing not only to tumor heterogeneity, which complicates potential treatment options, but also therapy resistance, as seen in other cancers [27,28].

During the metastatic cascade, tumor cells detach from the primary tumor, invade the surrounding tissue, intravasate, and stay alive in circulation before extravasation and successful colonization in secondary organs. Non-invasive procedures, such as liquid biopsy, are being investigated to find new prognostic factors and to track the natural course of the disease [29]. This is a technique in which bodily fluids are evaluated for tumor DNA, extracellular tumor vesicles, and/or circulating tumor cells (CTCs) [29]. Previously, our laboratory and others reported on the presence of CTCs in the peripheral blood of almost all patients with UM regardless of treatment, and they were thought to be predictors of poor prognosis and thus predictors of the development of metastasis [30–32]. These cells home at metastatic sites under a dormancy state, as we reported in a previous animal model study, which may be why micro- and macrometastases take place years after primary disease diagnosis [33].

The discovery of circulating hybrid cells (CHCs) emerged, and they were described as cells with dual-nature characteristics of both tumor cells and leukocytes [34]. These cells were found in the circulation of many epithelial and non-epithelial cancers, including UM [35]. In the context of UM, this novel cell type rivaled the hypotheses of CTCs by only finding CTCs in the blood of less than 60% of patients and finding CHCs in all patients and in greater quantities than their counterparts, making them a better predictor of metastasis and a vital component of better understanding UM progression [34]. In addition, the generation of hybrids and their presence in circulation and metastatic sites in cancer support the hypothesis that cell–cell fusion might be a mechanism associated with metastatic dissemination [36,37].

Dual-nature hybrid cells (DNCs), which are thought to correspond to CHCs found in the blood, have only been recently evaluated in the primary tumor [38]. Based on

these recent findings of hybrid cells in UM patients, we aimed to uncover the presence of DNCs in a larger sample size of primary UM lesions and determine the leukocytic cell types involved in their formation. In addition, the capacity of hybrid cell formation was also tested in vitro by co-incubating UM cells with peripheral blood mononuclear cells (PBMCs). Overall, DNCs were detected in the majority of primary UM samples displaying a dual phenotype of UM cells (i.e., HMB45) and that of leukocytes (i.e., CD45), including, mainly cytotoxic T cells and macrophages (i.e., $CD8^+$, and $CD68^+$, respectively). In vitro co-culture experiments showed that UM cells and PBMCs are inclined to hybridize. These findings support the involvement of heterotypic hybrid cells in primary solid tumors and the capacity of UM cells to fuse with normal leucocytes. This offers a step towards a better understanding of the metastatic process for the development of new UM therapies.

2. Materials and Methods

2.1. Patient Specimens

Thirty-eight specimens of UMs were collected from the MUHC–McGill University Ocular Pathology & Translational Research Laboratory between 1980 and 2020. Demographic information pertaining to age and sex were obtained when available.

For morphology, histopathological type was classified according to the revised Callender classification of epithelioid, spindle, or mixed cell type [39]. Mixed-cell tumors were then further classified according to their predominant cell type. Vascular loops, mitotic figures, and scleral invasion were evaluated through hematoxylin and eosin (H&E) analysis. Characteristics were validated using the original pathology report when available (Table 1).

Table 1. UM patient characteristics.

Patient	Age	Sex	Location	Size	Cell Type	Vascular Loops	Mitotic Figures	Scleral Invasion
1	63	M	Iris—CB	Small	Mixed—SP	No	Yes	No
2	N/A	M	Choroid	Small	Mixed—EP	No	Yes	Yes
3	81	F	Choroid	Small	Mixed—EP	No	No	No
4	51	M	Choroid	Large	Epithelioid	No	No	No
5	76	F	Choroid	Large	Mixed—EP	Yes	Yes	No
6	76	F	Choroid	Large	Mixed—SP	No	No	No
7	63	F	Choroid	Large	Mixed—EP	No	Yes	No
8	55	M	Choroid	Large	Epithelioid	No	Yes	No
9	65	M	Choroid	Large	Mixed—EP	No	Yes	Yes
10	72	F	Choroid	Large	Spindle	No	Yes	Yes
11	N/A	N/A	Choroid	Small	Mixed—EP	No	No	Yes
12	81	M	Choroid	Large	Epithelioid	No	No	No
13	N/A	N/A	Choroid	Large	Epithelioid	No	Yes	Yes
14	76	M	Choroid	Large	Mixed—EP	No	No	No
15	76	M	Choroid—CB	Large	Epithelioid	No	No	No
16	59	F	Choroid	Small	Mixed—SP	Yes	Yes	No
17	57	M	Choroid—CB	Large	Epithelioid	Yes	No	Yes
18	77	M	Choroid	Large	Mixed—EP	No	No	No
19	50	M	Choroid	Small	Mixed—SP	No	No	Yes
20	71	M	Choroid	Small	Mixed—SP	No	No	No
21	62	F	Choroid	Large	Epithelioid	Yes	No	No
22	58	F	Choroid	Small	Epithelioid	No	No	No
23	50	F	Choroid	Large	Spindle	Yes	No	No
24	N/A	F	Choroid	Large	Epithelioid	Yes	No	No
25	67	F	Choroid—CB	Small	Mixed—SP	Yes	No	No

Table 1. *Cont.*

Patient	Age	Sex	Location	Size	Cell Type	Vascular Loops	Mitotic Figures	Scleral Invasion
26	57	M	Choroid	Small	Mixed—SP	No	No	No
27	79	F	Choroid	Small	Mixed—EP	No	Yes	Yes
28	93	M	Choroid	Small	Mixed—EP	Yes	Yes	Yes
29	93	F	Choroid	Small	Mixed—SP	No	No	No
30	74	M	Choroid	Small	Mixed—EP	No	No	No
31	51	F	Choroid	Small	Mixed—SP	No	No	No
32	56	F	Choroid	Small	Mixed—EP	Yes	Yes	No
33	34	M	Choroid	Large	Mixed—SP	Yes	Yes	No
34	62	M	Choroid	Large	Mixed—SP	No	Yes	No
35	65	M	Choroid	Small	Mixed—EP	Yes	Yes	Yes
36	60	F	Choroid	Large	Mixed—SP	No	No	Yes
37	78	M	Choroid	Small	Epithelioid	Yes	Yes	No
38	47	M	Choroid	Large	Mixed—SP	No	No	No

N/A: not available; M: male; F: female; CB: ciliary body; EP: epithelioid-predominant; SP: spindle-predominant.

2.2. Histological Staining and Immunohistochemical (IHC) and Immunofluorescence (IF) Analyses

Formalin-fixed, paraffin-embedded sections (4 μm thick) from enucleated globes were deparaffinized and rehydrated for subsequent H&E staining and immunolabeling.

A standard H&E procedure was performed using the automated stainer with a coverslip applicator from Leica (Leica CV5030 and ST5020 Stainer, Leica Biosystems, Nussloch, Germany).

For IHC analysis, we performed both single and dual labeling using the Discovery Ultra system from Roche (Graz, Austria). Following antigen retrieval treatment using Tris-EDTA for 36 min (32 min for CD3 staining), the sections were incubated for 24 min at 37 °C with anti-HMB45 antibody (Ab) at 1/45 dilution (M0634, Dako, Hilden, Germany), prediluted anti-CD45 Ab (760-4279, Roche), prediluted anti-macrophage CD68 Ab (760-2931, Roche), prediluted anti-CD3 Ab (790-4341, Roche), or anti-MelanA Ab at 1/40 dilution (NCL-L-MelanA, Leica). After washing, slides were incubated with secondary Ab for 20 min (OmniMap anti-rabbit HRP 760-4311, Roche for CD3), followed by the detection Kit UltraView Universal DAB (760-159, Roche) or the Discovery Red HRP kit (760-260, Roche in the case of CD3 staining). Slides were then counterstained with the hematoxylin, dehydrated, and cleared, and a coverslip was applied.

For dual IHC labeling, sections were incubated for 24 min at 37 °C with anti-HMB45 Ab, washed, and incubated with the secondary Ab, OmniMap anti-Mouse (Mse) HRP (760-4310, Roche) at RT for 24min, followed by the detection Kit Discovery Purple (RUO, 760-229, Roche). After Ab denaturation, sections were incubated for 24 min at 37 °C with prediluted anti-CD45 Ab, prediluted anti-CD8 Ab (790-4460, Roche), or prediluted anti-CD68 Ab. They were then incubated with the secondary Ab, OmniMap anti-Mse HRP (760-4310, Roche), at RT for 20 min, followed by the detection kit Discovery Teal (RUO, 760-247, Roche) or the detection Kit Discovery Green (RUO, 760-271, Roche) for some of the CD68 double-labeled slides. Slides were then counterstained with the hematoxylin, dehydrated, and cleared, and a coverslip was applied.

For IF staining, slides were incubated for 24 min at 37 °C with anti-HMB45, washed, and. incubated with the secondary Ab, OmniMap anti-Mse HRP coupled with Fluorescein isothiocyanate (FITC; 760-232, Roche) at RT for 24 min. After Ab denaturation, sections were incubated for 24 min at 37 °C with prediluted anti-CD8 Ab. Then, the slides were incubated with the secondary Ab, OmniMap anti-Rb HRP (760-4311, Roche) coupled with Rhodamine (760-233, Roche), at RT for 20 min. Slides were then counterstained with the DAPI and rinsed, and a coverslip was applied with Permafluor mounting media.

Slides from all labeling processes were digitally scanned using a ZEISS AxioScan.Z1 and then analyzed using ZEISS ZEN blue software version 3.5 (Carl ZEISS AG, Oberkochen, Germany).

2.3. Cell Culture

2.3.1. Normal Choroidal Melanocyte (NCM) Culture Medium

NCM cells were gifted by Dr. Julia Burnier's laboratory (McGill University, Montreal). These cells were isolated as described previously from human cadaveric eyes in accordance with a protocol approved by the IRB of the Research Institute of the McGill University Health Centre (RI-MUHC) (IRB #2019-5314) [40]. Cells were maintained in Melanocyte Growth Medium M2 (C-24300, PromoCell, Heidelberg, Germany). Cells were incubated in a humidified incubator at 37 °C under 5% CO_2. Cell viability was assessed through trypan blue exclusion assay. The number of cells was calculated using the TC20 Automated cell counter (Bio-Rad, Mississauga, ON, Canada).

2.3.2. UM Cell Culture Medium

UM 92.1 cells were gifted by Dr. Martine Jager (Leiden University, The Netherlands) [41]. MEL270 and OMM2.5 cells were gifted by Dr. Vanessa Morales (University of Tennessee). Cells were maintained in RPMI 1640 medium supplemented with 10% fetal bovine serum (FBS), 10 mM HEPES, 2 mM of Glutagro supplement, 1 mM of sodium Pyruvate, 100 U/mL of penicillin, 100 µg/mL of streptomycin (all from CorningTM, Lauderdale, FL, USA), and 10 µg/mL of insulin (Millipore-SIGMA, Oakville, ON, Canada). Cells were incubated in a humidified incubator at 37 °C under 5% CO_2. Cell viability was assessed through trypan blue exclusion assay. The number of cells was calculated using the TC20 Automated cell counter (Bio-Rad).

2.3.3. Isolation of Peripheral Blood Mononuclear Cells (PBMCs)

Blood (10 mL) was collected from healthy individuals at the McGill Academic Eye Clinic in accordance with an approved ethics protocol (#2018-4187) by the Review Ethic Board of the RI-MUHC. The blood was diluted 1/1 (*v/v*) with cold phosphate-buffered saline (PBS) + 1 mM EDTA + 2% FBS, and density gradient centrifugation was used to isolate mononuclear cells using Lymphoprep solution and Sepmate tubes (StemCell Technologies, Vancouver, BC, Canada). Briefly, Lymphoprep was layered in the Sepmate tube insert, and the diluted blood was added slowly at the top of the insert. Samples were centrifuged at 1200 g for 10 min without the brake. The top layer was poured into a new tube and centrifuged at 300 g for 8 min. The supernatant was removed, and the pellet was washed twice with PBS-2% FBS-1mM EDTA at 300 g for 8 min. The pellet was resuspended in 10 mL of RPMI medium without serum, and PBMCs were counted and evaluated for viability.

2.3.4. UM Cells, PBMC Labeling, and Co-Culture

UM 92.1 cell mitochondria were tagged with Mitotracker M7514 (Invitrogen, San Diego, CA, USA). Cells were seeded the day before; therefore, the staining of the mitochondria was performed on adherent cells according to the manufacturer's instructions. Excess staining was removed, and the culture was washed twice with fresh media.

The membrane of PBMCs was stained with the PKH26 red fluorescent cell linker (Millipore-SIGMA) following the manufacturer's protocol. PBMCs were spun at 300 g for 10 min at room temperature (RT), and the pellet was resuspended in complete medium and transferred to a new tube. PBMCs were washed another 2 times at 300 g for 5 min at RT with complete medium to ensure the removal of unbound dye. Finally, the pellet was resuspended in complete medium, and PBMCs were counted and evaluated for viability.

Mitotracker-labeled 92.1 cells were trypsinized, counted, and combined with PKH26-labeled PBMCs. A total of 0.24×10^6 cells in a 24-well plate with different combinations between UM and PBMCs (UM cells/PBMCs: 1/10; 1/5; 1/3; 1/1; 3/1; and 5/1) were seeded, and the interactions between PBMCs and cancer cells were followed every two hours using the IncuCyte® S3 Live-Cell Analysis System. A standard scan type with 10× magnification was applied. Excitation/emission of 490/516 nm for the mitochondria tracker and

551/567 nm for the PBMCs' membrane staining were selected to identify fusion events between cancer cells and PBMCs.

On the other hand, UM 92.1 cells (0.6×10^6) were seeded into glass-bottom dishes (Mat Tek) for 24 h and stained with the Mitotracker. An equal number of PKH26-labeled PBMCs (0.6×10^6) was combined with Mitotracker-labeled adherent UM cells. Interactions between 92.1 cells and PBMCs were followed by capturing microscopic images for 30 s every 2.0 min for a total time of 90 min. Scanning was performed under Zeiss LSM780-NLO laser scanning confocal with IR-OPO lasers. The objective used was EC Plan-neofluor 10×/0.3 na. Laser red 551/567 and green 490/516 were used for data acquisition. At each phase, green and red images were recorded, and different movies were created to follow cell–cell interactions.

In a parallel set of experiments, UM cells and PBMCs were stained with PKH26 and PKH67 dyes, respectively. Cells were mixed at different ratios (UM cells/PBMCs: 1/3, 1/5, and 1/10) and incubated for 24 h in 8-well chamber slides. The slides were washed with PBS and mounted in DAPI-containing medium (Vector, Malvern, PA, USA). Images were acquired using an LSM780 confocal microscope (Zeiss, Malvern, PA, USA).

2.4. Phenotypic Determination of Co-Cultured NCM Cells and PBMCs, as Well as UM Cells and PBMCs

NCM cells and PBMCs were co-cultured in tissue culture slide flasks (177,453, Lab-Tek Flaskette Chamber Slide) for 3 days at different ratios (1:1, 2:1, 1:2). Adherent cells were fixed in 2% paraformaldehyde for 20 min at RT. The fixative was removed, and cells were washed twice with PBS. After antigen-retrieval treatment (EDTA buffer, 8 min), the slides were incubated for 24 min at 37 °C with anti-CD45 (760-4279, Roche). Next, secondary Ab incubation was performed with OmniMap anti-Mse HRP (760-4310, Roche) at RT for 20 min followed by the detection Kit Discovery purple (760-247). After Ab denaturation, the slides were incubated for 24 min at 37 °C with anti-HMB45 Ab at a dilution of 1/45 (M0634, Dako) and exposed to the secondary Ab OmniMap anti-Mse HRP (760-4310, Roche) at RT for 20 min, followed by the detection Kit Discovery Green kit (760-271, Roche). Slides were then counterstained with the hematoxylin, dehydrated, and cleared, and a coverslip was applied.

After 7 days of co-culture between 92.1 UM cells and PBMCs, adherent cells were trypsinized and counted. Collected cells (0.3×10^5) were replated in 8-well chamber slides. After cell adherence (24 h), cells were fixed in 4% paraformaldehyde for 25 min at RT. The fixative was removed, and cells were washed twice with PBS. Slides were incubated for 24 min at 37 °C with anti-HMB45 Ab at a dilution of 1/45 (M0634, Dako), washed, and exposed to the secondary Ab, OmniMap anti-Mse Horseradish peroxidase (HRP) (760-4310, Ventana-Roche) at RT for 24 min, followed by the detection Kit Discovery Purple (760-229, Ventana-Roche). After Ab denaturation, the slides were incubated for 24 min at 37 °C with prediluted anti-CD45 Ab (760-4279, Ventana-Roche), washed, and exposed to the same secondary Ab, followed by the detection kit Discovery Teal kit (RUO, 760-247, Roche). The slides were then counterstained with the hematoxylin, dehydrated, and cleared, and a coverslip was applied.

2.5. Statistical Analysis

All statistical analyses were performed using GraphPad Prism (GraphPad Prism version 9.5.0, GraphPad Software Inc., La Jolla, CA, USA). The Spearman's rank test was used for the correlation analysis between infiltrating inflammatory cells (i.e., $CD8^+$ T-cells and $CD68^+$ macrophages) and the presence of DNCs coupled with a linear regression. A Chi-squared test in conjunction with the Fisher's exact test was performed to test for a relationship between the presence of high-risk factors (HRFs) and the presence of DNCs.

3. Results

3.1. Immunohistochemical (IHC) Analysis of UM Tumors

From the 38 patients included in this study, demographic information pertaining to sex and age at the time of diagnosis were available for 36 and 34 of the patients, respectively (Table 1). Of the 36 patients, 56% (n = 20) were male and 44% (n = 16) were female. The mean age at diagnosis was 65.3 (±13.6) years (Table 1). All tumors expressed diffuse staining of UM-specific markers, HMB45 and MelanA (Figure S1).

In parallel, histopathological examination following H&E staining revealed that analyzed tumors exhibited HRFs associated with poor patient prognosis (i.e., large lesions (53%, n = 20), which were predominantly of the epithelioid cell type (61%, n = 23) and the presence of closed vascular loops (34%, n = 13), mitotic figures (42%, n = 16), and scleral invasion (29%, n = 11) (Figure S2).

3.2. Most UM Tumors Contained DNCs with HMB45$^+$/CD45$^+$-, HMB45$^+$/CD8$^+$-, and HMB45$^+$/CD68$^+$-Dominant Phenotypical Profiles

To test for the presence of hybrid cells in the primary UM tumor, IHC double labeling with the melanocytic marker, HMB45, and the pan-leukocytic marker, CD45, was performed on all 38 tumors. Of the 38 tumors, 9 were excluded due to the stain not being present on the slide or due to the tumor being too necrotic. Cells were considered to be HMB45$^+$/CD45$^+$ DNCs when the membrane and/or the cytoplasmic staining demonstrated positive labeling for both markers, and tumors were categorized as positive when at least one DNC was scored (Figure 1A). In contrast, tumors in which the cells had only one marker but were in close proximity to another cell or in which distinct cells were touching with unique nuclei and without any cytoplasmic involvement were considered to be negative. Using these criteria, we detected HMB45$^+$/CD45$^+$ DNCs in 90% (n = 26/29) of the tumors (Figure 1A). When looking at the hybrid cells, they all possessed a singular nucleus and one continuous cell membrane with areas of overlap in positivity between both markers. The melanosome marker, HMB45, displayed a more granular staining appearance in comparison to CD45, which displayed a much smoother or linear staining. Due to high variability in the overall morphology of the cancer and the leukocytic cells, no conformity in size or shape could be seen amongst the HMB45$^+$/CD45$^+$ DNCs.

To gain more insight into the identity of immune cells involved in DNC formation, we looked at the expression of immune-cell-specific markers, namely, cytotoxic T-cells and macrophages.

We evaluated the presence of tumor-infiltrating lymphocytes (TILs) in 30 of the primary tumors, including, mainly, T-cells, by using the pan-T-cell marker CD3. All were positive for CD3, with counts ranging from 1 to >100 TILs in 10 high-power fields (HPFs). Only 9 had moderate to high positivity (>50 TILs in 10 HPFs), with the 21 others having low positivity (<50 TILs in 10 HPFs; Figure S3A).

Despite many tumors having low CD3 positivity, all 38 were double-labeled with HMB45 and CD8, a marker for cytotoxic T-cells. Of the 38 tumors, 10 were removed from the analysis due to there being no stain present on the slide or the majority of the tumor being necrotic. Of the remaining 30 samples, CD8 positivity was seen in 100%, with counts ranging from 7 to >100 cells in 10 HPFs. Moderate to high positivity (>50 TILs in 10 HPFs) was seen in 12 (43%) of the tumors, and low positivity (<50 TILs in 10 HPFs) was seen in the other 16 (57%) tumors (Figure S3B). The presentation of the CD8 T-cells was mainly diffuse, with some multifocal nests. When searching for the presence of HMB45$^+$/CD8$^+$ DNCs, we used the same criteria as those used for HMB45$^+$/CD45$^+$ DNC evaluation. HMB45$^+$/CD8$^+$ DNCs were identified in 93% (n = 26/28) of the tumors (Figure 1B). These HMB45$^+$/CD8$^+$ DNCs had a single nucleus, and although they were all different in size, they demonstrated a similar pattern where the HMB45 marker was positive in most of the perinuclear region, whereas CD8 was positive only on a small portion (Figure 1B). Although the majority of HMB45$^+$/CD8$^+$ DNCs possessed a singular nucleus, multinucleated cells with a positive membrane and/or cytoplasmic staining could also be identified (Figure 1C). To look for a

relationship between the level of TILs and the presence of DNCs, a Spearman rank test was performed. This analysis revealed a significant positive correlation between the number of $CD8^+$ T-cells and the number of $HMB45^+/CD8^+$ hybrid cells counted in 10 HPFs (r = 0.839, linear regression $r^2 = 0.875$, $p < 0.0001$; Figure 1D). Following a Chi-squared test and Fisher's exact test, no statistically significant relationship could be observed between the presence of $HMB45^+/CD8^+$ DNCs and the HRFs present in the primary tumors (Table 2).

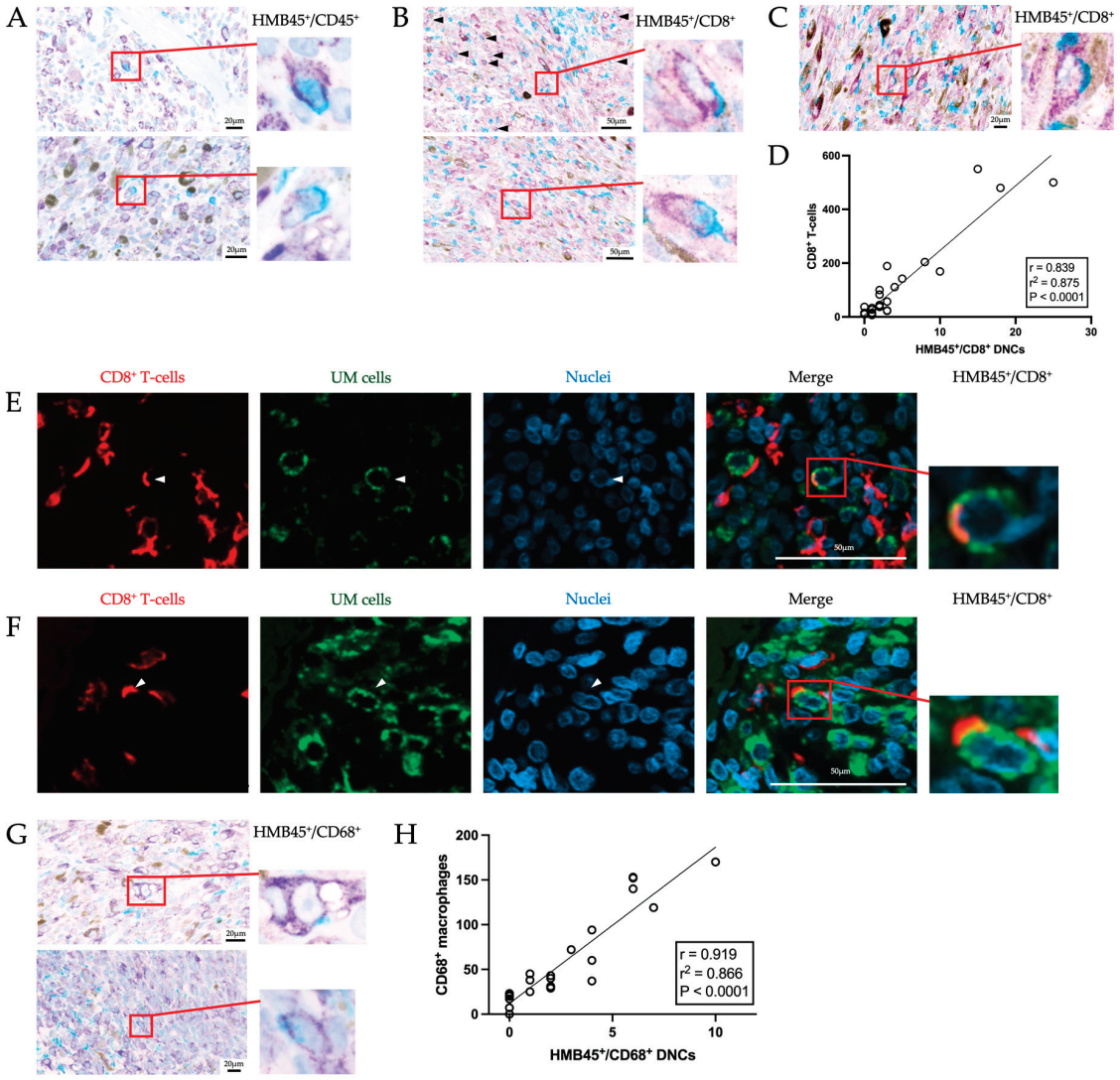


Figure 1. Phenotypic characterization of DNCs in the primary tumor. (**A**) HMB45-positive cells (purple), CD45-positive cells (teal), and $HMB45^+/CD45^+$ DNCs (red boxes) with a higher-power image of the DNCs. (**B**) HMB45-positive cells (purple), CD45-positive cells (teal), and $HMB45^+/CD8^+$ DNCs (black arrowheads and red boxes) with a higher-power image of the DNCs. (**C**) Multinucleated $HMB45^+/CD8^+$ DNC (red box) with a higher-power image of the DNC. (**D**) Spearman correlation of the number of $HMB45^+/CD8^+$ DNCs versus the number of $CD8^+$ T-cells with a significant r value (r = 0.839, $p < 0.0001$). The r^2 value was obtained through linear regression ($r^2 = 0.875$). (**E**) Immunofluorescence labeling with CD8 and HMB45 antibodies as well as DAPI (nuclei) showing an $HMB45^+/CD8^+$ DNC (merge; white arrowheads) and its higher-power image. (**F**) Immunofluorescence labeling with CD8 and HMB45 antibodies as well as DAPI (nuclei) showing a multinucleated $HMB45^+/CD8^+$ DNC (merge; white arrowheads) and its higher-power image. (**G**) HMB45-positive cells (purple), CD68-positive cells (teal), and $HMB45^+/CD68^+$ DNCs (red boxes) with a higher-power image of the DNCs. (**H**) Spearman correlation of the number of $HMB45^+/CD68^+$ DNCs versus the number of $CD68^+$ macrophages with a significant r value (r = 0.919, $p < 0.0001$). The r^2 value was obtained through linear regression ($r^2 = 0.866$).

Table 2. Association between histopathologically determined HRFs and the presence or absence of DNCs.

DNC Staining	Size		Cell Type		Vascular Loops		Mitotic Figures		Scleral Invasion	
	X^2	FET	X^2	FET	X^2	FET	X^2	FET	X^2	FET
HMB45/CD45 (n = 29)	0.0583	0.0996	0.6725	>0.9999	0.2155	0.2668	0.5844	>0.9999	0.2189	0.5320
HMB45/CD8 (n = 28)	>0.9999	>0.9999	0.8322	>0.9999	0.2378	0.5053	0.9136	>0.9999	0.3968	0.4444
HMB45/CD68 (n = 24)	0.6534	>0.9999	0.0247 *	0.0686	0.5254	0.6466	0.0577	0.0850	0.6123	>0.9999

X^2: Chi-squared test; FET: Fisher's exact test; * statistically significant at $p < 0.05$.

Next, five tumors with high numbers of HMB45$^+$/CD8$^+$ DNCs were labeled with immunofluorescent (IF) markers to verify the co-expression of both of these markers in a single cell. Notably, we observed cells with positivity for both the CD8 and the HMB45 marker (Figure 1E). In addition, from these IF-labeled tumors, a subset of HMB45$^+$/CD8$^+$ DNCs could be identified as bi- or multinucleated cells, which also demonstrated the co-localization of HMB45 and CD8 (Figures 1F and S4).

To test tumor-associated macrophages (TAMs) as a potential partner in the formation of DNCs, only 35 of the 38 tumors were double-labeled with HMB45 and CD68 due to some of the blocks being exhausted. Criteria to consider cells to be HMB45$^+$/CD68$^+$ DNC were as stated above for HMB45$^+$/CD45$^+$ DNCs. Of the 35 slides, 11 were removed from the analysis due to there being no stain present on the slide or if the majority of the tumor was necrotic. HMB45$^+$/CD68$^+$ DNCs were present in 71% (n = 17/24) of the tumors (Figure 1G). When looking at the presence of TAMs in the primary tumor, 1 tumor had no macrophages in 10 HPFs, moderate to high positivity (>50 TAMs in 10 HPFs) was seen in 8 tumors (33%), and low positivity (<50 TAMs in 10 HPFs) was seen in 16 tumors (67%) (Figure S3C). To look for a relationship between the level of TAMs and the presence of DNCs, a Spearman rank test was performed. This analysis revealed a significant and positive correlation between the number of CD68$^+$ macrophages and the number of HMB45$^+$/CD68$^+$ hybrid cells counted in 10 HPFs (r = 0.919, linear regression $r^2 = 0.866$, $p < 0.0001$; Figure 1H). Following a Chi-squared test, a statistically significant relationship could be observed between the presence of HMB45$^+$/CD68$^+$ DNCs and the cell type; however, this same significance was not observed after Fisher's exact test (Table 2). The presence of these hybrid cells showed no statistically significant relationship to any of the other HRFs using both tests.

3.3. NCM Cells and PBMCs Are Not Prone to Fusing In Vitro to Form DNCs

To begin, a co-culture between NCM cells and PBMCs was performed to test whether normal melanocytes possess the ability to spontaneously form bi- or multinucleated hybrid cells with normal PBMCs. After 72 h of co-culturing between NCMs and PBMCs, these cells were double-labeled with HMB45 and CD45 antibodies (Figure S5) to search for the presence of any HMB45$^+$/CD45$^+$ DNCs. We did not observe the presence of DNCs in these co-cultures; however, we did observe interactions between both cell types. Given that we defined the formation of DNCs as a single cell with both markers that is single- or multinucleated, the NCM and PBMC co-cultures did not fit these criteria. Conversely, we did observe a tendency for NCMs to form bi- or multinucleated populations within a cell of NCM origin (single-stained HMB45-positive) in the co-cultures but not in the single cultures (Figure S6). When counting at 40X, approximately 5% of the NCMs appeared to be multinucleated.

3.4. UM Cells and PBMCs Are Prone to Fusing In Vitro to Form DNCs

A co-culture approach was used to test if UM cells are capable of a spontaneous interaction with normal PBMCs to form hybrid cells (DNCs) in cell culture, which may be associated with the process of cell fusion. Following co-culture between 92.1 UM cells and PBMCs, as stated in the Materials and Methods, the cells were double-labeled with HMB45

and CD45 antibodies (Figure 2A). When searching for the presence of $HMB45^+/CD45^+$ DNCs, we found cells with a wide variety of shapes and sizes in addition to finding cells that were multinucleated. DNCs presented cytoplasmic positivity for CD45 in the perinuclear region within what we defined as a cancer cell based on its size and HMB45 positivity (Figure 2A).

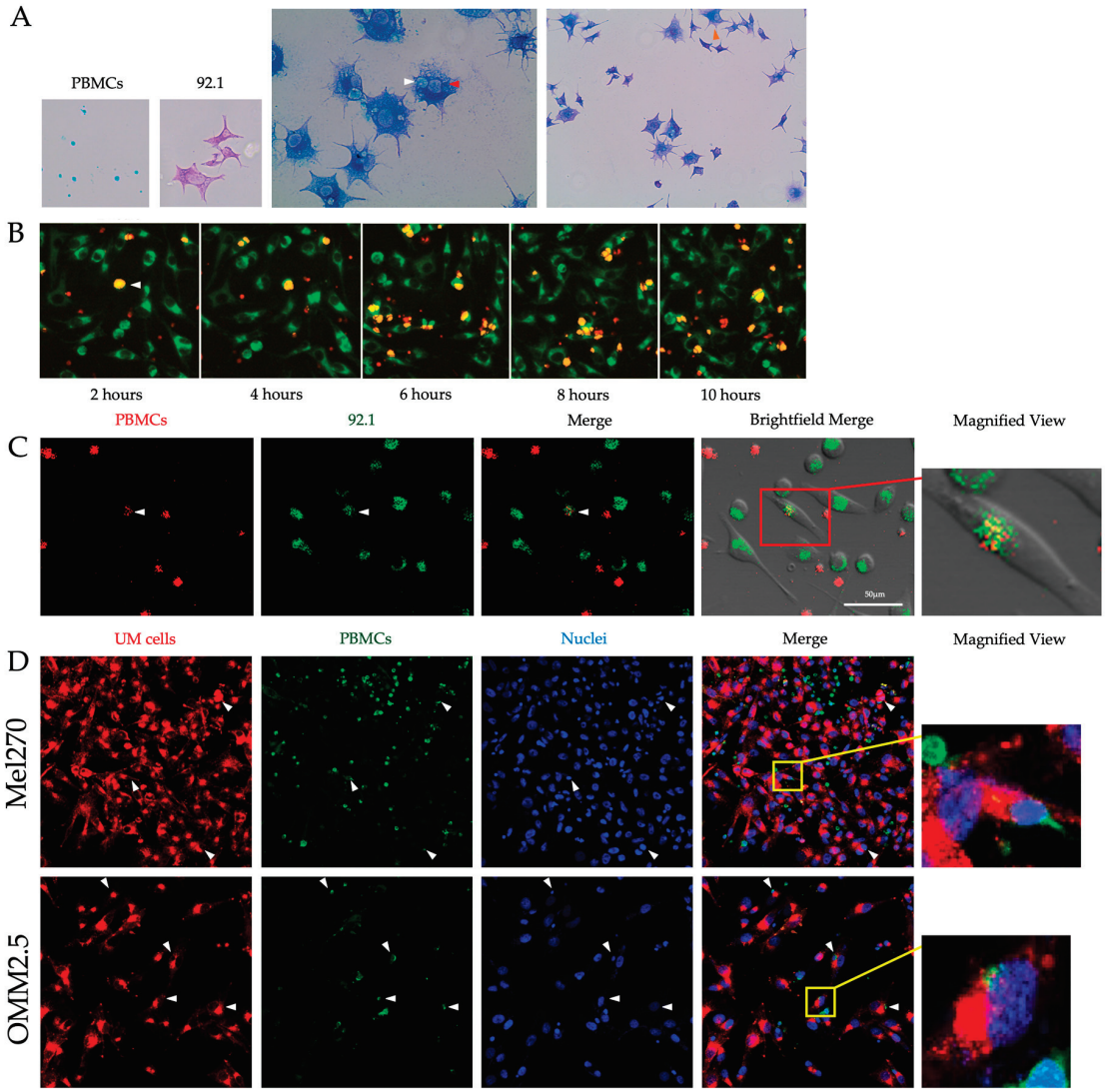


Figure 2. In vitro DNC formation between UM cells and PBMCs. (**A**) PBMCs co-cultured with 92.1 UM cells and immunolabeled with CD45 (teal) and HMB45 (purple), respectively. Multinucleated DNCs with CD45 positivity (white arrowhead) and HMB45 positivity (red arrowhead) imaged at 40× magnification as well as DNCs with CD45 positivity within the cytoplasmic perinuclear region (orange arrowhead) imaged at 20× magnification. (**B**) Real-time live imaging every 2 h under an IncuCyte System of Mitotracker-labeled 92.1 UM cells (green) co-cultured with PKH26-labeled PBMCs (red). Co-localization is interpreted as a positive cell fusion event (DNCs; yellow color, white arrowhead). (**C**) Time-lapse confocal microscopy of PKH26-labeled PBMCs (red) co-cultured with Mitotracker-labeled 92.1 UM cells (green). A cell undergoing fusion (DNC; white arrowhead) can be seen in the merged view coupled to a phase-contrast field view to show the shape of the cells. Higher magnification of the DNC (red box) is shown on the right. (**D**) Confocal microscopy of PBMCs (green; PKH67 dye) co-cultured with Mel270 or OMM2.5 (red; PKH26 dye). Nuclei stained with Dapi (blue). DNCs can be visualized in the merge view (white arrowheads), and a higher magnification of a DNC is shown on the right (yellow boxes).

Next, we performed real-time live cell imaging using the IncuCyte system by tagging 92.1 UM cells and PBMCs with fluorescent mitochondrial or membrane markers, respectively. The UM cells were adhered, stretched, and identified through the presence of perinuclear green staining, and PBMCs were identified as small, round, red moving cells (Figure 2B). Starting at 2 h following the co-cultures, we observed the formation of fused cells reminiscent of DNCs (as judged by the yellow fluorescence; Figure 2B). Notably, the number of fused cells increased in a time-dependent manner and reached a maximum 6 h post-co-culturing.

To further confirm the spontaneous heterotypic fusion event between these cell types, we subjected 92.1 UM cells and PBMC co-cultures to time-lapse confocal microscopy (Figure 2C). Cancer cells were adhered and stretched within the cell culture plate, whereas PBMCs were constantly moving in the medium. Movies were created with images taken every 2 min to address interactions between cells during the time of incubation. A representative snap-shot image showed that 92.1 UM cells and PBMCs fused to form a DNC-like cell. This heterotypic fusion between the two cell types is seen through the display of a yellow color (Figure 2C). Under the phase-contrast view, the PBMC is shown to be in the plane of the adherent cancer cell and, in particular, in close contact with the mitochondrial marker within the limits of the UM cell, thus confirming the cell fusion event (Figure 2C).

To continue elucidating the concept of cell fusion in vitro, the Mel270 and OMM2.5 UM cell lines, which were derived from a primary tumor, and its liver metastasis, respectively, were co-cultured with PBMCs for 24 h. Imaging of these cells was performed via confocal microscopy and revealed the presence of a population of fused cells displaying dual-cell membrane labeling (PKH26 and PKH67) (Figure 2D). These cells appeared to have a single nucleus representing what can be interpreted as a DNC cell similar to what was observed in the primary tumors. Altogether, these data provide evidence for UM cell and immune cell fusion in vitro.

4. Discussion

Seeding of metastasis in UM was initially thought to be predicted by the dissemination of CTCs in the peripheral blood of patients, as systemic disease could be found as early as the time of the primary diagnosis (i.e., treatment-naïve), which made these cells an important prognostic factor for disease progression [30–32,42]. The discovery of hybrid cells in various solid tumors, such as colon, prostate, breast, and intestinal cancers, where these cells are now thought to be a cause of metastasis has led to a shift in research [34,35,43,44]. These CHCs were also identified in the blood of UM patients, where they were studied as a predictor for metastasis [34,35]. Their characterization in patients' blood samples was based on dual phenotypic features; i.e., melanocytic and leukocytic phenotypes ($gp100^+/CD45^+$) [34]. A small subset of primary tumors (n =1 and n = 3) was found to have hybrid cells positive for CD45 and melanocytic markers (Figure 3) [38]. In our study, we tracked these cells in a larger subset of ocular UM lesions using the anti-melanosome HMB45 and CD45 markers. We identified $HMB45^+/CD45^+$ DNCs in 90% (n = 26/29) of the analyzed specimens (Figure 3). This percentage is very close to what was observed when patients' blood was analyzed, as hybrids were identified in 100% of the samples [34]. Given that research on CTCs has demonstrated that UM is much more of a systemic disease and that we know hybrid cells are present in the blood, any differences observed between the primary tumor and the blood may be explained by dissemination from the primary site having already taken place, or the evaluation of the primary tumor may represent an underestimation of the true number of DNCs as a result of the number of tissue sections taken from each tumor [30,34]. It is important to note that many of these hybrid cells might not survive the resolution of the multinucleation, causing only those that succeed to be found in the blood, which are potentially capable of propagating, thus leading to a larger population. Interestingly, in UM and other cancers from solid tumors, CHCs were identified in greater numbers in the blood in comparison to CTCs [34,35]. No statistically significant relationship was observed between the presence of $HMB45^+/CD45^+$

DNCs and HRFs. Overall, just like CHCs in the blood, DNCs in the primary tumor may represent a novel and promising prognostic biomarker and target cell in UM.

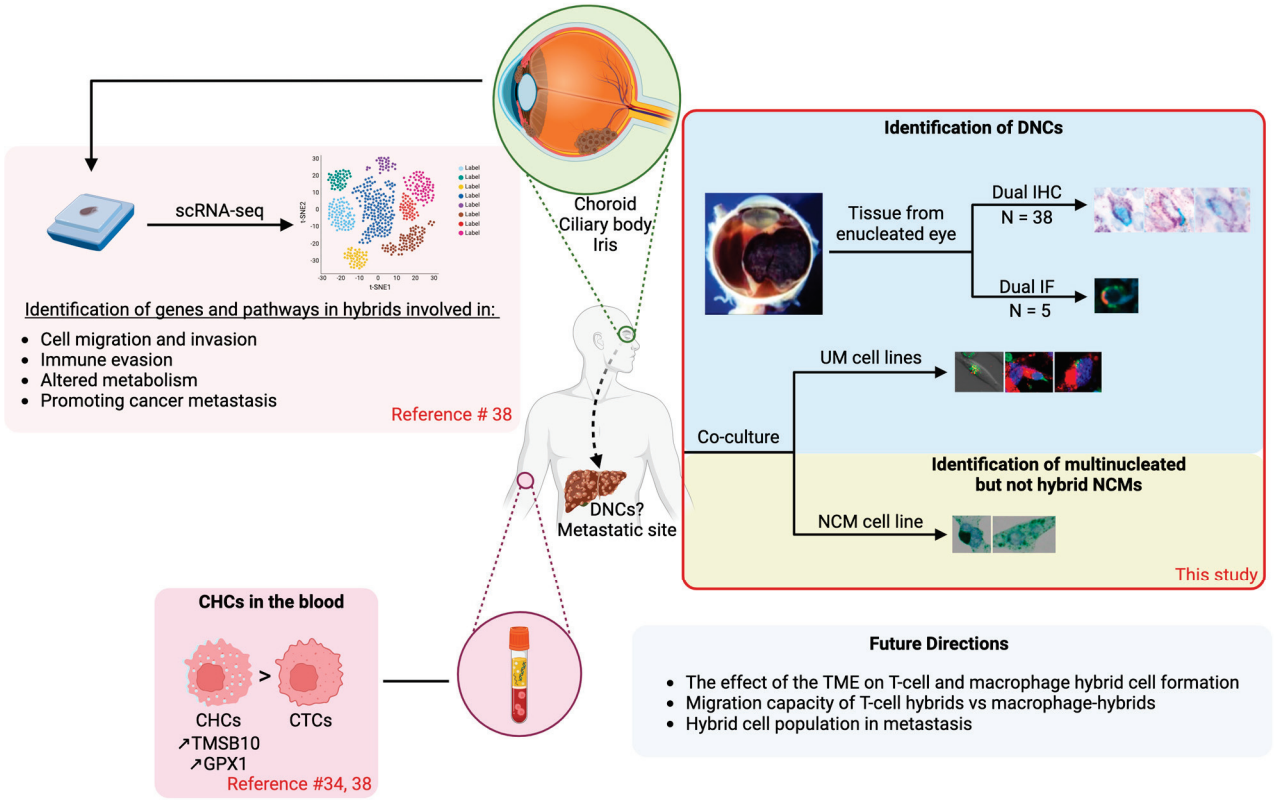


Figure 3. Schematic representation of our study and the relevant literature in relation to hybrid cell formation in UM. A proposed model is shown illustrating the results of NCM interactions and DNC formation in the primary tumor and UM cell lines in our study as well as the relevant hybrid cell literature investigating patient blood and primary samples using single-cell RNA sequencing. GPX1: Glutathione peroxidase 1; TMSB10: Thymosin beta 10. Figure made using BioRender.

We found that the main immune cell players involved in DNC formation were macrophages and cytotoxic T-cells (Figure 3). T-cells, which are part of the adaptive immune system, form a class that is subdivided into three subtypes (i.e., T-helper cells, cytotoxic T-cells, and T-regulatory cells) [23]. In general, hot tumors are characterized by high infiltration of non-exhausted T-cells, especially $CD8^+$ T-cells, whereas cold tumors lack T-cell infiltration and fail to induce T-cell priming [45]. In UM, T-cell infiltration, particularly $CD8^+$ cytotoxic T-cells, has been shown to be an indicator of worse patient prognosis through its correlation with the development of metastasis [12,22,23]. It is known that the most malignant UM tumors have monosomy in chromosome 3 and the absence of the expression of BRCA1-associated protein 1 (BAP1) [46]. BAP1-negative tumors, in particular, have been shown to display an immunosuppressive environment [46]. Furthermore, half of UM tumors display an increased expression of immunomodulatory molecules related to T-cell suppression [46]. This unfavorable immune response causes UM to differ from other solid tumors, including cutaneous melanoma, where the presence of TILs would usually represent a good patient prognosis [23,47]. In our study, we found $CD8^+$ T-cells to be present in 100% of the tumors, with variable levels of infiltration, which is in agreement with the literature [48]. Typically, there was diffuse presentation of these cells, with some focal areas of nest formation, which is also in agreement with the literature [22]. In our analyzed cohort (n = 28), $HMB45^+/CD8^+$ DNCs were identified in 93% (n = 26), with highly variable amounts ranging from 0 to 25 per 10 HPFs. Due to the knowledge that hybrid cells are present in the blood of patients with this disease, the

fluctuation in numbers could either be due to these cells having already migrated to the blood from the primary tumor or because formation has not yet occurred [34]. Given that no statistically significant relationship was observed between these hybrid cells and the analyzed HRFs, and in conjunction with the positive correlation between the number of $CD8^+$ T-cells and the number of $HMB45^+/CD8^+$ DNCs observed, these findings could be an indication that cytotoxic T-cell suppression may be involved in the occurrence of this event. One potential avenue of T-cell suppression is through T-regulatory (Treg) cells. An association has been demonstrated in the literature between the presence of Treg cells in cyclooxygenase-2-positive tumors; however, no direct relationship between the number of Tregs and survival has been shown [49,50]. When looking at the immune profile of UM tumors, CD8 T-cells represent the majority of the infiltration, with few CD4 or Treg cells present [49,51]. Nonetheless, these cells may play a crucial role in hybrid formation through the creation of an immune-suppressive environment. It is also important to note that the T-cell CD3-zeta chain is required for signal transduction, and some studies have shown that some T-cells in UM fail to differentiate or lack this zeta chain [52–54]. The inability to become activated, which is essential for an immune response (thus, the activation of cytotoxic functions in a subset of the T-cell population), may be a reason for T-cells being a predominant partner in this DNC formation. It is also possible that T-cells capable of being activated that are not exhausted or suppressed may still be able to participate in hybridization. More mechanistic studies are warranted to clarify this proposition.

Macrophages, which are part of the innate immune system and play a role in the inflammatory response, have been demonstrated to represent a worse patient prognosis in the context of UM, as opposed to other neoplasms, where the inflammatory response is usually favorable [20,21]. It is important to note that the eye is an immune-privileged site without lymphatics, which may explain this contradiction to other malignancies [55]. Tumor-associated macrophages (TAMs) are divided into the M1 and M2 subtypes. The former has been said to have pro-inflammatory or anti-tumor characteristics, whereas the latter promotes tumor progression through a reduction in T-cell responsiveness (i.e., immunosuppression) and the promotion of angiogenesis [56]. In UM, the M2 ($CD68^+/CD163^+$) population in particular has been shown to represent the majority of these macrophages, with some studies finding as many as 83% of the tumors to be positive for these cells, with moderate to high numbers [57,58]. Although we found the majority of our tumors to be positive for CD68-labeled macrophages (n = 23/24), 67% (n = 16/24) had a very low level of infiltration (<50 in 10 HPFs). This discrepancy, however, could be due to the heterogeneity of macrophages in UM tumors. A recent study characterized four different subtypes of macrophages in the context of this disease, which were present in different proportions for tumors with different classes of gene expression profiles [59]. Despite not finding moderate to high numbers of macrophages in the majority of our patient tumors, their potential role in DNC formation was still investigated, as the literature has shown macrophage–cancer cell fusion in breast and intestinal cancers, hinting that this cell type may still contribute to DNC formation [43,44]. In our study, $HMB45^+/CD68^+$ DNCs were identified in 71% (n = 17/24) of the tumors, and the quantity of these DNCs was found to positively correlate ($p < 0.0001$) with the level of TAM infiltration. When looking at the relationship between the presence of these hybrids and HRFs, significance was observed only with cell type following the Chi-squared test but not Fisher's exact test. Given the small N-value for the number of tumors absent for DNCs (n = 7) and that this value is then split between the two possible cell types (i.e., epithelioid vs. spindle), the Chi-squared test, which calculates an approximate P value, may not have been accurate enough. Since Fisher's exact test did not reveal this same significance, the result has been interpreted as not significant. Altogether, these results lead us to believe that macrophages do participate in DNC formation; however, the specific subtypes and their potential role after dissemination to the blood remains unclear.

Cell–cell fusion is still not a fully understood or characterized process. It is a tightly regulated and energy-dependent process where the plasma membranes of cells under

favorable conditions fuse, leading to the formation of a hybrid cell [36,37]. During a transitional state, hybrid cells carry two or more nuclei from different parental cells [36,37]. This is followed by a post-hybrid selection process to form a new, functional, altered hybrid cell [36,37]. Several studies have been published indicating that cell–cell fusion occurs in cancer, and that hybrid cells might include homotypic fusion between cancer cells or occur with normal cells from the microenvironment via heterotypic fusion [36]. In the context of normal melanocytes, exogenous (e.g., ultraviolet damage) or endogenous (e.g., oncogenic mutation) stressors as well as the development of a senescent phenotype can lead to the formation of multinucleated melanocytes [60,61]. As the literature suggests, our single cultures of NCMs did not reveal any polyploid cells. However, our results did demonstrate the presence of multinucleated melanocytes in the co-cultures, suggesting that the presence of PBMCs may either damage the NCMs or provide environmental stimuli, thus allowing for NCMs to multinucleate with one another (Figure 3). Moreover, normal melanocytes have also been shown to be capable of forming hybrids with melanoma cancer cells [62]. However, to the best of our knowledge, this hybridization has not been previously demonstrated between NCMs and PBMCs. Following these co-cultures, we did not observe the presence of hybrid cells but rather the presence of cell–cell interactions. In other words, this process of multinucleation appears to be a damage-induced or cancer-acquired trait. It is also important to note that the previous literature has not reported the presence of NCMs in the blood [30,63]. Therefore, these cells and their potential crosstalk with immune cells may be more relevant in the context of tumor initiation rather than its metastasis.

To expand on the in vitro context of cell–cell fusion, the 92.1 UM cell line used in the in vitro studies was derived from different areas of a primary tumor that had 2–3+ infiltrating macrophages and 1–2+ infiltrating CD3 cells [41]. This cell line conserves the same mutation in GNAQ Q209L mutation, the gene responsible for encoding the alpha subunit of a heterotrimeric G protein that controls the activation of various downstream signaling pathways [64,65]. The Mel270 and OMM2.5 cell lines conserve a mutation in GNAQ *Q209P*, and they were derived from the primary site and liver metastasis of the same patient, respectively [65]. In this study, we found that co-culturing 92.1, Mel270, and OMM2.5 UM cells with PBMCs demonstrated the presence of a spontaneous cell–cell interaction, representing the formation of bi- or multinucleated cells after incubation (Figure 3). The formation of these double-labeled cells may involve the attachment of the PBMC and the malignant melanocyte, followed by a subsequent fusion process, thus creating a heterokaryon if bi-nucleated or a synkaryon if multinucleated [66]. The polyploid cells observed in the 92.1 UM cell line did not appear to undergo the process of genetic hybridization, which would result in a single nucleus being present. The reason for this may be that the cells in culture needed more time or different conditions to allow this increased ploidy to be resolved. On the other hand, the increased ploidy may be beneficial for hybrid cells. In fact, it has been suggested that polyploid cells may harbor an advantage against normal cells under stressful situations, such as chemotherapy or radiation, which are common therapeutic strategies against cancers [66–69]. Despite this, in the primary tumors, the majority of cells that fit the inclusion criteria set to be considered a DNC appeared to have only one nucleus, which is similar to what was observed in vitro with the Mel270 and OMM2.5 cell lines. However, some cells in the primary tumor representing a multinucleated population were identified and were similar to what was observed in the 92.1 UM cell line in vitro co-culture experiments. It is important to note that other studies on hybrid cells in various cancers do support the idea of fusion through the discovery of novel sets of RNA transcripts, the incorporation of genetic material, and patterns of gene expression [44,70–72]. In addition to this, hybrid cells have also been demonstrated in studies through the existence of tumor DNA in non-cancer cells or the presence of the Y chromosome in female cancer patients with a former bone marrow transplantation [73]. Further analyses are necessary to confirm that fusion between both cell types is the reason for DNC formation in this situation. Moreover, the presence of hybrid cells in vitro in both the primary (Mel270) and metastatic (OMM2.5) cell lines derived from a single

patient suggests that these hybrids may in fact play a role in cancer progression and the development of metastasis. Further in vivo analyses would be required to draw specific conclusions about DNC involvement in metastasis. Nonetheless, the generation of DNCs in vitro might help in the study of the behavior of these cells and their use in platforms testing for novel UM therapeutics.

5. Conclusions

UM remains a disease with an unclear pathogenesis of systemic disease and metastasis. In this study, DNCs were identified in the majority of primary UMs tumors when double-labeled with HMB45 and the pan-leukocytic marker CD45. The discovery of this hybrid cell in the majority of the primary tumors suggests that these cells may play a role in the pathogenesis of the disease. When investigating leukocytic cell types capable of DNC formation, both $CD68^+$ macrophages and $CD8^+$ T-cells were identified as being able to participate in this event of hybrid cell formation. All of the primary melanomas in this study displayed T-cell infiltration, and the majority of them showed the presence of macrophages. Poor prognosis for patients with UM is associated with T-cell infiltration and a high density of macrophages; therefore, the presence of DNC formation with both cell types in primary UM suggests that this event may be a prominent mediator in the pathogenesis of the disease. The identification of the cell types capable of forming these novel DNCs creates a possible new therapeutic target. In addition to this, our studies revealed that UM cells retain the capacity to form DNCs in vitro in both primary (92.1 and Mel270) and metastatic (OMM2.5) cell lines, which may be the result of a heterotypic fusion.

We believe that this study will open new avenues to understanding UM development and progression. Future directions should investigate spontaneous DNC formation in vitro with other UM cell lines and PBMCs, including, in particular, CD8 T-cells and macrophages, to determine whether DNCs acquire any metastatic or growth advantages compared to the respective cancer cells. These in vitro co-cultures should also be expanded to include fluorescence in situ hybridization to assess for any genomic alterations (i.e., gain of function mutations) as a result of fusion. We also plan to study the tumorigenic capacity of DNCs in animal models to determine the kinetics of DNC genesis and to investigate whether drugs on the market or currently in clinical trials are able to target these cells for destruction to hopefully extend the period of progression-free survival for patients. In addition, upcoming studies should address the presence of DNCs at metastatic sites and assess the immune cell types involved in this hybrid cell formation. Finally, we plan to investigate the presence of $HMB45^+/CD68^+$ and $HMB45^+/CD8^+$ DNCs in the blood of UM patients and perform spatial transcriptomics on primary tumors to hopefully help shed more light on the pathogenesis of this disease.

Supplementary Materials: The following supporting information can be downloaded at https://www.mdpi.com/article/10.3390/cancers16183231/s1, Figure S1: Representative images of positive control special stains in UM at 10 × magnification; Figure S2: Representative images of UM lesions with histopathological high-risk factors in UM; Figure S3: Representative images of the levels of infiltration of inflammatory cells in primary UM tumors at 10× magnification; Figure S4: Multinucleated $HMB45^+/CD8^+$ DNCs; Figure S5: NCMs and PBMCs alone and their co-cultures; Figure S6: Multinucleated cell formation following co-culture experiments.

Author Contributions: Conceptualization, E.M., A.G., M.A. and M.N.B.J.; methodology, E.M., A.G. and M.A.; validation, E.M., A.G. and M.A.; formal analysis, E.M.; investigation, E.M., A.G. and M.A.; resources, E.M., A.G. and M.A.; data curation, E.M., A.G. and M.A.; writing—original draft preparation, E.M.; writing—review and editing, E.M., A.G., M.A., J.V.B. and M.N.B.J.; visualization, E.M., A.G. and M.A.; supervision, M.N.B.J.; project administration, E.M. and M.N.B.J.; funding acquisition, E.M. All authors have read and agreed to the published version of the manuscript.

Funding: E.M. received a scholarship/bursary through the Canada Graduate Scholarship Masters (CGS M) program of the Canadian Institutes of Health Research (CIHR) and a Studentship and Fellowship scholarship from the Research Institute of the McGill University Health Centre (RI-MUHC).

Institutional Review Board Statement: The study was conducted in accordance with the Declaration of Helsinki and approved by the Institutional Review Board of the RI-MUHC (protocol IRB #2018-4187, 20 December 2023; protocol IRB #2019-5314, 22 January 2019).

Informed Consent Statement: Informed consent was obtained from all subjects involved in this study.

Data Availability Statement: The original contributions presented in the study are included in the article/supplementary material, further inquiries can be directed to the corresponding author.

Acknowledgments: The authors are grateful for the help provided by the CORE Histopathology platform at the RI-MUHC and the CORE Molecular Imaging Platform of the RI-MUHC for their technical assistance. We would also like to thank Yunxi Chen from Julia Burnier's laboratory for providing the NCMs and for her expertise in the recovery of these cells.

Conflicts of Interest: The authors declare no conflicts of interest.

References

1. Singh, A.D.; Turell, M.E.; Topham, A.K. Uveal melanoma: Trends in incidence, treatment, and survival. *Ophthalmology* **2011**, *118*, 1881–1885. [CrossRef] [PubMed]
2. Virgili, G.; Gatta, G.; Ciccolallo, L.; Capocaccia, R.; Biggeri, A.; Crocetti, E.; Lutz, J.M.; Paci, E. Incidence of uveal melanoma in Europe. *Ophthalmology* **2007**, *114*, 2309–2315. [CrossRef]
3. Vajdic, C.M.; Kricker, A.; Giblin, M.; McKenzie, J.; Aitken, J.; Giles, G.G.; Armstrong, B.K. Incidence of ocular melanoma in Australia from 1990 to 1998. *Int. J. Cancer* **2003**, *105*, 117–122. [CrossRef]
4. Kaliki, S.; Shields, C.L. Uveal melanoma: Relatively rare but deadly cancer. *Eye* **2017**, *31*, 241–257. [CrossRef]
5. Shields, C.L.; Furuta, M.; Thangappan, A.; Nagori, S.; Mashayekhi, A.; Lally, D.R.; Kelly, C.C.; Rudich, D.S.; Nagori, A.V.; Wakade, O.A.; et al. Metastasis of uveal melanoma millimeter-by-millimeter in 8033 consecutive eyes. *Arch. Ophthalmol.* **2009**, *127*, 989–998. [CrossRef] [PubMed]
6. Damato, B.; Kacperek, A.; Errington, D.; Heimann, H. Proton beAm. radiotherapy of uveal melanoma. *Saudi J. Ophthalmol.* **2013**, *27*, 151–157. [CrossRef] [PubMed]
7. Jensen, O.A. Malignant melanomas of the human uvea: 25-year follow-up of cases in Denmark, 1943–1952. *Acta Ophthalmol.* **1982**, *60*, 161–182. [CrossRef]
8. Kujala, E.; Mäkitie, T.; Kivelä, T. Very long-term prognosis of patients with malignant uveal melanoma. *Investig. Ophthalmol. Vis. Sci.* **2003**, *44*, 4651–4659. [CrossRef]
9. Stålhammar, G.; Herrspiegel, C. Long-term relative survival in uveal melanoma: A systematic review and meta-analysis. *Commun. Med.* **2022**, *2*, 18. [CrossRef]
10. Collaborative Ocular Melanoma Study Group. Assessment of metastatic disease status at death in 435 patients with large choroidal melanoma in the Collaborative Ocular Melanoma Study (COMS): COMS report no. 15. *Arch. Ophthalmol.* **2001**, *119*, 670–676. [CrossRef]
11. Diener-West, M.; Reynolds, S.M.; Agugliaro, D.J.; Caldwell, R.; Cumming, K.; Earle, J.D.; Hawkins, B.S.; Hayman, J.A.; Jaiyesimi, I.; Jampol, L.M.; et al. Development of metastatic disease after enrollment in the COMS trials for treatment of choroidal melanoma: Collaborative Ocular Melanoma Study Group Report No. 26. *Arch. Ophthalmol.* **2005**, *123*, 1639–1643. [CrossRef] [PubMed]
12. Singh, A.D.; Shields, C.L.; Shields, J.A. Prognostic factors in uveal melanoma. *Melanoma Res.* **2001**, *11*, 255–263. [CrossRef] [PubMed]
13. Lamas, N.J.; Martel, A.; Nahon-Estève, S.; Goffinet, S.; Macocco, A.; Bertolotto, C.; Lassalle, S.; Hofman, P. Prognostic Biomarkers in Uveal Melanoma: The Status Quo, Recent Advances and Future Directions. *Cancers* **2021**, *14*, 96. [CrossRef]
14. Shields, C.L.; Kaliki, S.; Furuta, M.; Fulco, E.; Alarcon, C.; Shields, J.A. American Joint Committee on Cancer classification of posterior uveal melanoma (tumor size category) predicts prognosis in 7731 patients. *Ophthalmology* **2013**, *120*, 2066–2071. [CrossRef]
15. McLean, I.W.; Foster, W.D.; Zimmerman, L.E. Uveal melanoma: Location, size, cell type, and enucleation as risk factors in metastasis. *Hum. Pathol.* **1982**, *13*, 123–132. [CrossRef]
16. McLean, I.W.; Keefe, K.S.; Burnier, M.N. Uveal melanoma. Comparison of the prognostic value of fibrovascular loops, mean of the ten largest nucleoli, cell type, and tumor size. *Ophthalmology* **1997**, *104*, 777–780. [CrossRef] [PubMed]
17. Folberg, R.; Rummelt, V.; Parys-Van Ginderdeuren, R.; Hwang, T.; Woolson, R.F.; Pe'er, J.; Gruman, L.M. The prognostic value of tumor blood vessel morphology in primary uveal melanoma. *Ophthalmology* **1993**, *100*, 1389–1398. [CrossRef] [PubMed]
18. McLean, M.J.; Foster, W.D.; Zimmerman, L.E. Prognostic factors in small malignant melanomas of choroid and ciliary body. *Arch. Ophthalmol.* **1977**, *95*, 48–58. [CrossRef]

19. Affeldt, J.C.; Minckler, D.S.; Azen, S.P.; Yeh, L. Prognosis in uveal melanoma with extrascleral extension. *Arch. Ophthalmol.* **1980**, *98*, 1975–1979. [CrossRef]
20. Jager, M.J.; Ly, L.V.; El Filali, M.; Madigan, M.C. Macrophages in uveal melanoma and in experimental ocular tumor models: Friends or foes? *Prog. Retin. Eye Res.* **2011**, *30*, 129–146. [CrossRef]
21. Herwig, M.C.; Grossniklaus, H.E. Role of macrophages in uveal melanoma. *Expert Rev. Ophthalmol.* **2011**, *6*, 405–407. [CrossRef] [PubMed]
22. Whelchel, J.C.; Farah, S.E.; McLean, I.W.; Burnier, M.N. Immunohistochemistry of infiltrating lymphocytes in uveal malignant melanoma. *Investig. Ophthalmol. Vis. Sci.* **1993**, *34*, 2603–2606.
23. Triozzi, P.L.; Schoenfield, L.; Plesec, T.; Saunthararajah, Y.; Tubbs, R.R.; Singh, A.D. Molecular profiling of primary uveal melanomas with tumor-infiltrating lymphocytes. *Oncoimmunology* **2019**, *8*, e947169. [CrossRef] [PubMed]
24. Gelmi, M.C.; Bas, Z.; Malkani, K.; Ganguly, A.; Shields, C.L.; Jager, M.J. Adding the Cancer Genome Atlas Chromosome Classes to American Joint Committee on Cancer System Offers More Precise Prognostication in Uveal Melanoma. *Ophthalmology* **2022**, *129*, 431–437. [CrossRef]
25. Li, H.; Li, Q.; Dang, K.; Ma, S.; Cotton, J.L.; Yang, S.; Zhu, L.J.; Deng, A.C.; Ip, Y.T.; Johnson, R.L.; et al. YAP/TAZ Activation Drives Uveal Melanoma Initiation and Progression. *Cell Rep.* **2019**, *29*, 3200–3211. [CrossRef] [PubMed]
26. Yu, F.X.; Luo, J.; Mo, J.S.; Liu, G.; Kim, Y.C.; Meng, Z.; Zhao, L.; Peyman, G.; Ouyang, H.; Jiang, W.; et al. Mutant Gq/11 promote uveal melanoma tumorigenesis by activating YAP. *Cancer Cell* **2014**, *25*, 822–830. [CrossRef]
27. Boru, G.; Cebulla, C.M.; Sample, K.M.; Massengill, J.B.; Davidorf, F.H.; Abdel-Rahman, M.H. Heterogeneity in Mitogen-Activated Protein Kinase (MAPK) Pathway Activation in Uveal Melanoma With Somatic GNAQ and GNA11 Mutations. *Investig. Ophthalmol. Vis. Sci.* **2019**, *60*, 2474–2480. [CrossRef]
28. Mukhopadhyay, S.; Huang, H.Y.; Lin, Z.; Ranieri, M.; Li, S.; Sahu, S.; Liu, Y.; Ban, Y.; Guidry, K.; Hu, H.; et al. Genome-Wide CRISPR Screens Identify Multiple Synthetic Lethal Targets That Enhance KRASG12C Inhibitor Efficacy. *Cancer Res.* **2023**, *83*, 4095–4111. [CrossRef]
29. Jin, E.; Burnier, J.V. Liquid Biopsy in Uveal Melanoma: Are We There Yet? *Ocul. Oncol. Pathol.* **2021**, *7*, 1–16. [CrossRef]
30. Callejo, S.A.; Antecka, E.; Blanco, P.L.; Edelstein, C.; Burnier, M.N., Jr. Identification of circulating malignant cells and its correlation with prognostic factors and treatment in uveal melanoma. A prospective longitudinal study. *Eye* **2007**, *21*, 752–759. [CrossRef]
31. Torres, V.; Triozzi, P.; Eng, C.; Tubbs, R.; Schoenfiled, L.; Crabb, J.W.; Saunthararajah, Y.; Singh, A.D. Circulating tumor cells in uveal melanoma. *Future Oncol.* **2011**, *7*, 101–109. [CrossRef] [PubMed]
32. Anand, K.; Roszik, J.; Gombos, D.; Upshaw, J.; Sarli, V.; Meas, S.; Lucci, A.; Hall, C.; Patel, S. Pilot Study of Circulating Tumor Cells in Early-Stage and Metastatic Uveal Melanoma. *Cancers* **2019**, *11*, 856. [CrossRef] [PubMed]
33. Logan, P.T.; Fernandes, B.F.; Di Cesare, S.; Marshall, J.C.; Maloney, S.C.; Burnier, M.N., Jr. Single-cell tumor dormancy model of uveal melanoma. *Clin. Exp. Metastasis* **2008**, *25*, 509–516. [CrossRef] [PubMed]
34. Parappilly, M.S.; Chin, Y.; Whalen, R.M.; Anderson, A.N.; Robinson, T.S.; Strgar, L.; Sutton, T.L.; Conley, P.; Klocke, C.; Gibbs, S.L.; et al. Circulating Neoplastic-Immune Hybrid Cells Predict Metastatic Progression in Uveal Melanoma. *Cancers* **2022**, *14*, 4617. [CrossRef]
35. Dietz, M.S.; Sutton, T.L.; Walker, B.S.; Gast, C.E.; Zarour, L.; Sengupta, S.K.; Swain, J.R.; Eng, J.; Parappilly, M.; Limbach, K.; et al. Relevance of circulating hybrid cells as a non-invasive biomarker for myriad solid tumors. *Sci. Rep.* **2021**, *11*, 13630. [CrossRef]
36. Hass, R.; von der Ohe, J.; Dittmar, T. Hybrid Formation and Fusion of Cancer Cells In Vitro and In Vivo. *Cancers* **2021**, *13*, 4496. [CrossRef]
37. Tretyakova, M.S.; Subbalakshmi, A.R.; Menyailo, M.E.; Jolly, M.K.; Denisov, E.V. Tumor Hybrid Cells: Nature and Biological Significance. *Front. Cell Dev. Biol.* **2022**, *10*, 814714. [CrossRef] [PubMed]
38. Anderson, A.N.; Conley, P.; Klocke, C.D.; Sengupta, S.K.; Pang, A.; Farley, H.C.; Gillingham, A.R.; Dawson, A.D.; Fan, Y.; Jones, J.A.; et al. Detection of neoplastic-immune hybrid cells with metastatic properties in uveal melanoma. *Biomark Res.* **2024**, *12*, 67. [CrossRef]
39. McLean, I.W.; Foster, W.D.; Zimmerman, L.E.; Gamel, J.W. Modifications of Callender's classification of uveal melanoma at the Armed Forces Institute of Pathology. *Am. J. Ophthalmol.* **1983**, *96*, 502–509. [CrossRef]
40. Valtink, M.; Engelmann, K. Serum-free cultivation of adult normal human choroidal melanocytes. *Graefes Arch. Clin. Exp. Ophthalmol.* **2007**, *245*, 1487–1494. [CrossRef]
41. Jager, M.J.; Magner, J.A.; Ksander, B.R.; Dubovy, S.R. Uveal Melanoma Cell Lines: Where do they come from? (An American Ophthalmological Society Thesis). *Trans. Am. Ophthalmol. Soc.* **2016**, *114*, T5. [PubMed]
42. Finger, P.T.; Kurli, M.; Reddy, S.; Tena, L.B.; Pavlick, A.C. Whole body PET/CT for initial staging of choroidal melanoma. *Br. J. Ophthalmol.* **2005**, *89*, 1270–1274. [CrossRef] [PubMed]
43. Shabo, I.; Midtbö, K.; Andersson, H.; Åkerlund, E.; Olsson, H.; Wegman, P.; Gunnarsson, C.; Lindström, A. Macrophage traits in cancer cells are induced by macrophage-cancer cell fusion and cannot be explained by cellular interaction. *BMC Cancer* **2015**, *15*, 922. [CrossRef] [PubMed]
44. Powell, A.E.; Anderson, E.C.; Davies, P.S.; Silk, A.D.; Pelz, C.; Impey, S.; Wong, M.H. Fusion between Intestinal epithelial cells and macrophages in a cancer context results in nuclear reprogramming. *Cancer Res.* **2011**, *71*, 1497–1505. [CrossRef] [PubMed]

45. Raskov, H.; Orhan, A.; Christensen, J.P.; Gögenur, I. Cytotoxic CD8(+) T cells in cancer and cancer immunotherapy. *Br. J. Cancer* **2021**, *124*, 359–367. [CrossRef]
46. Gezgin, G.; Visser, M.; Ruano, D.; Santegoets, S.J.; de Miranda, N.; van der Velden, P.A.; Luyten, G.P.M.; van der Burg, S.H.; Verdegaal, E.M.; Jager, M.J. Tumor-Infiltrating T Cells Can Be Expanded Successfully from Primary Uveal Melanoma after Separation from Their Tumor Environment. *Ophthalmol. Sci.* **2022**, *2*, 100132. [CrossRef]
47. Tuthill, R.J.; Unger, J.M.; Liu, P.Y.; Flaherty, L.E.; Sondak, V.K. Risk assessment in localized primary cutaneous melanoma: A Southwest Oncology Group study evaluating nine factors and a test of the Clark logistic regression prediction model. *Am. J. Clin. Pathol.* **2002**, *118*, 504–511. [CrossRef]
48. Bronkhorst, I.H.; Vu, T.H.; Jordanova, E.S.; Luyten, G.P.; Burg, S.H.; Jager, M.J. Different subsets of tumor-infiltrating lymphocytes correlate with macrophage influx and monosomy 3 in uveal melanoma. *Investig. Ophthalmol. Vis. Sci.* **2012**, *53*, 5370–5378. [CrossRef]
49. Lagouros, E.; Salomao, D.; Thorland, E.; Hodge, D.O.; Vile, R.; Pulido, J.S. Infiltrative T regulatory cells in enucleated uveal melanomas. *Trans. Am. Ophthalmol. Soc.* **2009**, *107*, 223–228.
50. Mougiakakos, D.; Johansson, C.C.; Trocme, E.; All-Ericsson, C.; Economou, M.A.; Larsson, O.; Seregard, S.; Kiessling, R. Intratumoral forkhead box P3-positive regulatory T cells predict poor survival in cyclooxygenase-2-positive uveal melanoma. *Cancer* **2010**, *116*, 2224–2233. [CrossRef]
51. Bronkhorst, I.H.; Jager, M.J. Inflammation in uveal melanoma. *Eye* **2013**, *27*, 217–223. [CrossRef] [PubMed]
52. Niederkorn, J.Y. Immunoregulation of intraocular tumours. *Eye* **1997**, *11 Pt 2*, 249–254. [CrossRef]
53. Staibano, S.; Mascolo, M.; Tranfa, F.; Salvatore, G.; Mignogna, C.; Bufo, P.; Nugnes, L.; Bonavolontà, G.; De Rosa, G. Tumor infiltrating lymphocytes in uveal melanoma: A link with clinical behavior? *Int. J. Immunopathol. Pharmacol.* **2006**, *19*, 171–179. [CrossRef] [PubMed]
54. Irving, B.A.; Weiss, A. The cytoplasmic domain of the T cell receptor zeta chain is sufficient to couple to receptor-associated signal transduction pathways. *Cell* **1991**, *64*, 891–901. [CrossRef]
55. Zhou, R.; Caspi, R.R. Ocular immune privilege. *F1000 Biol. Rep.* **2010**, *2*, 1885–1889. [CrossRef]
56. Bronkhorst, I.H.; Jager, M.J. Uveal melanoma: The inflammatory microenvironment. *J. Innate Immun.* **2012**, *4*, 454–462. [CrossRef] [PubMed]
57. Bronkhorst, I.H.; Ly, L.V.; Jordanova, E.S.; Vrolijk, J.; Versluis, M.; Luyten, G.P.; Jager, M.J. Detection of M2-macrophages in uveal melanoma and relation with survival. *Investig. Ophthalmol. Vis. Sci.* **2011**, *52*, 643–650. [CrossRef]
58. Mäkitie, T.; Summanen, P.; Tarkkanen, A.; Kivelä, T. Tumor-infiltrating macrophages (CD68(+) cells) and prognosis in malignant uveal melanoma. *Investig. Ophthalmol. Vis. Sci.* **2001**, *42*, 1414–1421.
59. Li, K.; Sun, L.; Wang, Y.; Cen, Y.; Zhao, J.; Liao, Q.; Wu, W.; Sun, J.; Zhou, M. Single-cell characterization of macrophages in uveal melanoma uncovers transcriptionally heterogeneous subsets conferring poor prognosis and aggressive behavior. *Exp. Mol. Med.* **2023**, *55*, 2433–2444. [CrossRef]
60. Leikam, C.; Hufnagel, A.L.; Otto, C.; Murphy, D.J.; Mühling, B.; Kneitz, S.; Nanda, I.; Schmid, M.; Wagner, T.U.; Haferkamp, S.; et al. In vitro evidence for senescent multinucleated melanocytes as a source for tumor-initiating cells. *Cell Death Dis.* **2015**, *6*, e1711. [CrossRef]
61. Meierjohann, S. Effect of stress-induced polyploidy on melanoma reprogramming and therapy resistance. *Semin. Cancer Biol.* **2022**, *81*, 232–240. [CrossRef] [PubMed]
62. Wakeling, W.F.; Greetham, J.; Bennett, D.C. Efficient spontaneous fusion between some co-cultured cells, especially murine melanoma cells. *Cell Biol. Int.* **1994**, *18*, 207–210. [CrossRef] [PubMed]
63. Smith, B.; Selby, P.; Southgate, J.; Pittman, K.; Bradley, C.; Blair, G.E. Detection of melanoma cells in peripheral blood by means of reverse transcriptase and polymerase chain reaction. *Lancet* **1991**, *338*, 1227–1229. [CrossRef] [PubMed]
64. Silva-Rodríguez, P.; Fernández-Díaz, D.; Bande, M.; Pardo, M.; Loidi, L.; Blanco-Teijeiro, M.J. GNAQ and GNA11 Genes: A Comprehensive Review on Oncogenesis, Prognosis and Therapeutic Opportunities in Uveal Melanoma. *Cancers* **2022**, *14*, 3066. [CrossRef]
65. Griewank, K.G.; Yu, X.; Khalili, J.; Sozen, M.M.; Stempke-Hale, K.; Bernatchez, C.; Wardell, S.; Bastian, B.C.; Woodman, S.E. Genetic and molecular characterization of uveal melanoma cell lines. *Pigment. Cell Melanoma Res.* **2012**, *25*, 182–187. [CrossRef]
66. Shabo, I.; Svanvik, J.; Lindström, A.; Lechertier, T.; Trabulo, S.; Hulit, J.; Sparey, T.; Pawelek, J. Roles of cell fusion, hybridization and polyploid cell formation in cancer metastasis. *World J. Clin. Oncol.* **2020**, *11*, 121–135. [CrossRef]
67. Anatskaya, O.V.; Vinogradov, A.E. Genome multiplication as adaptation to tissue survival: Evidence from gene expression in mammalian heart and liver. *Genomics* **2007**, *89*, 70–80. [CrossRef]
68. Duncan, A.W.; Hickey, R.D.; Paulk, N.K.; Culberson, A.J.; Olson, S.B.; Finegold, M.J.; Grompe, M. Ploidy reductions in murine fusion-derived hepatocytes. *PLoS Genet.* **2009**, *5*, e1000385. [CrossRef]
69. Lindström, A.; Midtbö, K.; Arnesson, L.G.; Garvin, S.; Shabo, I. Fusion between M2-macrophages and cancer cells results in a subpopulation of radioresistant cells with enhanced DNA-repair capacity. *Oncotarget* **2017**, *8*, 51370–51386. [CrossRef]
70. Lu, X.; Kang, Y. Efficient acquisition of dual metastasis organotropism to bone and lung through stable spontaneous fusion between MDA-MB-231 variants. *Proc. Natl. Acad. Sci. USA* **2009**, *106*, 9385–9390. [CrossRef]
71. Pawelek, J.M.; Chakraborty, A.K. The cancer cell--leukocyte fusion theory of metastasis. *Adv. Cancer Res.* **2008**, *101*, 397–444. [CrossRef] [PubMed]

72. Sieler, M.; Weiler, J.; Dittmar, T. Cell-Cell Fusion and the Roads to Novel Properties of Tumor Hybrid Cells. *Cells* **2021**, *10*, 1465. [CrossRef] [PubMed]
73. Gast, C.E.; Silk, A.D.; Zarour, L.; Riegler, L.; Burkhart, J.G.; Gustafson, K.T.; Parappilly, M.S.; Roh-Johnson, M.; Goodman, J.R.; Olson, B.; et al. Cell fusion potentiates tumor heterogeneity and reveals circulating hybrid cells that correlate with stage and survival. *Sci. Adv.* **2018**, *4*, eaat7828. [CrossRef] [PubMed]

Disclaimer/Publisher's Note: The statements, opinions and data contained in all publications are solely those of the individual author(s) and contributor(s) and not of MDPI and/or the editor(s). MDPI and/or the editor(s) disclaim responsibility for any injury to people or property resulting from any ideas, methods, instructions or products referred to in the content.

cancers

MDPI

Review

GNAQ/GNA11-Related Benign and Malignant Entities—A Common Histoembriologic Origin or a Tissue-Dependent Coincidence

Justyna Pilch [1,†], Jakub Mizera [1,†], Maciej Tota [1] and Piotr Donizy [1,2,*]

[1] Department of Clinical and Experimental Pathology, Wroclaw Medical University, 50-556 Wroclaw, Poland
[2] Department of Pathology and Clinical Cytology, Jan Mikulicz-Radecki University Hospital, 50-556 Wroclaw, Poland
* Correspondence: piotr.donizy@umw.edu.pl; Tel.: +48-717-343-955
† These authors contributed equally to this work.

Simple Summary: Uveal melanoma (UM) is an aggressive cancer emerging from mutations in the *GNAQ* and *GNA11* genes. These mutations are also linked to other conditions with distinct morphological features (skin capillary malformations, hemangiomas, Sturge–Weber syndrome, choroidal nevi, blue nevi, hepatic small vessel neoplasm, Blitz nevi, iris and ciliary body melanocytoma, primary central nervous system melanocytic neoplasms, and aldosterone-producing adenomas). By examining the molecular pathways influenced by these mutations, we provide insights into potential targeted therapies for UM and related disorders. Additionally, we address the involvement of SOX10-positive perivascular cells in the complex pathophysiology of GNAQ/GNA11-related conditions.

Abstract: Uveal melanoma (UM), recognized as the most prevalent primary intraocular malignancy in adults, is primarily driven by mutations in the *GNAQ* and *GNA11* genes. These genetic alterations are also implicated in other conditions, which exhibit distinct morphological characteristics. In this article, we investigate the role of *GNAQ* and *GNA11* mutations across varied disorders (e.g., UM, skin blue nevi, and hemangiomas), emphasizing the shared pathogenic mechanisms that connect them despite their differing clinical manifestations. By investigating the molecular pathways affected by these mutations, we provide insights into the potential for targeted therapies that could address not only UM but also other disorders associated with *GNAQ*/*GNA11* mutations. Moreover, we discuss the role of SOX10-positive perivascular cells that may be implicated in the complex pathophysiology of GNAQ/GNA11-related entities. Understanding the common molecular foundation of these conditions opens new ways for research and treatment opportunities, potentially leading to more effective, personalized therapeutic strategies.

Keywords: uveal melanoma; GNAQ; GNA11; SOX10

1. Introduction

GNAQ/*GNA11* (*G protein subunits alpha q/11*) genes encode the alpha subunits of the heterotrimeric guanine nucleotide-binding proteins (G proteins), Gq and G11 [1]. G proteins are signal transducers that transmit signals from various neurotransmitters, hormones, chemokines, and other paracrine and autocrine factors. Interactions with this diversity of particles begin with the participation of the broad family of receptors with seven membrane-spanning regions, which then activate G proteins. Subsequently, signals can be routed to several distinct intracellular molecular pathways. These pathways cooperate to create a network responsible for the regulation of metabolic enzymes, transporters, ion channels, and other cellular machinery components. Moreover, they influence a wide range of cellular processes, including secretion, contractility, motility, and transcription. In turn, G proteins maintain organism homeostasis, and their dysfunction may lead to cellular

proliferation and even oncogenesis [2,3]. Hence, due to the variety of functions controlled by G proteins, mutations in GNAQ and GNA11 genes may be found in a diversity of conditions, from benign lesions such as common blue nevi, which remain relatively neutral for individuals' homeostasis, to aggressive malignant tumors with a poor prognosis like uveal melanoma [4,5].

Uveal melanoma (UM) is an aggressive malignancy originating from melanocytes in the eye, mainly affecting the choroid [4]. Even though it is the most common primary intraocular malignant neoplasm in adults, with approximately 5 cases per million per year, it can be classified as a rare cancer. Metastatic UM is an orphan disease that results in fewer therapeutic options and a lack of treatment guidelines. Due to molecular differences with cutaneous melanoma (CM), patients suffering from UM are often excluded from clinical trials regarding CM [6]. Early neoplasm detection is crucial for higher survival rates compared to patients with metastatic processes [7].

Some molecular findings regarding UM were made previously, and the role of genes *GNAQ* and *GNA11* in UM pathogenesis was highlighted as one of the most common molecular factors regarding this neoplasm [2,8]. Depending on the affected cell or the time of life when the mutation occurs, the same genetic changes can result in different phenotypic effects. Identical mutations can also be found in conditions such as skin blue nevi or hemangiomas [5]. Other mutations highly prevalent in UM are *BAP1* (*BRCA1-associated protein 1*), *EIF1AX* (*eukaryotic translation initiation factor 1A X-linked*), *SF3B1* (*splicing factor 3b subunit 1*), *CYSLTR2* (*cysteinyl-leukotriene receptor 2*), and *PLCB4* (*phospholipase C beta 4*) [9–11].

In the article, we attempt to comprise knowledge available from clinical trials and meta-analyses and assess whether there is any correlation between the occurrence of benign skin blue nevi or hemangiomas with uveal melanoma and other medical conditions caused by GNAQ and GNA11 mutations.

2. Biological Functions of *GNAQ* and *GNA11* Genes and Derived Proteins

2.1. GNAQ

GNAQ (*G protein subunit alpha q*) is a protein-coding gene located on chromosome 9 (9q21.2). It consists of 315,715 nt (nucleotides), including UTRs, with a total exon count of 7 [12]. Its aligned and CDS length amounts to 6882 nt and 1080 nt, respectively [13]. A study performed by Dong et al. proved that the GNAQ gene encodes 359 amino acids long protein, Gαq [14]. It is a guanine nucleotide-binding protein that constitutes a part of a trimeric G protein complex that mediates the stimulation of phospholipase C beta [5]. Guanine nucleotide-binding proteins form a family of heterotrimeric proteins coupling cell surface with 7-transmembrane domain receptors to signaling pathways inside a cell. The receptor activation process enables the catalysis of the exchange of GTP for GDP attached to the inactive G protein alpha subunit, causing a conformational change and dissociation of the complex. The activation process is terminated by a GTPase specific to the G-alpha subunit. Gαq, together with beta-gamma subunits, are proteins able to regulate various cellular effectors. They can manifest through various receptors, including the endothelin 1 receptor, vasopressin type 1A, and 1B receptors, angiotensin 2 receptor type I, α-1 adrenergic receptors, and others [14,15] [Figure 1].

Due to its essential cellular functions, the *GNAQ* gene is considered a proto-oncogene, especially referring to melanocytes and uveal melanomas. Nonetheless, *GNAQ* mutations play a significant role in other pathologies, such as Sturge–Weber syndrome, haemangiomas, or skin blue nevi [5]. They are concerned with codon Q209 and R183 hot spots. Interestingly, these mutations apply in the vast majority of mentioned pathologies (more than 80% of all cases) [1]. The Arg183Gln mutation, considering the *GNAQ* gene, affects the site of water autohydrolysis inside the GTP–GDP binding site of Gαq. Consequently, it is anticipated that the mutation reduces the effectiveness of autohydrolysis, which allows the guanine nucleotide protein to return to the deactivated (GDP-bound) state and complex with its GPCR (G protein-coupled receptor). Therefore, this mutation is hypothesized to result in

constitutive overactivation of downstream pathways. As for the R183Q mutation, it was proved that mutant cells were characterized by a significant increase in phosphorylated extracellular signal-regulated kinase (ERK) compared to normal cells [16]. The issue is concerning since ERK plays an important role in regulating immune cell function as well as impacts cell growth, proliferation, cell differentiation, and apoptosis [17,18].

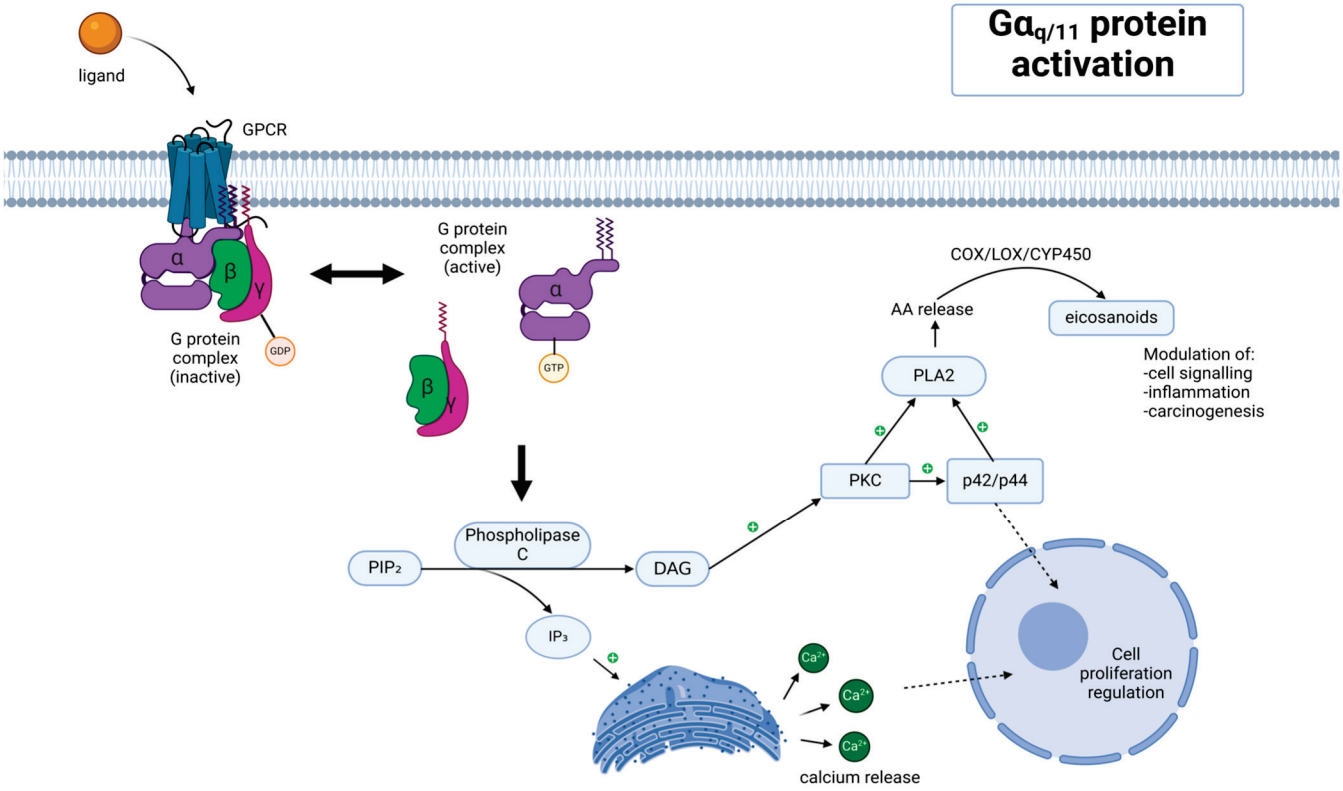


Figure 1. The signaling pathway associated with the activation of the Gαq/11 protein. A ligand binds to a GPCR (G-protein-coupled receptor) embedded in the cell membrane, triggering the activation of the G protein complex. The activated Gαq/11 subunit activates phospholipase C (PLC), which then catalyzes the hydrolysis of PIP_2 (phosphatidylinositol 4,5-bisphosphate) into two secondary messengers: diacylglycerol (DAG) and inositol trisphosphate (IP_3). IP_3 binds to its receptors on the endoplasmic reticulum, leading to the release of Ca^{2+} ions into the cytoplasm. The increase in intracellular calcium concentration acts as a signal for various cellular processes. DAG remains in the membrane and activates protein kinase C (PKC),which, in turn, can phosphorylate various target proteins involved in cell signaling. PKC also activates phospholipase A2 (PLA2), catalyzing the release of arachidonic acid (AA) from membrane phospholipids, which is then metabolized by enzymes such as COX (cyclooxygenase), LOX (lipoxygenase), and CYP450 (cytochrome P450) to produce eicosanoids. Eicosanoids are involved in modulating processes like cell signaling, inflammation, and carcinogenesis. The pathway ultimately influences the regulation of cell proliferation. Specifically, the signaling cascade involving PKC and p42/p44 (ERK1/2) MAP kinases contributes to the control of cell growth and division. The symbol of a white plus inside a green circle in the figure should be understood as an activation.

Furthermore, the same mutations mentioned above can result in vascular malformations, such as hemangiomas. However, it remains unclear why, in some cases, these mutations lead to carcinogenesis, while in others, they result in vascular malformations or benign hyperplasia. This variation is believed to depend on factors, such as the developmental stage at which the mutation occurs (germline vs. somatic), the specific cell type exposed to the mutation, or the presence of concurrent mutations. For instance, in aldosterone-producing adenomas, mutations in GNAQ and GNA11 remain clinically silent

unless there is an accompanying mutation in the CTNNB1 gene [5]. Considering UM and blue nevi, germline mutations causing these conditions have not been discovered. Yet, there is supposed to be a hereditary factor that provokes the occurrence of familial melanoma, and it seems crucial to investigate the genomics of these individuals [19].

2.2. GNA11

GNA11 (G protein subunit alpha 11) gene encodes the alpha subunit of G11 protein (Gα11)—an essential component of guanine nucleotide-binding protein complex (G proteins). The gene is located on chromosome 19p13.3 [20], and weighs 42,123 Da [21,22].

It was described by Strathmann and Simon while investigating the diversity of murine G protein [23]. Using methods based on PCR, they found evidence of a wide variety among G protein α subunits and divided them into three distinct groups: Gs, Gi, and Gq. Subunit Gα11 was classified into the Gq group along with the Gα14 [24]. In the same year, the human *GNA11* gene was cloned by Jiang et al., who found its product to be 359 amino acids long [25].

Heterotrimeric G11 protein, together with other G proteins, activates a complex network of crucial signaling pathways [1]. G11 protein, by cooperating with calcium-sensing receptors (CaSR), influences the processes responsible for regulating blood calcium levels [26]. Moreover, G11 signaling is involved in cell growth, proliferation, and apoptosis in various human tissues [27]. Hence, mutations in the GNA11 gene may result in diverse clinical disorders.

The *GNA11* gene may be affected by either germline or somatic mutations, both of them, are activating mutations, meaning that they lead to the production of an overactive Gα11 subunit of the G11 protein. In consequence, uncontrolled melanocyte proliferation in the uvea or the skin might be observed, as well as excessive inhibitory signaling, which blocks the increase in calcium levels despite them being below the normal range [28,29].

Germline mutations are generally inherited and occur in every cell of the body. In the case of *GNA11*, they result in various conditions associated with abnormal calcium concentration, such as autosomal dominant hypocalcemia type 2, also called autosomal dominant hypoparathyroidism due to inhibited production of parathyroid hormone (p.Arg60Leu, p.Arg60Cys, p.Arg181Gln, p.Ser211Trp, or p.Phe341Leu), or familial hypocalciuric hypercalcemia type 2 (p.Ile200del, p.Leu135Gln, or p.Thr54Met) [26,30,31].

Somatic mutations have been found in uveal melanomas [1]. Less commonly, they are associated with cutaneous or vascular lesions, such as blue nevus, [32], congenital extremity capillary malformation [33], Sturge–Weber syndrome [34], or cherry and congenital hemangioma [35,36].

Due to their significant role in UM pathogenesis, *GNA11* somatic mutations are being further investigated in various research centers. A study conducted by Raamsdonk et al. provided detailed data on the prevalence of the two main somatic mutations found in both UM and blue nevi: mutation affecting codon Q209 (substitution of glutamine 209 for leucine or proline—p.Q209L and p.Q209P, respectively) were identified in 57% of uveal melanoma metastases, 32% of primary uveal melanomas, and 7% of blue nevi by gene sequencing of exon 5. Mutations in the same residue (Q209) of the paralogue gene *GNAQ* were found in 22% of uveal melanoma metastases, 45% of primary uveal melanomas, and 55% of blue nevi. Furthermore, sequencing of exon 4 of both *GNA11* and *GNAQ* genes, affecting codon R183 (arginine 183), showed a lower prevalence of mutations: 4.9% of primary uveal melanomas and 2.1% of blue nevi. The research evinced that these mutations were mutually exclusive, except for one tumor that carried them both—at Q209 and R138 in *GNA11*. Overall, 83% of all investigated uveal melanomas had oncogenic mutations in either *GNA11* or *GNAQ* [37] [Figure 2].

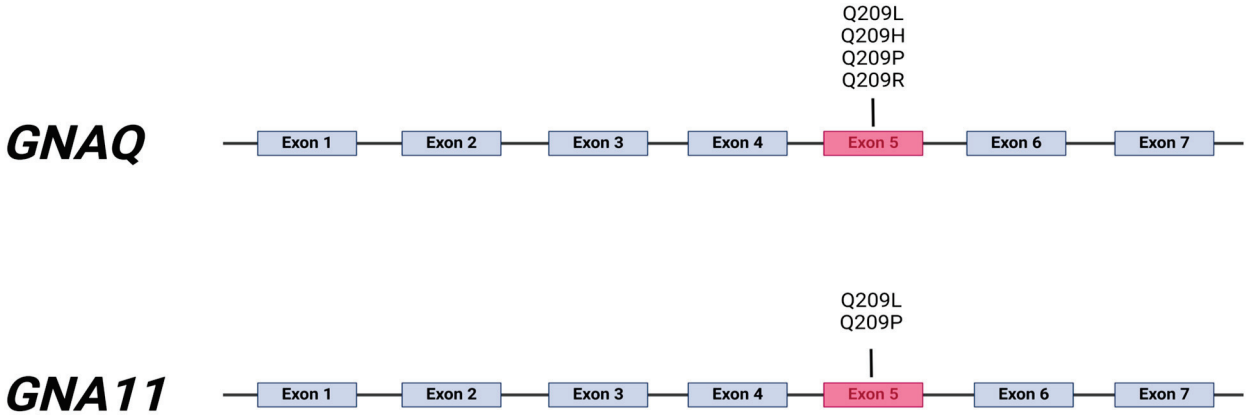


Figure 2. The most prevalent mutations within GNA genes—exon 5 in both *GNAQ* and *GNA11* appear to be a critical region, where specific mutations occur, particularly at the amino acid position Q209.

Notably, individuals with blue nevi or UMs seem to have normal blood calcium levels, and patients with an inherited *GNA11*-associated calcium concentration disorder do not appear to be at increased risk of developing either of these tumors [30]. This might result from the difference in underlying molecular pathogenesis, as different codons are affected by mutation within the same gene.

3. Disorders Associated with *GNAQ* and *GNA11* Mutations

3.1. Uveal Tract Tumors

3.1.1. Choroidal Nevi

A choroidal nevus is a common and benign tumor arising from melanocytes in the choroid, often discovered accidentally during an ophthalmic examination. It can be found in 5–6.5% of the population and occurs more often in people with higher BMI and whites. Moreover, the lesion is significantly less common in people with blond hair. An association has not been found between nevus occurrence and visual impairments, glaucoma, or cataracts [38,39]. Even though choroidal nevi are considered stable lesions, there is a slight probability (varying in the range of 0.78–7%) of their malignant transformation to uveal melanoma [40]. The transformation may be suspected by features such as the thickness of the lesion greater than 2mm, symptoms of flashes or blurred vision, subretinal fluid, margin less than 3mm from the optic disc, orange lipofuscin pigment, halo or drusen absence, and ultrasonographic hollowness. If three or more of these features are present, there is more than a 50% probability of transformation to melanoma within five years [39]. Hence, all patients with choroidal nevi require long-term ophthalmological follow-up [41].

It is well known that rarely melanoma can develop from pre-existing nevus, which refers to CM arising from cutaneous nevi and UM arising from choroidal nevi. Vader et al. conducted research on post-mortem human eye samples to examine the pathomorphological basis of the condition. Molecular analysis revealed that mutations in choroidal nevi occur in both *GNAQ* and *GNA11* genes. Hotspots include Q209P and Q209L for the *GNAQ* gene and Q209L for the *GNA11* gene (Table 1). The vast majority of samples presented one out of three of these hotspot mutations, and the most commonly mutated hotspot was Q209L in *GNA11* [42]. Interestingly, identical mutations can be found in UM, clarifying the linkage between these two conditions [43]. The potential of choroidal nevi for its malignant transformation may be explained by the oncogenic features of *YAP*, which are already associated with several other malignancies. Mutant *GNAQ* and *GNA11* may result in *YAP* activation and, as a consequence, can lead to cancer formation [29].

3.1.2. Uveal Melanoma

Mutations in the *GNAQ* and *GNA11* genes play a crucial role in the development of UM. In contrast to cutaneous melanomas, patients with UM rarely exhibit mutations in the

frequently altered BRAF, NRAS, or NF1 genes [44,45]. Instead, *GNAQ* and *GNA11* mutations dominate, being identified in approximately 80% of cases [1,46]. The most frequent mutations in *GNAQ* and *GNA11* occur at codon 209 in exon 5 (Q209P, Q209L), which is a critical site for the protein's GTPase activity [45]. These mutations result in impaired GTP hydrolysis, locking the Gα subunit in its active, GTP-bound form. This persistent activation leads to the constitutive stimulation of downstream signaling pathways, independent of external regulatory factors, thereby facilitating unregulated cellular proliferation and contributing to tumorigenesis [1]. Moreover, mutations at codon 183 (R183Q) can occur, although they are less common and typically exhibit reduced oncogenic potential compared to Q209 mutations [47]. The constitutive activation of *GNAQ* or *GNA11* via Q209 or R183 mutations leads to the sustained activation of multiple oncogenic pathways, such as the MAPK/ERK pathway, the Hippo/Yap-TAZ pathway, and the PI3K/AKT pathway [48–50].

Although mutations in both *GNAQ* and *GNA11* are present in primary UM (Table 1), research indicates that *GNA11* mutations, especially Q209L, have a stronger correlation with metastasis, particularly to the liver, which is the primary site for UM metastases [51]. About 50% of patients with UM develop metastatic disease, and the presence of *GNA11* mutations is frequently associated with a poor prognosis. Once metastasis has occurred, the disease is usually fatal, with few effective treatment options available [51].

The identification of *GNAQ* and *GNA11* mutations in UM has led to advancements in targeted therapies; however, direct inhibitors of these proteins have yet been developed. Present therapeutic strategies concentrate on inhibiting the downstream pathways activated by these mutations, using MEK inhibitors, YAP–TEAD pathway inhibitors, and PKC inhibitors [52–54]. Aforementioned treatment strategies are described in detail in Section 4.

3.1.3. Iris and Ciliary Body Melanocytoma

Iris and ciliary body melanocytomas (magnocellular nevi) are rare and unusual melanocytic tumors. Although these tumors are benign, due to their proliferative nature, they may cause ophthalmic symptoms, such as elevated intraocular pressure and glaucoma. However, lesions are most commonly asymptomatic, with clinical presentation of dark spots involving the ciliary body and iris. Melanocytomas require a differential diagnosis with melanoma because of their macroscopic resemblance. Moreover, melanocytoma can sometimes transform into melanoma. Most commonly, lesions can be distinguished by histopathologic criteria after surgical procedures, such as iridocyclectomy [55,56].

Iris and ciliary body melanocytomas were examined for *GNAQ* and *GNA11* missense mutations. In the research performed by Solomon et al., in which 16 melanocytomas were analyzed, 15 of them demonstrated mutated genes—10 with a mutation in hotspot Q209P in *GNAQ* and 7 with a mutation in hotspot Q209L in *GNA11* [57]. Other researchers, such as Francis et al. and Mudhar et al., also confirmed that *GNAQ* mutations (codon Q209L) are present in iridociliary and other intraocular melanocytomas (Table 1) [58,59].

3.1.4. Circumscribed Choroidal Hemangioma

Circumscribed choroidal hemangioma (CCH) is a benign vascular lesion, typically manifesting as a solitary orange-red mass localized at the posterior pole of the fundus. It is composed of an irregular, dilated, and congestive network of choroidal vessels separated by an intervascular septum. Unlike in the case of "true hemangiomas", CCH cells do not proliferate, and the tumor tends to present slow or no progression in size over time [60].

Since CCH usually presents no symptoms until adulthood, it is rarely detected before vision impairment occurs. Generally, it manifests between the second and fourth decades of life as visual problems caused by intraretinal or subretinal fluid within the macula region or exudative retinal detachment [61]. In most cases, diagnosis is established based solely on clinical findings and eventually on the results of fluorescein angiography (FLA). FLA is performed in order to distinguish CCH from other tumors, such as choroidal metastasis or uveal melanoma. Differential diagnosis must also include diffuse choroidal

hemangioma associated with Sturge–Weber Syndrome (SWS) and usually detected during childhood [62].

To determine the presence of oncogenic alterations of *GNAQ* and *GNA11* genes in CCH and their mutual profile, Le Guin et al. performed deep amplicon and Sanger sequencing of *GNAQ* and *GNA11* in DNA extracted from 33 samples diagnosed as CCH based on histological features. In 85% of the tissue samples (28/33), the identical *GNAQ* (p.Q209R) mutation was identified (Table 1). This narrow mutation spectrum of circumscribed choroidal hemangioma, restricted to *GNAQ* p.Q209R, may support researchers in establishing the diagnosis of CCH when clinical criteria are not sufficient or not enough biopsy samples are available to perform histological examination [63].

In the remaining five tissue samples, signals for oncogenic alleles at *GNAQ*/*GNA11* genes (p.Q209 or p.R183) were within the range of noise; hence, most probably, these samples do not have an oncogenic alteration at these sites. However, it is essential to consider that oncogenic activation of a G protein alpha subunit may occur due to a mutation at a different locus within the *GNAQ*/*GNA11* genes or within a gene encoding a different subunit, such as GNA1. [63,64].

3.2. Skin Capillary Malformations

Skin capillary malformations (SCMs) are congenital anomalies characterized by irregularities in capillary and venous blood vessels, presenting primarily in the skin. These malformations may also occur in the leptomeninges and choroid of the eye, particularly associated with Sturge–Weber Syndrome (SWS). In contrast, non-syndromic capillary malformations, which are more commonly observed, typically remain localized to the skin and do not extend to the brain or ocular structures [65]. SCMs may occur either as an isolated lesion or in association with different clinical findings, such as pigmentary birthmarks (characteristic of phacomatosis pigementovascularis) or leptomeningeal angiomatosis and glaucoma (characteristic of SWS). The use of targeted genetic sequencing has revealed that some of the SCMs subclassified by Happle into the "capillary naevi group"—nevus flammeus (port-wine stain), nevus anemicus, and cutis marmorata—are associated with postzygotic somatic mutations at residue 183 in *GNAQ* and *GNA11* genes [66,67].

The most frequent missense mutation in SCMs is *GNAQ* p.Arg183Gln, followed by other mutations affecting codon 183: p.Arg183Gly and p.Arg183Leu (Table 1). Since *GNAQ* and *GNA11* share more than 90% amino acid identity, a missense mutation in *GNA11* p.Arg183Cys and p.Arg183His was also found in patients suffering from a diffuse capillary malformation causing overgrowth and localized within an extremity [33].

To delineate the phenotype of patients with SCMs harboring an activating mutation in *GNAQ* or *GNA11*, Cuoto et al. analyzed 32 cases and concluded that nevus flammeus was associated with both *GNAQ* and *GNA11* mutations, with a slightly higher frequency of alterations regarding *GNAQ*. On the other hand, nevus anemicus and cutis marmorata were associated with *GNA11* mutations, while in nevus roseus—another subtype of capillary lesion—none of the *GNA*-associated mutations were found [33].

What is important is that nevus anemicus never manifested itself as a single lesion—it was always associated with another cutaneous capillary malformation (mainly cutis marmorata), giving rise to a lesion called nevus vascularis mixtus [33,68].

3.3. Sturge–Weber Syndrome

Sturge–Weber syndrome (SWS) is an uncommon and noninherited condition characterized by aberrant vasculature in the brain, skin, and eyes. It affects approximately 1 out of 20,000–50,000 people [69]. Patients with SWS frequently develop facial capillary malformations (also called port-wine birthmarks). Moreover, due to the abnormal blood vessels in the eye, they may suffer from ophthalmic disorders, such as glaucoma. Interestingly, glaucoma can be present at birth or develop later. SWS is also linked with altered cerebral perfusion, which leads to a high risk of seizures, venous stroke, and stroke-like events, and both motor and cognitive impairments in patients [70].

Recent studies suggest that the activating R183Q *GNAQ* somatic mutation is the most frequent mutation underlying SWS (Table 1). Furthermore, researchers point out the role of *GNA11* and *GNB2* somatic mutations in disease pathogenesis [70].

SWS caused by either *GNAQ* or *GNA11* mutation is clinically different. In the original study on the genetics of SWS performed by Dompmartin et al., 88% (23/26 examined) of the patients had a *GNAQ* mutation. They manifested dark homogenous SCMs, with the usual occurrence of nodules and continuous soft tissue hypertrophy of the face, causing a noticeable dysmorphism [34].

All three of the *GNA11*-SWS patients in the study exhibited patch and reticulated CMs that were pale at birth but gradually darkened with time, with the unusual appearance of nodules and restricted hypertrophy. Furthermore, patients with *GNA11*-SWS received a delayed diagnosis compared to those with *GNAQ*-SWS due to the more limited radiological features detected in brain MRI. As a result, two separate entities can be highlighted, *GNAQ*-SWS and *GNA11*-SWS, each of which has a unique clinical presentation and course [34,71].

Since the molecular basis of the SWS is complex and the condition may manifest in variable phenotypes, identifying the genetic basis in each individual seems crucial due to the different prognoses. As pharmacological therapies are developed to properly treat patients with vascular malformations, changes in molecular pathophysiology might affect responsiveness to therapies, increasing the importance of such genetically related phenotypic diagnoses [34].

3.4. GNA-Mutated Hemangiomas

3.4.1. Congenital Hemangiomas

Congenital hemangiomas are rare vascular tumors arising during prenatal development. Postnatally, they may evolve following one of two clinical patterns: "rapidly involuting congenital hemangioma" (RICH) if the tumor involutes quickly or "non-involuting hemangioma" (NICH) if it partially regresses and stabilizes [72,73].

RICH can be diagnosed prenatally and manifests in newborns as raised, solitary cutaneous tumor with ectatic vessels, telangiectasis, and a pale halo. The lesion usually has a gray-violaceous appearance, demonstrates fast flow, and may be associated with transient low-grade thrombocytopenia or congestive heart failure. In the absence of serious complications related to hemorrhagic ulceration or heart failure, the tumor spontaneously regresses within 6–14 months. It leaves a skin mark characterized by persistent fast-flow, subcutaneous atrophy, and dilated vessels. Moreover, RICH was found and described to occur in the liver, where it regresses spontaneously, similar to cutaneous lesions [36]. NICH is a purple-pink plaque-like tumor, well-circumscribed by a pale rim from unchanged skin, displaying coarse telangiectasia and fast flow. Contrary to RICH, no complete regression is observed throughout childhood, and NICH remains unchanged or slightly regressed. In the literature, some cases of RICH were described as failing to involute and transform into NICH [36,74]. Both types of congenital hemangioma should be differentiated from common infantile hemangiomas, which—contrary to RICH and NICH—tend to enlarge rapidly after birth and immunostain for GLUT1, a cell surface marker [75].

To understand the molecular pathogenesis of congenital hemangiomas, Ayturk et al. examined eight fresh frozen tissue samples from patients diagnosed with congenital hemangioma and performed mRNA sequencing. This research resulted in the identification of missense mosaic mutations leading to the alteration of glutamine at amino acid 209 (Glu 209) in both *GNAQ* (c.626A>T, c.626A>C, c.627A>C) and *GNA11* (c.626A>T) genes in all tested specimens (Table 1). Since mutations were mutually exclusive, 6/8 samples were found to be associated with *GNAQ* somatic mutations and 2/8 with *GNA11* somatic mutation. Furthermore, the fact that the same missense mutation (*GNAQ* c.626A>T and *GNA11* c.626A>T) was found in both RICH and NICH implies the influence of other factors (genetic, epigenetic, and environmental) on these tumors' different postnatal behavior [36].

3.4.2. Cherry Hemangioma

Cherry hemangioma, also known as Campbell de Morgan spot or senile hemangioma, is the most frequent benign vascular tumor in adults. The latter variant of this term originates from lesions' epidemiology—cherry hemangioma is extremely rare before puberty and particularly common in elderly people, as age appears to be one of the most crucial etiologic factors in its prevalence. Other potential etiologic factors reported in the literature are exposure to chemicals (e.g., sulfur mustard gas and bromide) and hormones (cherry hemangioma was described to occur in pregnant women and spontaneously regress after delivery). Senile hemangiomas typically manifest as well-circumscribed, small red-to-violaceous papules, primarily localize on the trunk and upper limbs. Histologically, they are composed of thin-walled capillary vessels, often surrounded by hyalinized stroma [35].

The molecular pathogenesis of cherry hemangioma is still poorly understood. Both non-neoplastic (which indicates that lesion may represent non-neoplastic proliferations, characterized by an overgrowth of mature vascular structures that closely resemble dermal venules) and neoplastic theories have been proposed as a potential etiology of the tumor. The absence of Ki-67 staining in tumor cells forms a base for non-neoplastic theory, while RAS mutations identified in 20% of senile hemangiomas suggest that some of them have neoplastic nature [76,77]. However, some of these findings should not be interpreted as definitive scientific conclusions due to the limitation of a small sample size. Nevertheless, we believe that the results are promising and warrant further investigation.

The results of the research conducted by Liau et al., comprising the molecular analysis of 68 cherry hemangioma samples and 17 cherry hemangioma-like hemangioma samples, allowed authors to establish the neoplastic nature of these vascular tumors. Both types of specimens had equal *GNA* gene mutation rates (82%). *GNAQ*, *GNA11*, and *GNA14* (particularly *GNA14* Q205L) mutations, which were mutually exclusive, were identified in approximately half of the cherry hemangiomas and cherry hemangioma-like hemangiomas. These outcomes provided solid evidence that cherry hemangiomas should be classified as benign vascular neoplasms caused most commonly by a mutation in the *GNA14* gene [35].

3.4.3. Anastomosing Hemangioma

Anastomosing hemangioma (AH) is a benign vascular tumor that may localize in the genitourinary system, adrenal glands, liver, digestive tract, and mediastinum [78,79]. Besides visceral sites, AH has a remarkable predilection for paravertebral soft tissues [80]. The lesion is typically well-circumscribed and does not manifest dissecting or destructive growth. Histologically, AH displays either non-lobulated or loosely lobulated proliferation of anastomosing sinusoid capillaries, lined by bland endothelial cells. These cells are characterized by hyperchromatic nuclei protruding into the lumen and a hobnail-like appearance. Within the tumors, mild cytological atypia may be observed together with eosinophilic hyaline globules (i.e., thanatosomes), extramedullary hematopoiesis, and fibrin thrombi. Approximately 50% of anastomosing hemangiomas also present intravascular growth. Thus, due to its histology, AH might be confused with angiosarcoma. However, multilayering is absent, the mitotic rate is very low, and no aggressive behavior in this neoplasm has been reported [78–80].

The molecular pathogenesis was investigated by Bean et al., who identified activating mutations in *GNAQ* (p.Gln209His, p.Gln209Leu, p.Gln209Pro) and *GNA14* (p.Gln205Leu) genes (Table 1), responsible for the development of AH [81–83]. This research confirmed the theory claiming that anastomosing hemangioma is characterized by a neoplastic nature. A follow-up study conducted by Liau et al. aimed to discover the role of *GNA11* mutations (p.Gln209Leu, p.Gln209His) in AH development since this gene shares the highest degree of homology with *GNAQ*. Sanger sequencing and MassARRAY analysis identified mutually exclusive mutations in exon 5 of *GNAQ*, *GNA14*, and *GNA11* genes in 20 of the 22 investigated tumors. No significant differences in phenotype and molecular features were noticed between *GNAQ*-, *GNA11*-, or *GNA14*-mutated tumors. The results of these stud-

ies implicate that the essential mechanism underlying the pathogenesis of anastomosing hemangioma is related to *GNAQ* mutations, as well as its paralogues: *GNA11* and *GNA14*.

3.4.4. Hepatic Small Vessel Neoplasm

Hepatic small vessel neoplasm (HSVN) is considered a benign or low-grade infiltrative vascular neoplasm of the liver, composed of thin-walled small vessels. Due to its infiltrative nature, HSVN can mimic angiosarcoma, but unlike this type of cancer, HSVN presents no cytologic atypia or increased proliferation [84].

Joseph et al. performed a targeted panel sequencing of 479 cancer genes and exome sequencing to investigate the molecular pathogenesis of HSVN. The study was conducted on 18 benign or low-grade hepatic vascular neoplasms, including eight HSVN. It resulted in the identification of activating hotspot mutations in 75% (6/8) of HSNV—*GNA14* (p.Q205L, 4/8) or *GNAQ* (p.Q209H, 2/8) (Table 1). Mutations in these two genes were mutually exclusive. The remaining two samples (25%) demonstrated identical, previously unknown missense mutation in *GNAQ* (p.G48L) [85].

Although HSVN is a recently described neoplasm that has yet to be investigated, obtained data suggest that it shares similar molecular pathogenesis to other vascular malformations, such as port wine stains, tufted angioma, anastomosing, and congenital hemangioma, since mutations in these lesions are localized in the *GNAQ*, *GNA11*, and *GNA14* genes [33,36,85].

3.5. Phacomatosis Pigmentovascularis

Phacomatosis pigmentovascularis (PPV) is a common term for a family of rare disorders characterized by the coexistence of melanocytic lesions and vascular abnormalities. Clinical manifestations of PPV conditions might be observed as merely cutaneous or multisystemic [86]. Based on cutaneous findings, in 2005, Happle grouped PPV into three phenotypically different categories: phacomatosis cesioflammea (associated with blue spots and nevus flammeus), phacomatosis spilorosea (associated with nevus spilus with pale-pink telangiectatic nevus), and phocomatosis cesiomarmorata (associated with blue spots and cutis marmorata telangiectatica congenita) [87]. In 2012, this classification was updated to include the fourth variant of PPV—phacomatosis melanorosea (associated with flag-like hyper-melanotic nevus) [88,89]. According to other classification, there are five types of PPV: (1) naevus flammeus with naevus pigmentosus et verrucosus; (2) naevus flammeus with aberrant mongolian spots, with or without naevus anaemicus; (3) naevus flammeus with naevus spilus or giant speckled lentiginous naevus, with or without naevus anaemicus; (4) naevus flammeus with aberrant mongolian spots and naevus spilus or giant speckled lentiginous naevus, with or without naevus anaemicus; and (5) cutis marmorata telangiectatica congenita and aberrant mongolian spots [90,91].

It was recently discovered that two of the PPV subtypes—cesioflammea and cesiomarmorata—may share identical mosaic somatic activating mutations in *GNAQ* (p.Arg183Gln) and *GNA11* (p.Arg183Cys, p.Arg183Ser) genes. These molecular findings place the above-mentioned disorders on a clinical spectrum comprising other *GNA11*- and *GNAQ*-related conditions and suggest recommendations for their management [86]. The molecular pathogenesis of spilorosea and melanorosea has yet to be identified [92].

The case study and literature review by Kumar et al. aimed to determine the optimal surveillance approach for extracutaneous complications in individuals with phacomatosis cesioflammea and cesiomarmorata. Similar to other disorders associated with *GNAQ* or *GNA11* mutations, important extracutaneous complications in PPV can be predicted based on the location of cutaneous lesions and ocular melanosis. According to their findings, most commonly, patients suffered from abnormalities of the eye (ocular melanoma, glaucoma) and of the brain (development delay, imaging abnormalities). Moreover, the analysis of the patterns of co-occurrence between diverse clinical findings led to the identification of a potential positive correlation between the occurrence of ocular melanoma and ocular pigmentation, facial vascular involvement and seizures with development delay, limb

asymmetry with either superficial or deep venous malformations [86]. The conclusion arising from this analysis is that individuals with ocular melanosis should be regularly followed up by an ophthalmologist [93], while those with facial vascular involvement should be evaluated by a neurologist or undergo brain imaging in case of neurological findings [94].

3.6. Blue Nevus

Blue nevi are common and benign melanocytic neoplasms that demonstrate a variety of clinical and morphological patterns, including common/dendritic, cellular, and atypical cellular subtypes. Like other nevi, they mostly develop in the skin but occasionally affect the lymph nodes, where they can be mistaken for metastatic melanoma [95]. Blue nevi can be characterized by the proliferation of dermal dendritic melanocytes. The spectrum of lesions associated with blue nevi ranges from common blue nevi, pigmented epithelioid melanocytoma to melanoma arising in blue naevus (MBN). MBN represents a range of histopathological features and genetic anomalies [96]. Melanomas that arise in the setting of blue nevi share a similar mutational and histopathological profile with uveal melanoma. The majority of UMs have the characteristic *GNA11* or *GNAQ* mutations, with additional *BAP1* mutations or deletions linked to a higher probability of metastases and worse prognosis overall [97].

Available data suggest that blue nevi are mostly positive for *GNAQ* (hotspot Q209L and Q209P) and *GNA11* (hotspot Q209L) mutations (Table 1). Estimates point out the fact that somatic mutations in codon 209 of *GNAQ* may be present in up to 80% of blue nevi. However, studies even reported that all examined lesions represented either *GNAQ* or *GNA11* mutations [32,98].

To sum up, *GNAQ* and *GNA11* gene mutations seem important for prognostic relevance, but other genes, such as *BAP1*, should also be considered as they seem to play an important role in the emergence of 'benign' metastases of blue nevi in lymph nodes or progression to aggressive malignant blue nevi [99,100].

3.7. Blitz Nevus

Blitz nevi are morphologically thought to show the mixed phenotype of Spitz and blue nevi, so genomically, they can also represent features of these lesions. While most blue nevi demonstrate *GNAQ* or *GNA11* mutations, Spitzoid neoplasms are known from either *HRAS* mutation or translocation involving *ROS*, *BRAF*, *MET*, *ALK1*, *RET*, and *NTRK1* [101]. To analyze possible genetic resemblance between blitz nevi and blue nevi, Isales et al. conducted research using NGS to examine lesions for *GNAQ* and *GNA11* mutations. The study revealed that 57% of blitz nevi acquired somatic mutations of these genes, also characteristic of blue nevi. Moreover, it was proved that all cases positive for *GNAQ* and *GNA11* mutations were at the same time negative for mutations characteristic of Spitzoid neoplasms. Hence, researchers suggest that genomically, blitz tumors should be categorized as a subset of blue nevi. However, this phenomenon requires further investigation and studies on a larger group of individuals [101].

3.8. Aldosterone-Producing Adenomas

An aldosterone-producing adenoma (APA) is a benign tumor affecting adrenal glands. The tumor causes primary hyperaldosteronism (PA), leading to higher salt retention in kidneys than in healthy people and, as a consequence, can cause hypertension or atrial fibrillation. The exact prevalence of adenomas is unknown, but they are estimated that they account for 60% of cases of primary hyperaldosteronism and 5–15% of all cases of hypertension [102]. The identification of PA and APA is crucial for decreasing cardiovascular morbidity and mortality, but current diagnostic techniques lack sensitivity and specificity, highlighting the need for new approaches [103].

Mostly, APA has somatic mutations in genes responsible for the function of ion channels or transporters, which puts a spotlight on this issue as a possible sensitive or

specific diagnostic feature. Current scientific findings identify the role of mutations in *GNA11* (p.Gln209Leu, p.Gln209His, p.Gln209Pro), *GNAQ*, and *CTNNB1* (Table 1). Yet, the frequency of these mutations in the aldosterone-producing cell clusters of healthy adrenal glands suggests an obligatory role of codriver mutations. Hence, without a mutation of *CTNNB1*, *GNAQ* and *GNA11* mutations remain clinically silent [104,105].

In some congenital lesions, the mutation of *GNAQ* and *GNA11* is mosaic and can be found in several disparate sites. *GNA11/Q* mutations may develop early and established circumstances for a second hit in *CTNNB1* to result in APA development. This theory is supported by examples of *GNA11/Q* mosaicism that have been observed, and by the isolated, distinct regions of *GNA11* mutation in the nearby hyperplastic zona glomerulosa [104,106].

3.9. Primary CNS Melanocytic Neoplasms

Primary melanocytic neoplasms of the central nervous system (CNS) are uncommon lesions originating from melanocytes of the leptomeninges. Based on the WHO classification, they include:

1. circumscribed meningeal melanocytic neoplasms: melanocytoma (benign and well-differentiated lesion) and melanoma (malignant);
2. diffuse meningeal melanocytic neoplasms: melanocytosis (Diffuse or multifocal benign proliferation of cytologically bland melanocytic cells originating from leptomeningeal melanocytes) and melanomatosis (diffuse or multifocal malignant proliferation of melanoma cells arising from leptomeningeal melanocytes, frequently exhibiting invasion into the central nervous system) [107,108].

Typically, tumors represent a morphology of darkly pigmented, solid masses, often involving necrotic or hemorrhagic areas, composed of sheets of pleomorphic cells with prominent nucleoli, numerous mitotic figures, and parenchymal invasion. Symptoms differ by the location of the melanocytic neoplasm. Back pain, muscle weakness, numbness, plegia, or urinary incontinence may be manifestations of spinal tumors, while seizures, subarachnoid hemorrhage, or focal neurological symptoms may be signs of an intracranial tumor [109].

Clinically, primary leptomeningeal melanocytic neoplasms (LMNs) must be distinguished from metastatic lesions, since the prognosis for individuals with metastatic disease is less favorable. Therefore, diagnostic methods for a primary CNS melanocytic tumor, such as molecular diagnostics, might be useful in clinical settings [110].

Primary CNS melanocytic tumors are frequently affected by mutations in the heterotrimeric G protein alpha subunits, *GNAQ* or *GNA11* [111]. Although the predictive value of mutations in G-protein genes *GNA11* and *GNAQ* in patients with primary CNA melanocytic neoplasms remains unknown, a lot of studies are held to find out if this feature might be useful for tumor diagnostics [112]. Researchers found out that LMNs share some genetic abnormalities with UMs, including *GNAQ* (p.Gln209Leu) and *GNA11* (p.Gln209Leu, p.Gln209Pro) mutations, but these mutations are less common in LMNs than in UMs. Mutations in *GNAQ* R183 and *GNA11* R183 were not found, implying that these mutations are uncommon in LMNs, similar to their rarity in UMs [113].

To sum up, all these findings, together with diagnostics of *BRAF*, *HRAS*, and *NRAS* hotspot mutations, may be useful in the differential diagnosis between primary CNS melanocytic neoplasms and metastases from a CM to the CNS. This seems particularly important due to the fact of very different prognosis of these conditions [113].

Table 1. A summary of medical conditions driven by mutations in *GNAQ*, *GNA11*, and *GNA14* genes.

GENE	CDS MUTATION	AA MUTATION	MEDICAL CONDITION
GNAQ	c.142_143delinsTT	p.Gly48Leu	Hepatic small vessel neoplasm
	c.143G>T	p.Gly48Val	Cherry hemangioma
	c.548G>A	p.Arg183Gln	SCMs Phacomatosis pigmentovascularis SWS
	c.547C>G	p.Arg183Gly	SCMs
	c.548G>T	p.Arg183Leu	SCMs
	c.623A>C	p.Gln208Pro	Iris and ciliary body melanocytoma
	c.626A>T c.625_626delinsTT	p.Gln209Leu	Congenital hemangioma Anastomosing hemangioma Choroidal nevi Iris and ciliary body melanocytoma Blue nevi Aldosterone-producing adenomas Primary CNS melanocytic neoplasms
	c.626A>G	p.Gln209Arg	Cherry hemangioma Circumscribed choroidal hemangioma
	c.627A>C	p.Gln209His	Congenital hemangioma Cherry hemangioma Anastomosing hemangioma Hepatic small vessel neoplasm
	c.626A>C	p.Gln209Pro	Congenital hemangioma Cherry hemangioma Anastomosing hemangioma Choroidal nevi Blue nevi
GNA11	c.546_547delinsTT c.547C>T	p.Arg183Cys	SCMs Phacomatosis pigmentovascularis SWS
	c.548G>A	p.Arg183His	SCMs
	c.547C>A	p.Arg183Ser	Phacomatosis pigmentovascularis
	c.626A>T c.626_627delinsTA c.626_627delinsTT	p.Gln209Leu	Congenital hemangioma Anastomosing hemangioma Choroidal nevi Iris and ciliary body melanocytoma Blue nevi Aldosterone-producing adenomas Primary CNS melanocytic neoplasms
	c.626A>C	p.Gln209Pro	Aldosterone-producing adenomas Primary CNS melanocytic neoplasms
	c.627G>C c.627G>T	p.Gln209His	Cherry hemangioma Anastomosing hemangioma Aldosterone-producing adenomas
GNA14	c.614A>T	p.Gln205Leu	Cherry hemangioma Anastomosing hemangioma Hepatic small vessel neoplasm

SWS—Sturge–Weber syndrome; CNS—central nervous system; SCMs—skin capillary malformations.

4. Potential Therapeutic Opportunities for UM and Other GNAQ/11-Related Disorders

Cells with mutated GNAQ and GNA11 genes present deregulation in several key signaling pathways, including MAPK (ERK1/2), PI3K/AKT, and YAP/TAZ [29,114,115], hence, potential therapeutic strategies involve targeting these pathways [1].

- **MAPK Pathway:** MEK inhibitors such as selumetinib and trametinib, have been tested to block the ERK1/2 signaling cascade. Although results from clinical trials show limited success, combining MEK inhibitors with other agents like immune checkpoint inhibitors may offer better efficacy [29].
- **YAP/TAZ Pathway:** Since GNAQ/GNA11 mutations activate the Hippo pathway through YAP, drugs targeting YAP or its upstream regulators could be beneficial. Verteporfin, which disrupts YAP-TEAD interactions, is an emerging therapy [29].
- **PKC Inhibition:** Protein kinase C (PKC), downstream of GNAQ/GNA11, is a target of interest, with drugs like AEB071 (sotrastaurin) and LXS196 (darovasertib) under investigation in clinical trials [116,117].

These approaches could reshape the treatment paradigm of UM, shifting focus from conventional UV-based therapies to personalized treatments targeting specific oncogenic drivers. Preclinical studies in vitro and in vivo, as well as early-phase clinical trials, have shown promise for these targeted therapies in improving outcomes for patients with metastatic UM [1]. Beyond UM, targeted therapies could also be explored for other benign and malignant tumors reviewed throughout the article. For example, MEK inhibitors may be useful in managing vascular malformations or benign proliferations like hemangiomas associated with GNAQ/GNA11 mutations [118]. Ongoing studies on the efficacy of targeted treatments in these conditions could expand therapeutic options for patients with other GNAQ/GNA11-driven tumors.

5. Future Directions: Potential Histogenetic Role of SOX10-Positive Neural Crest Cells with GNAQ/GNA11 Mutations

The neural crest constitutes an embryonic, multipotent cell population characterized by extensive migration, giving rise to a diverse array of derivatives throughout the body. These include melanocytes, peripheral neurons and glia, as well as craniofacial bone, cartilage, and connective tissue [119]. The embryonic development of neural crest cells and the subsequent differentiation of tissues are intricately regulated by specific transcription factors. Among these, SOX10, a member of the SOX gene family, is particularly remarkable. Located on chromosome 22q13, the *SOX10* (SRY-related HMG-box gene 10) gene encodes a transcription factor essential for the differentiation, migration, and maintenance of tissues derived from neural crest cells. It is pivotal in the development of various tissues, including the central and peripheral nervous systems, melanocytes, chondrocytes, and odontoblasts [120].

SOX10 is a nuclear transcription factor involved in the differentiation of neural crest progenitor cells into melanocytes [121]. During the processes of neural crest induction and migration, SOX10 plays a crucial role in the maintenance of the multipotent state of neural crest cells by inhibiting their differentiation [119]. In diagnostic histopathology, SOX10 immunostaining proves to be a valuable diagnostic tool, due to its high sensitivity in identifying melanocytic and peripheral nerve sheath neoplasms in a variety of neoplasms, including cutaneous adnexal neoplasms, salivary gland neoplasms, breast neoplasms, melanocytic lesions, and peripheral nerve sheath tumors [122].

In a study by Xu et al., the activation of SOX10 by TNF-α through the PI3K/AKT signaling pathway facilitates the differentiation of vascular smooth muscle cells (VSMCs) and promotes vascular inflammation. Silencing SOX10 reduces vascular inflammation and prevents neointimal hyperplasia in RGS5 knockout mice. This study demonstrated that SOX10 acts as a regulator of vascular inflammation and represents a potential control point in inflammation-related vascular diseases [123].

Recently, SOX10-positive perivascular cells were taken under consideration in melanoma studies. It is hypothesized that the perivascular SOX10-positive cells, which express a neural crest marker, are evenly distributed around the vascular adventitia and are oriented parallel to the vascular lumina, may represent cells undergoing Schwannian differentiation linked to mechanoreception. SOX10-positive cells undergo differentiation into pericytes and smooth muscle cells across various tissues and organs, such as the carotid artery, brain, eye, thymus, heart, lung, spleen, and kidney [124]. Studies have identified SOX10-positive perivascular cells in both developing and adult mice, which function as vascular stem cells involved in the development and repair of vascular structures [125]. To our knowledge, there is limited characterization of SOX10-positive perivascular cells in human tissues analyzed through routine pathological examination. We hypothesize that SOX10-positive scattered perivascular cells with GNAQ/GNA11 mutations located in the dermis are the possible source of blue nevi. Further research is required to accurately determine the nature of these cells. The benign nature of SOX10-positive perivascular cells is indicated by their small nuclear size, which often approximates or is smaller than that of small lymphocyte nuclei, their smooth spindled nuclear contours, scant cytoplasm, and evenly spaced perivascular arrangement. These characteristics contrast with metastatic melanoma cells, which typically exhibit nuclear enlargement, pleomorphism, variable amounts of cytoplasm, and irregular distribution [126]. Additionally, benign SOX10-positive perivascular cells are challenging to identify on H&E slides, lack significant atypia, and do not express other melanocytic markers such as Melan-A and HMB45. This helps to prevent potential diagnostic errors that could lead to a false-positive diagnosis of metastatic melanoma [105].

6. Conclusions

Uveal melanoma (UM), while exhibiting unique morphological features, shares considerable molecular disruptions with other conditions driven by GNAQ or GNA11 mutations. These mutations are pivotal in abnormal signaling pathways, thereby contributing to the pathogenesis of multiple disorders beyond the UM reviewed in this article. The title "GNAQ/GNA11-related benign and malignant entities—a common histoembryologic origin or a tissue-dependent coincidence", poses an important question regarding the relationship between the various benign and malignant conditions driven by GNAQ and GNA11 mutations. As presented in this review, these mutations affect a variety of cell types across different tissues, such as melanocytes in uveal melanoma, vascular endothelial cells in hemangiomas, and adrenal cells in aldosterone-producing adenomas. Thus, the specific outcomes of GNAQ and GNA11 mutations seem to depend on several factors, including tissue type, developmental stage, and additional genetic or environmental factors. Especially, the presence of co-occurring mutations or epigenetic changes, such as mutations in BAP1, can influence whether a GNAQ or GNA11 mutation leads to a benign lesion or a malignant tumor. Therefore, evidence suggests that manifestations of these mutations are rather tissue-dependent than the result of a common histoembryologic origin; however, the additional modifying factors undoubtedly play a significant role in determining tumor behavior.

Author Contributions: Conceptualization, J.P., J.M., M.T. and P.D.; writing—original draft preparation, J.P., J.M. and M.T.; writing—review and editing, J.P., J.M., M.T. and P.D., visualization, J.M.; supervision, P.D.; funding acquisition, P.D. All authors have read and agreed to the published version of the manuscript.

Funding: This research was funded by the Polish Ministry of Science and Higher Education subvention according to the number SUBZ.A430.24.049 from the IT simple system of Wroclaw Medical University.

Data Availability Statement: Not applicable as no datasets were created or generated during the study.

Conflicts of Interest: The authors declare no conflicts of interest.

References

1. Silva-Rodríguez, P.; Fernández-Díaz, D.; Bande, M.; Pardo, M.; Loidi, L.; Blanco-Teijeiro, M.J. GNAQ and GNA11 Genes: A Comprehensive Review on Oncogenesis, Prognosis and Therapeutic Opportunities in Uveal Melanoma. *Cancers* **2022**, *14*, 3066. [CrossRef] [PubMed]
2. Fallico, M.; Raciti, G.; Longo, A.; Reibaldi, M.; Bonfiglio, V.; Russo, A.; Caltabiano, R.; Gattuso, G.; Falzone, L.; Avitabile, T. Current Molecular and Clinical Insights into Uveal Melanoma (Review). *Int. J. Oncol.* **2021**, *58*, 10. [CrossRef] [PubMed]
3. Neves, S.R.; Ram, P.T.; Iyengar, R. G Protein Pathways. *Science* **2002**, *296*, 1636–1639. [CrossRef] [PubMed]
4. Smit, K.N.; Jager, M.J.; de Klein, A.; Kiliç, E. Uveal Melanoma: Towards a Molecular Understanding. *Prog. Retin. Eye Res.* **2020**, *75*, 100800. [CrossRef]
5. Busam, K.J. Melanoma Arising in Association with and/or Simulating a Blue Nevus. In *Pathology of Melanocytic Tumors*; Elsevier: Amsterdam, The Netherlands, 2019; pp. 226–234. [CrossRef]
6. Chattopadhyay, C.; Kim, D.W.; Gombos, D.S.; Oba, J.; Qin, Y.; Williams, M.D.; Esmaeli, B.; Grimm, E.A.; Wargo, J.A.; Woodman, S.E.; et al. Uveal Melanoma: From Diagnosis to Treatment and the Science in Between. *Cancer* **2016**, *122*, 2299–2312. [CrossRef]
7. Cerbone, L.; Van Ginderdeuren, R.; Van Den Oord, J.; Fieuws, S.; Spileers, W.; Van Eenoo, L.; Wozniak, A.; Sternberg, C.N.; Schöffski, P. Clinical Presentation, Pathological Features and Natural Course of Metastatic Uveal Melanoma, an Orphan and Commonly Fatal Disease. *Oncology* **2014**, *86*, 185–189. [CrossRef] [PubMed]
8. Van Raamsdonk, C.D.; Bezrookove, V.; Green, G.; Bauer, J.; Gaugler, L.; O'Brien, J.M.; Simpson, E.M.; Barsh, G.S.; Bastian, B.C. Frequent Somatic Mutations of GNAQ in Uveal Melanoma and Blue Naevi. *Nature* **2009**, *457*, 599–602. [CrossRef]
9. Decatur, C.L.; Ong, E.; Garg, N.; Anbunathan, H.; Bowcock, A.M.; Field, M.G.; Harbour, J.W. Driver Mutations in Uveal Melanoma: Associations with Gene Expression Profile and Patient Outcomes. *JAMA Ophthalmol.* **2016**, *134*, 728–733. [CrossRef]
10. Moore, A.R.; Ceraudo, E.; Sher, J.J.; Guan, Y.; Shoushtari, A.N.; Chang, M.T.; Zhang, J.Q.; Walczak, E.G.; Kazmi, M.A.; Taylor, B.S.; et al. Recurrent Activating Mutations of G-Protein-Coupled Receptor CYSLTR2 in Uveal Melanoma. *Nat. Genet.* **2016**, *48*, 675–680. [CrossRef]
11. Johansson, P.; Aoude, L.G.; Wadt, K.; Glasson, W.J.; Warrier, S.K.; Hewitt, A.W.; Kiilgaard, J.F.; Heegaard, S.; Isaacs, T.; Franchina, M.; et al. Deep Sequencing of Uveal Melanoma Identifies a Recurrent Mutation in PLCB4. *Oncotarget* **2016**, *7*, 4624–4631. [CrossRef]
12. NCBI. GNAQ G Protein Subunit Alpha q [Homo Sapiens (Human)]—Gene. Available online: https://www.ncbi.nlm.nih.gov/gene?Db=gene&Cmd=DetailsSearch&Term=2776 (accessed on 22 July 2024).
13. NCBI. GNAQ: Chr9-Genome Data Viewer. Available online: https://www.ncbi.nlm.nih.gov/gdv/browser/gene/?id=2776 (accessed on 22 July 2024).
14. Dong, Q.; Shenker, A.; Way, J.; Haddad, B.R.; Lin, K.; Hughes, M.R.; McBride, O.W.; Spiegel, A.M.; Battey, J. Molecular Cloning of Human Gαq CDNA and Chromosomal Localization of the Gαq Gene (GNAQ) and a Processed Pseudogene. *Genomics* **1995**, *30*, 470–475. [CrossRef]
15. Franklin, W.A.; Aisner, D.L.; Post, M.D.; Bunn, P.A.; Garcia, M.V. Pathology, Biomarkers, and Molecular Diagnostics. In *Abeloff's Clinical Oncology*, 5th ed.; Saunders: Philadelphia, PA, USA, 2014; pp. 226–252.e6. [CrossRef]
16. Comi, A.M.; Marchuk, D.A.; Pevsner, J. Sturge–Weber Syndrome. In *Rosenberg's Molecular and Genetic Basis of Neurological and Psychiatric Disease*, 5th ed.; Saunders: Philadelphia, PA, USA, 2015; pp. 945–953. [CrossRef]
17. Birkner, K.; Wasser, B.; Loos, J.; Plotnikov, A.; Seger, R.; Zipp, F.; Witsch, E.; Bittner, S. The Role of ERK Signaling in Experimental Autoimmune Encephalomyelitis. *Int. J. Mol. Sci.* **2017**, *18*, 1990. [CrossRef]
18. Sun, Y.; Liu, W.Z.; Liu, T.; Feng, X.; Yang, N.; Zhou, H.F. Signaling Pathway of MAPK/ERK in Cell Proliferation, Differentiation, Migration, Senescence and Apoptosis. *J. Recept. Signal Transduct.* **2015**, *35*, 600–604. [CrossRef] [PubMed]
19. Hawkes, J.E.; Campbell, J.; Garvin, D.; Cannon-Albright, L.; Cassidy, P.; Leachman, S.A. Lack of GNAQ and GNA11 Germ-Line Mutations in Familial Melanoma Pedigrees with Uveal Melanoma or Blue Nevi. *Front. Oncol.* **2013**, *3*, 48332. [CrossRef] [PubMed]
20. Wilkie, T.M.; Gilbert, D.J.; Olsen, A.S.; Chen, X.N.; Amatruda, T.T.; Korenberg, J.R.; Trask, B.J.; de Jong, P.; Reed, R.R.; Simon, M.I.; et al. Evolution of the Mammalian G Protein α Subunit Multigene Family. *Nat. Genet.* **1992**, *1*, 85–91. [CrossRef]
21. Sharma, A.; Stei, M.M.; Fröhlich, H.; Holz, F.G.; Loeffler, K.U.; Herwig-Carl, M.C. Genetic and Epigenetic Insights into Uveal Melanoma. *Clin. Genet.* **2018**, *93*, 952–961. [CrossRef] [PubMed]
22. NCBI. GNA11 G Protein Subunit Alpha 11 [Homo Sapiens (Human)]-Gene. Available online: https://www.ncbi.nlm.nih.gov/gene/2767 (accessed on 22 July 2024).
23. Strathmann, M.P.; Simon, M.I. G Alpha 12 and G Alpha 13 Subunits Define a Fourth Class of G Protein Alpha Subunits. *Proc. Natl. Acad. Sci. USA* **1991**, *88*, 5582–5586. [CrossRef]
24. Strathmann, M.; Simon, M.I. G Protein Diversity: A Distinct Class of Alpha Subunits Is Present in Vertebrates and Invertebrates. *Proc. Natl. Acad. Sci. USA* **1990**, *87*, 9113–9117. [CrossRef]
25. Jiang, M.; Pandey, S.; Tran, V.T.; Fong, H.K.W. Guanine Nucleotide-Binding Regulatory Proteins in Retinal Pigment Epithelial Cells. *Proc. Natl. Acad. Sci. USA* **1991**, *88*, 3907–3911. [CrossRef]
26. Vahe, C.; Benomar, K.; Espiard, S.; Coppin, L.; Jannin, A.; Odou, M.F.; Vantyghem, M.C. Diseases Associated with Calcium-Sensing Receptor. *Orphanet. J. Rare Dis.* **2017**, *12*, 19. [CrossRef]
27. Shoushtari, A.N.; Carvajal, R.D. GNAQ and GNA11 Mutations in Uveal Melanoma. *Melanoma Res.* **2014**, *24*, 525–534. [CrossRef] [PubMed]

28. Tenhola, S.; Voutilainen, R.; Reyes, M.; Toiviainen-Salo, S.; Jüppner, H.; Mäkitie, O. Impaired Growth and Intracranial Calcifications in Autosomal Dominant Hypocalcemia Caused by a GNA11 Mutation. *Eur. J. Endocrinol.* **2016**, *175*, 211–218. [CrossRef] [PubMed]
29. Yu, F.X.; Luo, J.; Mo, J.S.; Liu, G.; Kim, Y.C.; Meng, Z.; Zhao, L.; Peyman, G.; Ouyang, H.; Jiang, W.; et al. Mutant Gq/11 Promote Uveal Melanoma Tumorigenesis by Activating YAP. *Cancer Cell* **2014**, *25*, 822–830. [CrossRef] [PubMed]
30. Nesbit, M.A.; Hannan, F.M.; Howles, S.A.; Babinsky, V.N.; Head, R.A.; Cranston, T.; Rust, N.; Hobbs, M.R.; Hunter Heath, I.; Thakker, R.V. Mutations Affecting G-Protein Subunit A11 in Hypercalcemia and Hypocalcemia. *N. Engl. J. Med.* **2013**, *368*, 2476–2486. [CrossRef]
31. OMIM. Guanine Nucleotide-Binding Protein, Alpha-11; GNA11. Available online: https://www.omim.org/entry/139313#0003 (accessed on 22 July 2024).
32. Jaquemus, J.; Perron, E.; Buisson, A.; Ferrara, G.; Haddad, V.; de la Fouchardiere, A. Compound Blue Nevus: A Reappraisal of the Concept in the Genomic Era. *Virchows Arch.* **2020**, *476*, 439–443. [CrossRef]
33. Couto, J.A.; Ayturk, U.M.; Konczyk, D.J.; Goss, J.A.; Huang, A.Y.; Hann, S.; Reeve, J.L.; Liang, M.G.; Bischoff, J.; Warman, M.L.; et al. A Somatic GNA11 Mutation Is Associated with Extremity Capillary Malformation and Overgrowth. *Angiogenesis* **2017**, *20*, 303–306. [CrossRef]
34. Dompmartin, A.; van der Vleuten, C.J.M.; Dekeuleneer, V.; Duprez, T.; Revencu, N.; Désir, J.; te Loo, D.M.W.M.; Flucke, U.; Eijkelenboom, A.; Schultze Kool, L.; et al. GNA11-Mutated Sturge-Weber Syndrome Has Distinct Neurological and Dermatological Features. *Eur. J. Neurol.* **2022**, *29*, 3061–3070. [CrossRef]
35. Liau, J.Y.; Lee, J.C.; Tsai, J.H.; Chen, C.C.; Chung, Y.C.; Wang, Y.H. High Frequency of GNA14, GNAQ, and GNA11 Mutations in Cherry Hemangioma: A Histopathological and Molecular Study of 85 Cases Indicating GNA14 as the Most Commonly Mutated Gene in Vascular Neoplasms. *Mod. Pathol.* **2019**, *32*, 1657–1665. [CrossRef]
36. Ayturk, U.M.; Couto, J.A.; Hann, S.; Mulliken, J.B.; Williams, K.L.; Huang, A.Y.; Fishman, S.J.; Boyd, T.K.; Kozakewich, H.P.W.; Bischoff, J.; et al. Somatic Activating Mutations in GNAQ and GNA11 Are Associated with Congenital Hemangioma. *Am. J. Hum. Genet.* **2016**, *98*, 789–795. [CrossRef]
37. Van Raamsdonk, C.D.; Griewank, K.G.; Crosby, M.B.; Garrido, M.C.; Vemula, S.; Wiesner, T.; Obenauf, A.C.; Wackernagel, W.; Green, G.; Bouvier, N.; et al. Mutations in GNA11 in Uveal Melanoma. *N. Engl. J. Med.* **2010**, *363*, 2191–2199. [CrossRef]
38. Sumich, P.; Mitchell, P.; Wang, J.J. Choroidal Nevi in a White Population: The Blue Mountains Eye Study. *Arch. Ophthalmol.* **1998**, *116*, 645–650. [CrossRef] [PubMed]
39. Chien, J.L.; Sioufi, K.; Surakiatchanukul, T.; Shields, J.A.; Shields, C.L. Choroidal Nevus: A Review of Prevalence, Features, Genetics, Risks, and Outcomes. *Curr. Opin. Ophthalmol.* **2017**, *28*, 228–237. [CrossRef] [PubMed]
40. Brovkina, A.F.; Stoyukhina, A.S.; Musatkina, I.V. Transformation of Choroidal Nevus into Melanoma. *Vestn. Oftalmol.* **2021**, *137*, 5–17. [CrossRef]
41. Mashayekhi, A.; Siu, S.; Shields, C.L.; Shields, J.A. Slow Enlargement of Choroidal Nevi: A Long-Term Follow-up Study. *Ophthalmology* **2011**, *118*, 382–388. [CrossRef]
42. Vader, M.J.C.; Madigan, M.C.; Versluis, M.; Suleiman, H.M.; Gezgin, G.; Gruis, N.A.; Out-Luiting, J.J.; Bergman, W.; Verdijk, R.M.; Jager, M.J.; et al. GNAQ and GNA11 Mutations and Downstream YAP Activation in Choroidal Nevi. *Br. J. Cancer* **2017**, *117*, 884–887. [CrossRef]
43. Versluis, M.; De Lange, M.J.; Van Pelt, S.I.; Ruivenkamp, C.A.L.; Kroes, W.G.M.; Cao, J.; Jager, M.J.; Luyten, G.P.M.; Van Der Velden, P.A. Digital PCR Validates 8q Dosage as Prognostic Tool in Uveal Melanoma. *PLoS ONE* **2015**, *10*, e0116371. [CrossRef]
44. Karachaliou, N.; Pilotto, S.; Teixidó, C.; Viteri, S.; González-Cao, M.; Riso, A.; Morales-Espinosa, D.; Molina, M.A.; Chaib, I.; Santarpia, M.; et al. Melanoma: Oncogenic drivers and the immune system. *Ann. Transl. Med.* **2015**, *3*, 265. [CrossRef] [PubMed]
45. Pipek, O.; Vizkeleti, L.; Doma, V.; Alpár, D.; Bödör, C.; Kárpáti, S.; Timar, J. The Driverless Triple-Wild-Type (BRAF, RAS, KIT) Cutaneous Melanoma: Whole Genome Sequencing Discoveries. *Cancers* **2023**, *15*, 1712. [CrossRef]
46. Park, J.J.; Hamad, S.A.; Stewart, A.; Carlino, M.S.; Lim, S.Y.; Rizos, H. PKC-independent PI3K signalling diminishes PKC inhibitor sensitivity in uveal melanoma. *Oncogenesis* **2024**, *13*, 1–9. [CrossRef]
47. Toomey, C.B.; Fraser, K.; Thorson, J.A.; Goldbaum, M.H.; Lin, J.H. GNAQ and PMS1 Mutations Associated with Uveal Melanoma, Ocular Surface Melanosis, and Nevus of Ota. *Ocul. Oncol. Pathol.* **2019**, *5*, 267–272. [CrossRef]
48. Liu, X.; Run-Hua, Z.; Pan, J.; Li, Z.; Yu, L.; Li, Y. Emerging therapeutic strategies for metastatic uveal melanoma: Targeting driver mutations. *Pigment. Cell Melanoma Res.* **2024**, *37*, 411–425. [CrossRef] [PubMed]
49. Chen, X.; Wu, Q.; Depeille, P.; Chen, P.; Thornton, S.; Kalirai, H.; Coupland, S.E.; Roose, J.P.; Bastian, B.C. RasGRP3 Mediates MAPK Pathway Activation in GNAQ Mutant Uveal Melanoma. *Cancer Cell* **2017**, *31*, 685–696.e6. [CrossRef] [PubMed]
50. Feng, X.; Arang, N.; Rigiracciolo, D.C.; Lee, J.S.; Yeerna, H.; Wang, Z.; Lubrano, S.; Kishore, A.; Pachter, J.A.; König, G.M.; et al. A Platform of Synthetic Lethal Gene Interaction Networks Reveals that the GNAQ Uveal Melanoma Oncogene Controls the Hippo Pathway through FAK. *Cancer Cell* **2019**, *35*, 457–472.e5. [CrossRef] [PubMed]
51. García-Mulero, S.; Fornelino, R.; Punta, M.; Lise, S.; Varela, M.; del Carpio, L.P.; Moreno, R.; Costa-García, M.; Rieder, D.; Trajanoski, Z.; et al. Driver mutations in GNAQ and GNA11 genes as potential targets for precision immunotherapy in uveal melanoma patients. *OncoImmunology* **2023**, *12*, 2261278. [CrossRef]
52. Khalili, J.S.; Yu, X.; Wang, J.; Hayes, B.C.; Davies, M.A.; Lizee, G.; Esmaeli, B.; Woodman, S.E. Combination Small Molecule MEK and PI3K Inhibition Enhances Uveal Melanoma Cell Death in a Mutant GNAQ- and GNA11-Dependent Manner. *Clin. Cancer Res.* **2012**, *18*, 4345–4355. [CrossRef] [PubMed]

53. Lyubasyuk, V.; Ouyang, H.; Yu, F.-X.; Guan, K.-L.; Zhang, K. YAP inhibition blocks uveal melanogenesis driven by GNAQ or GNA11 mutations. *Mol. Cell. Oncol.* **2014**, *2*, e970957. [CrossRef]
54. Shoushtari, A.N.; Khan, S.; Komatsubara, K.; Feun, L.; Acquavella, N.; Singh-Kandah, S.; Negri, T.; Nesson, A.; Abbate, K.; Cremers, S.; et al. A Phase IB Study of Sotrastaurin, a PKC Inhibitor, and Alpelisib, a PI3Kα Inhibitor, in Patients with Metastatic Uveal Melanoma. *Cancers* **2021**, *13*, 5504. [CrossRef]
55. Lorusso, F.J.; Boniuk, M.; Font, R.L. Melanocytoma (Magnocellular Nevus) of the Ciliary Body: Report of 10 Cases and Review of the Literature. *Ophthalmology* **2000**, *107*, 795–800. [CrossRef]
56. Pubmed. Ciliary Body Melanocytoma with Anterior Segment Pigment Dispersion and Elevated Intraocular Pressure. Available online: https://pubmed.ncbi.nlm.nih.gov/10209730/ (accessed on 22 July 2024).
57. Solomon, D.A.; Ramani, B.; Eiger-Moscovich, M.; Milman, T.; Uludag, G.; Crawford, J.B.; Phan, I.; Char, D.H.; Shields, C.L.; Eagle, R.C.; et al. Iris and Ciliary Body Melanocytomas Are Defined by Solitary GNAQ Mutation Without Additional Oncogenic Alterations. *Ophthalmology* **2022**, *129*, 1429–1439. [CrossRef]
58. Francis, J.H.; Wiesner, T.; Milman, T.; Won, H.H.; Lin, A.; Lee, V.; Albert, D.M.; Folberg, R.; Berger, M.F.; Char, D.H.; et al. Investigation of Somatic GNAQ, GNA11, BAP1 and SF3B1 Mutations in Ophthalmic Melanocytomas. *Ocul. Oncol. Pathol.* **2016**, *2*, 171–177. [CrossRef]
59. Mudhar, H.S.; Doherty, R.; Salawu, A.; Sisley, K.; Rennie, I.G. Immunohistochemical and Molecular Pathology of Ocular Uveal Melanocytoma: Evidence for Somatic GNAQ Mutations. *Br. J. Ophthalmol.* **2013**, *97*, 924–928. [CrossRef]
60. Boned-Murillo, A.; Diaz-Barreda, M.D.; Honrubia-Grijalbo, A.; Esteban-Floria, O.; Puyuelo, F.J.A. Choroidal Hemangioma Associated with Hepatic Hemangioma: A Case Report and Literature Review. *Case Rep. Ophthalmol.* **2021**, *12*, 425–432. [CrossRef]
61. Shields, C.L.; Honavar, S.G.; Shields, J.A.; Cater, J.; Demirci, H. Circumscribed Choroidal Hemangioma: Clinical Manifestations and Factors Predictive of Visual Outcome in 200 Consecutive Cases. *Ophthalmology* **2001**, *108*, 2237–2248. [CrossRef]
62. Cheung, D.; Grey, R.; Rennie, I. Circumscribed Choroidal Haemangioma in a Patient with Sturge Weber Syndrome. *Eye* **2000**, *14 Pt 2*, 238–240. [CrossRef]
63. Le Guin, C.H.D.; Metz, K.A.; Kreis, S.H.; Bechrakis, N.E.; Bornfeld, N.; Zeschnigk, M.; Lohmann, D.R. GNAQ Q209R Mutations Are Highly Specific for Circumscribed Choroidal Hemangioma. *Cancers* **2019**, *11*, 1031. [CrossRef]
64. Lim, Y.H.; Bacchiocchi, A.; Qiu, J.; Straub, R.; Bruckner, A.; Bercovitch, L.; Narayan, D.; McNiff, J.; Ko, C.; Robinson-Bostom, L.; et al. GNA14 Somatic Mutation Causes Congenital and Sporadic Vascular Tumors by MAPK Activation. *Am. J. Hum. Genet.* **2016**, *99*, 443–450. [CrossRef]
65. Nasim, S.; Bichsel, C.; Pinto, A.; Alexandrescu, S.; Kozakewich, H.; Bischoff, J. Similarities and Differences between Brain and Skin GNAQ p.R183Q Driven Capillary Malformations. *bioRxiv* **2024**, *12*, 212. [CrossRef]
66. Davies, O.M.T.; Ng, A.T.; Tran, J.; Blumenthal, S.; Arkin, L.M.; Nopper, A.J.; Cottrell, C.E.; Garzon, M.; Siegel, D.H.; Frieden, I.J.; et al. Early-Onset Hypertension Associated with Extensive Cutaneous Capillary Malformations Harboring Postzygotic Variants in GNAQ and GNA11. *Pediatr. Dermatol.* **2022**, *39*, 914–919. [CrossRef]
67. Happle, R. Capillary Malformations: A Classification Using Specific Names for Specific Skin Disorders. *J. Eur. Acad. Dermatol. Venereol.* **2015**, *29*, 2295–2305. [CrossRef]
68. Beteta-Gorriti, V.; Vázquez-Osorio, I.; de Dios-Velázquez, Á.; Rodriguez-Laguna, L.; Viana-Huete, V.; García Torrijos, C.; Martinez-Glez, V.; Rodríguez-Díaz, E. Mixed Vascular Naevus Syndrome: Report of Three Children with Somatic GNA11 Mutation and New Systemic Associations. *Clin. Exp. Dermatol.* **2022**, *47*, 129–135. [CrossRef]
69. Higueros, E.; Roe, E.; Granell, E.; Baselga, E. Sturge-Weber Syndrome: A Review. *Actas Dermo-Sifiliográficas* **2017**, *108*, 407–417. [CrossRef]
70. Yeom, S.E.; Comi, A.M. Updates on Sturge-Weber Syndrome. *Stroke* **2022**, *53*, 3769–3779. [CrossRef]
71. Shirley, M.D.; Tang, H.; Gallione, C.J.; Baugher, J.D.; Frelin, L.P.; Cohen, B.; North, P.E.; Marchuk, D.A.; Comi, A.M.; Pevsner, J. Sturge–Weber Syndrome and Port-Wine Stains Caused by Somatic Mutation in GNAQ. *N. Engl. J. Med.* **2013**, *368*, 1971–1979. [CrossRef]
72. Berenguer, B.; Mulliken, J.B.; Enjolras, O.; Boon, L.M.; Wassef, M.; Josset, P.; Burrows, P.E.; Perez-Atayde, A.R.; Kozakewich, H.P.W. Rapidly Involuting Congenital Hemangioma: Clinical and Histopathologic Features. *Pediatr. Dev. Pathol.* **2003**, *6*, 495–510. [CrossRef]
73. Enjolras, O.; Mulliken, J.B.; Boon, L.M.; Wassef, M.; Kozakewich, H.P.W.; Burrows, P.E. Noninvoluting Congenital Hemangioma: A Rare Cutaneous Vascular Anomaly. *Plast. Reconstr. Surg.* **2001**, *107*, 1647–1654. [CrossRef]
74. Nasseri, E.; Piram, M.; McCuaig, C.C.; Kokta, V.; Dubois, J.; Powell, J. Partially Involuting Congenital Hemangiomas: A Report of 8 Cases and Review of the Literature. *J. Am. Acad. Dermatol.* **2014**, *70*, 75–79. [CrossRef]
75. North, P.E.; Waner, M.; Mizeracki, A.; Mihm, M.C. GLUT1: A Newly Discovered Immunohistochemical Marker for Juvenile Hemangiomas. *Hum. Pathol.* **2000**, *31*, 11–22. [CrossRef]
76. Tuder, R.M.; Young, R.; Karasek, M.; Bensch, K. Adult Cutaneous Hemangiomas Are Composed of Nonreplicating Endothelial Cells. *J. Investig. Dermatol.* **1987**, *89*, 594–597. [CrossRef]
77. Groesser, L.; Peterhof, E.; Evert, M.; Landthaler, M.; Berneburg, M.; Hafner, C. BRAF and RAS Mutations in Sporadic and Secondary Pyogenic Granuloma. *J. Investig. Dermatol.* **2016**, *136*, 481–486. [CrossRef]
78. Montgomery, E.; Epstein, J.I. Anastomosing Hemangioma of the Genitourinary Tract: A Lesion Mimicking Angiosarcoma. *Am. J. Surg. Pathol.* **2009**, *33*, 1364–1369. [CrossRef]

79. Lin, J.; Bigge, J.; Ulbright, T.M.; Montgomery, E. Anastomosing Hemangioma of the Liver and Gastrointestinal Tract: An Unusual Variant Histologically Mimicking Angiosarcoma. *Am. J. Surg. Pathol.* **2013**, *37*, 1761–1765. [CrossRef]
80. John, I.; Folpe, A.L. Anastomosing Hemangiomas Arising in Unusual Locations: A Clinicopathologic Study of 17 Soft Tissue Cases Showing a Predilection for the Paraspinal Region. *Am. J. Surg. Pathol.* **2016**, *40*, 1084–1089. [CrossRef]
81. Bean, G.R.; Joseph, N.M.; Gill, R.M.; Folpe, A.L.; Horvai, A.E.; Umetsu, S.E. Recurrent GNAQ Mutations in Anastomosing Hemangiomas. *Mod. Pathol.* **2017**, *30*, 722–727. [CrossRef]
82. Bean, G.R.; Joseph, N.M.; Folpe, A.L.; Horvai, A.E.; Umetsu, S.E. Recurrent GNA14 Mutations in Anastomosing Haemangiomas. *Histopathology* **2018**, *73*, 354–357. [CrossRef]
83. Liau, J.Y.; Tsai, J.H.; Lan, J.; Chen, C.C.; Wang, Y.H.; Lee, J.C.; Huang, H.Y. GNA11 Joins GNAQ and GNA14 as a Recurrently Mutated Gene in Anastomosing Hemangioma. *Virchows Archiv* **2020**, *476*, 475–481. [CrossRef]
84. Gill, R.M.; Buelow, B.; Mather, C.; Joseph, N.M.; Alves, V.; Brunt, E.M.; Liu, T.C.; Makhlouf, H.; Marginean, C.; Nalbantoglu, I.; et al. Hepatic Small Vessel Neoplasm, a Rare Infiltrative Vascular Neoplasm of Uncertain Malignant Potential. *Hum. Pathol.* **2016**, *54*, 143–151. [CrossRef]
85. Joseph, N.M.; Brunt, E.M.; Marginean, C.; Nalbantoglu, I.; Snover, D.C.; Thung, S.N.; Yeh, M.M.; Umetsu, S.E.; Ferrell, L.D.; Gill, R.M. Frequent GNAQ and GNA14 Mutations in Hepatic Small Vessel Neoplasm. *Am. J. Surg. Pathol.* **2018**, *42*, 1201–1207. [CrossRef]
86. Kumar, A.; Zastrow, D.B.; Kravets, E.J.; Beleford, D.; Ruzhnikov, M.R.Z.; Grove, M.E.; Dries, A.M.; Kohler, J.N.; Waggott, D.M.; Yang, Y.; et al. Extracutaneous Manifestations in Phacomatosis Cesioflammea and Cesiomarmorata: Case Series and Literature Review. *Am. J. Med. Genet. Part A* **2019**, *179*, 966–977. [CrossRef]
87. Happle, R. Phacomatosis Pigmentovascularis Revisited and Reclassified. *Arch. Dermatol.* **2005**, *141*, 385–388. [CrossRef]
88. Torchia, D. Phacomatosis Melanorosea, Unearthed. *Eur. J. Dermatol.* **2012**, *22*, 582–583. [CrossRef]
89. Torchia, D.; Happle, R. Segmental Hypomelanosis and Hypermelanosis Arranged in a Checkerboard Pattern Are Distinct Naevi: Flag-like Hypomelanotic Naevus and Flag-like Hypermelanotic Naevus. *J. Eur. Acad. Dermatol. Venereol.* **2015**, *29*, 2088–2099. [CrossRef]
90. Torrelo, A.; Zambrano, A.; Happle, R. Cutis Marmorata Telangiectatica Congenita and Extensive Mongolian Spots: Type 5 Phacomatosis Pigmentovascularis. *Br. J. Dermatol.* **2003**, *148*, 342–345. [CrossRef]
91. Du, G.; Zhang, X.; Zhang, T. Cutis Marmorata Telangiectatica Congenita and Aberrant Mongolian Spots: Type V Phacomatosis Pigmentovascularis or Phacomatosis Cesiomarmorata. *JAAD Case Rep.* **2016**, *2*, 28–30. [CrossRef]
92. Thomas, A.C.; Zeng, Z.; Rivière, J.B.; O'Shaughnessy, R.; Al-Olabi, L.; St.-Onge, J.; Atherton, D.J.; Aubert, H.; Bagazgoitia, L.; Barbarot, S.; et al. Mosaic Activating Mutations in GNA11 and GNAQ Are Associated with Phakomatosis Pigmentovascularis and Extensive Dermal Melanocytosis. *J. Investig. Dermatol.* **2016**, *136*, 770–778. [CrossRef]
93. Shields, C.L.; Kaliki, S.; Livesey, M.; Walker, B.; Garoon, R.; Bucci, M.; Feinstein, E.; Pesch, A.; Gonzalez, C.; Lally, S.E.; et al. Association of Ocular and Oculodermal Melanocytosis with the Rate of Uveal Melanoma Metastasis: Analysis of 7872 Consecutive Eyes. *JAMA Ophthalmol.* **2013**, *131*, 993–1003. [CrossRef]
94. Zallmann, M.; Mackay, M.T.; Leventer, R.J.; Ditchfield, M.; Bekhor, P.S.; Su, J.C. Retrospective Review of Screening for Sturge-Weber Syndrome with Brain Magnetic Resonance Imaging and Electroencephalography in Infants with High-Risk Port-Wine Stains. *Pediatr. Dermatol.* **2018**, *35*, 575–581. [CrossRef]
95. Colebatch, A.J.; Adhikari, C.; Diefenbach, R.J.; Rawson, R.V.; Ferguson, P.M.; Rizos, H.; Long, G.V.; McCarthy, S.W.; Thompson, J.F.; Wilmott, J.S.; et al. Comprehensive Clinical, Histopathologic, and Molecular Analysis and Long-Term Follow-up of Patients with Nodal Blue Nevi. *Am. J. Surg. Pathol.* **2022**, *46*, 1048–1059. [CrossRef]
96. Phadke, P.A.; Zembowicz, A. Blue Nevi and Related Tumors. *Clin. Lab. Med.* **2011**, *31*, 345–358. [CrossRef]
97. Chang, L.W.; Kazlouskaya, V.; Kazi, R.; Davar, D.; Ferris, R.L.; Ho, J.; Karunamurthy, A.; Jedrych, J.J.; Bunimovich, Y.L. Melanoma Ex Blue Nevus with GNA11 Mutation and BAP1 Loss: Case Report and Review of the Literature. *Am. J. Dermatopathol.* **2020**, *42*, 854–857. [CrossRef]
98. Emley, A.; Nguyen, L.P.; Yang, S.; Mahalingam, M. Somatic Mutations in GNAQ in Amelanotic/Hypomelanotic Blue Nevi. *Hum. Pathol.* **2011**, *42*, 136–140. [CrossRef]
99. Uguen, A.; Guibourg, B.; Costa, S.; Marcorelles, P. GNA11-Mutated and BAP1-Negative Melanomas Ex Blue Naevi: A Particularly Aggressive Entity. *Acta Derm. Venereol.* **2017**, *97*, 743–744. [CrossRef]
100. Shah, K.; Folpe, A.L.; Miller, M.; Morgan, J.A.; Raut, C.P.; Doyle, L.A. Primary Intra-Abdominal Melanoma Arising in Association with Extracutaneous Blue Naevus: A Report of Two Cases. *Histopathology* **2021**, *78*, 281–289. [CrossRef]
101. Isales, M.C.; Haugh, A.M.; Bubley, J.; Verzì, A.E.; Zhang, B.; Kudalkar, E.; Lee, C.Y.; Yazdan, P.; Guitart, J.; Gerami, P. Genomic Assessment of Blitz Nevi Suggests Classification as a Subset of Blue Nevus Rather Than Spitz Nevus: Clinical, Histopathologic, and Molecular Analysis of 18 Cases. *Am. J. Dermatopathol.* **2018**, *40*, 118–124. [CrossRef]
102. Vilela, L.A.P.; Almeida, M.Q. Diagnosis and Management of Primary Aldosteronism. *Arch. Endocrinol. Metab.* **2017**, *61*, 305–312. [CrossRef]
103. Hellman, P.; Björklund, P.; Åkerström, T. Aldosterone-Producing Adenomas. *Vitam. Horm.* **2019**, *109*, 407–431. [CrossRef]
104. Gomez-Sanchez, C.E.; Gomez-Sanchez, C.M.; Oki, K. Aldosterone-Producing Adenomas: More than Meets the Eye. *Hypertension* **2020**, *75*, 927–929. [CrossRef]

105. Zhou, J.; Azizan, E.A.B.; Cabrera, C.P.; Fernandes-Rosa, F.L.; Boulkroun, S.; Argentesi, G.; Cottrell, E.; Amar, L.; Wu, X.; O'Toole, S.; et al. Somatic Mutations of GNA11 and GNAQ in CTNNB1-Mutant Aldosterone-Producing Adenomas Presenting in Puberty, Pregnancy or Menopause. *Nat. Genet.* **2021**, *53*, 1360–1372. [CrossRef]
106. Nanba, K.; Omata, K.; Else, T.; Beck, P.C.C.; Nanba, A.T.; Turcu, A.F.; Miller, B.S.; Giordano, T.J.; Tomlins, S.A.; Rainey, W.E. Targeted Molecular Characterization of Aldosterone-Producing Adenomas in White Americans. *J. Clin. Endocrinol. Metab.* **2018**, *103*, 3869–3876. [CrossRef]
107. Liubinas, S.V.; Maartens, N.; Drummond, K.J. Primary Melanocytic Neoplasms of the Central Nervous System. *J. Clin. Neurosci.* **2010**, *17*, 1227–1232. [CrossRef]
108. Küsters-Vandevelde, H.V.N.; Küsters, B.; Van Engen-Van Grunsven, A.C.H.; Groenen, P.J.T.A.; Wesseling, P.; Blokx, W.A.M. Primary Melanocytic Tumors of the Central Nervous System: A Review with Focus on Molecular Aspects. *Brain Pathol.* **2015**, *25*, 209–226. [CrossRef]
109. Orphanet: Primary Melanoma of the Central Nervous System. Available online: https://www.orpha.net/en/disease/detail/252050 (accessed on 22 July 2024).
110. Cornejo, K.M.; Hutchinson, L.; Cosar, E.F.; Smith, T.; Tomaszewicz, K.; Dresser, K.; Deng, A. Is It a Primary or Metastatic Melanocytic Neoplasm of the Central Nervous System?: A Molecular Based Approach. *Pathol. Int.* **2013**, *63*, 559–564. [CrossRef]
111. Urtatiz, O.; Cook, C.; Huang, J.L.Y.; Yeh, I.; Van Raamsdonk, C.D. GNAQQ209L Expression Initiated in Multipotent Neural Crest Cells Drives Aggressive Melanoma of the Central Nervous System. *Pigment Cell Melanoma Res.* **2020**, *33*, 96–111. [CrossRef]
112. Zhou, H.W.; Tran, A.Q.; North, V.S.; Zagzag, D.; Sen, C.; Kazim, M. GNA11 Mutation in an Intracranial Melanocytoma with Orbital Involvement and Nevus of Ota. *Ophthalmic Plast. Reconstr. Surg.* **2022**, *38*, E47–E49. [CrossRef]
113. Küsters-Vandevelde, H.V.N.; Van Engen-Van Grunsven, I.A.C.H.; Coupland, S.E.; Lake, S.L.; Rijntjes, J.; Pfundt, R.; Küsters, B.; Wesseling, P.; Blokx, W.A.M.; Groenen, P.J.T.A. Mutations in G Protein Encoding Genes and Chromosomal Alterations in Primary Leptomeningeal Melanocytic Neoplasms. *Pathol. Oncol. Res.* **2015**, *21*, 439–447. [CrossRef]
114. Boru, G.; Cebulla, C.M.; Sample, K.M.; Massengill, J.B.; Davidorf, F.H.; Abdel-Rahman, M.H. Heterogeneity in Mitogen-Activated Protein Kinase (MAPK) Pathway Activation in Uveal Melanoma with Somatic GNAQ and GNA11 Mutations. *Investig. Ophthalmol. Vis. Sci.* **2019**, *60*, 2474–2480. [CrossRef]
115. Babchia, N.; Calipel, A.; Mouriaux, F.; Faussat, A.M.; Mascarelli, F. The PI3K/Akt and MTOR/P70S6K Signaling Pathways in Human Uveal Melanoma Cells: Interaction with B-Raf/ERK. *Investig. Ophthalmol. Vis. Sci.* **2010**, *51*, 421–429. [CrossRef]
116. Wu, X.; Li, J.; Zhu, M.; Fletcher, J.A.; Hodi, F.S. Protein Kinase C Inhibitor AEB071 Targets Ocular Melanoma Harboring GNAQ Mutations via Effects on the PKC/Erk1/2 and PKC/NF-KB Pathways. *Mol. Cancer Ther.* **2012**, *11*, 1905–1914. [CrossRef]
117. Ma, J.; Weng, L.; Bastian, B.C.; Chen, X. Functional Characterization of Uveal Melanoma Oncogenes. *Oncogene* **2021**, *40*, 806–820. [CrossRef]
118. Comi, A. Current Therapeutic Options in Sturge-Weber Syndrome. *Semin. Pediatr. Neurol.* **2015**, *22*, 295–301. [CrossRef]
119. Prasad, M.S.; Charney, R.M.; García-Castro, M.I. Specification and Formation of the Neural Crest: Perspectives on Lineage Segregation. *Genesis* **2019**, *57*, e23276. [CrossRef]
120. Bahmad, H.F.; Thiravialingam, A.; Sriganeshan, K.; Gonzalez, J.; Alvarez, V.; Ocejo, S.; Abreu, A.R.; Avellan, R.; Arzola, A.H.; Hachem, S.; et al. Clinical Significance of SOX10 Expression in Human Pathology. *Curr. Issues Mol. Biol.* **2023**, *45*, 10131–10158. [CrossRef]
121. Willis, B.C.; Johnson, G.; Wang, J.; Cohen, C. SOX10: A Useful Marker for Identifying Metastatic Melanoma in Sentinel Lymph Nodes. *Appl. Immunohistochem. Mol. Morphol.* **2015**, *23*, 109–112. [CrossRef]
122. Sy, A.L.; Hoang, M.P. SOX10. *J. Clin. Pathol.* **2023**, *76*, 649–653. [CrossRef]
123. Xu, X.; Zhang, D.D.; Kong, P.; Gao, Y.K.; Huang, X.F.; Song, Y.; Zhang, W.-D.; Guo, R.J.; Li, C.L.; Chen, B.W.; et al. Sox10 Escalates Vascular Inflammation by Mediating Vascular Smooth Muscle Cell Transdifferentiation and Pyroptosis in Neointimal Hyperplasia. *Cell. Rep.* **2023**, *42*, 112869. [CrossRef]
124. Wang, D.; Wu, F.; Yuan, H.; Wang, A.; Kang, G.J.; Truong, T.; Chen, L.; McCallion, A.S.; Gong, X.; Li, S. Sox10^{+} Cells Contribute to Vascular Development in Multiple Organs—Brief Report. *Arterioscler. Thromb. Vasc. Biol.* **2017**, *37*, 1727–1731. [CrossRef]
125. Colon Cartagena, L.; Wang, G.Y.; Idowu, M.O.; Smith, S.C.; Mochel, M.C. SOX10-Positive Perivascular Cells in Sentinel Lymph Nodes: A Reliably Intrinsic Internal Control. *J. Cutan. Pathol.* **2020**, *47*, 415–417. [CrossRef]
126. Pathology Outlines. Invasive Melanoma. Available online: https://www.pathologyoutlines.com/topic/skintumormelanocyticmelanoma.html (accessed on 13 August 2024).

Disclaimer/Publisher's Note: The statements, opinions and data contained in all publications are solely those of the individual author(s) and contributor(s) and not of MDPI and/or the editor(s). MDPI and/or the editor(s) disclaim responsibility for any injury to people or property resulting from any ideas, methods, instructions or products referred to in the content.

cancers

MDPI

Article

Survival Benefit of Primary Tumor Treatment in Uveal Melanoma: A Re-Analysis of the Collaborative Ocular Melanoma Study (COMS) and Natural History Study (NHS) Cohorts

Hans Witzenhausen [1] and Gustav Stalhammar [1,2,3,*]

[1] St. Erik Ophthalmic Pathology Laboratory, St. Erik Eye Hospital, 17164 Stockholm, Sweden
[2] Department of Clinical Neuroscience, Division of Eye and Vision, Karolinska Institutet, 17177 Stockholm, Sweden
[3] Ocular Oncology Service, St. Erik Eye Hospital, 17164 Stockholm, Sweden
* Correspondence: gustav.stalhammar@ki.se

Simple Summary: Uveal melanoma is a life-threatening cancer of the eye. There has been ongoing debate about whether treating the main tumor in the eye can actually help patients live longer. In our study, we compared previously published results from patients who received treatment for their eye tumor with those who chose not to receive treatment. By analyzing survival data from both groups, we discovered that patients who did not undergo treatment had a higher risk of death. This finding suggests that treating the primary eye tumor can provide a significant survival benefit for patients with uveal melanoma. Our results also emphasize the importance of timely treatment and may influence future medical guidelines and decisions, ultimately improving patient care for this serious eye cancer.

Abstract: Objective: To evaluate whether primary tumor treatment provides a survival benefit in uveal melanoma by comparing patients who declined treatment (Natural History Study, NHS) with those who received treatment in the Collaborative Ocular Melanoma Study (COMS) for medium-sized choroidal melanomas. Methods: Individual-level survival data were reverse-engineered from cumulative all-cause mortality curves in the original COMS and NHS publications. Censoring patterns were estimated from numbers at risk and descriptive statistics. A Bonferroni-corrected significance level of 0.017 was applied. Additionally, to ensure a conservative approach, NHS cohort data were iteratively adjusted by reducing the 8-year cumulative mortality by one percentage point if the Cox regression hazard ratio for all-cause mortality, the unadjusted risk ratio for death, and the 95% confidence intervals (CIs) of the Kaplan–Meier curves did not show a smaller survival difference than originally reported. Results: Kaplan–Meier analysis revealed significantly higher cumulative mortality in the NHS cohort compared to the COMS cohort (log–rank $p = 0.012$). When restricting the analysis to the first 8 years to account for unclear censoring patterns beyond this period, the NHS cohort still demonstrated worse survival ($p = 0.008$). A sensitivity analysis, varying censoring times by ±25% over 1000 iterations, confirmed worse survival in the NHS cohort in 100% of cases. Conclusions: In this re-evaluation, patients who declined treatment for medium-sized choroidal melanomas had significantly worse survival, suggesting a potential survival benefit of primary tumor treatment.

Keywords: uveal melanoma; choroidal melanoma; prognosis; survival; metastasis; deferral; primary tumor treatment

1. Introduction

In 2003, Straatsma and colleagues evaluated the survival outcomes for 42 patients eligible for the Collaborative Ocular Melanoma Study randomized trial for medium-sized

choroidal melanomas (COMS) who declined enrollment and chose not to undergo treatment [1,2]. Patients who initially deferred treatment but later received melanoma therapy within 45 days of COMS eligibility were excluded from the analysis, which was conducted as part of the Natural History Study (NHS). Of the 42 patients, 22 ultimately opted for treatment (eye-conserving radiation therapy or enucleation) at a mean of 1.4 years after declining initial participation (standard deviation (SD) 1.4).

The five-year all-cause mortality was 30% (95% confidence interval (CI), 18–47%) for NHS patients, compared with 18% (95% CI, 16–20%) for COMS patients. The unadjusted risk ratio for death in NHS patients was 1.79 (95% CI, 1.08–2.97), which decreased to 1.54 (95% CI, 0.93–2.56) after adjusting for baseline age and tumor size. While these results suggested a higher mortality rate in untreated patients, the authors emphasized that the findings were probative but not conclusive evidence of a survival benefit from treatment. The clinical importance of demonstrating a survival benefit from primary tumor treatment, or the lack thereof, cannot be overstated, as it would define the intervention as either life-saving or purely palliative.

The statistical methods employed consisted of Kaplan–Meier survival estimates and Cox proportional hazards modeling. However, Cox regression generates hazard ratios, not risk ratios. Hazard ratios compare the rate of events (e.g., death) between groups over time, while risk ratios compare the overall proportion of events over a fixed period. It is possible that Straatsma and colleagues mistakenly referred to hazard ratios as risk ratios. This distinction is important, as hazard ratios are more appropriate for time-to-event analyses. Notably, no risk ratios were provided for later time points beyond 5 years, even though additional mortality events occurred, seemingly at a higher rate in the NHS cohort. Additionally, while Kaplan–Meier survival curves were generated, no test statistics or *p*-values were reported to assess the significance of the survival differences between the NHS and COMS cohorts.

Subsequent literature has debated the survival benefits of timely treatment for primary tumors and in some cases, the benefit of treatment at all [3–8]. To address these concerns, we re-evaluated the NHS and COMS cohorts and performed a statistical comparison of their survival curves to assess the survival implications of deferring treatment in medium-sized choroidal melanoma.

2. Materials and Methods

Patients in the COMS and NHS had been evaluated at 43 clinical centers located in the United States and Canada [9]. Individuals with a clinically confirmed diagnosis of choroidal melanoma by a COMS-certified ophthalmologist between November 1986 and 31 July 1998 were reported to the COMS Coordinating Center in Baltimore, Maryland. The diagnosis was based on a comprehensive ophthalmic examination, which included best-corrected visual acuity, tumor size and location assessment, A-scan and B-scan ultrasonography, fundus photography, and fluorescein angiography. To be eligible for COMS (which also included a trial of pre-enucleation radiation versus no radiation for patients with large melanomas undergoing enucleation, an observational study of small tumors, reports of radiation-induced conditions, second primary cancers, etc., but herein only refers to the trial of enucleation versus iodine-125 plaque brachytherapy for patients with medium-sized tumors), patients had to have a choroidal melanoma measuring 2.5 to 10.0 mm in apical height and no more than 16.0 mm in basal diameter. Between November 1986 and November 1990, the inclusion criteria allowed for tumors between 3.1 and 8.0 mm in apical height. Patients with peripapillary tumors (within 2.0 mm from the optic disk) were included only if plaque placement could cover the entire tumor and an appropriate margin. In addition, patients had to meet several general eligibility criteria: a primary choroidal melanoma in one eye, be 21 years of age or older, have no other primary tumor, and have no serious concurrent illness expected to limit survival to less than five years. The best-corrected visual acuity in the fellow eye had to be 20/200 or better. Patients with previous treatment for choroidal or ciliary body melanoma, or any condition secondary to

the tumor, were excluded, as were those with significant extra scleral extension (>2.0 mm), as described in the original publications [10,11].

The NHS cohort included patients who were eligible for the COMS trial but declined treatment or enrollment. Patients who initially declined but subsequently received melanoma treatment within 45 days of COMS eligibility were excluded from the NHS. For patients who died, medical reports, histopathological data, and laboratory findings were reviewed by the COMS Mortality Coding Committee to determine metastatic status [1].

To obtain raw data, we contacted all named authors of the original publication by email in 2021. The second author responded but no longer had access to the dataset. Attempts to contact the other authors were unsuccessful, and in 2024, the data were reverse-engineered as follows:

Figure 2 from the original publication (figure titled "Kaplan–Meier curves of the cumulative proportion of patients with medium choroidal melanoma who died by time after determination of eligibility for the COMS medium melanoma trial; enrolled COMS medium tumor trial patients NHS patients with 95% CI", reprinted with permission from Elsevier [1]) was uploaded to the Plot Digitizer Online App (version 3.1.5, https://plotdigitizer.com/app, accessed on 6 September 2024). This tool allows for data extraction from graphs. A minimum of 60 data points were obtained from each cumulative proportion curve for the NHS and COMS cohorts. Two datasets were generated, each with x-values (years after enrollment/decline of enrollment) and y-values (cumulative percent dead from any cause), creating an initial dataset representing 1317 COMS patients and 42 NHS patients, with mortality proportions identical to the original figure. The data collection process is illustrated in Supplementary Figure S1.

Censoring rates were estimated using the number-at-risk table from the 2006 COMS publication, which reported the 12-year survival for patients treated with plaque brachytherapy or enucleation (Figure 1A, titled "Cumulative percentage of patients dead [from all causes] by time since enrollment and treatment arm") [12]. The reduction in the number at risk, minus deaths, was considered the number of censored events per interval and assigned to the midpoint of each interval [13]. As explicit censoring data for the NHS cohort were unavailable, estimates were derived using published survival figures, narrative data on median follow-up and range, and the number of patients with known vital status at 5 and 10 years from the original study, as detailed in the "Censoring and Sensitivity Analysis" section. The final individual-level dataset is provided in Supplementary Table S1.

This study adhered to the tenets of the Declaration of Helsinki. As declared in the Swedish Ethical Review Act (2003:460), approval from the Swedish Ethical Review Authority was not required as this study involved the re-analysis of publicly available data [14]. It did not involve any treatments, tests, examinations, interviews, or other interventions with study subjects. Additionally, it did not affect the subjects physically or psychologically, did not involve biological samples, and did not include any data or sensitive information that could be traced back to any individual.

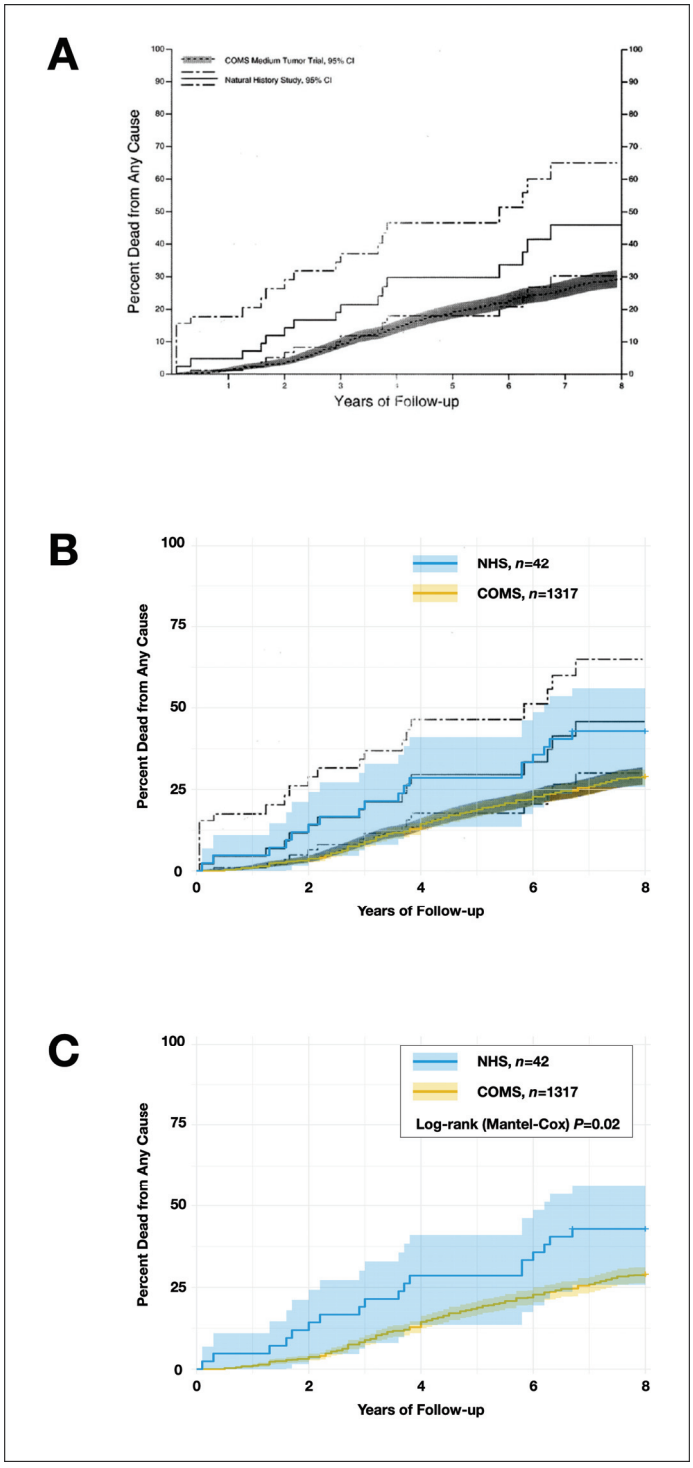


Figure 1. Kaplan–Meier survival curves show the cumulative proportion of deaths from any cause in the NHS and COMS cohorts. (**A**) The original figure from the 2003 publication, which did not include formal statistical comparisons of the curves. Dashed lines represent limits of the 95% confidence intervals (Cis) (**B**) Overlaying the reverse-engineered survival curves for the NHS and COMS cohorts onto the original curves revealed that the 95% CIs for the reverse-engineered data were closer than in the original study, confirming our conservative methodology. (**C**) Despite this, the log–rank (Mantel–Cox) test yielded a p of 0.02. Note that these analyses do not account for censoring, which will be addressed in the next step (Figure 2). The figure from the original publication was reprinted with permission from Elsevier [1]. COMS, Collaborative Ocular Melanoma Study. NHS, Natural History Study.

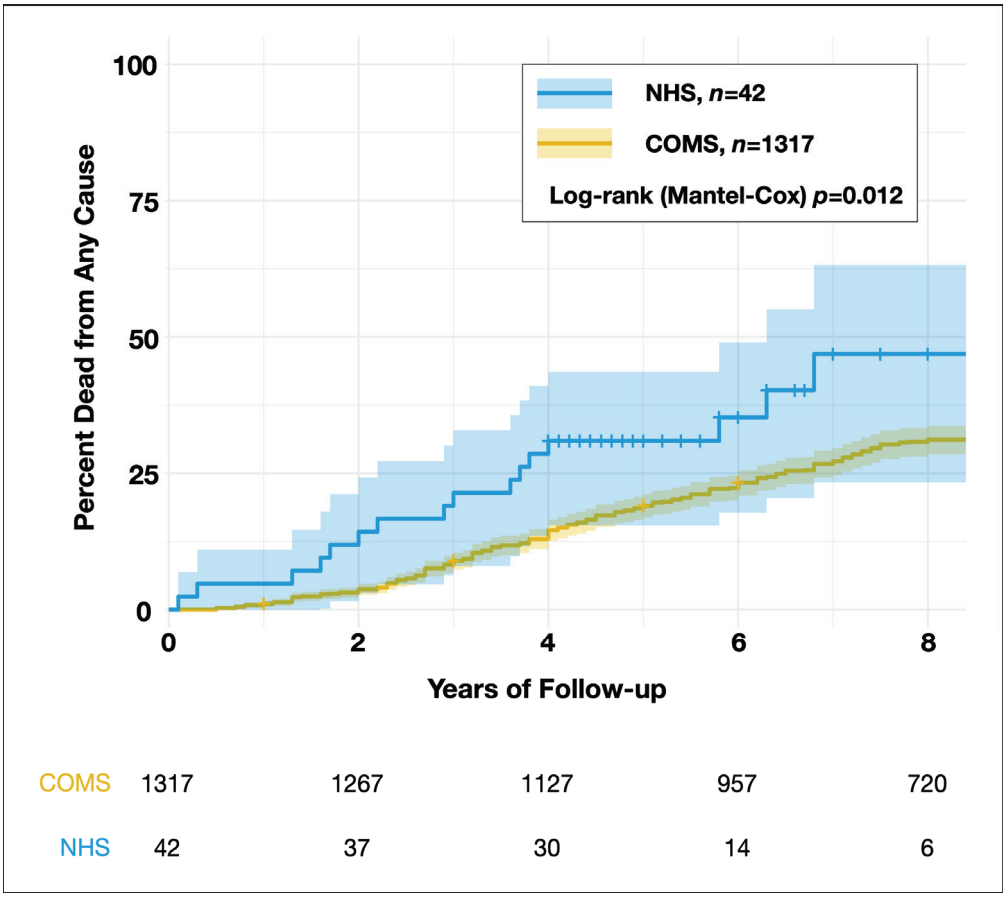


Figure 2. Kaplan–Meier survival curve showing the cumulative proportion of deaths from any cause in the NHS and COMS cohorts, accounting for censoring assumptions. The number at risk for the COMS cohort was extracted from the original publication' s reported data. For the NHS cohort, censoring rates were estimated from the published survival figure and narrative data, including median follow-up, range, and the number of patients with known vital status at 5 and 10 years. COMS, Collaborative Ocular Melanoma Study. NHS, Natural History Study.

Statistical Methods

Kaplan–Meier survival curves were generated for the NHS and COMS cohorts using the survival, survminer, and readxl packages in R (R Foundation for Statistical Computing, version 4.4.1, Vienna, Austria). Survival distributions between the cohorts were compared using the log–rank (Mantel–Cox) test. To ensure accuracy, the log–rank test results were cross-verified using SPSS Statistics, version 29.0 (Armonk, NY, USA). To control for Type I errors, the significance threshold was adjusted using the Bonferroni correction, dividing the conventional 0.05 level by 3 (reflecting the number of statistical tests yielding p values). Thus, a two-sided p-value of less than 0.017 was considered statistically significant. As an additional measure of conservativeness, we required that the lower limit of the 95% confidence interval (CI) for the Kaplan–Meier curve we generated for the NHS cohort be lower than the corresponding lower limit of the 95% CI reported in the original publication at all time points [1]. This adjustment ensured that we were assessing a smaller survival difference between the NHS and COMS cohorts than was reported in the original comparison. To verify this, we calculated 8-year risk ratios and Cox proportional hazards ratios between the NHS and COMS cohorts. If these ratios for the NHS cohort were not lower than those reported in the original publication, or if the 95% CIs of the Kaplan–Meier curves did not indicate a smaller survival difference, we iteratively adjusted the NHS cohort data by reducing the 8-year cumulative mortality by one percentage point until these criteria were met.

3. Results

3.1. Descriptive Statistics

As reported in the original study, the 1317 patients enrolled in the COMS trial had a mean age of 60 years at the time of enrollment, while the 42 patients in the NHS cohort had a mean age of 66 years. Data on the anatomical extent of the primary tumor, such as ciliary body involvement or extraocular extension, were not provided. However, patients with predominantly ciliary body melanomas or extraocular extension greater than 2 mm were excluded from both cohorts as dictated by the study design. At baseline, COMS tumors were larger than NHS tumors, with a mean largest basal diameter (LBD) of 11.4 mm versus 10.3 mm and a mean thickness of 4.8 mm versus 3.8 mm, respectively.

3.2. Risk Ratios

The initial Cox proportional hazards model produced a hazard ratio of 1.51 (95% CI, 0.92–2.50) for NHS patients, with an 8-year risk ratio of 1.31 (95% CI, 0.69–1.93). Both these estimates were lower than those reported in the original publication, consistent with our pre-specified approach that required smaller survival differences than those in the original study.

3.3. Initial Kaplan–Meier Curves

The Kaplan–Meier survival curve of the cumulative proportion of deaths in the NHS and COMS cohorts, as reported in the original publication [1], was compared to the Kaplan–Meier curves generated from our reverse-engineered datasets. The comparison confirmed that the separation between our newly generated curves and their 95% confidence intervals was smaller than in the original publication, supporting our more conservative approach.

Although the curves were less separated, the log–rank (Mantel–Cox) yielded a log–rank p of 0.02, Figure 1. These results did not account for censoring, which will be addressed in the next step, and are not fully reliable. However, as the primary effect of censoring is on the variability and precision of the Kaplan–Meier curve—particularly the 95% confidence intervals—and given that these intervals in our analysis closely resembled those from the original publication, the impact of properly accounting for censoring may be limited.

3.4. Censoring and Sensitivity Analysis

In the final step, we performed a Kaplan–Meier survival analysis incorporating censoring rates for the COMS cohort based on the available number-at-risk table from the original study (e.g., 1317 patients at 0 years, 1301 at 1 year, 1267 at 2 years, etc.). Since explicit censoring data for the NHS cohort was not available, we estimated censoring rates using information derived from the published survival curves, narrative data on median follow-up time, range, and the number of patients with known vital status at 5 and 10 years, as reported in the original study. Specifically, the study stated: "Based on time since COMS eligibility, vital status was known at 5 and 10 years for 32 and 20 of the 42 NHS medium melanoma patients, respectively, [. . .] a total of 16 medium melanoma patients had died". From this, we inferred that among the original 42 NHS patients, 16 had died, 4 were still alive at 10 years, and 22 had unknown vital status, indicating that they were censored earlier than 10 years post-COMS eligibility. At 5 years, 10 patients had unknown vital status. The median follow-up was 5.3 years (range 4–10.7 years), suggesting that 10 patients were censored between years 4 and 5, and the remaining 12 were censored between 5 and 10.7 years. Therefore, in our reverse-engineered cohort, the 22 patients with unknown vital status at 10 years were censored between 4 and 9 years, the 23rd patient was censored at 10.7 years (to achieve an identical median follow-up of 5.3 years), and the remaining 2 patients were censored at 11 years. The 720 COMS patients who remained at risk at 8 years were also censored at 11 years. The reconstructed individual-level data are provided in Supplementary Table S1. A Kaplan–Meier analysis of this dataset yielded a log–rank test p-value of 0.012 (Table 1, Figure 2). Even when accounting for the unclear censoring pattern beyond 8 years through a life-table analysis restricted to the 0–8 year

period, the NHS cohort demonstrated significantly worse survival than the COMS cohort (Wilcoxon [Gehan] $p = 0.008$), reinforcing the robustness of this finding.

Table 1. Kaplan–Meier Overall Survival (OS) Point Estimates with 95% Confidence Intervals for COMS and NHS Cohorts.

	COMS				NHS			
Time (Years)	Number at Risk	Kaplan–Meier OS Estimate	95% CI Lower	95% CI Upper	Number at Risk	Kaplan–Meier OS Estimate	95% CI Lower	95% CI Upper
1	1306	99%	98%	99%	40	95%	89%	100%
2	1267	96%	95%	97%	37	86%	76%	97%
3	1200	91%	90%	93%	34	79%	67%	92%
4	1127	85%	84%	87%	30	69%	56%	85%
5	1054	81%	79%	83%	20	69%	56%	85%
6	957	77%	74%	79%	14	65%	51%	82%
7	763	73%	70%	75%	8	53%	37%	77%
8	720	69%	66%	72%	6	53%	37%	77%

CI, Confidence Interval. COMS, Collaborative Ocular Melanoma Study. NHS, Natural History Study.

To further test the robustness of the survival difference to variations in censoring assumptions, we performed a sensitivity analysis. In this analysis, censoring times for both cohorts were randomly varied by ±25% over 1000 iterations. For each iteration, we generated a Kaplan–Meier survival curve and performed a log–rank test to assess whether the NHS cohort had worse survival than the COMS cohort. The sensitivity analysis revealed that in 100% of the iterations, the NHS cohort exhibited worse survival outcomes compared to the COMS cohort. This consistency across all iterations highlights that the observed survival difference is robust to variations in censoring assumptions, confirming that NHS patients consistently experienced poorer survival than COMS patients, irrespective of the censoring strategy applied.

4. Discussion

In this study, we re-evaluated the results from the landmark Collaborative Ocular Melanoma Study, particularly focusing on the Natural History Study cohort, comprising patients who declined treatment. Despite several factors that could have reduced the chances of observing a statistically significant survival benefit of treatment—such as smaller baseline tumor sizes in NHS patients and our adjustments to minimize survival differences beyond those reported in the original publication to reduce the risk of type I error—we found that survival outcomes remained significantly worse for the NHS cohort. This finding reinforces the hypothesis that primary tumor treatment provides a survival benefit in uveal melanoma.

These findings have critical implications for the clinical management of primary uveal melanoma. If treatment is believed to reduce the risk of metastasis and subsequent death, it not only underscores the importance of primary tumor treatment—potentially shifting the perception from ocular treatment being purely palliative to it having a curative role for some patients—but also highlights the significance of early detection and treatment [15]. If the prognosis worsens the longer a uveal melanoma remains untreated, timely intervention becomes essential, given the high propensity of uveal melanoma to metastasize, typically with fatal consequences [16,17]. On the other hand, if one argues against a survival benefit from primary tumor treatment, the urgency of early detection diminishes, and the potential adverse effects of prompt treatment, such as visual impairment, would weigh more heavily in treatment decisions [3].

Assuming that treatment does confer a survival benefit, healthcare systems must enhance screening protocols for early detection of small melanomas and refine strategies to distinguish between low- and high-risk lesions. Decentralized surveillance programs, utilizing optometrists or opticians with advanced imaging technologies such as fundus

photography and optical coherence tomography (OCT), supported by remote consultations with experts and deep-learning algorithms, could play a pivotal role in expanding early detection efforts [18–20]. Furthermore, genetic and molecular profiling through biopsy techniques and chromosome 3 testing of circulating tumor cells (CTC) could help identify lesions with higher metastatic potential, providing critical insights for more personalized treatment and surveillance strategies [21–23].

It is evident that treatment cannot be initiated for tumors that have not yet been detected, and some observation for growth is necessary to differentiate between benign and malignant choroidal melanocytic lesions. However, once melanoma is diagnosed, delaying treatment may allow additional tumor cells to disseminate from the eye. Continued growth of the primary tumor also provides the opportunity to acquire further aggressive traits, potentially accelerating the growth rate of any metastases seeded after such events. By treating the primary tumor promptly, we may prevent additional tumor cell spread and mitigate further worsening of prognosis.

Some studies have not observed a significant relationship between treatment delays and prognosis, including Damato et al., who concluded that "Deferring treatment of choroidal melanomas until documentation of growth may delay iatrogenic visual loss by months or years and is associated with minimal increase in metastatic mortality, at least with small tumors with usual growth rates of up to 40% per year" [6,24]. However, this interpretation now warrants reevaluation: The 4.3% yearly growth rate observed for 24 tumors by Damato et al. would correspond to a volume doubling time of approximately 2008 days, assuming a semi-spheroidal shape and similar growth in thickness and diameter, which is in exceptionally slow, as demonstrated in our meta-analysis [8]. In fact, even the reported worst-case scenario involving an annual growth rate of 40%, corresponding to a doubling time of 752 days, is still rather slow. This rate aligns with a metastatic death risk increase of 1.3% per month in 40-year-old females with a 10-mm diameter monosomy-3 melanoma. In other words, this analysis, performed by an independent research team with independent datasets, draws similar conclusions about the prognostic impact of treatment delays, when taking the differences in assumed growth rate into account.

Furthermore, some previous observations may have been slightly overinterpreted in the field. For example, reports of *BAP1* mutations and other canonical aberrations arising in an early, punctuated burst do not necessarily preclude the possibility of later aberrations that could further accelerate metastasis growth [25]. Similarly, findings of shared mutations between primary tumors and metastases should not be misread as indicating that all metastases ultimately cause patient death are invariably seeded very early. Nor should calculations based on constant doubling time assumptions imply that metastases resulting in patient death always "occur at a time when the primary uveal melanoma is too small to be clinically detected" [26,27].

Shain and colleagues observed that while "metastatic dissemination occurred early during the development of the primary tumor", they also identified additional driver mutations arising in later stages, which were shared with metastases [28]. These later mutations included *CDKN2A*, loss of chromosome 3 (including *PBRM1*), gain of 8q, and gain of 1p. Supplementary data from Shain's study suggest that 5 of 35 (14%) patients had metastases originating from later branches in the phylogenetic trees (cases A11, A16, A50, A59, and A60). Two of these patients (A50 and A60) had small, potentially asymptomatic tumors, making earlier detection less likely.

This suggests two important points: first, that if effective primary tumor treatment, such as enucleation, had been performed in the three remaining cases with larger tumors before these additional genetic aberrations developed, the specific metastases that were analyzed could have been prevented (though not necessarily others); and second, that if tumor cells had already been seeded from older parts of these three tumors and managed to establish growing macrometastases, these cells may have carried fewer driver mutations, potentially resulting in slower growth.

Limitations

This study has several limitations. First, our results rely on reverse-engineered survival data reconstructed to approximate the original COMS study outcomes. Despite considerable efforts to ensure the validity of the simulated NHS cohort, discrepancies between real-world data and the reverse-engineered data may have introduced bias. Although the timing of mortality events could be deduced from the survival plots, the reverse-engineering approach could not precisely capture the timing of censoring events in the NHS cohort. Instead, these were estimated based on the available descriptive statistics, including median follow-up, range, and the number of patients with known vital status at 5 and 10 years. This means that while the exact timing of censoring events is not fully accounted for, the estimated censoring should be reasonably accurate.

Additionally, comparing survival between two reverse-engineered cohorts cannot account for potentially unbalanced risk factors between the COMS and NHS cohorts, as data on additional risk factors were not available and thus could not be reverse-engineered. This represents a significant limitation, similar to the Kaplan–Meier curves in the original publication, which also did not account for risk factors.

Future studies could address the limitations of our approach by conducting prospective studies that collect real-world survival data directly from patients who decline treatment. Such studies would enable a more accurate assessment of survival outcomes without the potential biases of data reconstruction. Additionally, expanding access to large, multi-institutional databases may allow for more robust comparisons between treated and untreated cohorts, incorporating key genetic and molecular markers.

Lastly, the original COMS study itself had inherent limitations, including potential selection bias. Patients who declined treatment may have differed from those who enrolled, particularly in unmeasured factors such as chromosome 3 or 8q aberrations, BAP1 mutations, and gene expression profiles—key prognostic markers in uveal melanoma. Notably, NHS patients were older and presented with smaller tumors at baseline, which are positive and negative prognostic factors, respectively [16,29,30].

5. Conclusions

In this re-evaluation, patients who declined treatment for medium-sized primary choroidal melanomas had significantly worse survival compared to those treated promptly, suggesting a potential survival benefit of primary tumor treatment.

Clinically, these findings indicate that treating uveal melanoma at an earlier stage may reduce the risk of metastasis and improve overall survival. The results also suggest that healthcare systems should prioritize early detection, focusing on identifying the few malignant choroidal melanocytic lesions among the many benign counterparts to enable prompt treatment.

However, factors such as patient age and tumor size may influence these findings, as the original publication found that statistical significance was negated when adjusted for in regression analyses. Future studies should address the limitations of reverse-engineered data by focusing on prospective, real-world data collection. Ultimately, definitive evidence of causality would require a randomized clinical trial, though such a study would present ethical challenges.

Supplementary Materials: The following supporting information can be downloaded at: https://www.mdpi.com/article/10.3390/cancers16223839/s1; Figure S1: Illustration of data collection from the original curves. Table S1: Reverse-Engineered Raw data for the COMS and NHS cohorts. Reference [1] is cited in the supplementary materials.

Author Contributions: Conceptualization, G.S.; methodology, G.S.; software, G.S.; validation, G.S. and H.W.; formal analysis, G.S. and H.W.; investigation, G.S.; resources, G.S.; data curation, G.S.; writing—original draft preparation, G.S.; writing—review and editing, G.S. and H.W.; visualization, G.S.; supervision, G.S.; project administration, G.S.; funding acquisition, G.S. All authors have read and agreed to the published version of the manuscript.

Funding: This research and APC was funded by Region Stockholm (RS-2019-1138); The Swedish Cancer Society (20 0798 Fk); The Swedish Society of Medicine, Cronqvists stiftelse (SLS-1000962).

Institutional Review Board Statement: This study adhered to the tenets of the Declaration of Helsinki. As declared in the Swedish Ethical Review Act (2003:460), approval from the Swedish Ethical Review Authority was not required as this study involved the re-analysis of publicly available data [14]. It did not involve any treatments, tests, examinations, interviews, or other interventions with study subjects. Additionally, it did not affect the subjects physically or psychologically, did not involve biological samples, and did not include any data or sensitive information that could be traced back to any individual.

Informed Consent Statement: Not applicable.

Data Availability Statement: All data for the present study are openly available from the original publications and in the supplementary table.

Conflicts of Interest: The authors declare no conflicts of interest. The funders had no role in the design of the study; in the collection, analyses, or interpretation of data, in the writing of the manuscript, or in the decision to publish the results.

References

1. Straatsma, B.R.; Diener-West, M.; Caldwell, R.; Engstrom, R.E.; Collaborative Ocular Melanoma Study, G. Mortality after deferral of treatment or no treatment for choroidal melanoma. *Am. J. Ophthalmol.* **2003**, *136*, 47–54. [CrossRef] [PubMed]
2. Diener-West, M.; Earle, J.D.; Fine, S.L.; Hawkins, B.S.; Moy, C.S.; Reynolds, S.M.; Schachat, A.P.; Straatsma, B.R.; Collaborative Ocular Melanoma Study Group. The COMS randomized trial of iodine 125 brachytherapy for choroidal melanoma, III: Initial mortality findings. COMS Report No. 18. *Arch. Ophthalmol.* **2001**, *119*, 969–982. [PubMed]
3. Damato, B. Does ocular treatment of uveal melanoma influence survival? *Br. J. Cancer* **2010**, *103*, 285. [CrossRef] [PubMed]
4. Damato, B.; Coupland, S. Does delayed treatment shorten the life of patients with fatal choroidal melanoma? *Acta Ophthalmol.* **2009**, *87*. [CrossRef]
5. Stalhammar, G. Delays between Uveal Melanoma Diagnosis and Treatment Increase the Risk of Metastatic Death. *Ophthalmology* **2024**, *131*, 1094–1104. [CrossRef]
6. Hussain, R.; Coupland, S.E.; Heimann, H.; Eleuteri, A. Re: Stalhammar G: Delays between uveal melanoma diagnosis and treatment increase the risk of metastatic death. *Ophthalmology* **2024**, *131*, 1094–1104. [CrossRef]
7. Harbour, J.W.; Correa, Z.M.; Stacey, A.W. Do Short Delays in Treatment Affect Uveal Melanoma Prognosis? *Ophthalmology* **2024**, *131*, 1105–1106. [CrossRef]
8. Stalhammar, G.; Hagstrom, A.; Conradi, M.E.; Williams, P.A. Choroidal nevi and melanoma doubling times and implications for delays in treatment: A systematic review and meta-analysis. *Surv. Ophthalmol.* 2024, *in press*. [CrossRef]
9. The Collaborative Ocular Melanoma Study Group. Design and methods of a clinical trial for a rare condition: The Collaborative Ocular Melanoma Study. COMS Report No. 3. *Control. Clin. Trials* **1993**, *14*, 362–391. [CrossRef]
10. Collaborative Ocular Melanoma Study, G. Comparison of clinical, echographic, and histopathological measurements from eyes with medium-sized choroidal melanoma in the collaborative ocular melanoma study: COMS report no. 21. *Arch. Ophthalmol.* **2003**, *121*, 1163–1171. [CrossRef]
11. Diener-West, M.; Earle, J.D.; Fine, S.L.; Hawkins, B.S.; Moy, C.S.; Reynolds, S.M.; Schachat, A.P.; Straatsma, B.R.; Collaborative Ocular Melanoma Study Group. The COMS randomized trial of iodine 125 brachytherapy for choroidal melanoma, II: Characteristics of patients enrolled and not enrolled. COMS Report No. 17. *Arch. Ophthalmol.* **2001**, *119*, 951–965. [CrossRef] [PubMed]
12. COMS. The COMS Randomized Trial of Iodine 125 Brachytherapy for Choroidal Melanoma: V. Twelve-Year Mortality Rates and Prognostic Factors: COMS Report No. 28. *Arch. Ophthalmol.* **2006**, *124*, 1684–1693. [CrossRef] [PubMed]
13. Earle, C.C.; Pham, B.; Wells, G.A. An assessment of methods to combine published survival curves. *Med. Decis. Mak.* **2000**, *20*, 104–111. [CrossRef] [PubMed]
14. The Swedish Riksdag. *The Ethical Review Act 2003:460*; The Swedish Riksdag: Stockholm, Sweden, 2003.
15. Singh, A.D.; Zabor, E.C.; Radivoyevitch, T. Estimating Cured Fractions of Uveal Melanoma. *JAMA Ophthalmol.* **2021**, *139*, 174–181. [CrossRef] [PubMed]
16. Stalhammar, G. Comprehensive causes of death in uveal melanoma: Mortality in 1530 consecutively diagnosed patients followed until death. *JNCI Cancer Spectr.* **2023**, *7*, pkad097. [CrossRef] [PubMed]
17. Khoja, L.; Atenafu, E.G.; Suciu, S.; Leyvraz, S.; Sato, T.; Marshall, E.; Keilholz, U.; Zimmer, L.; Patel, S.P.; Piperno-Neumann, S.; et al. Meta-analysis in metastatic uveal melanoma to determine progression free and overall survival benchmarks: An international rare cancers initiative (IRCI) ocular melanoma study. *Ann. Oncol.* **2019**, *30*, 1370–1380. [CrossRef] [PubMed]
18. Shields, C.L.; Dalvin, L.A.; Ancona-Lezama, D.; Yu, M.D.; Di Nicola, M.; Williams, B.K., Jr.; Lucio-Alvarez, J.A.; Ang, S.M.; Maloney, S.; Welch, R.J.; et al. Choroidal nevus imaging features in 3 806 cases and risk factors for transformation into melanoma in 2355 cases: The 2020 Taylor R. Smith and Victor T. Curtin Lecture. *Retina* **2019**, *39*, 1840–1851. [CrossRef]

19. Dalvin, L.A.; Shields, C.L.; Ancona-Lezama, D.A.; Yu, M.D.; Di Nicola, M.; Williams, B.K., Jr.; Lucio-Alvarez, J.A.; Ang, S.M.; Maloney, S.M.; Welch, R.J.; et al. Combination of multimodal imaging features predictive of choroidal nevus transformation into melanoma. *Br. J. Ophthalmol.* **2019**, *103*, 1441–1447. [CrossRef]
20. Sabazade, S.; Lumia Michalski, M.; Bartoszek, J.; Fili, M.; Holmström, M.; Stålhammar, G. Development and Validation of a Deep Learning Algorithm for Differentiation of Choroidal Nevi from Small Melanoma in Fundus Photographs. *Ophthalmol. Sci.* **2025**, *5*, 100613. [CrossRef]
21. Hagström, A.; Witzenhausen, H.; Stålhammar, G. Tailoring Surveillance Imaging in Uveal Melanoma Based on Individual Metastatic Risk. *Can. J. Ophthalmol.* 2024, *in press*. [CrossRef]
22. Decatur, C.L.; Ong, E.; Garg, N.; Anbunathan, H.; Bowcock, A.M.; Field, M.G.; Harbour, J.W. Driver Mutations in Uveal Melanoma: Associations With Gene Expression Profile and Patient Outcomes. *JAMA Ophthalmol.* **2016**, *134*, 728–733. [CrossRef]
23. Grisanti, S.; Schindler, F.; Merz, H.; Kakkassery, V.; Sonntag, S.R.; Tura, A. Detection of Circulating Tumor Cells in Patients with Small Choroidal Melanocytic Lesions. *Ophthalmology* **2023**, *130*, 1290–1303. [CrossRef] [PubMed]
24. Augsburger, J.J.; Vrabec, T.R. Impact of delayed treatment in growing posterior uveal melanomas. *Arch. Ophthalmol.* **1993**, *111*, 1382–1386. [CrossRef] [PubMed]
25. Field, M.G.; Durante, M.A.; Anbunathan, H.; Cai, L.Z.; Decatur, C.L.; Bowcock, A.M.; Kurtenbach, S.; Harbour, J.W. Punctuated evolution of canonical genomic aberrations in uveal melanoma. *Nat. Commun.* **2018**, *9*, 116. [CrossRef]
26. Singh, A.D. Uveal melanoma: Implications of tumor doubling time. *Ophthalmology* **2001**, *108*, 829–830. [CrossRef] [PubMed]
27. Eskelin, S.; Pyrhönen, S.; Summanen, P.; Hahka-Kemppinen, M.; Kivelä, T. Tumor doubling times in metastatic malignant melanoma of the uvea: Tumor progression before and after treatment. *Ophthalmology* **2000**, *107*, 1443–1449. [CrossRef]
28. Shain, A.H.; Bagger, M.M.; Yu, R.; Chang, D.; Liu, S.; Vemula, S.; Weier, J.F.; Wadt, K.; Heegaard, S.; Bastian, B.C.; et al. The genetic evolution of metastatic uveal melanoma. *Nat. Genet.* **2019**, *51*, 1123–1130. [CrossRef]
29. Kujala, E.; Mäkitie, T.; Kivelä, T. Very long-term prognosis of patients with malignant uveal melanoma. *Investig. Ophthalmol. Vis. Sci.* **2003**, *44*, 4651–4659. [CrossRef]
30. Shields, C.L.; Furuta, M.; Thangappan, A.; Nagori, S.; Mashayekhi, A.; Lally, D.R.; Kelly, C.C.; Rudich, D.S.; Nagori, A.; Wakade, O.A.; et al. Metastasis of uveal melanoma millimeter-by-millimeter in 8033 consecutive eyes. *Arch. Ophthalmol.* **2009**, *127*, 989–998. [CrossRef]

Disclaimer/Publisher's Note: The statements, opinions and data contained in all publications are solely those of the individual author(s) and contributor(s) and not of MDPI and/or the editor(s). MDPI and/or the editor(s) disclaim responsibility for any injury to people or property resulting from any ideas, methods, instructions or products referred to in the content.

cancers

MDPI

Article

Microdissection of Distinct Morphological Regions Within Uveal Melanomas Identifies Novel Drug Targets

Elsa Toumi [1,2,3,†], Luke B. Hesson [3,4,5,†], Vivian Lin [3], Dale Wright [6,7], Elektra Hajdu [4], Li-Anne S. Lim [8], Michael Giblin [8], Fanfan Zhou [9], Alexandra Hoffmeister [2], Farida Zabih [2], Adrian T. Fung [10,11], R. Max Conway [8] and Svetlana Cherepanoff [2,3,12,*]

1 Department of Ophthalmology, University Hospital of Nice, 06000 Nice, France; elsatoumi@hotmail.fr
2 SydPath, St Vincent's Hospital Sydney, Darlinghurst, NSW 2010, Australia; ahoff82@gmail.com (A.H.); farida.zabih@gmail.com (F.Z.)
3 Medicine & Health, UNSW Sydney, Randwick, NSW 2031, Australia; l.hesson@unsw.edu.au (L.B.H.); vivian.lin.vl@gmail.com (V.L.)
4 Kinghorn Centre for Clinical Genomics, Garvan Institute of Medical Research, Darlinghurst, NSW 2010, Australia; e.hajdu@garvan.org.au
5 Department of Molecular Genetics, Douglass Hanly Moir Pathology, Macquarie Park, NSW 2113, Australia
6 Department of Cytogenetics, Sydney Genome Diagnostics, The Children's Hospital at Westmead, Westmead, NSW 2145, Australia; dale.wright@health.nsw.gov.au
7 Discipline of Paediatrics & Child Health, Faculty of Medicine and Health, The University of Sydney, Sydney, NSW 2050, Australia
8 Ocular Oncology Unit, Sydney Eye Hospital, Sydney, NSW 2000, Australia; limlianne@gmail.com (L.-A.S.L.); emgiblin@ozemail.com.au (M.G.); drmaxconway@gmail.com (R.M.C.)
9 Sydney Pharmacy School, The University of Sydney, Sydney, NSW 2050, Australia; fanfan.zhou@sydney.edu.au
10 Westmead and Central Clinical Schools, Specialty of Ophthalmology and Eye Health, The University of Sydney, Sydney, NSW 2050, Australia; adrian.fung@sydney.edu.au
11 Department of Ophthalmology, Faculty of Medicine, Health and Human Sciences, Macquarie University, Sydney, NSW 2113, Australia
12 School of Medicine, University of Notre Dame, Sydney Campus, Darlinghurst, NSW 2010, Australia
* Correspondence: s.cherepanoff@unsw.edu.au; Tel.: +61-2-8382-9168; Fax: +61-2-8382-2489
† These authors contributed equally to this work.

Simple Summary: Separately sequencing morphologically distinct regions within large, high-risk uveal melanomas provides deeper insights into tumour biology and identifies additional targets for therapy. Uveal melanomas are rare intraocular malignancies that exhibit significant heterogeneity, with macroscopic and microscopic differences between tumour regions. This study used microdissection and targeted sequencing to analyse melanotic and amelanotic regions within the same tumours. In four of seven cases, distinct molecular profiles were identified, including a MET exon 14 skipping transcript predictive of sensitivity to crizotinib. Additional variants were detected in genes relevant to active clinical trials. These findings highlight the importance of analysing spatially distinct tumour regions to identify actionable genetic alterations that may be missed in whole tumour aggregate analyses. This approach has implications for the molecular testing of uveal melanomas, guiding personalised therapies, and expanding eligibility for clinical trials in patients with advanced disease.

Abstract: Background/Objectives: Uveal melanomas (UMs) are rare but often deadly malignancies that urgently require viable treatment options. UMs often exhibit tumour heterogeneity, with macroscopic and microscopic differences in morphology between different regions of the same tumour. However, to date, the clinical significance of this and how it may help guide personalised therapy have not been realised. **Methods**: Using targeted DNA and RNA sequencing of a small case series of large, high-risk primary UMs, we explored whether morphologically distinct regions of the same tumour were associated with distinct molecular profiles. **Results**: In four of the seven tumours analysed, we detected different sets of genetic variants following the separate analysis of microdissected melanotic and amelanotic regions of the same tumour. These included a *MET* exon 14 skipping RNA transcript that predicts sensitivity to crizotinib and variants in other genes

that are important in active clinical trials for patients with UM and advanced solid tumours. The integration of TCGA data also identified recurrent mutational events in genes that were not previously implicated in UM development (*FANCA*, *SLX4*, *BRCA2*, and *ATRX*). **Conclusions**: Our findings show that the molecular analysis of spatially separated and morphologically distinct regions of the same tumour may yield additional, therapeutically relevant genetic variants in uveal melanomas and have implications for the future molecular testing of UMs to identify targeted therapies.

Keywords: uveal melanomas; tumour heterogeneity; microdissection; sequencing; cancer

1. Introduction

Uveal melanoma (UM) is the most common primary intraocular malignancy among adults [1]. Despite their shared embryonic neural crest origin, UM and mucocutaneous melanoma differ substantially in their aetiology, molecular profile, and clinical course [2,3]. The advent of targeted therapies and immunotherapy has markedly improved the survival of patients with metastatic cutaneous melanoma in the past decade [4]. There has been no substantial improvement in survival for metastatic UM for over 30 years [5]; although, clinical trials of new drugs are ongoing [6]. Despite effective primary treatment, nearly 50% of UM patients develop metastases. Due to a lack of available therapy, 20–30% of patients diagnosed with a UM die of systemic metastases within 5 years of diagnosis and 45% within 15 years [7–9]. Reducing this stark disparity in survival rates is a priority in ocular oncology.

The risk of UM metastasis can be accurately predicted using the American Joint Committee on Cancer (AJCC) TNM staging system [10–13], as well as established clinical and histopathologic features. Risk prognostication can be further refined by combining clinical, histopathological, and copy number changes in chromosomes 3 and 8q [14,15]. Metastatic risk can be also stratified based on four molecular categories using data from The Cancer Genome Atlas (TCGA) [3], confirmed in larger cohorts [16,17]. Unlike mucocutaneous melanoma or other solid tumours, somatic variants in the UM driver genes (GNAQ, GNA11, EIF1AX, SF3B1, PLCB4, CYSLTR2, and BAP1) are not molecular targets of currently approved therapies. Trials of targeted cancer therapies in UM patients have, thus far, shown disappointing results [18–21], as have trials of immunotherapy [22,23].

We hypothesised that identifying actionable targets in UM may require a more nuanced approach. Tumour heterogeneity is a well-documented phenomenon, whereby populations of cells within the same primary tumour show different macroscopic, histological, or molecular features. UM tumour heterogeneity has been demonstrated in multiple studies using fluorescence in situ hybridisation, gene expression profiling, single-cell sequencing, and epigenetic analyses [24–32]. In our experience with UMs observed over time, different tumour regions can often be discernible by way of pigmentation, growth pattern, growth rate, and echogenicity. In larger UMs, macroscopic photography in the pathology laboratory can reveal two or more conspicuous morphological regions. Furthermore, corresponding histological differences may also be observed by way of cell type, extravascular matrix pattern, growth pattern (solid versus diffuse), and differences in tumour-infiltrating macrophages and lymphocytes.

In this study, we analysed different morphological regions of the same tumour to investigate whether they are associated with different molecular features and whether this can identify additional therapeutically relevant sequence variants.

2. Materials and Methods

2.1. Study Cohort Selection Criteria

Cases included in this series met the following criteria: (i) large choroidal or ciliochoroidal tumour (at least TNM pT3, AJCC 8th edition [10]); (ii) tumour heterogeneity as defined by at least two morphologically conspicuous regions on macroscopic assessment;

(iii) high metastatic risk, as determined by the minimal or absent nuclear expression of BAP1 immunohistochemistry (IHC) and monosomy or chromosome 3 or loss of 3p by CGH/SNP chromosome microarray; (iv) no previous treatment; and (v) tumour uncomplicated by infarction, necrosis, or haemorrhage.

2.2. Patient and Tumour Characteristics

Patient and tumour variables determined at each patient's pre-enucleation examination were age, intraocular tumour location (choroidal or cilio-choroidal), largest basal diameter, and maximal thickness of the tumour in millimetres, as measured by B-scan ultrasonography. Post-enucleation, tumour basal diameter and thickness were confirmed by macrophotography in the laboratory (see below), as was the presence of heterogeneous tumour clones. The presence or absence of extrascleral extension and vortex vein involvement were determined at the time of specimen grossing and macrophotography. Each pathological parameter was confirmed using microscopic examination. One of the patients (Case 3) had a history of familial breast cancer and known germline BRCA2 mutation; none of the other patients had a known cancer predisposition syndrome.

2.3. Enucleation Grossing

Enucleated eyes were oriented according to established protocols [33]. Transillumination was performed to localise each tumour, and the eye was opened to best demonstrate the tumour mass within the pupil to the optic nerve block and to ensure that the tumour was included in the first calotte removed. The location, thickness, and basal diameter of the tumour were documented, including the involvement of the ciliary body and other structures and the presence of extrascleral extension or vortex vein involvement. A fresh tumour sample was harvested from the first calotte and submitted for CGH/SNP chromosome microarray analysis in RPMI medium. The open eye was then fixed for 48 h in 10% neutral buffered formalin (NBF). Eyes were submerged in 70% alcohol before macrophotography (Olympus SZ61 dissecting microscope, DP22 camera and cellSense software v2.0; Olympus Corporation, Notting Hill, VIC, Australia) to confirm tumour location, size, and the presence of distinct clones. The second calotte was removed after fixation, and the entire eye was subjected to paraffin embedding, sectioning, H&E staining, and microscopic examination in the following blocks: (i) vortex veins, (ii) optic nerve margin, (iii) pupil to optic nerve block, (iv) calotte #1, and (v) calotte #2.

2.4. Histology and Immunohistochemistry

Tissue cassettes containing tumours were processed on the Tissue Tek VIP 3 (Leica Biosystems) overnight cycle (2 h additional 10% NBF, followed by progressive dehydration with alcohol, xylol clearing, and paraplast (paraffin wax) embedding. Tissue blocks were then sectioned at 3 μm on a Leica RM2235 rotary microtome (Leica Biosystems, Wetzlar, Germany) onto frosted glass slides (Trajan Scientific and Medical, Bethel, CT, USA), dried, and stained with haematoxylin and eosin on a Tissue Tek Prisma Plus automated slide stainer (Sakura Finetek, Torrance, CA, USA), and cover slipped on an automated Tissue Tek Glas cover slipper (Sakura Finetek, USA).

Melanocytic differentiation was confirmed by haematoxylin and eosin (H&E) staining and MART1 immunohistochemistry.

Histological tumour characteristics were reported in a synoptic format according to the AJCC 8th edition [34] criteria. A set panel of immunohistochemical studies was performed as part of the standard UM protocol. Paraffin-embedded tissues were cut at 3 μm onto charged glass slides (Trajan Scientific and Medical). Immunohistochemistry was performed using the Ventana BenchMark Ultra platform (Roche Diagnostics, Basel, Switzerland). The primary antibodies, antigen retrieval, and incubation time are summarised in Supplementary Table S1. Positive and negative control tissue (informed by the datasheet of each primary antibody) was included on each slide submitted for immunohistochemistry.

BAP1 immunohistochemistry was interpreted as "aberrant" when there was minimal or absent staining in tumour nuclei.

2.5. Comparative Genomic Hybridisation (CGH)/Single Nucleotide Polymorphism (SNP) Chromosome Microarrays

For tumour samples received prior to mid-2020, a CGH/SNP chromosome microarray was performed at SydPath. Genomic DNA from fresh tumour samples was extracted using the Gentra Puregene kit (Qiagen, Hilden, Germany) using the manual DNA extraction method with overnight proteinase-K + buffer ALT (lysis buffer) tissue digestion at 56 °C, followed by DNA purification and precipitation. CGH/SNP chromosome microarray was performed using the Applied Biosystems Cytoscan 750K assay (Thermo Fisher Scientific, Waltham, MA, USA) according to the manufacturer's protocol. Microarray data were analysed as a CEL file using Chromosome Analysis Suite v3.1 (Thermo Fisher Scientific), with an average copy number resolution of ~0.1 Mb.

CGH/SNP chromosome microarray of tumour samples received after mid-2020 were tested at The Children's Hospital at Westmead. Genomic DNA was extracted from fresh tissue samples using the Wizard Genomic DNA purification kit (Promega, Madison, WI, USA), but with slight modifications that involved overnight proteinase-K (Qiagen) buffered tissue digestion at 56 °C, followed by DNA purification and precipitation. SNP microarray analysis was performed using the CytoSNP 850K Beadchip v1.2 (Illumina, San Diego, CA, USA) with microarray data analysed using BlueFuse Multi v4.5 (Illumina) using a mean effective resolution of ~0.05 Mb for copy number and ~5 Mb for the copy-neutral loss of heterozygosity.

2.6. Reporting Criteria for CGH/SNP Chromosome Microarray Abnormalities

Similar reporting criteria were applied for both CytoScan-750K and CytoSNP-850K BeadChip assays (Illumina). Chromosome copy number abnormalities were reported when involving non-mosaic whole chromosomes (gain, loss, or copy-neutral loss of heterozygosity [CNLOH]) or segmental chromosome abnormalities (defined as >5 Mb in size). Copy number imbalances < 5 Mb were reported in overlapping tumour-relevant consensus cancer genes as per the Catalogue of Somatic Mutations in Cancer (COSMIC). Mosaic or subclonal copy number imbalances and CNLOH were reported when present in >30% of cells, as determined by assessment of the Log R and altered allele and B-allele frequency plots of SNP probes [35].

2.7. Extraction of DNA and RNA from FFPE Tissue

Macrodissection was performed from a minimum of 12 μm tissue, and DNA and RNA were extracted using the AllPrep DNA/RNA FFPE Kit (Qiagen, Hilden, Germany) and QIAcube instrument (Qiagen, Hilden, Germany). DNA quantity was determined using a Qubit dsDNA HS Assay kit (Thermo Fisher Scientific) and a Qubit 4 Fluorometer (Thermo Fisher Scientific).

2.8. Targeted Sequencing of DNA and RNA

Libraries were built using Oncomine Comprehensive Assay v3 (OCAv3, Thermo Fisher Scientific), which is an amplicon-based panel targeting the DNA or RNA of a total of 161 genes relevant to solid tumours (see Supplementary Table S2 for a full description of the targeted genes and gene fusion events). Briefly, DNA (20 ng) was subjected to multiplex polymerase chain reaction (PCR) amplification using an Ion AmpliSeq Library Plus Kit (Thermo Fisher Scientific) and DNA Oncomine Comprehensive Panel v3M (Thermo Fisher Scientific). RNA (40 ng) was subjected to reverse transcription using a SuperScript IV VILO Master Mix (Thermo Fisher Scientific), followed by library generation using an Ion AmpliSeq Library Plus Kit (Thermo Fisher Scientific) and RNA Oncomine Comprehensive Panel v3M (Thermo Fisher Scientific). The PCR products were ligated to the IonCode Adapter (Thermo Fisher Scientific) and purified using Agencourt AMPure XP beads (Beck-

man Coulter, Brea, CA, USA). DNA and RNA libraries were quantified on a QuantStudio 7 real-time thermocycler (Thermo Fisher Scientific) using an Ion Library TaqMan Quantitation Kit (Thermo Fisher Scientific). Each purified library sample (50 pM) was pooled and prepared for sequencing on an IonChef instrument (Thermo Fisher Scientific) using an Ion S5 Chef Kit and Ion 540 Chip (Thermo Fisher Scientific). Ion semiconductor sequencing was performed using an S5 GeneStudio (400 flows or equivalent to ~200 bp, Thermo Fischer Scientific). Sequencing was performed to a mean coverage of $\geq$1000$\times$ for DNA targets and $\geq$0.5 M total mapped reads for RNA. DNA and RNA sequencing quality was assessed using Torrent Suite v5.10.1 (Thermo Fisher Scientific).

2.9. Variant Calling, Annotation, and Curation

Reads were aligned to the hg19 human reference genome sequence using Ion Reporter™ Software v.5.8 (Thermo Fisher Scientific). Variant calling was performed using Ion Reporter™ with a variant allele fraction (VAF) threshold of 5%. All variants were annotated manually using Alamut Visual v2.15 software (Interactive Biosoftware, Sofia Genetics, Lausanne, Switzerland) with reference to the RefSeq transcripts provided in Supplementary Tables S2 and S3. The clinical actionability of variants was curated according to standards and guidelines described by the Association for Molecular Pathology, American Society of Clinical Oncology, and College of American Pathologists (AMP/ASCO/CAP) [36]. Allele frequencies were determined using gnomAD (v3.1.2). Variants identified as Tier IV (AMP/ASCO/CAP criteria) or with an allele frequency $\geq$ 0.01 in any population were excluded from the study.

3. Results

3.1. Tissue Heterogeneity in Large UMs

Of the 46 enucleated UMs submitted to our diagnostic pathology laboratory between 2017 and 2020, 39 were primary referrals, and 7 were second opinion consultations from outside laboratories. Of the primary referrals, seven met the inclusion criteria for the current study (see the study cohort selection criteria in Section 2). Six of the seven UMs showed ciliary body involvement. None of the patients exhibited extraocular extension. At the time of writing, three patients developed metastases, two died of metastatic disease, and one received post-surgical fotemustine treatment. The patient and tumour characteristics are summarised in Table 1.

Table 1. Patient and tumour characteristics.

Patient and Tumour Characteristics		*n*/years
Age at enucleation (years)	Range	40–82
	Average	59.3
Sex	Male	6
	Female	1
Patient status	Alive	5
	Deceased	2
Affected eye	Left	4
	Right	3
Ciliary body involvement	Yes	6
	No	1
Tumour thickness	<12 mm	6
	12–15 mm	1

Table 1. *Cont.*

Patient and Tumour Characteristics		*n*/years
Tumour basal diameter	<15 mm	1
	15–18 mm	5
	>18 mm	1
Extraocular extension	Absent	7
	Present	0
pTNM stage	pT2	0
	pT3a	0
	pT3b	5
	pT4a	1
	pT4b	1
Metastasis	Present	3
	Absent	4

pTNM stage was determined according to AJCC 2017 criteria [10].

Upon macroscopic assessment, at least two regions exhibiting clear pigmentation differences were identified in each tumour (Figure 1), hereafter referred to as Region A (melanotic) and Region B (amelanotic).

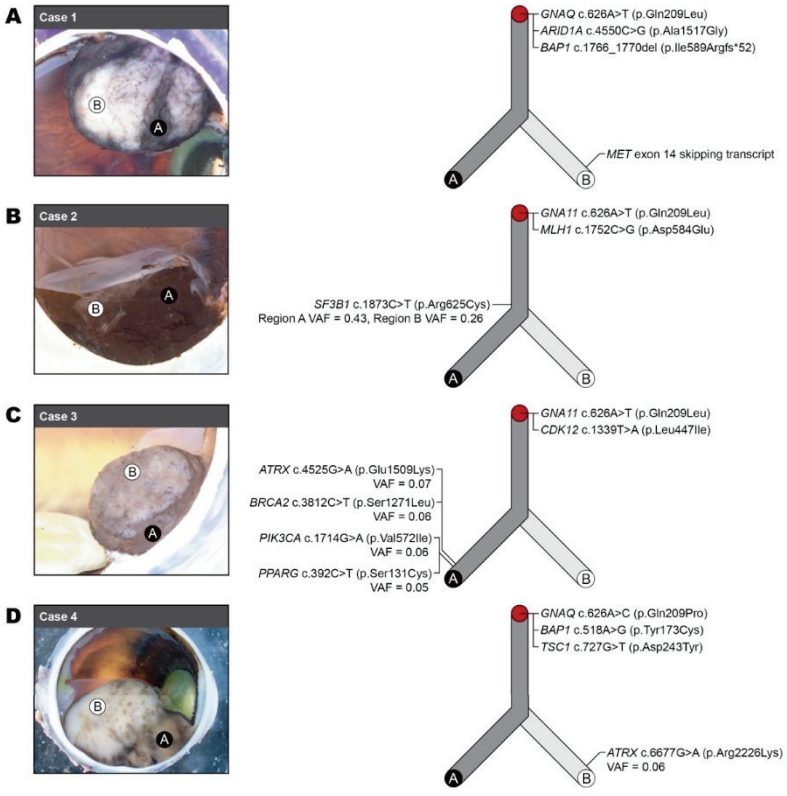


Figure 1. *Cont.*

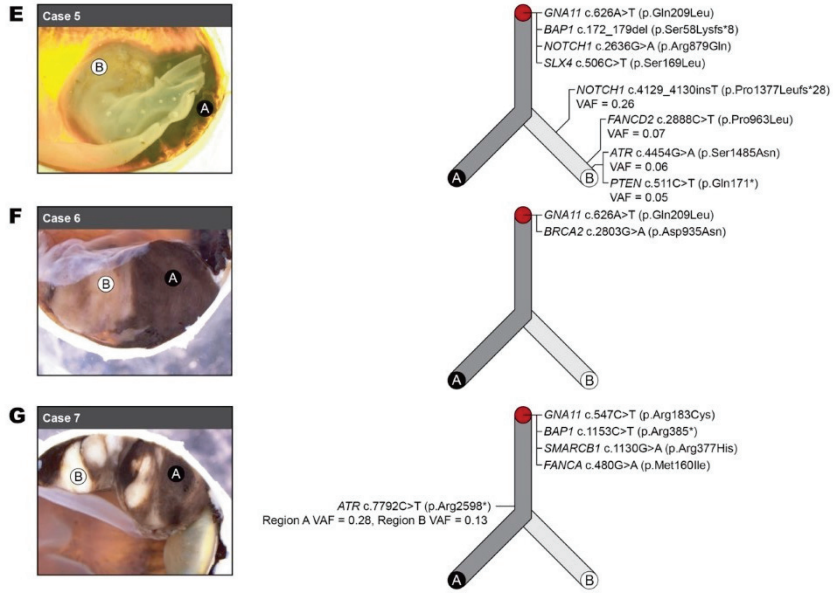


Figure 1. Molecular heterogeneity between morphologically distinct regions of the same tumour. Photographs on the left of panels (**A**–**G**) show the macroscopic appearance of each tumour investigated (Cases 1 to 7). Region A indicates the highly pigmented region analysed; Region B indicates the less pigmented region analysed. Schematic on the right of each panel represents a hypothesised phylogenetic tree of the molecular events in each tumour with dark grey representing highly pigmented tissue (Region A) and light grey representing less pigmented tissue (Region B). Initiating events found in the majority (≥60%) of tumour cells based on VAF are indicated at the top (red circle). Variants specific to Region A or B are indicated in respective branches with later molecular events (lower VAF) appearing towards the end of the branch. The VAF for subclonal variants (<60%) is indicated.

Histological examination also revealed microscopic differences between these regions. Specifically, the tumour growth pattern was "solid" in Region B from all tumours but a mixture of "solid and diffuse" in Region A from two tumours, and microvascular density was lower in Region B when compared with Region A in five of seven tumours (Table 2).

Differences were also observed in the extravascular matrix pattern, tumour-infiltrating lymphocytes, and tumour-infiltrating CD68+/CD163+ macrophage subsets; although, these differences were not consistent between Regions A and B across the tumours.

3.2. Molecular Features of High Metastatic Risk in All Tumours Examined

Loss of *BAP1* is associated with a high risk of metastasis in UMs. We investigated BAP1 protein expression by immunohistochemistry, as well as *BAP1* copy number and mutation status. Copy number analysis by comparative genomic hybridisation/single nucleotide polymorphism (CGH/SNP) chromosome microarrays was performed on bulk tumour DNA extracts only (i.e., without microdissection), in accordance with routine diagnostic testing. We observed aberrant BAP1 protein levels with immunohistochemistry (IHC) in all seven tumours (Table 3). The biallelic loss of *BAP1* was confirmed in four of the seven tumours by a combination of monosomy 3 or loss of chromosome 3p and sequence variants; whereas, in three tumours, only monosomy 3 or loss of chromosome 3p was detected. In addition, chromosome 8q gain, another molecular feature of high metastatic risk, was observed in five tumours (Table 3).

Table 2. Histopathological characteristics of Regions A and B in each UM.

Case #	**1**		**2**		**3**		**4**		**5**		**6**		**7**	
Region	**A**	**B**	**A**	**B**	**A**	**B**	**A**	**B**	**A**	**B**	**A**	**B**	**A**	**B**
Tumour pigmentation	+++	−	+++	++	+	−	+	−	+++	+	+++	++	+++	+
Tumour growth pattern	Solid	Solid	Solid and diffuse	Solid	Solid	Solid	Solid	Solid	Solid	Solid	Solid	Solid	Solid & diffuse	Solid
Cell type	Mixed	Mixed	Mixed	Mixed	Mixed	Mixed	Mixed	Mixed	Mixed	Mixed	Mostly spindled	Mostly spindled	Epithelioid	Epithelioid
Mitosis per 40 HPF	21	ND	23	ND	23	ND	23	ND	12	ND	18	ND	19	ND
Microvascular density [1]	Low	Low	High	Mod	Mod	Low	High	Mod	Low	Very low	High	High	Very high	High
Extravascular matrix pattern	Loops	LFN	Loops absent	Loops	LFN	LFN	LFN	LFN	LFN	Loops	LFN	LFN	Loops	LFN
Vascular lakes	Present	Present	Present	Present	Present	Present	Present	Present	Present	Absent	Present	Present	Absent	Present
Infiltrating lymphocytes	Low	Low	Low	Low	High	High	High	High	Low	High	Low	Low	High	Low
Infiltrating macrophages	CD68+ High CD163+ Very high	CD68+ Mod CD163+ Mod	CD68+ High CD163+ Low	CD68+ Low CD163+ Low	CD68+ Low CD163+ High	CD68+ Low CD163+ Mod	CD68+ High CD163+ High	CD68+ Very high CD163+ Very high	CD68+ Low CD163+ Low	CD68+ Low CD163+ Mod	CD68+ Mod CD163+ High	CD68+ Mod CD163+ High	CD68+ High CD163+ Very high	CD68+ Low CD163+ High

Histopathologic features the cohort. The two distinct morphological regions in each tumour (1 to 7; top row) are identied as A and B (second row). +++ Heavily pigmented. ++ Moderately pigmented. + Lightly pigmented. − Amelanotic. ND, not determined. [1]. Microvascular density by CD31 immunohistochemistry. LFN = loop-forming networks, Mod = moderate. Grey shading indicates tumour regions with highest pigmentation.

Table 3. High metastatic risk features in all tumours examined.

	Case #						
	1	**2**	**3**	**4**	**5**	**6**	**7**
BAP1 IHC	**Aberrant**	**Aberrant**	**Aberrant**	**Aberrant**	**Aberrant**	**Aberrant**	**Aberrant**
Chromosome 3	Monosomy 3	Loss of 3p (1 copy) *	Monosomy 3	Monosomy 3	Monosomy 3	Monosomy 3	Loss of 3p (1 copy) *
Chromosome 8q	Gain (5 copies)	Disomy	Gain (3 copies)	Gain (4–5 copies)	Gain (3 copies)	Disomy	Gain (3 copies)
BAP1 sequence variants	Detected c.1766_1770 del	Not detected	Not detected	Detected c.518A>G	Detected c.172_179del	Not detected	Detected c.1153C>T

High metastatic risk features are defined as loss of monosomy 3 and chromosome 8q gain. CGH/SNP chromosome microarray and *BAP1* sequence variants, identified using targeted sequencing. *BAP1* variants are described relative to RefSeq transcript NM_004656.4. * Deletions encompass the *BAP1* locus on 3p.

Taken together, these findings identify poor prognostic features indicative of high metastatic risk in all seven tumours.

3.3. Molecular Heterogeneity Revealed by Microdissection and Targeted Sequencing

Regions A and B were separately microdissected (Supplementary Figure S1) and sequenced using a gene panel targeting a total of 161 genes at the DNA and RNA levels, including the known UM driver genes *GNAQ*, *GNA11*, *SF3B1*, and *BAP1* (Table 4).

Table 4. Sequence variants identified by targeted sequencing in Regions A and B in each tumour.

Case #	**Gene and Variant (HGVS)**	**Region A VAF**	**Region B VAF**	**gnomAD AF (Allele Count [Homozygotes])**	**AMP/ASCO/CAP Tier**	**Gene Implicated Previously in UM**
1	NM_002072.4(*GNAQ*):c.626A>T (p.Gln209Leu)	0.51	0.48	Not present	Tier 2C	Yes [3,34,37]
	NM_006015.5(*ARID1A*):c.4550C>G (p.Ala1517Gly)	0.90	0.94	Not present	Tier 2C	No
	NM_004656.4(*BAP1*):c.1766_1770del (p.Ile589Argfs*52)	0.80	0.81	Not present	Tier 2C	Yes [3,34,37]
	NM_001127500.2:*MET* exon 14 skipping transcript variant $^{\Delta}$	ND	Detected	NA	Tier 2C	No
2	NM_002067.4(*GNA11*):c.626A>T (p.Gln209Leu)	0.44	0.33	Not present	Tier 2C	Yes [3,34,37]
	NM_012433.3(*SF3B1*):c.1873C>T (p.Arg625Cys)	0.43	0.26	Not present	Tier 2C	Yes [3,34,37]
	NM_000249.3(*MLH1*):c.1752C>G (p.Asp584Glu)	0.87	0.72	Not present	Tier 3	No
3	NM_002067.4(*GNA11*):c.626A>T (p.Gln209Leu)	0.48	0.40	Not present	Tier 2C	Yes [3,34,37]
	NM_016507.3(*CDK12*):c.1339T>A (p.Leu447Ile)	0.51	0.51	0.0001315 (20[0])	Tier 3	Yes [3]
	NM_000059.3(*BRCA2*):c.3812C>T (p.Ser1271Leu)	0.06	ND	Not present	Tier 2C	Yes, [3]
	NM_000489.5(*ATRX*):c.4525G>A (p.Glu1509Lys)	0.07	ND	Not present	Tier 2C	Yes [37]
	NM_006218.3(*PIK3CA*):c.1714G>A (p.Val572Ile)	0.06	ND	Not present	Tier 3	No
	NM_138712.3(*PPARG*):c.392C>T (p.Ser131Cys)	0.05	ND	Not present	Tier 3	No

Table 4. *Cont*.

Case #	Gene and Variant (HGVS)	Region A VAF	Region B VAF	gnomAD AF (Allele Count [Homozygotes])	AMP/ASCO/CAP Tier	Gene Implicated Previously in UM
4	NM_002072.4(*GNAQ*):c.626A>C (p.Gln209Pro)	0.46	0.54	Not present	Tier 2C	Yes [3,37]
	NM_004656.4(*BAP1*):c.518A>G (p.Tyr173Cys)	0.86	0.76	Not present	Tier 2C	Yes [3,37]
	NM_000368.4(*TSC1*):c.727G>T (p.Asp243Tyr)	0.48	0.47	Not present	Tier 3	No
	NM_000489.5(*ATRX*):c.6677G>A (p.Arg2226Lys)	ND	0.06	Not present	Tier 2C	Yes [37]
5	NM_002067.4(*GNA11*):c.626A>T (p.Gln209Leu)	0.33	0.39	Not present	Tier 2C	Yes
	NM_004656.4(*BAP1*):c.172_179del (p.Ser58Lysfs*8)	0.41	0.78	Not present	Tier 2C	Yes
	NM_017617.5(*NOTCH1*):c.2636G>A (p.Arg879Gln)	0.44	0.52	0.0001051 (16[0])	Tier 3	Yes [37]
	NM_032444.3(*SLX4*):c.506C>T (p.Ser169Leu)	0.36	0.36	Not present	Tier 2C	Yes [34,37]
	NM_017617.5(*NOTCH1*):c.4129_4130 (p.Pro1377Leufs*28)	ND	0.26	Not present	Tier 3	Yes [37]
	NM_033084.4(*FANCD2*):c.2888C>T (p.Pro963Leu)	ND	0.07	Not present	Tier 3	No
	NM_001184.3(*ATR*):c.4454G>A (p.Ser1485Asn)	ND	0.06	Not present	Tier 2C	No
	NM_000314.7(*PTEN*):c.511C>T (p.Gln171*)	ND	0.05	Not present	Tier 3	No
6	NM_002067.4(*GNA11*):c.626A>T (p.Gln209Leu)	0.46	0.42	Not present	Tier 2C	Yes [3,34,37]
	NM_000059.3(*BRCA2*):c.2803G>A (p.Asp935Asn)	0.48	0.50	0.0006506 (99[0])	Tier 2C	Yes [3]
7	NM_004656.4(*BAP1*):c.1153C>T (p.Arg385*)	0.64	0.75	Not present	Tier 2C	Yes [3,34,37]
	NM_002067.4(*GNA11*):c.547C>T (p.Arg183Cys)	0.41	0.44	Not present	Tier 2C	Yes [3,34,37]
	NM_003073.4(*SMARCB1*):c.1130G>A (p.Arg377His)	0.36	0.44	0.000006568 (1[0])	Tier 3	No
	NM_000135.4(*FANCA*):c.480G>A (p.Met160Ile)	0.46	0.42	0.0002891 (44[0])	Tier 2C	Yes [3,34,37]
	NM_001184.3(*ATR*):c.7792C>T (p.Arg2598*)	0.28	0.13	Not present	Tier 2C	No

Variants annotated according to Human Genome Variation Society (HGVS) nomenclature. Variants curated based on potential therapeutic, diagnostic, or prognostic significance according to standards and guidelines from the Association for Molecular Pathology, American Society of Clinical Oncology, and College of American Pathologists (AMP/ASCO/CAP) [36]. Note that the AMP/ASCO/CAP tier provided may change over time as evidence and literature accumulates. AF (allele frequency) was obtained using The Genome Aggregation Database (gnomAD, v3.1.2). VAF, variant allele fraction. ND, not detected. NA, not applicable. UM, uveal melanoma. $^{\Delta}$ The specific DNA variant that results in this transcript (e.g., exon 14 deletion or splicing variant) was not identified. Grey shading indicates region-specific variants.

All seven tumours contained a hotspot variant in either *GNAQ* (two tumours) or *GNA11* (five tumours), consistent with somatic variants in these genes being common initiating events in UMs. The variant allele fraction (VAF) of these *GNAQ* and *GNA11* variants indicated their presence in the majority (66–100%) of cells in both Regions A and B of all tumours. We also detected *BAP1* variants in both regions in four tumours, as described above, each with a VAF consistent with their presence in most or all tumour cells (82–100%) and concomitant deletion of the other *BAP1* allele.

We also detected a range of additional variants that are not typically associated with UM (Figure 1 and Table 4). In Case 1, we identified a variant in *ARID1A*, located within chromosome band 1p36, in both regions with a VAF of 0.90 and 0.94 (Table 4), consistent with a concomitant deletion of the other allele. Inspection of the CGH/SNP chromosome microarray data identified a heterozygous deletion in 100% of cells encompassing chromosome bands 1p36.33-p34.3 (37.88 Mb), which contains the *ARID1A* locus. In the RNA from this tumour, we detected a *MET* exon 14 skipping transcript with a total of 1025 *MET* exons 13–15 spanning reads in Region B (0 reads were detected in Region A). Resequencing following RNA extraction without microdissection failed to detect the *MET* exon 14 skipping transcript. Closer inspection of the raw data indicated that *MET* exons 13–15 spanning reads were present; however, the number of reads (413) fell below the limit of detection for the assay (1000 reads). This suggests that the *MET* exon 14 skipping transcript originated from only a subset of cells analysed, which is consistent with the fact that this transcript is present specifically in Region B of this tumour. In Case 2, a variant in *MLH1*, located within chromosome band 3p22, was detected with a high VAF (0.87 and 0.72 in Regions A and B, respectively). CGH/SNP chromosome microarray data showed that, in addition to the heterozygous loss of chromosome 3p (3p26.3-p14.3 (55.28 Mb) in 80–100% of cells), a region including *BAP1* and *MLH1*, this tumour also exhibited the heterozygous loss of chromosome 3q (3q25.32-q29 (35.29 Mb) in 80–100% of cells) and heterozygous loss of chromosome 6q (6q16.2-q27). Although a loss of a copy of MLH1 has been demonstrated in monosomy 3 UM, and variants in PMS2 and MSH3 are extremely rare in UM, a variant in the remaining MLH gene has not been reported [38]. Case 2 also contained an *SF3B1* variant with a VAF of 0.43 in Region A and 0.26 in Region B. No variants that were specific to Region A or Region B were identified. In Case 3, a *CDK12* variant was detected in all cells of Regions A and B; whereas, four variants in *ATRX*, *BRCA2*, *PIK3CA*, and *PPARG* were detected specifically in Region A. All four variants displayed low VAFs (0.05–0.07), indicating a late molecular event present in a small subset of cancer cells. In Case 4, a *TSC1* variant was detected in all cells of Regions A and B (VAF 0.48 and 0.47, respectively), and an *ATRX* variant was detected specifically in Region B with a VAF of 0.06, indicating a late molecular event. This *ATRX* variant was different from that detected in Case 3. Case 5 contained a *NOTCH1* and an *SLX4* variant in all cells of Regions A and B; however, four additional variants specific to Region B were also detected. This included a second variant in *NOTCH1* with a VAF of 0.26, suggesting that it arose early, following the divergence of cells in Region B; whereas, the variants in *FANCD2*, *ATR*, and *PTEN* (VAF 0.07, 0.06, and 0.05, respectively) are late molecular events. In Case 6, no variants that were specific to Region A or Region B were identified; however, a *BRCA2* variant was detected in all cells in both regions. In Case 7, *SMARCB1* and *FANCA* variants were detected in the majority of cells (62–92%) in both regions; however, the VAF of an *ATR* variant (0.28 and 0.13 in Regions A and B, respectively) indicated that this was a later event in the development of this tumour. No variants that were specific to Region A or Region B were identified.

We determined which of the genes identified were listed in the eligibility criteria for existing clinical trials. Variants in 10 of the genes implicated in our cohort of UMs served as eligibility criteria for current phase I/II clinical trials in UM or advanced solid tumours (Table 5).

Importantly, four genes (*MET*, *ATRX*, *ATR*, and *BRCA2*) associated with active clinical trials were mutated specifically in one region of the tumours investigated, suggesting that may have been missed if tumour heterogeneity had not been considered.

3.4. Recurrently Mutated Genes in UM

The mining of data from TCGA [3] and Johansson et al. [39] identified 108 UMs profiled for SNVs and indels, copy number alterations, and structural variants. We determined the frequency of these types of genetic alterations in all genes identified as mutated in our study (Figure 2). Five genes (*GNAQ*, *GNA11*, *BAP1*, *SF3B1*, and *FANCA*) were mutated across all three studies. We also identified genes that were mutated once in our cohort of

UMs and in at least one other study (CDK12, BRCA2, and SLX4) or multiple times in our cohort of UMs (ATRX, NOTCH1, ATR, and ARID1A). In summary, our data confirmed the importance of known canonical genes but also identified novel recurrently mutated genes in the development of UM.

Table 5. Mutated genes and associated clinical trials.

Clinical Trials (Phase)	Tumour Type	Gene(s)
NCT03947385 (Phase I/II)	UM	*GNAQ*, *GNA11*
NCT02693535 (Phase II)	Advanced solid tumours	*MET* exon 14 skipping transcript *
NCT03207347 (Phase I/II)	UM	*ARID1A*, *ATR* *, *BAP1*, *PTEN* *, *SLX4*
NCT03767075 (Phase II)	Advanced solid tumours	DNA repair genes (*ATRX* *, *ATR* *, *BAP1*, *BRCA2* *, *SLX4*, *ARID1A*)
NCT01971515 (Phase I)	Advanced malignancies	*PIK3CA* *, *PTEN* *, *TSC1*
NCT02961283 (Phase I)	Advanced solid tumours	*PIK3CA* *, *PTEN* *
NCT04171700 (Phase II)	Advanced solid tumours	*BRCA2* *, *FANCA*

* Indicates genes with variants identified specifically in one region of a tumour investigated in this study. UM, uveal melanoma. Clinical trial information was obtained from Clinical Trials.gov. Eligibility dependent on inclusion and exclusion criteria for each trial. Grey shading indicates trials that were active and recruiting at time of writing.

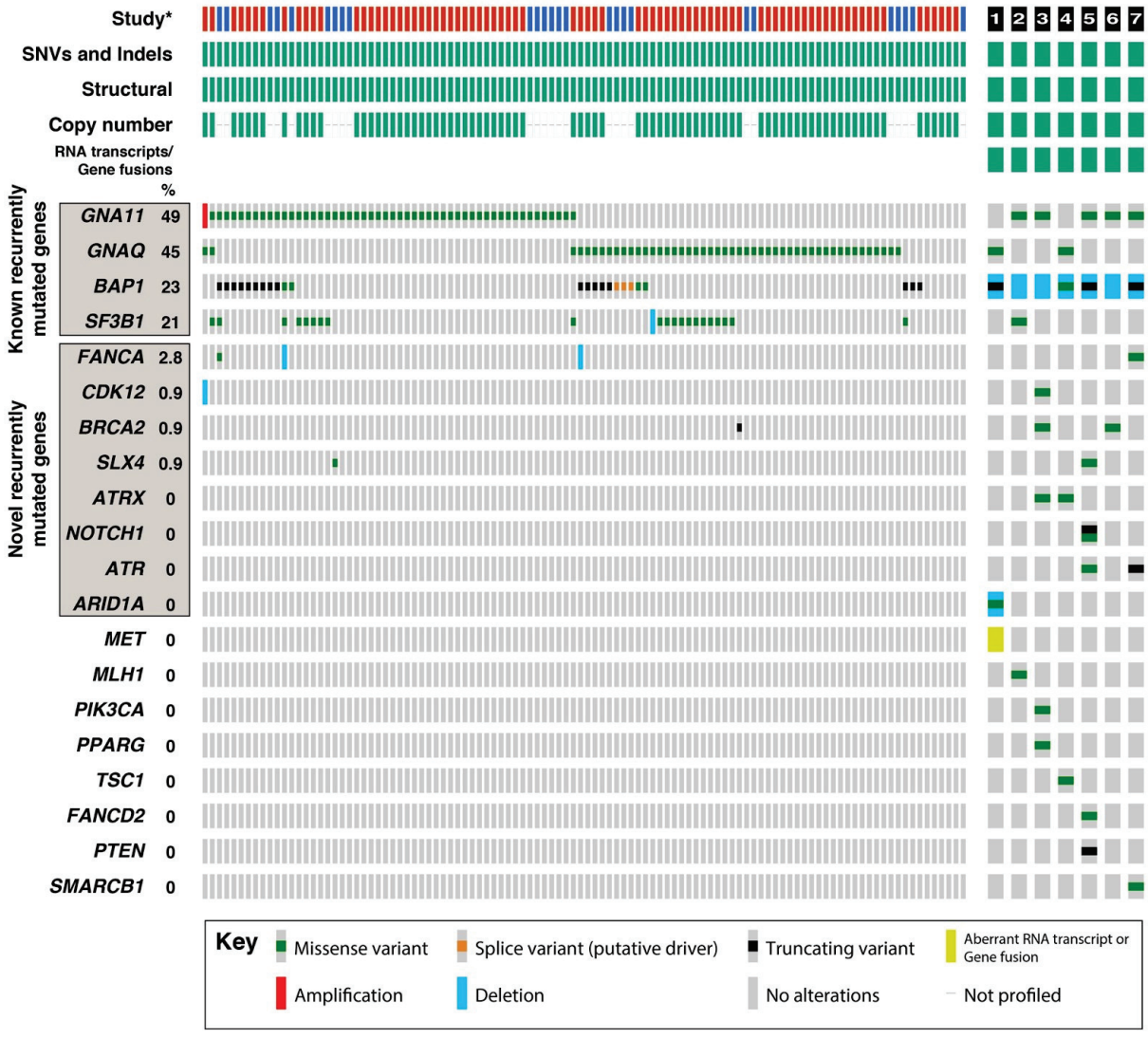


Figure 2. Recurrently mutated genes in UM. Top panel, left: Gene mutations and chromosome copy number changes as identified by * TCGA study [3] (n = 80) and Johansson et al. [39] (n = 28). Each column

represents a TCGA single case. Top panel, right: Patients 1 to 7 in our study cohort (n = 7). Bottom panel, left: Recurrent and rarer gene mutations identified by TCGA. Bottom panel, right: Mutations identified in our study cohort. In addition to the common UM gene variants, we identified gene variants not previously described in all 7 cases, 3 of which were recurrent. which are indicated by the red, blue, and black boxes, respectively. Mutations include sequence variants (SNVs and indels), inversions and translocations (structural), and copy number alterations (deletions or amplifications). Gene fusions identified by RNA transcripts were not reported by TCGA. Recurrently mutated genes were defined as those showing multiple alterations in these datasets. Percentage values next to each gene symbol represent the frequency of alterations in data from TCGA [3] and Johansson et al. [39]. Genes are listed in order of mutation frequency. Note that deletions involving MLH1 have been omitted, as these are part of chromosome 3 deletions also involving BAP1.

4. Discussion

There is no established cure for metastatic UM; therefore, the identification of potential therapies and clinical trials for these patients offers a rare opportunity to extend disease-free survival. We show that heterogeneity in pigmentation can be used to guide the microdissection and molecular testing of UMs and to identify therapeutically relevant variants that might otherwise be missed due to tumour heterogeneity. The rationale for using heterogeneity in pigmentation as a guide for microdissection is that, in our experience, it is a relatively common and conspicuous finding in larger, enucleated UMs, is readily discerned on macrophotography, and lends itself well to microdissection on corresponding paraffin sections. Since melanin production is a marker of melanocytic differentiation, loss of melanin may indicate tumour progression via dedifferentiation. Enucleation is typically reserved for advanced-stage tumours, too large for plaque brachytherapy; these UMs have a higher risk of metastasis, presenting a compelling opportunity to investigate gene variants associated with metastasis or those potentially amenable to available targeted therapies.

Molecular heterogeneity within primary UMs has been previously described [40–42]. Shain et al. [41] documented molecular heterogeneity in 16 of 35 primary UMs and showed that, when separate regions were microdissected for sequencing, additional alterations, such as *BAP1* variants and chromosome 8q gain, were identified. Significantly, variants found in liver metastases matched those found in specific regions of the primary tumour. Our study extends on these findings by showing that molecular heterogeneity can be captured through the analysis of macroscopically distinct regions. We used pigmentation as a visible differential, but other differences across a tumour, such as histological or immunohistochemical differences, may equally serve as adequate markers of molecular heterogeneity. While our findings add to the emerging evidence that UM heterogeneity may influence metastatic behaviour, proof of this concept will require the comparison of the gene variants in matched, primary metastasis tumour pairs.

While tumour heterogeneity is unlikely to be restricted to large UMs, undertaking proof of concept studies in smaller tumours is logistically challenging. While a tissue diagnosis is a core tenet of best practice for managing all UMs, the tumour sample available for patients with smaller tumours undergoing plaque brachytherapy is a small, fine-needle aspiration biopsy. In the event there is sufficient tissue excess for routine diagnostic and prognostic needs, detecting tumour heterogeneity (by single-cell sequencing technologies, for example) cannot overcome the reality that an aspirate is unlikely to be representative of the entire tumour.

Across many different tumour types, including UM, molecular heterogeneity and the accumulation of additional molecular changes are the basis of tumour progression and metastasis [37]. In UM, cellular and molecular heterogeneity within the primary tumour has been linked to a molecular switch that drives metastasis [40]. Early evidence confirms that the mutational signatures of metastatic UM closely match the phylogenetically advanced regions of heterogenous primaries [41]. This heterogeneity suggests that no single

targeted therapy will be effective in the treatment of all metastatic UM. Accounting for this heterogeneity may become increasingly important when determining treatment and prognosis. Though preliminary, our findings encourage the ongoing investigation of heterogeneity in primary UM based on morphologically discernible tumour regions, with the eventual goal of identifying additional treatment options for metastatic disease.

Our study presents the two following significant findings: (1) we identified therapeutically relevant variants in our cohort of UMs, and (2) we identified novel, recurrently mutated genes associated with UM development. One of the most intriguing findings in our study was the detection of a *MET* exon 14 skipping transcript in Region B of one tumour. The *MET* exon 14 skipping transcript is an emerging biomarker in metastatic non-small cell lung cancer [43–47] and other solid tumour types [48] that predicts sensitivity to capmatinib, crizotinib, and tepotinib. These targeted therapies are recommended by multiple professional guidelines, including NCCN and ESMO, as treatment options for patients with non-small cell lung cancer that harbour *MET* exon 14 skipping variants. The presence of this biomarker specifically in one region indicates a later event in the development of this tumour. The *MET* (Mesenchymal to Epithelial Transition) gene encodes the hepatocyte growth factor receptor, a receptor tyrosine kinase that is important in embryogenesis, and cellular survival, migration, and invasion. The expression of exon 14 skipping transcripts results in constitutively active kinase activity due to the in-frame exclusion of a regulatory juxtamembrane domain. While *MET* exon 14 skipping transcripts have not previously been reported in primary UMs, there is emerging evidence of cMET protein overexpression in primary and metastatic UM [25], indicating a promising therapeutic target for patients with metastatic disease. Importantly, we identified this biomarker using targeted RNA sequencing, which is currently not performed as part of the routine testing of UMs. Further research utilising RNA sequencing or targeted gene fusion analysis should be performed to determine whether this transcript, or gene fusions, are recurrent events. Finally, we identified four current (at the time of writing) clinical trials for patients with UM and advanced solid tumours with eligibility criteria that included variants in genes that were identified specifically in one region of a tumour in our study. This provides further support for the analysis of multiple regions in heterogeneous tumours for identifying additional relevant clinical trials or possible targeted therapies, such as capmatinib, crizotinib, or tepotinib.

Comparisons with previous studies allowed us to identify eight genes (*FANCA*, *CDK12*, *SLX4*, BRCA2, *ATRX*, *NOTCH1*, *ATR*, and *ARID1A*) that were either not previously described or very rarely reported in UM. Two of these genes (*NOTCH1* and *ARID1A*) were each targeted by two mutational events in two different tumours. The specificity of two mutational events targeting the same gene in a single tumour suggests that they are important in the pathogenesis of that particular tumour; whereas, the identification of genes that are recurrently mutated across a relatively small cohort of UMs implicates them more broadly in UM development. The importance of these novel genes is supported by another recent study that used whole-genome sequencing to identify variants present in an additional 103 UMs [48]. When cases from our study (n = 7), TCGA [3] (n = 80), Johansson et al. [39] (n = 28), and Johansson et al. [48] (n = 103) were combined (n = 218), four genes were identified as mutated in <2% of UM cases: *FANCA* (1.8%, four cases), *SLX4* (1.8%, four cases), *BRCA2* (1.4%, three cases), and *ATRX* (1.4%, three cases). None of the specific variants identified were common among these studies, and the role of these genes in UM development remains to be determined. However, the established role of *FANCA*, *SLX4*, *BRCA2*, and *ATRX* in DNA repair pathways is unlikely to be coincidental, especially considering that we identified mutations in other DNA repair pathway genes, including *ATR*, which was mutated in two tumours in our study. The association between germline BRCA2 mutations and UM risk requires further investigation; earlier literature suggests less than 2% of UMs is attributable to germline BRCA2 variants [49–51].

In three tumours, our analysis failed to identify variants that were specific to Region A or Region B of the tumour. We attribute this to the possible presence of variants in genes that were not targeted in our study. Specifically, our analysis did not target the

other known driver genes involved in UM (*PLCB4*, *CYSLTR2*, and *EIF1AX*) or significantly mutated genes that have recently been identified, such as *TP53BP1*, *CSMD1*, *TTC28*, *DLK2*, *KTN1*, *RPL5*, and *CENPE* [2,48]. Nevertheless, a strength of our study is the depth of the sequencing performed (mean coverage depth $\geq 1000\times$) in different regions of the same tumour, which enabled us to identify several novel genes not identified in previous studies.

5. Conclusions

Our observations support the approach of separately sequencing distinct morphological regions within larger UMs to better identify therapeutically relevant mutations. This includes the identification of existing targeted therapies that are approved in other tumour types or the identification of relevant clinical trials. Our observations require confirmation in a larger case series and prospective studies. This may include analysis using other platforms, including transcriptome sequencing, to further characterise differences in the mutational and transcriptional landscapes of UM.

Supplementary Materials: The following supporting information can be downloaded at: https://www.mdpi.com/article/10.3390/cancers16244152/s1, Figure S1: Tumour microdissection. Table S1: The primary antibodies, antigen retrieval, and incubation time are summarised. Tables S2 and S3: a full description of the targeted genes and gene fusion events.

Author Contributions: Conceptualization, L.B.H., S.C. and R.M.C.; methodology, L.B.H. and S.C.; validation, L.B.H., S.C., E.H., E.T., F.Z. (Fanfan Zhou), D.W. and A.H.; formal analysis, L.B.H., S.C., E.H. and E.T.; resources, R.M.C., L.-A.S.L., A.T.F. and M.G.; data curation, L.B.H., S.C., E.T., F.Z. (Farida Zabih), D.W., A.H. and V.L.; writing—original draft preparation, L.B.H., S.C. and E.T.; writing—review and editing, E.T., L.B.H., V.L., D.W., E.H., L.-A.S.L., M.G., F.Z. (Fanfan Zhou), A.H., F.Z. (Farida Zabih), A.T.F., R.M.C. and S.C.; visualization, L.B.H., S.C. and E.T.; supervision, S.C. and R.M.C.; project administration, S.C.; funding acquisition, L.B.H. All authors have read and agreed to the published version of the manuscript.

Funding: Financial support for this research was obtained by Luke Hesson from MTPConnect, grant number PRJ2017-55, and BioMedTech Horizons, grant number BMTH06, Department of Health, Australia.

Institutional Review Board Statement: The study was approved by the St Vincent's Hospital Human Research Ethics Committee (2019/ETH03554) and monitored by the St Vincent's Hospital Research Office; the study adhered to the tenets of the Declaration of Helsinki.

Informed Consent Statement: Informed consent was obtained from each patient.

Data Availability Statement: Raw data for this study were generated at the Kinghorn Centre for Clinical Genomics Sequencing Laboratory, Garvan Institute of Medical Research. The data supporting the findings of this study are available in the NCBI Gene Expression Omnibus repository (https://www.ncbi.nlm.nih.gov/geo/ (accessed on 9 November 2023)).

Acknowledgments: We thank Hayley Espanol for the preparation of samples for NGS, Gary Gracie for technical assistance with immunohistochemical studies, and Denise Riley and Yoomee Kim for their assistance preparing FFPE sections for molecular analysis. We thank Nikita Garg for her kind assistance in manuscript submission administration.

Conflicts of Interest: The authors declare no conflicts of interest.

References

1. Pandiani, C.; Béranger, G.E.; Leclerc, J.; Ballotti, R.; Bertolotto, C. Focus on cutaneous and uveal melanoma specificities. *Genes Dev.* **2017**, *31*, 724–743. [CrossRef] [PubMed]
2. Royer-Bertrand, B.; Torsello, M.; Rimoldi, D.; El Zaoui, I.; Cisarova, K.; Pescini-Gobert, R.; Raynaud, F.; Zografos, L.; Schalenbourg, A.; Speiser, D.; et al. Comprehensive genetic landscape of uveal melanoma by whole-genome sequencing. *Am. J. Hum. Genet.* **2016**, *99*, 1190–1198. [CrossRef] [PubMed]
3. Robertson, A.G.; Shih, J.; Yau, C.; Gibb, E.A.; Oba, J.; Mungall, K.L.; Hess, J.M.; Uzunangelov, V.; Walter, V.; Danilova, L.; et al. Integrative analysis identifies four molecular and clinical subsets in uveal melanoma. *Cancer Cell* **2017**, *32*, 204–220.e15. [CrossRef] [PubMed]

4. Schvartsman, G.; Taranto, P.; Glitza, I.C.; Agarwala, S.S.; Atkins, M.B.; Buzaid, A.C. Management of metastatic cutaneous melanoma: Updates in clinical practice. *Ther. Adv. Med. Oncol.* **2019**, *11*, 1758835919851663. [CrossRef] [PubMed]
5. Lane, A.M.; Kim, I.K.; Gragoudas, E.S. Survival rates in patients after treatment for metastasis from uveal melanoma. *JAMA Ophthalmol.* **2018**, *136*, 981–986. [CrossRef]
6. Nathan, P.; Hassel, J.C.; Rutkowski, P.; Baurain, J.-F.; Butler, M.O.; Schlaak, M.; Sullivan, R.J.; Ochsenreither, S.; Dummer, R.; Kirkwood, J.M.; et al. Overall Survival Benefit with Tebentafusp in Metastatic Uveal Melanoma. *N. Engl. J. Med.* **2021**, *385*, 1196–1206. [CrossRef]
7. Kujala, E.; Makitie, T.; Kivela, T. Very long-term prognosis of patients with malignant uveal melanoma. *Investig. Ophthalmol. Vis. Sci.* **2003**, *44*, 4651–4659. [CrossRef]
8. Singh, A.D.; Turell, M.E.; Topham, A.K. Uveal melanoma: Trends in incidence, treatment, and survival. *Ophthalmology* **2011**, *118*, 1881–1885. [CrossRef]
9. Yang, J.; Manson, D.K.; Marr, B.P.; Carvajal, R.D. Treatment of uveal melanoma: Where are we now? *Ther. Adv. Med. Oncol.* **2018**, *10*, 1758834018757175. [CrossRef]
10. Edition, S.; Edge, S.; Byrd, D. *AJCC Cancer Staging Manual*, 8th ed.; Springer International Publishing: Cham, Switzerland, 2017.
11. Collaborative Ocular Melanoma Study Group. Assessment of metastatic disease status at death in 435 patients with large choroidal melanoma in the Collaborative Ocular Melanoma Study (COMS): COMS report no. 15. *Arch. Ophthalmol.* **2001**, *119*, 670–676. [CrossRef]
12. Shields, C.L.; Kaliki, S.; Furuta, M.; Fulco, E.; Alarcon, C.; Shields, J.A. American Joint Committee on Cancer Classification of Posterior Uveal Melanoma (Tumor Size Category) Predicts Prognosis in 7731 Patients. *Ophthalmology* **2013**, *120*, 2066–2071. [CrossRef] [PubMed]
13. Shields, C.L.; Kaliki, S.; Furuta, M.; Mashayekhi, A.; Shields, J.A. Clinical spectrum and prognosis of uveal melanoma based on age at presentation in 8033 cases. *Retina* **2012**, *32*, 1363–1372. [CrossRef] [PubMed]
14. Damato, B.; Eleuteri, A.; Taktak, A.F.; Coupland, S.E. Estimating prognosis for survival after treatment of choroidal melanoma. *Prog. Retin. Eye Res.* **2011**, *30*, 285–295. [CrossRef] [PubMed]
15. Cunha Rola, A.; Taktak, A.; Eleuteri, A.; Kalirai, H.; Heimann, H.; Hussain, R.; Bonnett, L.J.; Hill, C.J.; Traynor, M.; Jager, M.J.; et al. Multicenter External Validation of the Liverpool Uveal Melanoma Prognosticator Online: An OOG Collaborative Study. *Cancers* **2020**, *12*, 477. [CrossRef] [PubMed]
16. Vichitvejpaisal, P.; Dalvin, L.A.; Mazloumi, M.; Ewens, K.G.; Ganguly, A.; Shields, C.L. Genetic Analysis of Uveal Melanoma in 658 Patients Using the Cancer Genome Atlas Classification of Uveal Melanoma as A, B, C, and D. *Ophthalmology* **2019**, *126*, 1445–1453. [CrossRef]
17. Mazloumi, M.; Vichitvejpaisal, P.; Dalvin, L.A.; Yaghy, A.; Ewens, K.G.; Ganguly, A.; Shields, C.L. Accuracy of The Cancer Genome Atlas Classification vs American Joint Committee on Cancer Classification for Prediction of Metastasis in Patients with Uveal Melanoma. *JAMA Ophthalmol.* **2020**, *138*, 260–267. [CrossRef]
18. Sacco, J.J.; Nathan, P.D.; Danson, S.; Lorigan, P.; Nicholson, S.; Ottensmeier, C.; Corrie, P.; Steven, N.; Goodman, A.; Larkin, J.M.G.; et al. Sunitinib versus dacarbazine as first-line treatment in patients with metastatic uveal melanoma. *J. Clin. Oncol.* **2013**, *31*, 9031. [CrossRef]
19. Carvajal, R.D.; Sosman, J.A.; Quevedo, J.F.; Milhem, M.M.; Joshua, A.M.; Kudchadkar, R.R.; Linette, G.P.; Gajewski, T.F.; Lutzky, J.; Lawson, D.H.; et al. Effect of selumetinib vs chemotherapy on progression-free survival in uveal melanoma: A randomized clinical trial. *JAMA* **2014**, *311*, 2397–2405. [CrossRef]
20. Piperno-Neumann, S.; Kapiteijn, E.; Larkin, J.M.G.; Carvajal, R.D.; Luke, J.J.; Seifert, H.; Roozen, I.; Zoubir, M.; Yang, L.; Choudhury, S.; et al. Phase I dose-escalation study of the protein kinase C (PKC) inhibitor AEB071 in patients with metastatic uveal melanoma. *J. Clin. Oncol.* **2014**, *32*, 9030. [CrossRef]
21. Shoushtari, A.N.; Kudchadkar, R.R.; Panageas, K.; Murthy, R.K.; Jung, M.; Shah, R.; O'Donnell, B.; Khawaja, T.T.; Shames, Y.; Prempeh-Keteku, N.A.; et al. A randomized phase 2 study of trametinib with or without GSK2141795 in patients with advanced uveal melanoma. *J. Clin. Oncol.* **2016**, *34*, 9511. [CrossRef]
22. Algazi, A.P.; Tsai, K.K.; Shoushtari, A.N.; Munhoz, R.R.; Eroglu, Z.; Piulats, J.M.; Ott, P.A.; Johnson, D.B.; Hwang, J.; Daud, A.I.; et al. Clinical outcomes in metastatic uveal melanoma treated with PD-1 and PD-L1 antibodies. *Cancer* **2016**, *122*, 3344–3353. [CrossRef] [PubMed]
23. Carvajal, R.D.; Schwartz, G.K.; Tezel, T.; Marr, B.; Francis, J.H.; Nathan, P.D. Metastatic disease from uveal melanoma: Treatment options and future prospects. *Br. J. Ophthalmol.* **2017**, *101*, 38–44. [CrossRef]
24. Sandinha, T.; Farquharson, M.; McKay, I.; Roberts, F. Correlation of heterogeneity for chromosome 3 copy number with cell type in choroidal melanoma of mixed-cell type. *Investig. Ophthalmol. Vis. Sci.* **2006**, *47*, 5177–5180. [CrossRef] [PubMed]
25. Dopierala, J.; Damato, B.E.; Lake, S.L.; Taktak, A.F.; Coupland, S.E. Genetic heterogeneity in uveal melanoma assessed by multiplex ligation-dependent probe amplification. *Investig. Ophthalmol. Vis. Sci.* **2010**, *51*, 4898–4905. [CrossRef] [PubMed]
26. Chang, M.Y.; Rao, N.P.; Burgess, B.L.; Johnson, L.; McCannel, T.A. Heterogeneity of monosomy 3 in fine needle aspiration biopsy of choroidal melanoma. *Mol. Vis.* **2013**, *19*, 1892.
27. Augsburger, J.J.; Correa, Z.M.; Augsburger, B.D. Frequency and implications of discordant gene expression profile class in posterior uveal melanomas sampled by fine needle aspiration biopsy. *Am. J. Ophthalmol.* **2015**, *159*, 248–256. [CrossRef]

28. Miller, A.K.; Benage, M.J.; Wilson, D.J.; Skalet, A.H. Uveal melanoma with histopathologic intratumoral heterogeneity associated with gene expression profile discordance. *Ocul. Oncol. Pathol.* **2017**, *3*, 156–160. [CrossRef]
29. Herwig-Carl, M.C.; Sharma, A.; Höller, T.; Holz, F.G.; Schlitter, A.M.; Loeffler, K.U. Spatial intratumor heterogeneity in uveal melanoma: Tumor cell subtypes with a presumed invasive potential exhibit a particular epigenetic staining reaction. *Exp. Eye Res.* **2019**, *182*, 175–181. [CrossRef]
30. Durante, M.A.; Rodriguez, D.A.; Kurtenbach, S.; Kuznetsov, J.N.; Sanchez, M.I.; Decatur, C.L.; Snyder, H.; Feun, L.G.; Livingstone, A.S.; Harbour, J.W. Single-cell analysis reveals new evolutionary complexity in uveal melanoma. *Nat. Commun.* **2020**, *11*, 496. [CrossRef]
31. Karlsson, J.; Nilsson, L.M.; Mitra, S.; Alsén, S.; Shelke, G.V.; Sah, V.R.; Forsberg, E.M.V.; Stierner, U.; All-Eriksson, C.; Einarsdottir, B.; et al. Molecular profiling of driver events in metastatic uveal melanoma. *Nat. Commun.* **2020**, *11*, 1894. [CrossRef]
32. Pandiani, C.; Strub, T.; Nottet, N.; Cheli, Y.; Gambi, G.; Bille, K.; Husser, C.; Dalmasso, M.; Béranger, G.; Lassalle, S.; et al. Single-cell RNA sequencing reveals intratumoral heterogeneity in primary uveal melanomas and identifies HES6 as a driver of the metastatic disease. *Cell Death Differ.* **2021**, *28*, 1990–2000. [CrossRef] [PubMed]
33. Rosa, R.; Green, R. Eye. In *Surgical Pathology Dissection: An Illustrated Guide*; Westra, W., Hubran, R., Phelps, T., Isacson, C., Eds.; Springer: New York, NY, USA, 2003; pp. 194–200.
34. Amin, M.B.; Greene, F.L.; Edge, S.B.; Compton, C.C.; Gershenwald, J.E.; Brookland, R.K.; Meyer, L.; Gress, D.M.; Byrd, D.R.; Winchester, D.P. The eighth edition AJCC cancer staging manual: Continuing to build a bridge from a population-based to a more "personalized" approach to cancer staging. *CA Cancer J. Clin.* **2017**, *67*, 93–99. [CrossRef] [PubMed]
35. Conlin, L.K.; Thiel, B.D.; Bonnemann, C.G.; Medne, L.; Ernst, L.M.; Zackai, E.H.; Deardorff, M.A.; Krantz, I.D.; Hakonarson, H.; Spinner, N.B. Mechanisms of mosaicism, chimerism and uniparental disomy identified by single nucleotide polymorphism array analysis. *Hum. Mol. Genet.* **2010**, *19*, 1263–1275. [CrossRef] [PubMed]
36. Li, M.M.; Datto, M.; Duncavage, E.J.; Kulkarni, S.; Lindeman, N.I.; Roy, S.; Tsimberidou, A.M.; Vnencak-Jones, C.L.; Wolff, D.J.; Younes, A.; et al. Standards and Guidelines for the Interpretation and Reporting of Sequence Variants in Cancer: A Joint Consensus Recommendation of the Association for Molecular Pathology, American Society of Clinical Oncology, and College of American Pathologists. *J. Mol. Diagn.* **2017**, *19*, 4–23. [CrossRef]
37. Hanahan, D.; Weinberg, R.A. Hallmarks of cancer: The next generation. *Cell* **2011**, *144*, 646–674. [CrossRef]
38. Toomey, C.B.; Protopsaltis, N.J.; Phou, S.; Bakhoum, M.F.; Thorson, J.A.; Ediriwickrema, L.S.; Korn, B.S.; Kikkawa, D.O.; Goldbaum, M.H.; Lin, J.H. Prevalence of mismatch repair gene mutations in uveal melanoma. *Retina* **2020**, *40*, 2216–2220. [CrossRef]
39. Johansson, P.; Aoude, L.G.; Wadt, K.; Glasson, W.J.; Warrier, S.K.; Hewitt, A.W.; Kiilgaard, J.F.; Heegaard, S.; Isaacs, T.; Franchina, M.; et al. Deep sequencing of uveal melanoma identifies a recurrent mutation in PLCB4. *Oncotarget* **2016**, *7*, 4624–4631. [CrossRef]
40. de Lange, M.J.; van Pelt, S.I.; Versluis, M.; Jordanova, E.S.; Kroes, W.G.; Ruivenkamp, C.; van der Burg, S.H.; Luyten, G.P.; van Hall, T.; Jager, M.J.; et al. Heterogeneity revealed by integrated genomic analysis uncovers a molecular switch in malignant uveal melanoma. *Oncotarget* **2015**, *6*, 37824. [CrossRef]
41. Shain, A.H.; Bagger, M.M.; Yu, R.; Chang, D.; Liu, S.; Vemula, S.; Weier, J.F.; Wadt, K.; Heegaard, S.; Bastian, B.C.; et al. The genetic evolution of metastatic uveal melanoma. *Nat. Genet.* **2019**, *51*, 1123–1130. [CrossRef]
42. de Lange, M.J.; Nell, R.J.; van der Velden, P.A. Scientific and clinical implications of genetic and cellular heterogeneity in uveal melanoma. *Mol. Biomed.* **2021**, *2*, 25. [CrossRef]
43. Ou, S.H.; Kwak, E.L.; Siwak-Tapp, C.; Dy, J.; Bergethon, K.; Clark, J.W.; Camidge, D.R.; Solomon, B.J.; Maki, R.G.; Bang, Y.J.; et al. Activity of crizotinib (PF02341066), a dual mesenchymal-epithelial transition (MET) and anaplastic lymphoma kinase (ALK) inhibitor, in a non-small cell lung cancer patient with de novo MET amplification. *J. Thorac. Oncol.* **2011**, *6*, 942–946. [CrossRef] [PubMed]
44. Frampton, G.M.; Ali, S.M.; Rosenzweig, M.; Chmielecki, J.; Lu, X.; Bauer, T.M.; Akimov, M.; Bufill, J.A.; Lee, C.; Jentz, D.; et al. Activation of MET via diverse exon 14 splicing alterations occurs in multiple tumor types and confers clinical sensitivity to MET inhibitors. *Cancer Discov.* **2015**, *5*, 850–859. [CrossRef] [PubMed]
45. Paik, P.K.; Drilon, A.; Fan, P.-D.; Yu, H.; Rekhtman, N.; Ginsberg, M.S.; Borsu, L.; Schultz, N.; Berger, M.F.; Rudin, C.M.; et al. Response to MET inhibitors in patients with stage IV lung adenocarcinomas harboring MET mutations causing exon 14 skipping. *Cancer Discov.* **2015**, *5*, 842–849. [CrossRef]
46. Awad, M.M.; Oxnard, G.R.; Jackman, D.M.; Savukoski, D.O.; Hall, D.; Shivdasani, P.; Heng, J.C.; Dahlberg, S.E.; Jänne, P.A.; Verma, S.; et al. MET exon 14 mutations in non-small-cell lung cancer are associated with advanced age and stage-dependent MET genomic amplification and c-Met overexpression. *J. Clin. Oncol.* **2016**, *34*, 721–730. [CrossRef] [PubMed]
47. Pilotto, S.; Gkountakos, A.; Carbognin, L.; Scarpa, A.; Tortora, G.; Bria, E. MET exon 14 juxtamembrane splicing mutations: Clinical and therapeutical perspectives for cancer therapy. *Ann. Transl. Med.* **2017**, *5*, 2. [CrossRef]
48. Johansson, P.A.; Brooks, K.; Newell, F.; Palmer, J.M.; Wilmott, J.S.; Pritchard, A.L.; Broit, N.; Wood, S.; Carlino, M.S.; Leonard, C.; et al. Whole genome landscapes of uveal melanoma show an ultraviolet radiation signature in iris tumours. *Nat. Commun.* **2020**, *11*, 2408. [CrossRef]
49. Hearle, N.; Damato, B.E.; Humphreys, J.; Wixey, J.; Green, H.; Stone, J.; Easton, D.F.; Houlston, R.S. Contribution of germline mutations in BRCA2, P16(INK4A), P14(ARF) and P15 to uveal melanoma. *Investig. Ophthalmol. Vis. Sci.* **2003**, *44*, 458–462. [CrossRef]

50. Easton, D.F.; Steele, L.; Fields, P.; Ormiston, W.; Averill, D.; Daly, P.A.; McManus, R.; Neuhausen, S.L.; Ford, D.; Wooster, R.; et al. Cancer risks in two large breast cancer families linked to BRCA2 on chromosome 13q12-13. *Am. J. Hum. Genet.* **1997**, *61*, 120–128. [CrossRef]
51. Houlston, R.S.; Damato, B.E. Genetic predisposition to ocular melanoma. *Eye* **1999**, *13*, 43–46. [CrossRef]

Disclaimer/Publisher's Note: The statements, opinions and data contained in all publications are solely those of the individual author(s) and contributor(s) and not of MDPI and/or the editor(s). MDPI and/or the editor(s) disclaim responsibility for any injury to people or property resulting from any ideas, methods, instructions or products referred to in the content.

cancers

MDPI

Article

Long-Term Clinical Outcomes for Adolescent and Young-Adult Uveal Melanoma Patients Treated with Dedicated Particle-Beam Radiation †

Carly Zako [1], Arina Nisanova [1,2], Vivian Weinberg [1], Jessica Scholey [1], Carisa Swason [3], Armin R. Afshar [4], Jeanne Quivey [1], Inder K. Daftari [1], Tony Tsai [5], Susanna S. Park [2], Michael Seider [6], Robert N. Johnson [7], Devron H. Char [3] and Kavita K. Mishra [1,*]

[1] Department of Radiation Oncology, University of California San Francisco, San Francisco, CA 94115, USA
[2] Department of Ophthalmology & Vision Science, University of California Davis, Sacramento, CA 95817, USA
[3] Tumori Foundation, San Francisco, CA 94114, USA
[4] Ocular Oncology Service, Department of Ophthalmology, University of California San Francisco, San Francisco, CA 94115, USA
[5] Retinal Consultants Medical Group, Sacramento, CA 95825, USA
[6] Department of Ophthalmology Kaiser Permanente Medical Center, Los Angeles, CA 90027, USA
[7] West Coast Retina Medical Group, San Francisco, CA 94109, USA
* Correspondence: kavita.mishra@ucsf.edu
† This article is a revised and expanded version of a paper entitled "Long Term Clinical Outcomes with Dedicated Proton Ocular Beam and Helium Ion Radiation for Uveal Melanoma Patients Aged 45 and Younger", which was presented at the 2021 American Society for Radiation Oncology Meeting in Chicago, IL, USA, 24–27 October 2021.

Simple Summary: Uveal melanoma (UM) is a rare eye cancer, especially in adolescent and young-adult patients (AYAs), and it can significantly impact vision, quality of life, and survival. This study examines the long-term clinical outcomes of AYA UM patients (aged 13 to 45) treated with proton-beam (PBRT) and helium-ion radiation. We aim to determine the effectiveness of these treatments by measuring clinical outcomes, including local control, eye preservation, distant metastasis (DM), and overall survival. The results confirm excellent long-term local control and eye preservation (15 years: 94% PBRT and 99% Helium cohort) and demonstrate better DM-free and overall survival rates at 15 years in AYAs than older UM patients.

Abstract: Background: Limited long-term data exist regarding post-particle-beam radiation (RT) for adolescents and young adults (AYA) with uveal melanoma (UM), and hence an in-depth analysis of clinical outcomes is presented. **Methods:** We identified AYA patients with UM (aged 13 to 45) treated with proton-beam radiation (PBRT, dose 56 GyE, $n = 240$) and helium-ion RT (median dose 70 GyE, $n = 78$). Patients were analyzed for local control (LC), eye preservation, distant metastasis (DM), and overall survival (OS) with univariate and multivariate analysis. **Results:** For the PBRT cohort, the median age and follow-up were 38.3 years (13.3–45.9) and 85.7 months (3–301), respectively. The 15-year (y) LC rate was 94%. Ciliary body (CB) tumors showed lower LC ($p = 0.01$). Largest tumor diameter (LTD) was the only independent predictor of LC (hazard ratio (HR) = 1.19, $p = 0.017$)). The 10-year eye preservation was 83%. Improved eye preservation was noted with a $\leq$50% dose delivered to the lens ($p = 0.004$), disc ($p = 0.001$), and nerve ($p = 0.0004$), and <20% of CB volume ($p = 0.0002$). Decreased tumor height (HR = 1.12, 95% CI: 1.01–1.2, $p = 0.036$), dose < 20% to CB (HR = 1.04, 95% CI: 1.01–1.06, $p = 0.0002$), and tumor–disc distance > 2 mm (HR = 0.27, $p = 0.0003$) were independent predictors of eye preservation. The 15-year DM-free rate was 73%, and the 15-year OS rate was 76%. The T category was the most significant predictor of DM ($p < 0.0001$), followed by LTD ($p = 0.04$). For the

Helium cohort, median age and follow-up were 37.1 years (18.1–45.5) and 256.7 months (24–450), respectively. The Helium cohort 15-year LC was 99%, with 82% 10-year eye preservation. The 15-year DM-free and OS rates for Helium patients were both 83%. **Conclusions:** Excellent long-term LC and eye preservation can be seen in AYA UM patients treated with proton and helium-ion radiation. AYAs with UM appear to have better DM-free and overall survival rates than older patients with UM. Specific clinical and dose–volume parameters can help improve treatment planning and prognosis for younger patients with UM.

Keywords: uveal melanoma; UM; proton-beam radiation therapy; PBRT; helium-ion radiation; local control; LC; outcomes; adolescent and young adult; AYA

1. Introduction

Uveal melanoma (UM) is a rare tumor and a challenging diagnosis for adolescent and young-adult (AYA) patients, as it can threaten vision, quality of life, and life expectancy. Radiation therapy (RT) with charged particles, including proton (PBRT), helium, and carbon ion therapy, as well as plaque brachytherapy and stereotactic photon techniques, is the standard of care for UM [1]. Particle-beam radiotherapy with dedicated ocular beamlines is associated with excellent local tumor control and eye preservation due to the uniform dose distribution, minimal scatter, and sharp dose fall-off near critical structures [1]. Survival rates post-radiotherapy are similar to those observed with enucleation [2]. However, limited long-term data exist post-particle-beam radiation specifically for AYA UM patients, with few studies detailing clinical characteristics in younger individuals [3–8].

UM is the most common primary intraocular tumor in adults, occurring in older Caucasian individuals between 60 and 79 years of age [5,9,10]. The annual incidence is estimated at 5–9 new cases per million persons in the US and Europe [11]. Uveal melanoma is rare in younger populations, with children and teenagers representing approximately 1% of all cases [12,13]. The annual incidence of UM increases with age per million population: from 0.2 for ages 10–14 to 1.0 for ages 20–24, 3.4 for ages 30–34, and 6.3 for ages 40–44 [14]. The rates jump significantly thereafter to 17 for ages 50–54, 26.6 for ages 60–64, and 42.3 for ages 70–74 [14]. Across the cancer continuum, there is an increasing awareness of the differences in medical, psychological, and social needs and challenges for younger-aged cancer patients and the gaps in knowledge regarding AYA oncology [15,16]. The AYA age cutoffs vary from 24 to 50 years for "young adults" in different cancer studies [15,17,18]. For these reasons, the AYA cutoff in our cohort was set at 45 years old.

Previous UM reports studying children and teenagers found similar outcomes to older cohorts, though metastatic prognosis is improved for very young patients (<16–20 years) [4,6,10,12,19,20]. A study of 8033 eyes with UM found smaller tumor dimensions and lower tumor-related metastasis rates at 10 years in patients under 20 years old (9%) than those aged 21–60 (23%) and over 60 years old (28%) [10]. An examination of 43 patients aged <21 revealed superior metastatic control and survival rates compared to matched adult counterparts (n = 129), with comparable responses in eye retention and preservation of functional vision observed in both age groups [3]. One recent study with proton therapy for patients 15–39 years old and matched adults over 40 years of age reported that local tumor control, metastasis incidence, and overall survival were similar in both groups [11].

The aim of this analysis was to report long-term clinical outcomes and patient-tumor-planning characteristics for adolescent and young-adult UM patients aged 13 to 45 years undergoing particle-beam treatment, to better inform patients and clinical teams. To our

knowledge, this report is among the few long-term studies of post-proton treatment and is the first study of helium ion to focus on this younger UM age group.

2. Materials and Methods

2.1. Patient Population

Patients were identified in a single institution's prospectively maintained database (n = 2558) of eye treatment with proton-beam radiation (PBRT, 1994–2020) and helium-ion RT (He^+, 1979–1992). All included patients were treated for non-metastatic UM. The exclusion criteria included age below 13 or above 45 at the time of RT, subtherapeutic RT dose, and patients treated with post-local eyewall resection or salvage RT. AYA patients were aged 13 to 45 years (i.e., not yet turned 46 years of age) at the time of radiation, resulting in 78 helium-ion RT and 247 PBRT patients evaluable for statistical analyses.

All patients received standard comprehensive uveal melanoma evaluation, detailed in the prior literature [21–24]. All PBRT patients (n = 240) included in the analysis were treated with our current standard protocol of 56 gray equivalent (GyE; proton relative biological effectiveness, RBE = 1.1) in 4 fractions over 4 days. Median dose for He^+ ion RT was 70 GyE in 5 fractions (range, 48–80 GyE, RBE = 1.3). Patients were followed post-treatment in a standardized manner, including complete clinical evaluation, fundus photographs, and ultrasonography post-RT at approximately 3 months, 6 months, and then yearly, on average. We conducted a retrospective review of the patients' medical records to document treatment outcomes, survival, and complications between August 2020 and August 2021. This study was performed in accordance with the Declaration of Helsinki and with the University of California, San Francisco's Institutional Review Board's approval.

2.2. Radiation Technique

The tumor base and spatial coordinates were outlined by tantalum markers placed intraoperatively at 4 scleral points. The spatial coordinates were obtained from 2 orthogonal X-ray films. Treatment utilized a customized facemask and dental bite block or chin rest for immobilization. EYEPLAN® software (v3.06, Clatterbridge, UK) was used for treatment planning, including eye and tumor modeling, gaze angle optimization, aperture design, beam parameter delineation, dose–volume histogram (DVH) analysis, marker alignment, and daily treatment positioning.

A 2.5–3 mm lateral aperture perimeter was placed around the tumor projection in the beam's-eye view, representing the 50% isodose line. This aperture margin accounts for possible microscopic tumor extension, minor patient setup error or movement, and beam penumbra. The distal margin on the tumor range was 3–4 mm, per standard protocol.

To reduce dose delivery to critical structures, modifications, including adjusting the gaze angle to minimize dose to the lens, ciliary body (CB), optic disc, and/or macula, were made when safe and clinically appropriate. The aperture margin at the lens, macula, or disc was focally reduced to 2 mm to reduce the critical-structure dose in certain cases. Similarly, the distal margin was reduced to 2–2.5 mm in particular cases to reduce the dose to the disc, macula, or nerve.

The eye position was monitored throughout the treatment to ensure proper alignment via a closed-circuit television camera system. Custom eyelid retractors helped withdraw the eyelids from the beam path as much as possible. If a significant amount of eyelid remained in the field, then the distal range was adjusted accordingly to compensate for the additional tissue exposure. All patients were treated with a single anterior port using a 67.5-MeV horizontal proton beam generated by a 76-inch isochronous cyclotron or a helium 184″ beam.

2.3. Statistical Analysis

For each cohort, descriptive statistics were tabulated to characterize patient, tumor, and outcome features. Patient data included age, sex, eye involved, date of treatment, and co-existing medical issues. Tumor size and location were recorded along with the treatment details, such as radiation dose, fractionation, and duration of follow-up.

Clinical outcomes included local control (LC), eye preservation, distant metastasis (DM), and overall survival (OS) recorded post-RT. Durations were calculated from the date of the start of RT until the date of recurrence for local and distant disease, the date of enucleation, and the date of death due to any cause for OS. If the endpoint did not occur, the duration was censored on the date of the last available contact. The probability of LC, ocular retention, being free of DM, and OS were estimated and graphically displayed using the Kaplan–Meier product limit method [25]. Local control is defined as remaining free of local failure post-RT and was recorded when tumor growth (base or thickness) was detected post-RT by clinical examination, A-scan or B-scan ultrasonography, ultrasound biomicroscopy, or serial comparison of fundus photographs and fluorescein angiograms. For patients who had the UM eye enucleated, we recorded the reason for enucleation. Metastatic disease was recorded through clinical and histopathologic examination at the metastatic site. All reported DMs were confirmed to be of UM origin. Overall survival was defined as not dying due to any cause.

A chi-square test was used to evaluate the association between categorical variables, analysis of variance (ANOVA) methods were used to compare subsets for continuous variables, and Pearson's correlation was calculated to evaluate the relationship between continuous variables. Univariate analyses for time-to-failure outcomes were performed using the log-rank test for categorical variables and Cox's proportional hazard model using the likelihood ratio (LLR) test for continuous variables. Variables evaluated included gender, age, right/left eye, tumor location, height, largest tumor diameter (LTD), tumor T category, distances to disc and fovea, CB involvement, and dose–volume relationships for the lens, CB, macula, disc, and optic nerve. Multivariate analyses using Cox's proportional hazard model identified independent predictors of each clinical outcome using a forward stepwise approach with a probability of 0.05 to enter the model and 0.10 to be removed. Only variables not significantly related to each other were considered as predictors in a single analysis, with the model LLR test determining the best fit. Results were summarized by the hazard ratio (HR) and 95% confidence interval (CI) for each predictor in the model. For all analyses, a probability of <0.05 was considered to be statistically significant. Analyses were performed using Stata (v12.1 StatCorp, College Station, TX, USA) and Statistica (v12, StatSoft, Inc., Tulsa, OK, USA) Graphs were generated using Statistica statistical software.

3. Results

3.1. AYA UM Proton Patient and Tumor Characteristics

The final PBRT cohort included 240 patients treated with 56 GyE in four fractions. Of 247 PBRT patients meeting inclusion criteria, 7 early patients treated between 1994 and 1995 were excluded from the analysis due to the lower RT dose (48 GyE in four fractions). The patient and tumor features of the UM PBRT cohort are shown in Table 1. The median follow-up was 85.7 months (range, 3–301 months). Of the 240 patients, 47.5% were male, and 55% of tumors affected the left eye. The median age at RT was 38.3 years (13.3–45.9), the median tumor height was 4.5 mm (0.8–15.8), and the median LTD was 10.5 mm (2.3–25.1).

Of the 240 patients, 119 (49.6%) had an FNA biopsy at the time of initial treatment. Of the accessible pathology results (n = 98), 68 (69.4% of 98) were confirmed as spindle cell/low-grade, 21 (21.9%) had epithelioid features, and 9 (9.2%) had mixed-cell features. Of the specific gene expression profiling (GEP) results available (n = 64),

38 (59.4% of 64) patients had class 1A tumors, 12 (18.8%) had type 1B, and 14 (21.9%) had type 2 tumors. Next-generation sequencing for 13 patients showed that the specific somatic genetic mutations were most commonly GNAQ (n = 6), SF3B1 (n = 5), EIF1AX (n = 3), and GNA11 (n = 3). Three pathogenic germline mutations were identified in two patients and included CDH1 (n = 1), PABL2 (n = 1), and NF1 (n = 1).

Table 1. Features of uveal melanoma (UM) and characteristics of adolescents and young adults (age 13 to 45) with UM treated with proton-beam radiation therapy (n = 240).

	Median	**Range**
Follow-Up (months)	85.7	3–301
Age at RT (years)	38.3	13.3–45.9
Tumor Height (mm)	4.5	0.8–15.8
Largest Tumor Diameter (mm)	10.5	2.3–25.1
Tumor Distance to Disc (mm)	3.2	0–24.0
Tumor Distance to Fovea (mm)	2.0	0–24.0
%Tumor 0–2 mm of Disc	41%	
%Tumor 0–2 mm of Fovea	52%	
%Ciliary Body Tumors	11%	

Abbreviations: GyE = gray equivalent; RT = radiation therapy.

The primary tumor location was 87% choroidal, 12% ciliary body, and 1% iris only. Patients with ciliary body tumors were more likely to have higher category tumors ($p < 0.001$); choroidal tumors had a significantly shorter tumor height and LTD than ciliary body tumors ($p = 0.02$ for each). Of patients with ciliary body tumors (n = 20), 65% were over 40 years of age at RT ($p = 0.015$).

The LTD was significantly correlated with the tumor height (r = 0.66, $p < 0.001$). The median tumor distances to the fovea and disc were 2.0 mm and 3.2 mm, respectively, with 52% of tumors within 0–2 mm of the fovea and 41% within 0–2 mm of the disc. There was no relationship between age and any of the distances or dimensions. Table 2 shows the comparison of tumor dimensions by age.

Table 2. Comparison of tumor dimensions in the proton-beam radiation therapy (PBRT) and helium-ion RT cohorts by age: mean (SD).

PBRT	**≤30 n = 46**	**>30–35 n = 43**	**>35–40 n = 59**	**>40–45 n = 92**	**ANOVA Probability Value**
Height	5.5 (3.2)	5.3 (2.5)	4.6 (2.4)	5.5 (3.1)	$p = 0.24$
Max Diameter	11.4 (4.6)	10.3 (2.9)	10.4 (3.7)	11.0 (3.9)	$p = 0.41$
Helium-Ion RT	**≤30 n = 14**	**>30–35 n = 19**	**>35–40 n = 18**	**>40–45 n = 27**	**Kruskal–Wallis Probability Value**
Height	5.5 (3.2)	5.3 (2.5)	4.6 (2.4)	5.5 (3.1)	$p = 0.30$
Max Diameter	11.4 (4.6)	10.3 (2.9)	10.4 (3.7)	11.0 (3.9)	$p = 0.74$

Abbreviations: ANOVA = analysis of variance, SD = standard deviation.

3.2. Local Control PBRT

Figure 1 shows post-radiation Kaplan–Meier LC estimates for proton-irradiated AYA patients at RT. In total, 11 patients had a local recurrence (LR) in the PBRT cohort, with a 5-year LC of 96% (92–98%), 10-year LC of 95% (95% CI: 91–98%), and 15-year LC of 94% (95% CI: 87–97%).

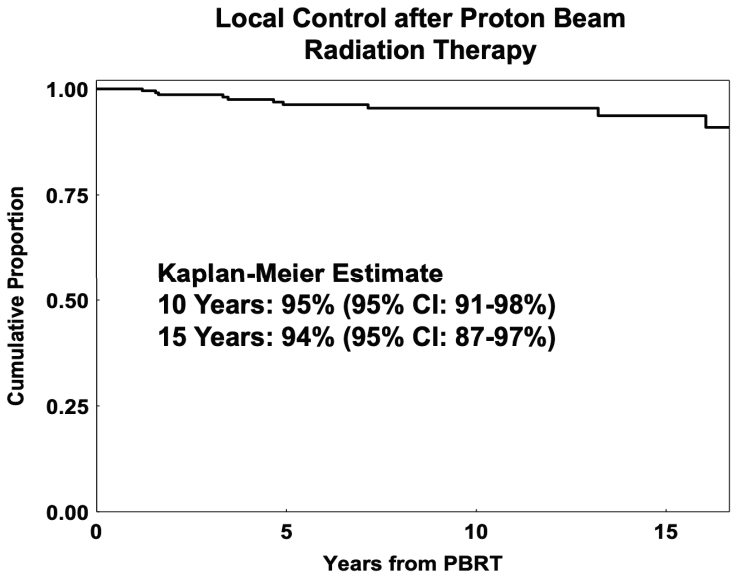


Figure 1. Kaplan–Meier estimates of local control for young-adult and adolescent (age 13 to 45) uveal melanoma patients treated with proton beam radiation therapy (PBRT).

With the univariate analysis, patients with ciliary body tumors alone showed a lower LC ($p = 0.01$) than those with choroidal tumors. Patients with tumors closer to the fovea (0–2 mm vs. >2 mm) had better local control ($p = 0.02$). As a continuous variable, increasing LTD was associated with an increased likelihood of local recurrence ($p = 0.017$).

In the multivariate analysis, LTD was the only independent predictor of LC, with greater LTD having lower LC (HR = 1.19, 95% CI: 1.04–1.36, $p = 0.017$). For patients with no iris involvement ($n = 229$), tumors closer to the fovea ($\leq$2 mm vs. $\geq$2 mm) had better local control (HR = 5.53, 95% CI: 1.19–25.65; $p = 0.01$). The PBRT cohort had limited late failures, with three patients having very late local failures at 13.2, 16.1, and 17.5 years, with all three tumors showing spindle-cell cytology on biopsy (one at initial diagnosis and two at recurrence).

3.3. Eye Preservation in PBRT

The 5-year and 10-year eye preservation in the PBRT cohort was 85% (95% CI: 79–89%) and 83% (95% CI: 77–88%), respectively. Table 3 summarizes the variables predicting improved eye preservation. In total, 84% of all enucleations (31 out of 37) occurred within five years post-PBRT. Specifically, the time to enucleation after proton therapy ranged from 0.3 to 17.7 years, with 16 patients undergoing enucleation within two years of RT, 31 patients within five years of RT, and 6 patients after five years of RT. The reasons for enucleation included painful eye in 24 (65%) patients, frequently secondary to neovascular glaucoma, and local recurrence in 10 (27%) eyes. One eye (3%) was enucleated due to presumed LR, but there was no evidence of LR on pathologic examination. The reason for enucleation was unknown in 2 eyes (5%), but there was no evidence of LR in either eye.

Based on the American Joint Committee on Cancer classification [26], the UM T-categories were 95 T1 (39.6%), 89 T2 (37.1%), 46 T3 (19.2%), and 10 T4 (4.2%). Patients with category T1–T2 tumors showed better eye preservation than those with category T3–T4 ($p = 0.002$). Patients with increased tumor-to-disc distance (0–2 vs. >2 mm) had better eye preservation ($p = 0.0007$). Univariately, decreased enucleation was predicted by decreased tumor height (HR = 1.21, 95% CI: 1.10–1.33; $p = 0.0003$) and increased tumor–disc distance (HR = 0.32, 95% CI: 0.16–0.65; $p = 0.0008$), as shown in Table 3. Improved eye preservation was also observed with certain tissue dose parameters (Table 3), including $\leq$50% dose to the lens ($p = 0.004$), disc ($p = 0.001$), nerve length ($p = 0.0004$), macula ($p = 0.06$), and

<20% CB volume (p = 0.0002) (LLR tests). Figure 2 shows eye preservation by distance to disc.

Table 3. Variables predicting improved eye preservation for adolescent and young-adult (age 13 to 45) patients with uveal melanoma (UM) treated with proton-beam radiation therapy.

Significant Univariate Predictors	Hazard Ratio (95% CI)	LLR Test Probability Value
↓ Tumor Height	1.21 (1.10–1.33)	0.0003
↑ Tumor–Disc Distance (≤2 vs. >2 mm)	0.32 (0.16–0.65)	0.0008
↓ Dose to:		
≤50% Nerve	1.17 (1.07–1.26)	0.0004
≤ 50% Lens	1.02 (1.01–1.03)	0.004
≤50% Disc	1.01 (1.004–1.02)	0.001
≤20% Ciliary Body	1.04 (1.02–1.06)	0.0002
Multivariate Independent Predictors		
↓ Tumor Height	1.12 (1.01–1.25)	0.036
↓ ≤20% Dose to Ciliary Body	1.04 (1.01–1.06)	0.0002
↑ Tumor–Disc Distance (≤2 vs. >2 mm)	0.27 (0.13–0.54)	0.0003

Abbreviations: CI = confidence interval; LLR = likelihood ratio, ↑ = increasing, ↓ = decreasing

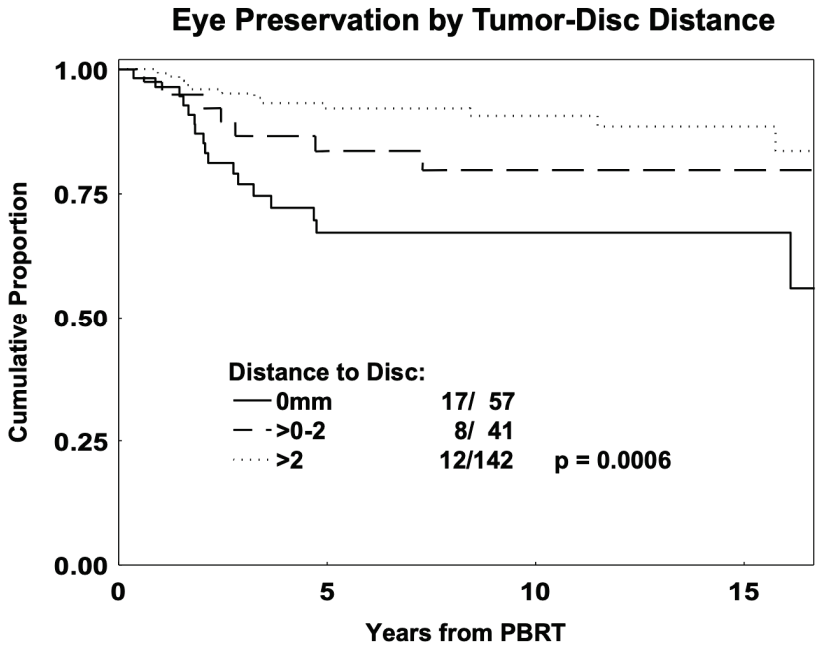


Figure 2. Kaplan–Meier estimates of eye preservation by tumor–disc distance for young-adult and adolescent (age 13 to 45) patients with uveal melanoma (n = 240) treated with proton-beam radiation therapy (PBRT).

Using multivariate methods (Table 3), decreased tumor height (HR = 1.12, 95% CI: 1.01–1.2, p = 0.036), decreased dose to 20% to the ciliary body (HR = 1.04, 95% CI: 1.01–1.06, p = 0.0002), and tumor distance to disc > 2 mm (HR = 0.27, 95% CI: 0.13–0.54, p = 0.0003) were independent predictors of eye preservation. For patients without iris involvement, decreased dose to 20% to the ciliary body (p = 0.0001) and distance to the disc > 2 mm (p = 0.0008) were independent predictors of eye preservation.

3.4. Distant Metastasis and Overall Survival

The 5-, 10-, and 15-year DM-free rates in the PBRT cohort were 87% (95% CI: 82–91%), 81% (95% CI: 74–86%), and 73% (95% CI: 64–80%), respectively. The 5-, 10-, and 15-year OS rates were 90% (95% CI: 85–94%), 84% (95% CI: 78–89%), and 76% (95% CI: 67–83%). Of the 240 patients at the time of the last available follow-up during the study, 189 were alive without recurrence, 6 were alive after LR, 6 were alive after DM, 2 were alive after LR and DM, 3 died without any recurrence, 3 died after LR and DM, and 31 died after DM.

Univariate analysis indicated that patients with T1 tumors had better overall survival than those with category T2–T4 UMs ($p = 0.0006$). Patients with early-category tumors also had decreased DM ($p < 0.001$). Patients with choroidal tumors had better overall survival ($p = 0.037$) and decreased risk of DM ($p = 0.02$) than those with ciliary body tumors without iris involvement. None of the 11 patients with tumors invading the iris (8 with CB involvement and 3 with iris alone) died or had DM recurrence. The median OS for these patients was 83 months (range, 5 to 215). Patients with tumors closer to the fovea (0–2 mm vs. >2 mm) had better overall survival ($p = 0.007$) and decreased DM ($p = 0.01$). Increased LTD was associated with decreased overall survival (HR = 1.15, 95% CI: 1.07–1.24; $p = 0.0006$) and decreased DM control (HR = 1.17, 95% CI: 1.09–1.25; $p < 0.0001$). Figure 3 shows the proportion of patients free of DM by LTD.

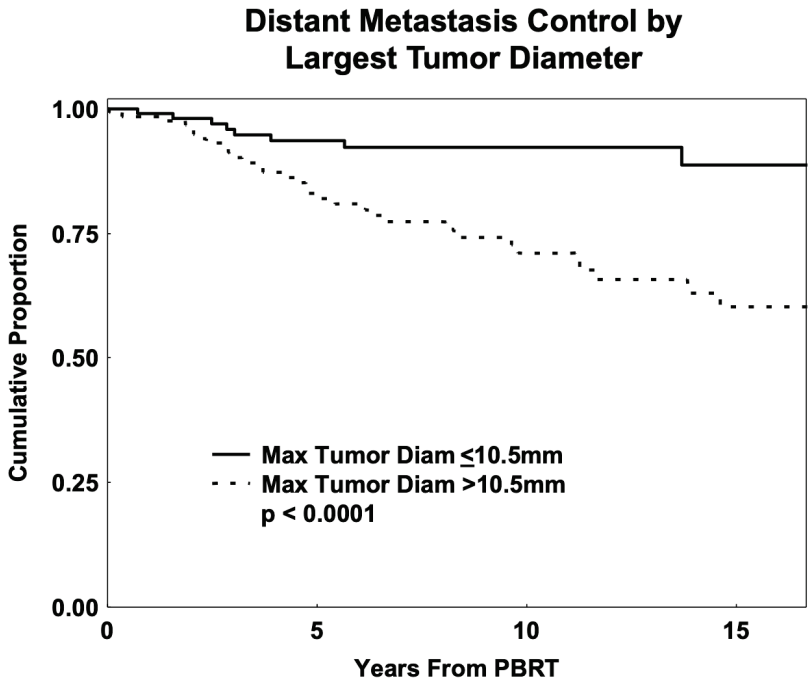


Figure 3. Kaplan–Meier estimates of distant metastasis control by largest tumor diameter for young-adult and adolescent (age 13 to 45) patients with uveal melanoma ($n = 240$) treated with proton-beam radiation therapy (PBRT).

The most significant predictor of overall survival was T category, with patients with T1-category tumors having better overall survival compared to those with T2, T3, and T4 tumors combined (HR = 4.04, 95% CI: 1.69–9.70; $p = 0.0003$). T category was also the most significant predictor of DM ($p = 0.0001$), with T1-category tumors having better DM control compared with category T2–T4 (HR = 3.65, 95% CI: 1.28–10.40; $p < 0.0001$) followed by better DM control with a decreased LTD (HR = 1.09, 95% CI: 1.01–1.20, $p = 0.04$). The age ≤ 30 subgroup ($n = 46$) had a 5-year DM-free rate of 97% and had only 4% CB tumors.

3.5. Helium-Ion RT Cohort

Patient and tumor features for the Helium cohort are summarized in Table 4. In total, 78 patients were treated between 1979 and 1992. There were slightly more female (53%) than male patients (47%), and tumors were found mostly in the left eye (56% left vs. 44% right). The Helium cohort's median follow-up was 256.7 months (24–450). The median age at RT was 37.1 (18.1–45.5), the tumor height was 6.0 mm (2.9–14), the LTD was 10.5 mm (5–25), the distance to disc/fovea was 3.5/3.0 mm, and 22% had tumors with ciliary body involvement. The LTD was larger for ciliary body tumors ($p < 0.0001$) and smaller for tumors near the disc ($p = 0.03$) or fovea ($p < 0.0001$). The median (range) dose for helium RT was 70 GyE (48–80).

The Helium cohort had a 5-, 10-, and 15-year LC of 98.6% (95% CI: 90.3–99.8%) with only one failure at 58.6 months after helium-ion RT. Figure 4 shows the Kaplan–Meier curves for local control after helium-ion RT. The 5- and 10-year eye preservation rates were 84% (95% CI: 74–91%) and 82% (95% CI: 71–89%), respectively. The 5-, 10-, and 15-year estimates of overall survival were 90% (95% CI: 81–95%), 86% (95% CI: 76–92%), and 83% (95% CI: 73–90%), respectively. There were a total of 21 deaths in the Helium cohort; 17 patients died with distant metastases, and 4 died without recurrence or DM. The 5-, 10-, and 15-year estimates of DM-free survival were 87% (95% CI: 77–93%), 85% (95% CI: 74–91%), and 79% (95% CI: 68–87%), respectively.

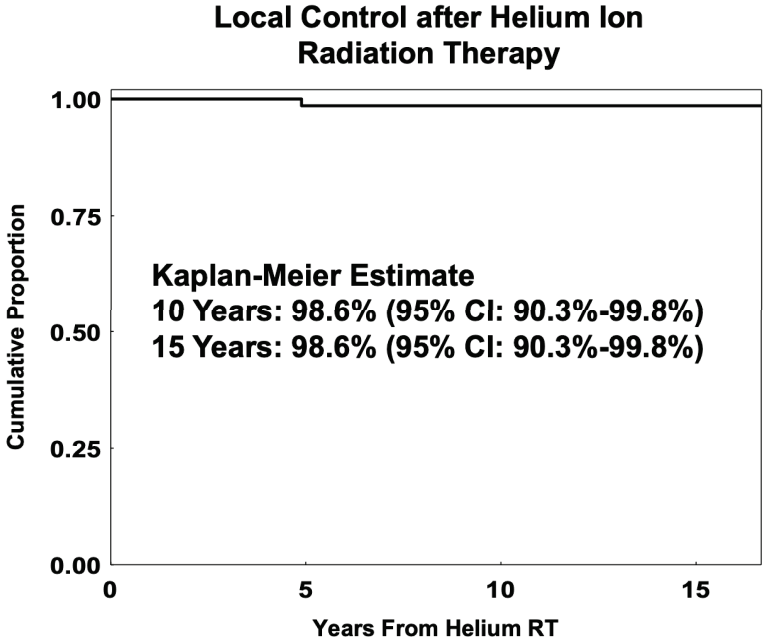


Figure 4. Kaplan–Meier estimates of local control for young-adult and adolescent (age 13 to 45) patients with uveal melanoma ($n = 78$) treated with helium ion radiation therapy (RT).

Table 4. Characteristics of adolescents and young adults (age 13 to 45) with uveal melanoma (UM) treated with helium-ion radiation therapy ($n = 78$) and UM features.

	Median	Range
Follow-Up (months)	256.7	24–450
Age at RT (years)	37.1	18.1–45.5
Median Dose (GyE)	70	48–80
Tumor Height (mm)	6.0	2.9–14.0
Largest Tumor Diameter (mm)	10.5	5.0–25.0
Tumor Distance to Disc (mm)	3.5	0–13.0

Table 4. *Cont.*

	Median	Range
Tumor Distance to Fovea (mm)	3.0	0–10.5
%Tumor 0–2 mm of Disc	33%	
%Tumor 0–2 mm of Fovea	44%	
%Ciliary Body Tumors	22%	

Abbreviations: GyE = gray equivalent; RT = radiation therapy.

4. Discussion

Uveal melanoma presents a rare and challenging diagnosis for adolescents and young adults, considering the potential for dramatic implications on vision, quality of life, and life expectancy [1,9,27,28]. Uveal melanoma typically presents in advanced age, and the unique characteristics and outcomes of younger patients may aid in personalized care for this subset of patients. Limited long-term data exist on post-particle-beam radiation for this age group, though there is increasing awareness of the need to study the cancer course and outcomes in AYAs [3,4,7,11,13]. Additionally, outcomes for AYAs are frequently grouped with a broader adult category, masking unique characteristics of this understudied population [29]. In this work, the study presented at the American Society for Radiation Oncology meeting [30] is expanded upon. Our study adds to this body of work by including a detailed analysis of long-term outcomes for AYAs with UM treated with proton and helium-ion RT. This age group had a more favorable genetic and cytologic UM profile and demonstrated excellent 15-year local control (94% PBRT, 99% helium RT) and higher 15-year overall survival (76% PBRT, 83% helium RT) post-particle RT compared to older UM patients.

Local control was high for proton-irradiated AYA patients, with LC at 95% at 10 years and 94% at 15 years. These results are consistent with the limited current research in young UM populations [3–5,11]. In our population, greater LTD was the most important predictor for lower LC. Ciliary body tumors tended to have a higher T category, larger size, and lower local control in our young patient cohort. The incidence of CB tumors increased with age and was more commonly seen in patients > 40 years of age at RT. For non-iris tumors, those closer to the fovea were smaller and had better LC, OS, and DM control, likely due to earlier detection with visual disturbance. Additionally, considering that T1-category tumors have significantly better OS and DM control, it is imperative to develop risk-assessment tools to identify AYAs at risk of UM and introduce regular screening and earlier intervention to reduce the disease burden in this age group [7,31]. A recent case-control study identified novel risk factors and confirmed established risk factors for AYAs with UM; thus, continued research is critical to delineate particular characteristics of this understudied population [7].

The PBRT dose was consistent at 56 GyE in four fractions, resulting in high local control; however, seven early proton patients not included in the analysis received 48 GyE total in four fractions and had local recurrences. The institutional team had made the empirical clinical adjustment to 56 GyE due to these early failures. At Massachusetts General Hospital (Boston, MA, USA), the standard dose is 70 GyE in five consecutive daily fractions, and small posterior macular tumors may be given 50 GyE in five fractions [32]. A nonrandomized study at Lawrence–Berkeley Laboratory (median follow-up 8.5 years) found that reduction from 80 GyE in five fractions to 48 GyE in four fractions with helium resulted in no LC difference (96%) at 80, 70, 60, or 50 GyE in five fractions [33]. However, LC fell to 87% with 48 GyE in four fractions [33]. If 50 GyE in five fractions is utilized for non-macular tumors at select institutions, the biologic equivalence of 48 GyE/four fractions

and 50 GyE/five fractions may need to be further studied, and local control should be followed long-term for young UM patients [34].

Five- and 10-year eye preservation rates in our PBRT cohort were 85% and 83%, respectively, with most enucleations (84%) occurring in the first 5 years post-PBRT. The average overall enucleation rate for general UM patients is ~10% (range, 0–25%) at 5 years and ~15% at 15 years [35,36]. The most significant factors predicting eye preservation were decreased dose to 20% of the ciliary body, distance to disc > 2 mm, and decreased tumor height. Similarly, dose–volume parameters at the 50% dose level to the nerve/disc have shown an important association with side effects, such as neovascular glaucoma and enucleation [20,21]. Utilizing such parameters can assist in communicating patient prognosis and in treatment planning choices regarding margins and normal tissue-sparing techniques.

The 10-year DM free rate in our PBRT cohort (81%) is consistent with Pica et al.'s proton data showing a similar 10-year DM free rate of 80.3% in patients aged 15–39 [11]. In our cohort, the 10-year OS rate was 84%, reflecting the lower metastatic rate compared to older adults and close follow-up after metastatic diagnosis. Although our group had a lower 10-year OS rate (84%) than reported for the AYAs by Pica et al. (94.6%) [11], the Pica et al. comparative data may have under-reporting of deaths, given that the 10-year metastatic incidence was 19.7%, potentially due to their international population and geographical circumstances [37]. The OS rate was well within the range of other younger UM patient studies post-plaque and proton irradiation (10-year rate of 52–100%), most of which have much smaller cohort sizes [3–6,9–13,15,38].

Analysis showed LTD as a significant predictor for DM, similar to Kaliki et al. [19]. Using multivariate methods, tumor T category was the most significant predictor of DM in our cohort. This was followed by LTD. The age $\leq$ 30 subgroup had a 5-year DM-free rate of 97% and had only 4% CB tumors. Previous UM reports on children and teenagers had found better metastatic prognosis in patients under 16–20 years of age [3,4,10,13,19]. A study of 8033 patients showed smaller tumor dimensions and lower tumor-related metastasis rate at 10 years: 9% (age $\leq$ 20) vs. 23% (age 21–60) vs. 28% (age > 60) [10]. The recent age-matched study (15–39 vs. >40 years) reported that LC, DM, and OS rates were similar [11], in contrast to these prior studies showing improved survival in younger UM series.

The modern workup of uveal melanoma includes FNA biopsy for risk stratification [39–41]. Among the PBRT cohort, approximately half had an FNA biopsy. The majority of UMs in this cohort had spindle-cell cytology, contrary to the cytologic distribution reported for the general UM population, with most tumors generally being of mixed or epithelioid features [42,43]. Epithelioid cytology is an established predictor of poor prognosis [42–44] but was identified in only 21.4% of the tested cohort. Additionally, the majority of the tested patients in our cohort had GEP class 1 tumors, which have a low metastatic risk [44]. These findings suggest that UM in AYAs may have a more favorable cytologic portfolio and, by extension, better prognosis, although for unclear reasons. These results require validation in larger cohorts, and future research may further delineate genetic patterns, risk factors, and potential therapeutic targets to support younger UM patients better.

The Helium cohort had a similar age distribution and tumor dimensions to those of the PBRT group. The group exhibited excellent 15-year LC at 99%, 10-year eye preservation of 82%, and 15-year OS rate of 83%, similar to the PBRT patients. No other similar study exists for younger helium-RT-treated UM patients.

The limitations of this study are the retrospective nature of the report and the lack of an age-adjusted cohort for comparison. The survival estimates may be overestimated

since we relied on the availability of information in the medical records for DM and death reports. However, given the rarity of this disease and the importance of further study in this unique population, the current study provides insight into an important subset of patients. Further work in genetic testing and molecular therapeutic targets needs to be assessed for UM patients, specifically younger patients at risk for metastatic disease.

5. Conclusions

Excellent long-term local control (at 15 years, 94% for PBRT and 99% for Helium cohort) and good eye preservation (at 10 years, 83% for PBRT and 82% for Helium cohort) are seen in AYA UM patients aged 13 to 45 treated with proton and helium-ion radiation. Long-term survival rates were comparable to those reported in multiple other younger cohorts, and adults under 30 demonstrated notably higher DM-free survival. Tumor height, tumor–disc distance, and decreased dose to the ciliary body were independent predictors of eye preservation. Thus, specific clinical and dose–volume parameters may be used to assess patient prognosis, aid in treatment planning, and anticipate secondary complications. LTD and tumor T category were the most important predictors of OS and DM control, underscoring the need for early detection through developing and implementing standardized risk-assessment tools for UM, particularly in AYAs. To our knowledge, this report is one of the few long-term studies focusing on the adolescent and young-adult UM age group post-proton treatment and is the first study of this age group in helium-ion treatment. Results demonstrate particle therapy to be an effective therapy for younger UM patients, and further study into the genetic markers, risk factors, quality of life, and long-term effects of treatment may add to the personalized care of younger patients with uveal melanoma.

Author Contributions: Conceptualization: K.K.M.; data curation: V.W., A.N., I.K.D., C.S. and C.Z.; formal analysis: V.W.; investigation: J.S., T.T., A.R.A., J.Q., I.K.D., T.T., S.S.P., M.S., R.N.J., D.H.C. and K.K.M.; methodology: V.W.; project administration: K.K.M.; resources: K.K.M.; software: V.W.; supervision: K.K.M.; validation: K.K.M.; visualization: K.K.M., V.W. and C.Z.; writing original draft: K.K.M., C.Z. and V.W.; writing—review and editing: K.K.M., V.W., C.Z., J.Q. and A.N. All authors have read and agreed to the published version of the manuscript.

Funding: This research received no external funding.

Institutional Review Board Statement: The study was conducted in accordance with the Declaration of Helsinki and approved by the Institutional Review Board of the University of California, San Francisco (protocol code 11-06194).

Informed Consent Statement: Informed consent was obtained in accordance with the Institutional Review Board regulations for retrospective studies.

Data Availability Statement: Data from this study are available via the corresponding author upon reasonable request.

Conflicts of Interest: Tony Tsai was employed by the Retinal Consultants Medical Group and Robert N. Johnson was employed by the West Coast Retina Medical Group. The remaining authors declare that the research was conducted in the absence of any commercial or financial relationships that could be construed as a potential conflict of interest.

Abbreviations

The following abbreviations are used in this manuscript:

ANOVA	Analysis of variance
AYA	Adolescent and young-adult
CB	Ciliary body
CI	Confidence interval
DM	Distant metastasis
DVH	Dose–volume histogram
GEP	Gene expression profiling
GyE	Gray equivalent
HR	Hazard ratio
LC	Local control
LLR	Likelihood ratio
LR	Local recurrence
LTD	Largest tumor diameter
OS	Overall survival
PBRT	Proton-beam radiation therapy
RBE	Relative biological effectiveness
RT	Radiation therapy
UM	Uveal melanoma

References

1. Mishra, K.K.; Afshar, A.R.; Jessica, S.; Kacperek, A.; Damato, B.E. Ocular Malignancies. In *Principles and Practice of Particle Therapy*; Wiley Online Library: Hoboken, NJ, USA, 2022. Available online: https://onlinelibrary.wiley.com/doi/10.1002/9781119707530.ch14 (accessed on 7 March 2025).
2. Conway, R.M.; Poothullil, A.M.; Daftari, I.K.; Weinberg, V.; Chung, J.E.; O'Brien, J.M. Estimates of Ocular and Visual Retention Following Treatment of Extra-Large Uveal Melanomas by Proton Beam Radiotherapy. *Arch. Ophthalmol.* **2006**, *124*, 838–843. [CrossRef] [PubMed]
3. Petrovic, A.; Bergin, C.; Schalenbourg, A.; Goitein, G.; Zografos, L. Proton Therapy for Uveal Melanoma in 43 Juvenile Patients: Long-Term Results. *Ophthalmology* **2014**, *121*, 898–904. [CrossRef] [PubMed]
4. Rana'a, T.; Cassoux, N.; Desjardins, L.; Damato, B.; Konstantinidis, L.; Coupland, S.E.; Heimann, H.; Petrovic, A.; Zografos, L.; Schalenbourg, A.; et al. The Pediatric Choroidal and Ciliary Body Melanoma Study. *Ophthalmology* **2016**, *123*, 898–907.
5. Pogrzebielski, A.; Orłowska-Heitzman, J.; Romanowska-Dixon, B. Uveal melanoma in young patients. *Graefe's Arch. Clin. Exp. Ophthalmol.* **2006**, *244*, 1646–1649. [CrossRef]
6. Fry, M.V.; Augsburger, J.J.; Hall, J.; Corrêa, Z.M. Posterior uveal melanoma in adolescents and children: Current perspectives. *Clin. Ophthalmol.* **2018**, *12*, 2205–2212. [CrossRef] [PubMed]
7. Nisanova, A.; Park, S.S.; Amin, A.; Zako, C.; Wilson, M.D.; Scholey, J.; Afshar, A.R.; Tsai, T.; Char, D.H.; Mishra, K.K. Novel risk factors for uveal melanoma in adolescent and young adult patients: A comprehensive case-control analysis. *Ophthalmol. Sci.* **2024**, *5*, 100687. [CrossRef]
8. Kornblau, I.; King, B.A.; CERNICHIARO-ESPINOSA, L.A.A.; Wilson, M.W. Clinical characteristics and outcomes in young patients with uveal melanoma from the mid-south United States. *Invest. Ophthalmol. Vis. Sci.* **2023**, *64*, 898.
9. Mishra, K.K.; Quivey, J.M.; Daftari, I.K.; Char, D.H. 64. Uveal Melanoma. In *Leibel and Phillips Textbook of Radiation Oncology*, 3rd ed.; Hoppe, R.T., Phillips, T.L., Roach, M., Eds.; W.B. Saunders: Philadelphia, PA, USA, 2010; pp. 1400–1421. [CrossRef]
10. Shields, C.L.; Kaliki, S.; Furuta, M.; Mashayekhi, A.; Shields, J.A. CLINICAL SPECTRUM AND PROGNOSIS OF UVEAL MELANOMA BASED ON AGE AT PRESENTATION IN 8,033 CASES. *RETINA* **2012**, *32*, 1363. [CrossRef]
11. Pica, A.; Weber, D.C.; Schweizer, C.; Chaouch, A.; Zografos, L.; Schalenbourg, A. Clinical Outcomes in AYAs (Adolescents and Young Adults) Treated with Proton Therapy for Uveal Melanoma: A Comparative Matching Study with Elder Adults. *Cancers* **2023**, *15*, 4652. [CrossRef]
12. Fry, M.V.; Augsburger, J.J.; Corrêa, Z.M. Clinical Features, Metastasis, and Survival in Patients Younger Than 21 Years With Posterior Uveal Melanoma. *JAMA Ophthalmol.* **2019**, *137*, 75–81. [CrossRef]
13. Vavvas, D.; Kim, I.; Lane, A.M.; Chaglassian, A.; Mukai, S.; Gragoudas, E. Posterior Uveal Melanoma in Young Patients Treated with Proton Beam Therapy. *RETINA* **2010**, *30*, 1267. [CrossRef] [PubMed]
14. Singh, A.D.; Topham, A. Incidence of uveal melanoma in the United States: 1973–1997. *Ophthalmology* **2003**, *110*, 956–961. [CrossRef]
15. Aubin, S.; Barr, R.; Rogers, P.; Schacter, B.; Bielack, S.S.; Ferrari, A.; Manchester, R.A.; McMaster, K.; Morgan, S.; Patterson, M. What Should the Age Range Be for AYA Oncology? *J. Adolesc. Young Adult Oncol.* **2011**, *1*, 3–10. [CrossRef]

16. Bhatia, S.; Pappo, A.S.; Acquazzino, M.; Allen-Rhoades, W.A.; Barnett, M.; Borinstein, S.C.; Casey, R.; Choo, S.; Chugh, R.; Dinner, S.; et al. Adolescent and Young Adult (AYA) Oncology, Version 2.2024, NCCN Clinical Practice Guidelines in Oncology. *J. Natl. Compr. Cancer Netw.* **2023**, *21*, 851–880. [CrossRef]
17. Smith, A.W.; Seibel, N.L.; Lewis, D.R.; Albritton, K.H.; Blair, D.G.; Blanke, C.D.; Bleyer, A.W.; Freyer, D.R.; Geiger, A.M.; Hayes-Lattin, B.; et al. Next Steps for Adolescent and Young Adult Oncology Workshop: An Update on Progress and Recommendations for the Future. *Cancer* **2016**, *122*, 988–999. [CrossRef]
18. Adolescent and Young Adult Oncology Progress Review Group. *Closing the Gap: Research and Care Imperatives for Adolescents and Young Adults with Cancer*; NIH Publication No. 06-6067; NIH Publication: Bethesda, MD, USA, 2006.
19. Kaliki, S.; Shields, C.L.; Mashayekhi, A.; Ganesh, A.; Furuta, M.; Shields, J.A. Influence of Age on Prognosis of Young Patients with Uveal Melanoma: A Matched Retrospective Cohort Study. *Eur. J. Ophthalmol.* **2013**, *23*, 208–216. [CrossRef]
20. Mishra, K.K.; Daftari, I.K.; Weinberg, V.; Cole, T.; Quivey, J.M.; Castro, J.R.; Phillips, T.L.; Char, D.H. Risk Factors for Neovascular Glaucoma After Proton Beam Therapy of Uveal Melanoma: A Detailed Analysis of Tumor and Dose–Volume Parameters. *Int. J. Radiat. Oncol.* **2013**, *87*, 330–336. [CrossRef] [PubMed]
21. Polishchuk, A.L.; Mishra, K.K.; Weinberg, V.; Daftari, I.K.; Nguyen, J.M.; Cole, T.B.; Phillips, T.L.; Char, D.H.; Quivey, J.M. Temporal Evolution and Dose-Volume Histogram Predictors of Visual Acuity After Proton Beam Radiation Therapy of Uveal Melanoma. *Int. J. Radiat. Oncol. Biol. Phys.* **2017**, *97*, 91–97. [CrossRef]
22. Mishra, K.K.; Quivey, J.M.; Daftari, I.K.; Weinberg, V.; Cole, T.B.; Patel, K.; Castro, J.R.; Phillips, T.L.; Char, D.H. Long-term Results of the UCSF-LBNL Randomized Trial: Charged Particle With Helium Ion Versus Iodine-125 Plaque Therapy for Choroidal and Ciliary Body Melanoma. *Int. J. Radiat. Oncol. Biol. Phys.* **2015**, *92*, 376–383. [CrossRef]
23. Daftari, I.K.; Mishra, K.K.; Singh, R.P.; Shadoan, D.J.; Phillips, T.L. An Overview of the Control System for Dose Delivery at the UCSF Dedicated Ocular Proton Beam. *Int. J. Med. Phys. Clin. Eng. Radiat. Oncol.* **2016**, *5*, 242–262. [CrossRef]
24. Egger, E.; Schalenbourg, A.; Zografos, L.; Bercher, L.; Boehringer, T.; Chamot, L.; Goitein, G. Maximizing local tumor control and survival after proton beam radiotherapy of uveal melanoma. *Int. J. Radiat. Oncol. Biol. Phys.* **2001**, *51*, 138–147. [CrossRef] [PubMed]
25. Kaplan, E.L.; Meier, P. Nonparametric Estimation from Incomplete Observations. *J. Am. Stat. Assoc.* **1958**, *53*, 457–481. [CrossRef]
26. Gershenwald, J.E.; Scolyer, R.A.; Hess, K.R.; Sondak, V.K.; Long, G.V.; Ross, M.I.; Lazar, A.J.; Faries, M.B.; Kirkwood, J.M.; McArthur, G.A.; et al. Melanoma staging: Evidence-based changes in the American Joint Committee on Cancer eighth edition cancer staging manual. *CA Cancer J. Clin.* **2017**, *67*, 472–492. [CrossRef]
27. Egger, E.; Zografos, L.; Schalenbourg, A.; Beati, D.; Bhringer, T.; Chamot, L.; Goitein, G. Eye retention after proton beam radiotherapy for uveal melanoma. *Int. J. Radiat. Oncol. Biol. Phys.* **2003**, *55*, 867–880. [CrossRef] [PubMed]
28. Rodrigues, M.; de Koning, L.; Coupland, S.E.; Jochemsen, A.G.; Marais, R.; Stern, M.-H.; Valente, A.; Barnhill, R.; Cassoux, N.; Evans, A.; et al. So Close, yet so Far: Discrepancies between Uveal and Other Melanomas. A Position Paper from UM Cure 2020. *Cancers* **2019**, *11*, 1032. [CrossRef] [PubMed]
29. Miller, K.D.; Fidler-Benaoudia, M.; Keegan, T.H.; Hipp, H.S.; Jemal, A.; Siegel, R.L. Cancer statistics for adolescents and young adults, 2020. *CA Cancer J. Clin.* **2020**, *70*, 443–459. [CrossRef]
30. Zako, C.; Scholey, J.; Daftari, I.K.; Weinberg, V.K.; Swason, C.; Quivey, J.M.; Char, D.H.; Mishra, K.K. Long Term Clinical Outcomes with Dedicated Proton Ocular Beam and Helium Ion Radiation for Uveal Melanoma Patients Aged 45 and Younger. In Proceedings of the 2021 American Society for Radiation Oncology Meeting, Chicago, IL, USA, 24–27 October 2021.
31. Nayman, T.; Bostan, C.; Logan, P.; Burnier, M.N., Jr. Uveal Melanoma Risk Factors: A Systematic Review of Meta-Analyses. *Curr. Eye Res.* **2017**, *42*, 1085–1093. [CrossRef]
32. Gragoudas, E.S.; Lane, A.M.; Regan, S.; Li, W.; Judge, H.E.; Munzenrider, J.E.; Seddon, J.M.; Egan, K.M. A Randomized Controlled Trial of Varying Radiation Doses in the Treatment of Choroidal Melanoma. *Arch. Ophthalmol.* **2000**, *118*, 773–778. [CrossRef]
33. Castro, J.R.; Char, D.H.; Petti, P.L.; Daftari, I.K.; Quivey, J.M.; Singh, R.P.; Blakely, E.A.; Phillips, T.L. 15 years experience with helium ion radiotherapy for uveal melanoma. *Int. J. Radiat. Oncol. Biol. Phys.* **1997**, *39*, 989–996. [CrossRef]
34. Hartsell, W.F.; Kapur, R.; Hartsell, S.O.C.; Sweeney, P.; Lopes, C.; Duggal, A.; Cohen, J.; Chang, J.; Polasani, R.S.; Dunn, M.; et al. Feasibility of Proton Beam Therapy for Ocular Melanoma Using a Novel 3D Treatment Planning Technique. *Int. J. Radiat. Oncol. Biol. Phys.* **2016**, *95*, 353–359. [CrossRef]
35. Gragoudas, E.S. Proton Beam Irradiation of Uveal Melanomas: The First 30 Years The Weisenfeld Lecture. *Investig. Opthalmology Vis. Sci.* **2006**, *47*, 4666–4673. [CrossRef] [PubMed]
36. Gragoudas, E.; Li, W.; Goitein, M.; Lane, A.M.; Munzenrider, J.E.; Egan, K.M. Evidence-Based Estimates of Outcome in Patients Irradiated for Intraocular Melanoma. *Arch. Ophthalmol.* **2002**, *120*, 1665–1671. [CrossRef]
37. Pica, A.; (San Francisco, CA, USA). Personal communication, 2024.
38. Shields, C.L.; Kaliki, S.; Arepalli, S.; Atalay, H.T.; Manjandavida, F.P.; Pieretti, G.; Shields, J.A. Uveal melanoma in children and teenagers. *Saudi J. Ophthalmol.* **2013**, *27*, 197–201. [CrossRef]

39. Field, M.G.; Decatur, C.L.; Kurtenbach, S.; Gezgin, G.; van der Velden, P.A.; Jager, M.J.; Kozak, K.N.; Harbour, J.W. PRAME as an independent biomarker for metastasis in uveal melanoma. *Clin. Cancer Res.* **2016**, *22*, 1234–1242. [CrossRef] [PubMed]
40. Afshar, A.R.; Damato, B.E.; Stewart, J.M.; Zablotska, L.B.; Roy, R.; Olshen, A.B.; Bastian, B.C.; Joseph, N.M. Next-Generation Sequencing of Uveal Melanoma for Detection of Genetic Alterations Predicting Metastasis. *Transl. Vis. Sci. Technol.* **2019**, *8*, 18. [CrossRef]
41. Scholes, A.G.M.; Damato, B.E.; Nunn, J.; Hiscott, P.; Grierson, I.; Field, J.K. Monosomy 3 in Uveal Melanoma: Correlation with Clinical and Histologic Predictors of Survival. *Investig. Opthalmology Vis. Sci.* **2003**, *44*, 1008–1011. [CrossRef]
42. Damato, B.; Duke, C.; Coupland, S.E.; Hiscott, P.; Smith, P.A.; Campbell, I.; Howard, P.; Douglas, A. Cytogenetics of Uveal Melanoma: A 7-Year Clinical Experience. *Ophthalmology* **2007**, *114*, 1925–1931.e1. [CrossRef]
43. Kaliki, S.; Shields, C.L.; Shields, J.A. Uveal melanoma: Estimating prognosis. *Indian J. Ophthalmol.* **2015**, *63*, 93–102. [CrossRef]
44. Harbour, J.W. A Prognostic Test to Predict the Risk of Metastasis in Uveal Melanoma Based on a 15-Gene Expression Profile. In *Molecular Diagnostics for Melanoma*; Humana: Totowa, NJ, USA, 2013. Available online: https://link.springer.com/protocol/10.1007/978-1-62703-727-3_22 (accessed on 7 March 2025).

Disclaimer/Publisher's Note: The statements, opinions and data contained in all publications are solely those of the individual author(s) and contributor(s) and not of MDPI and/or the editor(s). MDPI and/or the editor(s) disclaim responsibility for any injury to people or property resulting from any ideas, methods, instructions or products referred to in the content.

cancers

MDPI

Review

Understanding and Exacerbating the Biological Response of Uveal Melanoma to Proton Beam Therapy

Laura Hawkins [1], Helen Kalirai [2], Karen Aughton [2], Rumana N. Hussain [3], Sarah E. Coupland [2] and Jason L. Parsons [1,4,*]

[1] Institute of Cancer and Genomic Sciences, University of Birmingham, Edgbaston, Birmingham B15 2TT, UK
[2] Department of Eye and Vision Science, Institute of Life Course and Medical Science, University of Liverpool, Liverpool L7 8TX, UK
[3] Liverpool Ocular Oncology Centre, Liverpool University Hospitals Trust, Liverpool L7 8XP, UK
[4] School of Physics and Astronomy, University of Birmingham, Edgbaston, Birmingham B15 2TT, UK
* Correspondence: j.parsons.3@bham.ac.uk; Tel.: +44-121-414-6850

Simple Summary: Proton beam therapy is a well-established precision radiotherapy treatment for cancers of the eye (uveal melanoma) that minimises damage to the surrounding normal tissues and preserves vision. The treatment effectiveness stems from the induction of DNA damage in tumour cells, which can overwhelm the repair mechanisms, driving cellular death. Despite the success of proton therapy, a subset of patients exhibit suboptimal responses, with some experiencing local recurrence and/or development of metastasis. This review presents current evidence on the biological factors, such as DNA repair mechanisms and reduced oxygen (hypoxia), that drive the responses of uveal melanoma to proton therapy. We also discuss emerging strategies aimed at treatment effectiveness, including targets for combination therapies. Understanding these aspects is critical for optimising treatment outcomes for eye cancer patients.

Abstract

Uveal melanoma (UM) is the most common primary intraocular malignancy in adults, associated with a high tendency for metastasis to the liver. Proton beam therapy (PBT) is the preferred external radiotherapy treatment for primary UM of certain sizes and locations in the eye, due to its efficacy and good local tumour control, as well as its precision to spare surrounding ocular structures. PBT is an effective alternative to surgical enucleation and other non-precision-targeted radiotherapies. Despite this, the radiobiology of UM in response to PBT is still not fully understood. This enhanced knowledge would help to further optimise UM treatment and improve patient outcomes through reducing radiation dosage to ocular structures, treating larger tumours that would otherwise require enucleation, or even offering a treatment strategy for the otherwise fatal liver metastases. In this review, we explore current knowledge of the treatment of UM with PBT, evaluating the biological responses to the therapy. Molecular factors, such as tumour size, oxygen tension levels, DNA damage proficiency, and autophagy, are known to influence the cellular response to radiotherapy, and these will be discussed. Furthermore, we examine innovative strategies to enhance radiotherapy outcomes, such as combination therapies with DNA damage repair and autophagy modulators, as well as advancements in PBT planning and delivery. By integrating current research and emerging technologies, we aim to provide opportunities to improve the therapeutic effectiveness of PBT in UM management.

Keywords: autophagy; DNA damage; DNA repair; hypoxia; ionising radiation; proton beam therapy; uveal melanoma

1. Introduction

Uveal melanoma (UM) is a rare and aggressive malignancy that originates from transformed melanocytes in the eye. It is the most common primary intraocular cancer in adults, with approximately 2–8 cases per million population per year [1,2]. Approximately 50% of UM patients will eventually develop metastases, most commonly to the liver, with a median survival of around 4–7 months once metastatic disease is detected [3,4]. The survival of UM patients with metastases has not greatly improved over the last three decades, with recent clinical trials involving chemotherapies and immunotherapies showing limited clinical efficacy and severe adverse effects [2,5,6]. Standard-of-care treatment for primary UM is typically radiotherapy administered as ocular brachytherapy, involving the surgical placement of a radioisotope plaque onto the tumour site, if the size and location of the tumour permit. Alternatively, the primary tumour may be treated with proton beam therapy (PBT), an external form of radiation [7,8]. Stereotactic radiosurgery, Gamma Knife and CyberKnife have also been shown to be effective; however, they are reportedly associated with higher rates of adverse effects to other ocular structures [9]. Local surgical resection of the tumour can be performed with the eye remaining intact; however, this is performed only on a small percentage of UM patients and only in some ocular oncology centres [10]. Otherwise, surgical removal (enucleation) of the eye is still performed regularly; this causes permanent vision loss and often psychological, social, and emotional distress [11,12]. There is no current proven survival advantage between any of these treatment options [7,13].

In the UK, approximately 70% of UM patients receive radiotherapy as their initial treatment, with 40–50% receiving Ruthenium-106 plaque brachytherapy and between 20 and 40% of patients treated with PBT [14]. The remaining 30% of patients undergo enucleation. Treatment trends for UM patients in the UK varies depending on which of the four ocular oncology centres are managing the case. These centres are located in Sheffield, Glasgow, London, and Liverpool, and treatment decisions depend on surgeon preference, experience, and accessibility [15]. The Clatterbridge Cancer Centre in Liverpool is home to the UK's only Eye PBT centre, which has been delivering treatment for ocular melanomas since 1989. Patients registered at the Liverpool Ocular Oncology Centre have higher use of PBT as their initial treatment compared to patients in Ireland, a reflection of the increased access to this modality [15]. PBT is well-established as a core radiotherapy treatment for UM, as opposed to conventional X-ray/photon radiotherapy used to treat most other cancer types. Amongst PBT centres across the globe, an estimated 43,000 UM patients have been treated with targeted PBT [14,16]. In the US, more than 1600 patients have been treated at the Crocker Nuclear Laboratory at the University of California, San Francisco, another specialised facility for ocular radiotherapy [16]. There is a wealth of knowledge and experience in utilising PBT for UM.

Despite PBT forming a large part of the primary treatment of UM, surprisingly, the radiobiology of the tumour response to this modality is still not well understood. PBT is a precision-targeted treatment where much of the radiation dose can be delivered directly to the tumour. However, there is uncertainty regarding the biological mechanism of action and clinical response, which are influenced by the linear energy transfer (LET) of the proton beam. With PBT, there are known increases in LET at and around the Bragg peak, where the radiation dose is deposited, which influences the biological (DNA) damage created.

This also affects the cellular mechanisms that respond to the damage, although these details are not well understood.

In this review, we present current knowledge surrounding the use of PBT in the treatment of UM and provide an overview of the key biological processes reported to influence treatment efficacy. By increasing our understanding of the response of UM to PBT, strategies to enhance the effectiveness of the radiotherapy treatment can be developed, with the goals being to preserve the eye and vision and to prevent tumour recurrence and metastasis.

2. Proton Beam Therapy

PBT is a highly precise form of external beam radiotherapy that uses protons to precisely deliver ionising radiation within the tumour. PBT for UM patients is typically delivered in four fractions over four consecutive days, up to a final dose of approximately 60 Gy [17,18]. The major advantage of PBT is the accurate targeting of the tumour via dose deposition through the Bragg peak (Figure 1A). PBT delivers a low entrance and exit dose, which minimises the irradiation risk to surrounding normal tissues and structures proximal to the tumour being treated. Furthermore, the energy deposition can be modulated to a defined narrow depth, specifically targeting only the tumour and thereby reducing radiotherapy-induced side effects [19,20]. However, energy deposition via the Bragg peak also leads to an increase in LET as the protons reduce in speed and lose energy as they pass through the tissue. The increase in LET leads to a higher frequency of ionisation events along the radiation track, which, in the context of cellular DNA, can lead to elevated levels and complexity of DNA damage (Figure 1B). Complex DNA damage (CDD) is more challenging for cells to repair than isolated DNA damage, contributing to increased cell death and a greater relative biological effectiveness (RBE) [21]. Combining beams with different initial energies can create a spread-out Bragg peak (SOBP), thus allowing the targeting of tumours with large size and volume. PBT can be utilised for UM in any location in the eye and with any tumour thickness. This is a significant advantage compared to brachytherapy, which cannot be placed too close to the optic nerve [22–24].

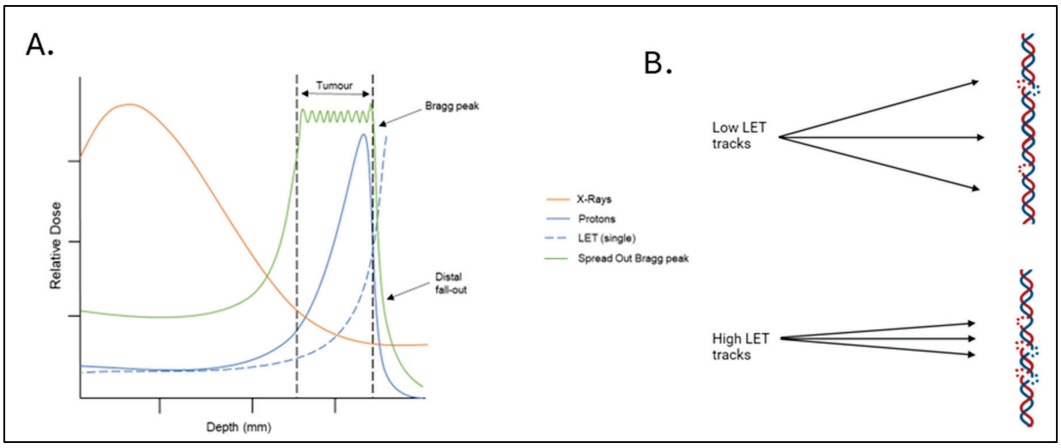


Figure 1. Depth–dose distribution of PBT relative to the Bragg peak and the relationship to ionisation density/LET. (**A**) PBT shows a relatively low entrance and exit dose (blue solid line), with the maximal energy being deposited in a well-defined region called the Bragg peak, that can be targeted to the tumour. This is in comparison to X-rays/photons where the dose is highest close to the source (orange line). LET (dashed blue line) increases at and around the Bragg peak. Several proton beams can be modulated and combined to create a spread-out Bragg peak (green line) to target larger tumours. (**B**) Low-LET radiation tracks cause regions of isolated DNA damage, such as NDA breaks within the tumour cell, whereas more densely ionising high-LET tracks cause regions of CDD. Created in BioRender. Hawkins, L. (2025) https://app.biorender.com/illustrations/6724f4364b0df48f0107bd27?slideId=4ed920ab-b703-4e06-a8cf-d1f8ea75740d (accessed on 13 September 2025).

3. Evaluating the Clinical Response to Proton Beam Therapy

There are no current prospective randomised trials that have evaluated the efficacy of PBT for UM, but there are multiple reviews and meta-analyses that demonstrate good survival rates and the safety of this treatment [25–27]. The most relevant reports of patient outcomes following PBT, including studies containing at least 50 patients, are summarised in Table 1. This table has been modified from Yilmaz et al., 2024 [28].

Table 1. A table of reviews evaluating UM patient outcomes after PBT.

Time	Patient Numbers	Dose	Median Follow up	Local Control	Eye Preservation	Overall Survival	Toxicity	Ref
1984–1999	2648	60 Gy in 5 fractions	24 months	5-year 95.8% 10-year 94.8%	91.8%	10-year 73%		[29]
1993–2003	349	53.1 Gy in 4 fractions	37 months	5-year 96.5%	92%	5-year 90%	17.9% glaucoma 12.8% rubeosis 16.7% pain 9% vitreous haemorrhage 38% retinal detachment	[30]
1991–2001	1406	60 Gy in 4 fractions	73 months	5-year 96%	92.3%	5-year 79%	66.5% maculopathy 23.4% papillopathy 28.6% glaucoma 61.8% cataract 11.5% keratitis 13.9% vitreous haemorrhage	[18]
1991–2007	886	60 Gy in 4 fractions	64 months	5-year 93.9% 10-year 92.1%	92.2%	5-year 79.4% 10-year 64.1%	7% glaucoma 27.5% retinopathy 31.7% cataract	[31]
1993–2008	147	58 Gy in 4 fractions	53 months		5-year 71.3%	5-year 87.8%		[32]
1995–2007	59	60 Gy in 4 fractions	125 months	5-year 91%	5-year 93.2%	5-year 85%	74% radiation retinopathy 64% optic nerve neuropathy 29.6% cataract	[33]
1998–2008	982	60 Gy in 4 fractions	60.7 months	5-year 96% 10-year 94%	5-year 95%	5-year 80% 10-year 60%	12.1% neovascular glaucoma	[34]
1991–2015	492	60 Gy in 4 fractions	61.9 months	5-year 60% 10-year 47%	80.5%		39.8% cataracts 27% neovascular glaucoma 23.4% retinopathy	[35]

This evidence demonstrates that there is a consistent similarity in dosing protocols, with most tumours receiving a fractionated dose of 50–60 Gy RBE. PBT has been evidenced to be effective at controlling the primary tumour with reported local control rates of 91–96.5% over 5 years and 92.1–94% over 10 years [18,29,33,34]. This is coupled with good rates of eye preservation ranging from 91 to 93.2% [29,33]. Collectively, these results show that PBT is excellent at controlling the primary tumour, with high levels of local tumour control and eye retention rates. Despite this, some degree of toxicity has been reported in patients treated with PBT, although the rates are quite variable and likely attributed to tumour location and volume. It is also worth noting that some of these studies are over twenty years old. Among reported toxicities, radiation retinopathy, a common and devastating visual side effect causing disruption of vascular structures in the eye [32,33], is most frequently observed at rates of 27–74%. Secondary neovascular glaucoma has also been recognised as a side effect of PBT, with rates of 7–28%, because of

the so-called 'toxic tumour syndrome', i.e., the release of enzymes and factors from the dying melanoma cells that induce tissue lysis as well as neovascularisation [36]. Toxic tumour syndrome often necessitates either prompt removal of the tumour via local resection or, more often, secondary enucleation [24,37]. It is, however, difficult to determine whether other complications, such as haemorrhage and retinal detachment rates, are caused by the PBT or the tumour itself.

Despite PBT being a relatively effective treatment for primary UM, as seen in Table 1, approximately 10% of patients fail in local control [31,33,34]. The rate of metastasis following treatment is up to 50%, and PBT-treated UM patients have a 74–91% survival rate for 10 years; however, these outcomes are comparable across all primary treatment methods, including enucleation and plaque brachytherapy [7,13]. This suggests that metastasis and long-term survival rates are influenced more by underlying factors such as chromosomal aberrations and genetic mutations, rather than the choice of treatment modality [38–42]. Importantly, PBT offers distinct advantages: it can reduce the need for enucleation, limit certain side effects such as pain, and is equally effective in treating primary tumours in terms of patient outcomes when compared to other established therapies. Research is needed to assess the variability in response to PBT, identify the underlying factors, and determine whether combinatorial treatments may improve the long-term survival of UM. Understanding the radiobiological response to PBT is therefore critical to optimising the treatment to enable good tumour control for eye and vision preservation as much as possible.

4. Key Molecular Factors Known to Influence Cellular Response to PBT

The radiobiological responses to PBT depend on several cellular and molecular factors, which are discussed below.

4.1. DNA Damage Repair Proficiency

The therapeutic efficacy of PBT primarily depends on inducing substantial DNA damage in tumour cells, overwhelming their capacity for repair, and ultimately driving them towards cell death. A variety of DNA lesions can form along the radiation track of the proton beam, including DNA base damage and DNA single-strand breaks (SSBs). However, the most critical lesions contributing to PBT-induced cell death are DNA double-strand breaks (DSBs) and CDD, due to the difficult nature of their repair [43]. These lesions increase in frequency at and around the Bragg peak due to the increasing LET, that causes clustering of the radiation-induced events [44]. There are several important cellular DNA damage response (DDR) pathways that are utilised to resolve the DNA damage induced by PBT (summarised in Figure 2).

Despite the abundance of SSB and DNA base lesions after PBT, they are relatively quick and easy for the cell to repair, with an approximate half-life for accurate repair of several minutes in most cells [45–47]. These lesions, including oxidative base damage and abasic sites, are repaired through the base excision repair (BER) pathway [48]. The more complicated the DNA damage, the more challenging the repair and the more harmful these lesions are for the cell. Indeed, DSBs and CDD are lethal lesions induced by PBT, and it is thought that just one unrepaired DSB can be fatal to the cell [44,49]. Cells have evolved two main pathways to repair DSBs: non-homologous end joining (NHEJ) and homologous recombination (HR). NHEJ is active throughout the cell cycle and therefore thought to be the most utilised DSB repair pathway, which can be sub-classified into classical NHEJ (cNHEJ) and alternative NHEJ (aNHEJ), which differ in speed, accuracy of repair, and mechanism [50,51]. Whilst NHEJ enables rapid repair of the lesion, it is also error-prone, as there is no homologous template available during repair, and so there can

be small insertions or deletions [52,53]. HR, in contrast, utilises the sister chromatid for more accurate repair and is therefore error-free, although this pathway can only occur in the S and G2 cell cycle phases [44,54].

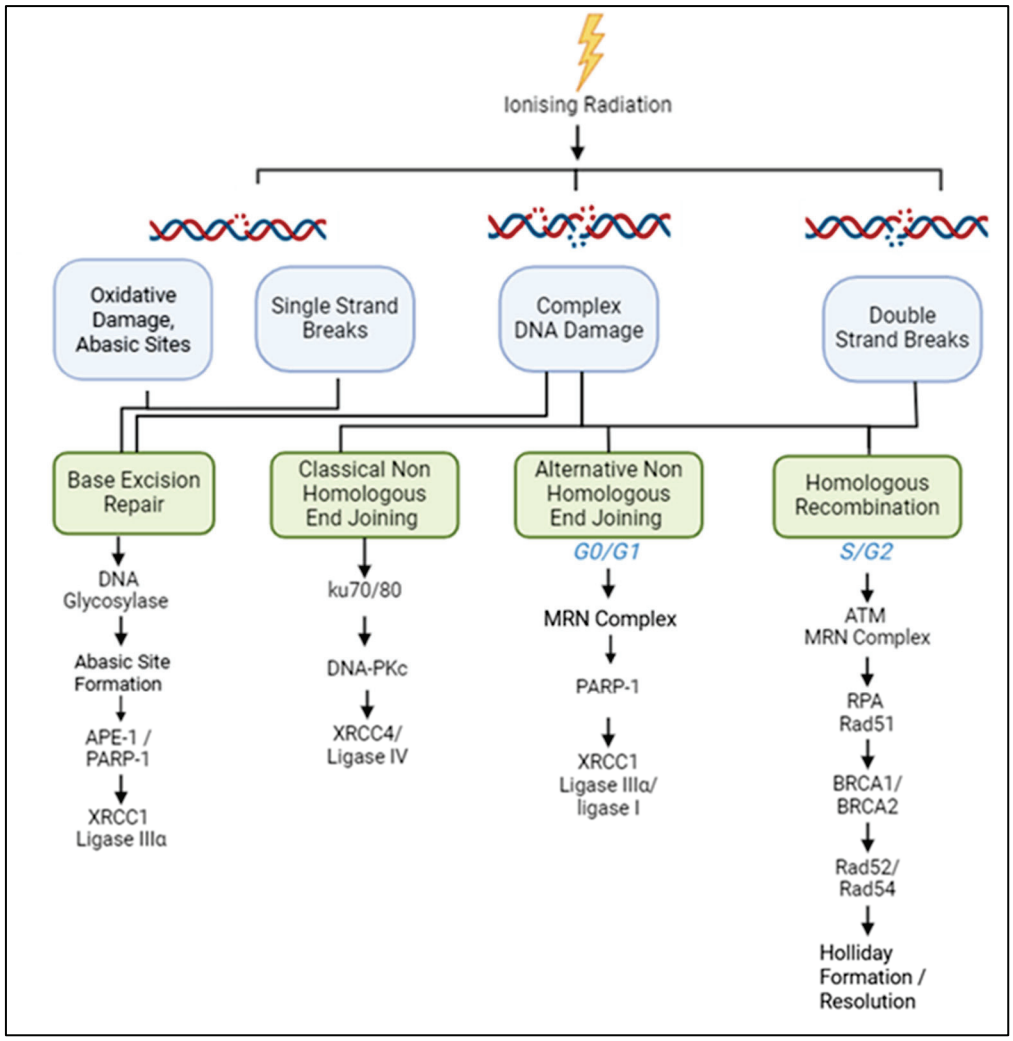


Figure 2. The major cellular DDR pathways responsive to PBT-induced DNA damage. Ionising radiation induces a variety of DNA lesions that are repaired by DDR pathways. SSBs and base damage are repaired by base excision repair (BER), where damage-specific DNA glycosylases create abasic sites, which are cleaved by APE1, generating SSBs recognised by PARP-1. DNA polymerase β and the XRCC1-DNA ligase IIIα complex fill and seal the gap. DSB repair depends on the cell cycle stage: NHEJ (classical and alternative) is active throughout the cell cycle, with cNHEJ initiated by Ku70/80 binding and recruitment of DNA-PKcs and XRCC4-DNA ligase IV; A-NHEJ involves MRN complex resection, PARP-1 binding, and ligation by DNA ligase I or XRCC1-DNA ligase IIIα. In the S/G2 cell cycle phase, HR repairs DSBs via MRN complex resection, RPA and RAD51 binding, strand invasion by RAD52 and RAD54, and Holliday junction resolution. CDD requires multiple pathways to resolve the lesions, which will depend on the specific nature of the damage. Efficient coordination of these pathways is crucial for the timely repair of PBT-induced damage, promoting cell survival.

CDD is defined as two or more DNA lesions within one to two helical turns of the DNA, and like DSBs, is a major contributor to PBT-induced cell death [20]. The nature of the CDD induced by PBT can be generally classified into either non-DSB or DSB clusters and is therefore likely to require both BER and DSB repair pathways. However, the contribution of different DNA repair pathways to the CDD generated by PBT is unclear. Recent research has demonstrated that BER/SSB repair proteins, including PARP-1, PARG, and OGG1 are critical for the repair of DNA damage induced by relatively high-LET protons delivered

via the Bragg peak, indicating that this is largely SSB-associated [55,56]. However, there is conflicting evidence in the literature for the increased involvement of either NHEJ or HR in the repair of DSBs induced by protons with increasing LET [21,57–59].

Despite the clinical relevance of PBT in UM, the efficiency of the cellular DDR to PBT-induced damage remains surprisingly underexplored. Emerging evidence suggests that variability in treatment response may be influenced by altered levels of key DNA damage-coordinating proteins, some of which are associated with poorer prognosis [59,60]. Downregulation of ATR, or even a complete absence of this protein, has been associated with significantly worse overall survival in UM [60]. ATR is a master protein kinase regulator in response to DSBs and replication fork stabilisation during HR [60]. DNA-PKcs is another crucial kinase involved in facilitating cNHEJ of DNA DSBs, and its gene expression has been shown to be highly expressed in metastatic UM and associated with poor survival [61]. This study also found that low PARP-1 expression could be used to predict better disease-free survival [61]. Collectively, these data suggest there is an important potential role for DNA-PKc and PARP-1 in the initial response to primary UM treatment. Loss of nuclear ATM has additionally been linked with reduced disease-free survival, which is important as ATM is a master regulator kinase involved in DSB repair detection and transduction, cell cycle control, and pathway selection [44,49,62]. Data from our group has recently shown that different UM cell lines show altered expression of ATM, which partly correlates with their response to both X-rays and PBT [63]. Here, high ATM-expressing UM cells were demonstrated to display increased radioresistance driven through enhanced DSB repair rates, compared to lower ATM-expressing cells. Further studies are nevertheless needed to explore the efficiency of the DDR in UM cells, specifically following PBT. Noteworthy is that the majority of studies investigating the role of DDR proteins in mediating ionising radiation-induced cell death have been conducted using X-rays or γ-rays. In contrast, there is a notable lack of evidence elucidating the specific mechanisms underlying PBT-induced cell death. This discrepancy is partly attributable to the limited accessibility of PBT, which requires specialised infrastructure, incurs higher costs, and is subject to geographic disparities compared to more widely available ionising radiation modalities [64]. Nevertheless, given the shared physical and biological principles underlying different forms of ionising radiation, findings from studies using X-rays or other conventional sources are likely to yield comparable insights and should not be disregarded [49]. However, evaluating DNA damage proficiency of UM cells is essential for understanding their response to PBT radiation-induced injury, as any deficiencies or abundance in any of these pathways can significantly influence the therapeutic efficacy of PBT.

4.2. The Autophagy Response

Autophagy is a highly conserved process responsible for breaking down damaged macromolecules, cellular structures, and organelles through lysosomal degradation to maintain cellular homeostasis, promoting either cell survival or cell death (Figure 3) [65,66]. Ionising radiation, including PBT, also increases reactive oxygen species (ROS) levels, impairing mitochondrial function, causing protein misfolding, and triggering the release of calcium from the endoplasmic reticulum to the cytoplasm, all of which are factors shown to induce autophagy [65,67]. Cancer cells exploit autophagy pathways to enhance stress tolerance and act as a protective mechanism against therapeutics, including ionising radiation [67,68]. Autophagy can act as a cryoprotective mechanism against PBT-induced stress through the clearing of damaged organelles and proteins, the maintenance of cellular energy levels, and the modulation of apoptotic pathways [69,70]. However, if cellular damage and metabolic stress exceed the cellular repair capacity, extensive autophagic flux

can lead to accelerated cell death. Autophagy-driven cell death may occur directly or involve other key cell death pathways, such as apoptosis or necrosis, particularly under severe damage [71,72]. Therefore, the cellular balance of protective autophagy compared to extensive autophagy is likely to play a huge role in the impact of PBT damage and the cellular response.

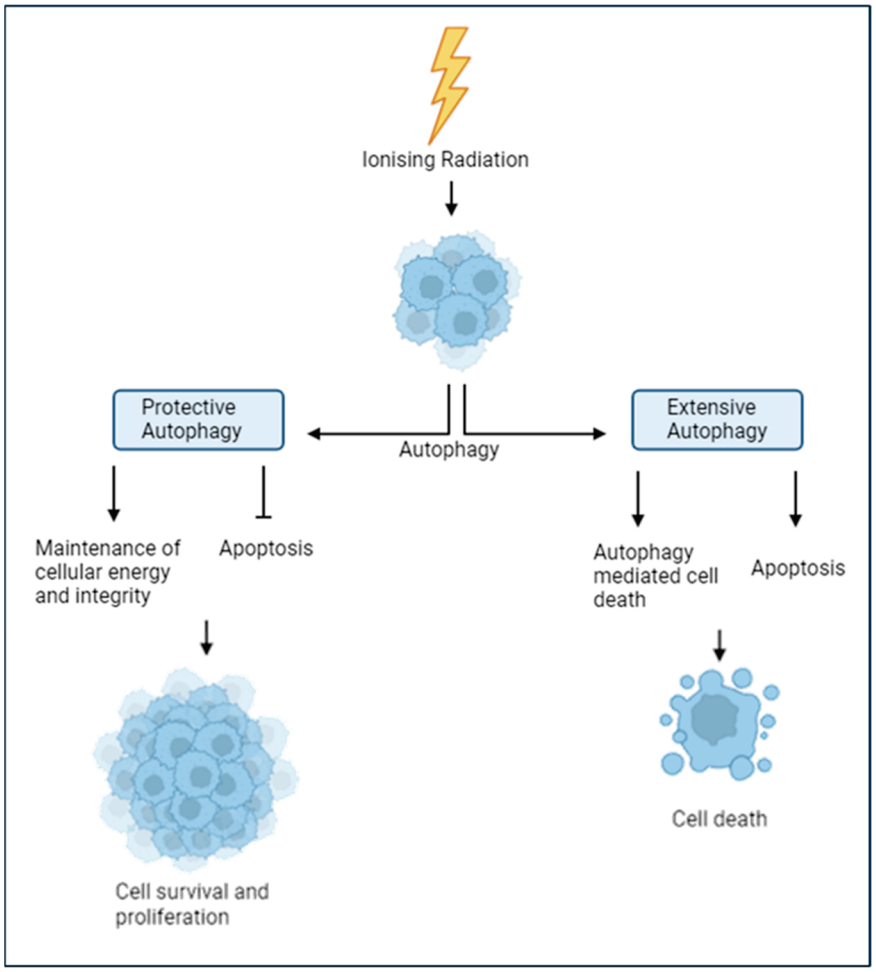


Figure 3. Autophagy can have a major influence on cell fate after ionising radiation. In response to radiation, such as PBT, autophagy can be activated to promote either tumour cell survival or death. Protective autophagy can lead to inhibition of apoptosis and the mitigation of oxidative stress, whilst maintaining the integrity of energy homeostasis. Conversely, extensive autophagy, stimulated through either excessive damage or individual cellular preferences, can lead to uncontrolled degradation of essential cellular components, disrupt homeostasis, and trigger cell death either directly through crosstalk with apoptosis, or indirectly through amplifying necroptosis and autophagy-dependent cell death pathways. The dark blue of the cell represents the nucleus, whereas the lighter blue represents the cytoplasm. Image created in BioRender. Hawkins, L. (2025) https://app.biorender.com/illustrations/67373569041045f9a52893c7?slideId=9ffb5c00-6e63-43ff-8466-b9f117882195 (accessed on 13 September 2025).

Precisely how autophagy mediates and influences the impact of PBT and the cellular response in UM remains largely unclear. It has been suggested that autophagy plays an important role in UM cells, as it has been estimated that these cells increase autophagic activity by around 40–50% above basal levels in their non-cancerous counterparts [73]. This increase in autophagy activity could be a byproduct of the hypoxia-induced metabolic stress in tumour cells or may suggest that autophagy offers significant survival and tumorigenic advantages. Evidence indicates that autophagy may play an actively protective role in

UM, as shown with the inhibition of autophagy with chloroquine, which led to enhanced apoptosis and increased autophagic flux (64). Chloroquine has also been shown to sensitise UM cells and tumours harbouring GNAQ/GNA11 mutations, which are present in over 90% of UM cases, to the MEK1/2 inhibitor trametinib [74]. Although data remain limited, existing evidence suggests that UM cells may exhibit elevated autophagy activity and are partially dependent on its protective functions, such as inhibiting apoptosis, preserving energy stores, and maintaining cellular integrity, to support tumour cell survival under normal conditions. This reliance on the protective mechanisms of autophagy could reduce the effectiveness of PBT in some UM, as enhanced autophagic responses may help cells better withstand the stress induced by the radiation. However, it is currently impossible to rule out the dual roles that autophagy may play in the biological effect of PBT. To fully understand the therapeutic implications, further research is needed, especially with PBT.

4.3. Hypoxia and the Tumour Microenvironment

Hypoxia is defined as the reduction of oxygen in tissues and is often the result of the metabolic demands of the growing tumour exceeding the supply of oxygen [75]. Reductions in cellular oxygen levels can also strongly impact the effectiveness of radiotherapy [76,77]. Under normal physiological conditions, ionising radiation reacts with molecular oxygen in the tissue, producing ROS, which in turn cause further damage to vital cellular components such as DNA and organelles [76]. Molecular oxygen also enables the creation of fixed peroxyl adducts onto the DNA structure, which are incredibly difficult for the cell to repair, termed the "oxygen fixation hypothesis", and are dangerous if these lesions are carried through to DNA replication [76,78]. During hypoxia, less molecular oxygen is available as a substrate for ROS generation, resulting in decreased DNA damage, theoretically reducing the efficacy of PBT in hypoxic tumours. Therefore, the levels of oxygen in the tumour at the time of PBT are a crucial factor in the biological response of this treatment.

A hypoxic microenvironment is an important feature of UM and is strongly associated with malignant progression, tumour aggressiveness, and reduced overall survival [75,79]. Studies have shown that hypoxia correlates with elevated genomic instability and *BAP1* mutations, resulting in promotion of cell survival through cell cycle checkpoint interference and less favourable clinical outcomes [75,80]. The development of a hypoxic tumour microenvironment is also associated with modulation of the immune response and results in reduced immune cell infiltration, due to newly formed leaky blood vessels, which further enables cell proliferation and metastasis [75,81]. The adaptation to hypoxia is regulated by hypoxia-induced-factors (HIF), where HIF-1α stabilisation is a crucial early event in the cellular response to hypoxia [82,83]. HIF-1α protein is reportedly highly expressed in UM and supports cell survival through regulation of DNA damage pathways, cellular metabolism, apoptosis, and autophagy [75,84]. The cellular and metabolic response to PBT in a hypoxic cell compared to a normoxic cell may be different based on these transcriptional changes and enrichment of pro-survival pathways. However, the impact that this has on the efficacy of PBT, and importantly how this can be harnessed to enhance treatment effectiveness, is not known.

5. Strategies to Exacerbating the PBT Response in UM

There is an urgent need to explore options to further enhance the radiotherapeutic response to PBT in UM in a safe manner, as current treatments can cause unpleasant adverse effects, such as toxic tumour syndrome and radiation retinopathy, which greatly diminish quality of life [33,35,85]. Some primary tumours also do not respond well to treatment or relapse and reoccur shortly after PBT, events which are associated with a poorer prognosis

and increased tendency to metastasise [86]. The most promising approaches to improve the radiobiological effectiveness of PBT in UM are evaluated below.

5.1. Targeting DNA Damage Repair

Given that the primary therapeutic effect of PBT relies on inducing DNA damage, targeting the DDR with specific inhibitors represents a promising strategy to enhance treatment efficacy and improve patient outcomes. Some of the major cellular targets for drugs and inhibitors that have been developed to date are shown below (Figure 4).

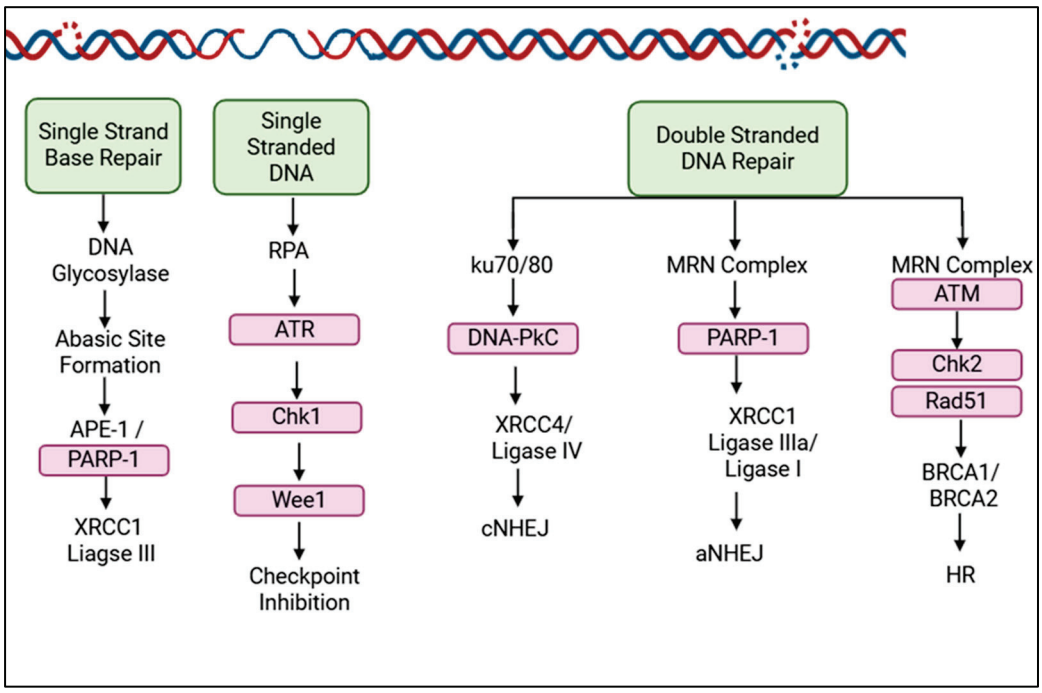


Figure 4. Cellular proteins within the DDR currently under investigation for drug/inhibitors to enhance radiotherapy efficacy. The major repair proteins within the key pathways responsible for co-ordinating the signalling and/or repair of DNA damage induced by PBT are shown. The proteins highlighted in pink have been studied as radiosensitisation targets, and inhibitors have been developed against them with the aim to further increasing the cellular response to radiation. Created in BioRender. Hawkins, L. (2025) https://app.biorender.com/illustrations/662e6ad9a3cc858692ca7beb?slideId=c85d73e2-92cc-40d6-a481-b6f1809d2103 (accessed on 13 September 2025).

Inhibiting the proteins governing the repair of lethal lesions such as DSBs and CDD is a promising therapeutic strategy to sensitise UM cells to PBT [21,60,87]. These include the three major protein kinases ATM, DNA-PKcs, and ATR, which are involved in the signalling and coordination of the DDR [63,88]. Recent evidence indicated that targeting ATM with a potent and specific inhibitor can increase the radiosensitivity of four different UM cell lines with different genetic backgrounds to both X-rays and PBT, mediated through inhibition of DSB repair [63]. Inhibition of DNA-PKcs has also been demonstrated to radiosensitise UM cell lines and xenograft mouse models to γ-radiation [89,90]; theoretically, this radiosentisation effect could also apply to the radiation-induced damage caused by PBT.

PARP inhibitors are another class of promising radiosensitisers and have already been approved for the treatment of BRCA-mutated breast and ovarian cancers [91]. Inhibiting this key SSB repair protein results in increased DSBs formed through the collapse of the DNA replication forks, which are particularly toxic to cells with HR deficiency, a concept known as 'synthetic lethality' [92,93]. In UM, HR deficiency is not usually present [89,90]; however, there is a growing amount of research that suggests that some genetic alterations, such as loss of *BAP1* or the *SF3B1* hotspot mutations, may confer sensitivity to PARP

inhibitors [94–96]. The combination of PARP inhibitors plus radiation, particularly PBT, therefore requires further research to determine potential synergistic effects. Combining the precision of PBT with the favourable toxicity profile of PARP inhibitors presents a particularly promising therapeutic strategy, potentially offering enhanced radiobiological effects with minimal adverse outcomes.

Nevertheless, evidence examining the impact of DDR inhibitors to radiosensitise UM models is very limited. Investigating this approach is crucial, as enhancing the radiobiological effects of PBT by disrupting efficient DNA repair could have significant clinical implications, such as enabling lower radiation doses to minimise side effects or expanding treatment options for larger tumours, potentially preserving the eye and vision.

5.2. Other Potential Radiosensitisation Targets

Since autophagy can either support cell survival or promote cell death, its role in enhancing the efficacy of PBT in UM remains uncertain, making it a challenging therapeutic target. One study has reported that elaiophylin, an inhibitor of autophagosome formation, has demonstrated potential as a monotherapy in UM cell lines, inducing autophagic cell death via mitophagy suppression and the accumulation of oxidative stress [97]. Chloroquine and hydroxychloroquine, as autophagy inhibitors, have been investigated in other tumour types, but with no clear clinical benefit established [98]. mTOR inhibition, a central negative regulator of autophagy, has been explored as a strategy to promote autophagy [99,100]. Rapamycin is a potent mTOR inhibitor that has shown some potential in enhancing tumour cell responses to radiation by increasing autophagic activity [101]. However, the lack of reliable biomarkers to predict patient responses to autophagy agents further complicates their clinical utility. Regardless, it would be interesting to examine whether modulating autophagy through these promising targets could increase the effect of radiation in UM cells and tissues, and their subsequent response, particularly with targeted PBT.

Overcoming radioresistance caused by tumour hypoxia is another strategy to promptly drive an increased PBT response. An early approach used to achieve this was through carbogen to directly increase the oxygen inside the tumour, although this may paradoxically increase the sensitivity of healthy tissues to radiation, potentially worsening adverse side effects [102]. More recent strategies have focussed on inhibiting key proteins involved in the hypoxic response, such as HIF1α, which is a promising target in UM as it is known to be overexpressed in metastatic tumours [84]. An inhibitor of HIF1α in mouse models has been shown to suppress UM primary tumour growth, liver metastasis, and subsequent survival as a monotherapy whilst being well tolerated [103]. Unfortunately, there is no further evidence in UM to investigate HIF1α as a target for radiosensitisation. Additionally, it is thought that HIF2α is involved in more of a chronic response to hypoxia, whereas HIF1α rapidly mediates the acute response [104,105]. Therefore, investigating HIF2α as a target in UM is also a potential strategy that warrants future research. Targeting the hypoxic response presents a promising strategy to enhance the effectiveness of PBT, as alleviating hypoxia could increase DNA damage and diminish the cell's ability to manage radiation-induced stress. By disrupting this adaptive survival mechanism, tumour cells may become more vulnerable to treatment, potentially leading to improved therapeutic outcomes.

5.3. Radiotherapy Advances

Advances in treatment planning and delivery of precision-targeted PBT could further improve the outcomes of UM treatment whilst still sparing the eye. The efficacy of PBT is highly dependent on the accurate positioning of the Bragg peak to the tumour, although issues such as complex dose calculations and limited optimisation algorithms hinder this

process [106]. Advancing already established radiotherapy techniques is another method to improve treatment for UM patients. This includes stereotactic radiosurgery using the Gamma Knife (GK-SRS), an alternative globe-sparing radiotherapy for UM. A large systematic analysis found that this GK-SRS treatment is as effective as PBT in achieving five-year survival rates [107]. While GK-SRS offers similar local tumour control to PBT, it is associated with higher rates of adverse side effects, including vitreous haemorrhage and secondary glaucoma, occurring in up to 47% of patients [108,109]. An in-silico study comparing GK-SRS and PBT found that, whilst both therapies offer precise tumour targeting, PBT provides better retina sparing and reduces toxicity, particularly haemorrhage [108]. This underscores the advanced precision of PBT and the ongoing challenge of optimising its delivery in UM treatment.

5.4. FLASH Radiotherapy

FLASH radiotherapy, characterised by ultra-high dose rates (>40 Gy/s), has emerged as a promising technique to reduce normal tissue toxicity while maintaining effective tumour control [110]. This approach is particularly relevant for tumours such as UM, which are typically small, thin lesions located near critical structures like the optic nerve and the retinal pigment epithelium (RPE) [85]. Combining the precision of PBT with the ability of FLASH delivery to spare surrounding healthy tissue could offer a powerful alternative to further reduce adverse side effects in UM treatment. Although PBT is highly accurate, it can still cause vision-threatening complications, including radiation retinopathy and optic neuropathy (as shown in Table 1). FLASH radiotherapy may help protect the RPE during UM treatment, which is essential for maintaining the survival of photoreceptors crucial for vision [85]. Recent studies have demonstrated that FLASH treatment enhances the viability of ARPE-19 cells and results in a milder decline in motor function in treated mice compared to conventional irradiation [111].

However, preclinical and clinical data on the use of FLASH in ocular applications remain limited. Neither FLASH nor conventional irradiation was shown to affect depth perception in a mouse model, although the radiation dose was delivered to the brain, not the eye, which may explain the lack of sensitivity in the assay [111]. Moreover, the development of FLASH was not ranked as a high priority in the 2022 Second International Survey of ocular proton centres. Instead, increased access to PBT and the creation of a commercially available, sustainable treatment planning system were considered more critical for ongoing development [112]. So, while FLASH PBT shows promise for UM treatment and early data are generally encouraging, further research is needed to fully explore its potential in mitigating the adverse side effects associated with PBT in UM.

6. Concluding Remarks and Future Directions

UM is a sight-threatening and often fatal intraocular cancer. Primary treatment with PBT is effective, resulting in high local control and overall survival rates of ~80–90%. However, some patients still experience poor outcomes due to treatment resistance, relapse, or metastasis. Whilst the precision of PBT allows for the treatment of tumours regardless of size or location within the eye, the biological factors influencing differential responses are not yet fully understood. Emerging evidence suggests that cellular mechanisms such as the DDR, tumour hypoxia, and autophagy play important roles in modulating the effectiveness of radiotherapy. Yet, there is a surprising lack of data identifying the specific proteins and pathways involved in the response of UM to PBT. This gap in knowledge limits our ability to optimise treatment strategies and personalise therapy. Future research should focus on dissecting the molecular landscape of UM using both immortalised and patient-derived cell models with diverse genetic backgrounds to better understand how genetic and cellular

processes influence radiation sensitivity. In particular, exploring the potential of DDR inhibitors, hypoxia-targeting agents, and autophagy modulators in combination with PBT could pave the way for more effective, tailored therapeutic approaches that improve patient outcomes while minimising the significant adverse effects.

It is accepted that the most lethal lesions induced by PBT are DSBs and CDD. Therefore, targeting the DDR is considered a primary strategy through which radiotherapy effectiveness could be enhanced. Whilst not studied in great depth, there is some evidence to suggest that ATM and DNA-PKc inhibition can increase the sensitivity of UM models to PBT. However, there is also the potential for the use of autophagy or hypoxia modulators to enhance cell death after radiation treatment. Despite this, there is generally limited data for the application of these treatment strategies in UM to enhance the PBT response, where more extensive preclinical research is needed to identify their potential. These strategies need to be explored in vitro, using both cultured cell lines and also more advanced models including patient-derived organoids, as well as in vivo using the appropriate animal models. Such research is vital for identifying strategies in enhancing the effectiveness of PBT in the treatment of patients with UM, contributing towards improving patient outcomes and quality of life. This could also lead to preventing tumour recurrence and/or fatal liver metastasis.

Author Contributions: Conceptualization, L.H. and J.L.P.; investigation, L.H.; writing—original draft preparation, L.H.; writing—review and editing, L.H., H.K., K.A., S.E.C., R.N.H., and J.L.P.; supervision, H.K., K.A., S.E.C., R.N.H., and J.L.P.; funding acquisition, J.L.P. All authors have read and agreed to the published version of the manuscript.

Funding: This research was funded by Fight for Sight, grant number 5173/5174.

Acknowledgments: The authors would like to thank the Liverpool Ocular Oncology Centre (Heinrich Heimann and team).

Conflicts of Interest: The authors declare no conflicts of interest.

References

1. Tsotridou, E.; Loukovitis, E.; Tsiropoulos, G.N.; Zapsalis, K.; Pentara, I.; Tzima, K.; Eminidou, V.; Anogeianakis, G. Radiation treatment methods in uveal melanoma. *Med. Hypothesis Discov. Innov. Ophthalmol.* **2021**, *10*, 32. [CrossRef]
2. Jager, M.J.; Shields, C.L.; Cebulla, C.M.; Abdel-Rahman, M.H.; Grossniklaus, H.E.; Stern, M.H.; Carvajal, R.D.; Belfort, R.N.; Jia, R.; Shields, J.A.; et al. Uveal melanoma. *Nat. Rev. Dis. Primers* **2020**, *6*, 24. [CrossRef]
3. Khoja, L.; Atenafu, E.G.; Suciu, S.; Leyvraz, S.; Sato, T.; Marshall, E.; Keilholz, U.; Zimmer, L.; Patel, S.P.; Piperno-Neumann, S.; et al. Meta-analysis in metastatic uveal melanoma to determine progression free and overall survival benchmarks: An international rare cancers initiative (IRCI) ocular melanoma study. *Ann. Oncol.* **2019**, *30*, 1370–1380. [CrossRef]
4. Lane, A.M.; Kim, I.K.; Gragoudas, E.S. Survival Rates in Patients After Treatment for Metastasis from Uveal Melanoma. *JAMA Ophthalmol.* **2018**, *136*, 981. [CrossRef] [PubMed]
5. Olofsson Bagge, R.; Nelson, A.; Shafazand, A.; Cahlin, C.; Carneiro, A.; Helgadottir, H.; Levin, M.; Rizell, M.; Ullenhag, G.; Wirén, S.; et al. A phase Ib randomized multicenter trial of isolated hepatic perfusion in combination with ipilimumab and nivolumab for uveal melanoma metastases (SCANDIUM II trial). *ESMO Open* **2024**, *9*, 103623. [CrossRef] [PubMed]
6. Orloff, M. Clinical Trials in Metastatic Uveal Melanoma: Immunotherapy. *Ocul. Oncol. Pathol.* **2021**, *7*, 168. [CrossRef]
7. Bolling, J.P.; Dagan, R.; Rutenberg, M.; Mamalui-Hunter, M.; Buskirk, S.J.; Heckman, M.G.; Hochwald, A.P.; Slopsema, R. Treatment of Uveal Melanoma With Radioactive Iodine 125 Implant Compared with Proton Beam Radiotherapy. *Mayo Clin. Proc. Innov. Qual. Outcomes* **2021**, *6*, 27. [CrossRef]
8. Carvajal, R.D.; Sacco, J.J.; Jager, M.J.; Eschelman, D.J.; Olofsson Bagge, R.; Harbour, J.W.; Chieng, N.D.; Patel, S.P.; Joshua, A.M.; Piperno-Neumann, S. Advances in the clinical management of uveal melanoma. *Nat. Rev. Clin. Oncol.* **2023**, *20*, 99–115. [CrossRef]
9. Özcan, G.; Gündüz, A.K.; Mirzayev, İ.; Oysul, K.; Uysal, H. Early results of stereotactic radiosurgery in uveal melanoma and risk factors for radiation retinopathy. *Turk. J. Ophthalmol.* **2020**, *50*, 156–162. [CrossRef]
10. Damato, B.; Kacperek, A.; Errington, D.; Heimann, H. Proton beam radiotherapy of uveal melanoma. *Saudi J. Ophthalmol.* **2013**, *27*, 151. [CrossRef]

11. Davies, C.; Brown, S.L.; Fisher, P.; Hope-Stone, L.; Fisher, D.; Morgan, A.; Cherry, M.G. Predictors of emotional distress in uveal melanoma survivors: A systematic review. *Eye* **2022**, *37*, 907–924. [CrossRef]
12. Brown, S.L.; Fisher, P.L.; Hope-Stone, L.; Hussain, R.N.; Heimann, H.; Damato, B.; Cherry, M.G. Predictors of long-term anxiety and depression in uveal melanoma survivors: A cross-lagged five-year analysis. *Psychooncology* **2020**, *29*, 1864–1873. [CrossRef]
13. Nathan, P.; Cohen, V.; Coupland, S.; Curtis, K.; Damato, B.; Evans, J.; Fenwick, S.; Kirkpatrick, L.; Li, O.; Marshall, E.; et al. Uveal Melanoma UK National Guidelines. *Eur. J. Cancer* **2015**, *51*, 2404–2412. [CrossRef]
14. Hussain, R.N.; Chiu, A.; Pittam, B.; Taktak, A.; Damato, B.E.; Kacperek, A.; Errington, D.; Cauchi, P.; Chadha, V.; Connolly, J.; et al. Proton beam radiotherapy for choroidal and ciliary body melanoma in the UK—National audit of referral patterns of 1084 cases. *Eye* **2022**, *37*, 1033–1036. [CrossRef]
15. Kent, D.; Noonan, C.P.; Damato, B.E. Management of Irish patients with intraocular melanoma referred to Liverpool, England. *Acta Ophthalmol. Scand.* **1998**, *76*, 584–588. [CrossRef] [PubMed]
16. Daftari, I.K.; Renner, T.R.; Verhey, L.J.; Singh, R.P.; Nyman, M.; Petti, P.L.; Castro, J.R. New UCSF proton ocular beam facility at the Crocker Nuclear Laboratory Cyclotron (UC Davis). *Nucl. Instrum. Methods Phys. Res. A* **1996**, *380*, 597–612. [CrossRef]
17. Sayan, M.; Mamidanna, S.; Oncel, D.; Jan, I.; Vergalasova, I.; Weiner, J.; Ohri, N.; Acikalin, B.; Chundury, A. Clinical management of uveal melanoma: A comprehensive review with a treatment algorithm. *Radiat. Oncol. J.* **2020**, *38*, 162–169. [CrossRef] [PubMed]
18. Dendale, R.; Lumbroso-Le Rouic, L.; Noel, G.; Feuvret, L.; Levy, C.; Delacroix, S.; Meyer, A.; Nauraye, C.; Mazal, A.; Mammar, H.; et al. Proton beam radiotherapy for uveal melanoma: Results of Curie Institut–Orsay Proton Therapy Center (ICPO). *Int. J. Radiat. Oncol. Biol. Phys.* **2006**, *65*, 780–787. [CrossRef]
19. Wang, S.; Gonzalez, G.; Sun, L.; Xu, Y.; Pandey, P.; Chen, Y.; Xiang, S. (Liangzhong). Real-time tracking of the Bragg peak during proton therapy via 3D protoacoustic Imaging in a clinical scenario. *NPJ Imaging* **2024**, *2*, 34. [CrossRef]
20. Byun, H.K.; Han, M.C.; Yang, K.; Kim, J.S.; Yoo, G.S.; Koom, W.S.; Kim, Y.B. Physical and Biological Characteristics of Particle Therapy for Oncologists. *Cancer Res. Treat. Off. J. Korean Cancer Assoc.* **2021**, *53*, 611. [CrossRef]
21. Wilkinson, B.; Hill, M.A.; Parsons, J.L. The Cellular Response to Complex DNA Damage Induced by Ionising Radiation. *Int. J. Mol. Sci.* **2023**, *24*, 4920. [CrossRef]
22. Jarczak, J.; Karska-Basta, I.; Romanowska-Dixon, B. Deterioration of Visual Acuity after Brachytherapy and Proton Therapy of Uveal Melanoma, and Methods of Counteracting This Complication Based on Recent Publications. *Medicina* **2023**, *59*, 1131. [CrossRef]
23. Damato, B.E. Treatment selection for uveal melanoma. *Dev. Ophthalmol.* **2012**, *49*, 16–26. [CrossRef]
24. Chan, A.W.; Lin, H.; Yacoub, I.; Chhabra, A.M.; Choi, J.I.; Simone, C.B., 2nd. Proton Therapy in Uveal Melanoma. *Cancers* **2024**, *16*, 3497. [CrossRef]
25. Kosydar, S.; Robertson, J.C.; Woodfin, M.; Mayr, N.A.; Sahgal, A.; Timmerman, R.D.; Lo, S.S. Systematic Review and Meta-Analysis on the Use of Photon-based Stereotactic Radiosurgery Versus Fractionated Stereotactic Radiotherapy for the Treatment of Uveal Melanoma. *Am. J. Clin. Oncol.* **2021**, *44*, 32–42. [CrossRef]
26. Wang, Z.; Nabhan, M.; Schild, S.E.; Stafford, S.L.; Petersen, I.A.; Foote, R.L.; Murad, M.H. Charged particle radiation therapy for uveal melanoma: A systematic review and meta-analysis. *Int. J. Radiat. Oncol. Biol. Phys.* **2013**, *86*, 18–26. [CrossRef]
27. Bekkering, G.E.; Rutjes, A.W.S.; Vlassov, V.V.; Aebersold, D.M.; Von Bremen, K.; Jüni, P.; Kleijnen, J. The effectiveness and safety of proton radiation therapy for indications of the eye: A systematic review. *Strahlenther. Und Onkol.* **2009**, *185*, 211–221. [CrossRef]
28. Yilmaz, M.T.; Sari, S.Y.; Zorlu, F.; Yazici, G. External Beam Radiotherapy in the Management of Uveal Melanoma. *Curr. Treat. Options Oncol.* **2024**, *25*, 932. [CrossRef] [PubMed]
29. Egger, E.; Zografos, L.; Schalenbourg, A.; Beati, D.; Böhringer, T.; Chamot, L.; Goitein, G. Eye retention after proton beam radiotherapy for uveal melanoma. *Int. J. Radiat. Oncol. Biol. Phys.* **2003**, *55*, 867–880. [CrossRef] [PubMed]
30. Damato, B.; Kacperek, A.; Chopra, M.; Campbell, I.R.; Errington, R.D. Proton beam radiotherapy of choroidal melanoma: The Liverpool-Clatterbridge experience. *Int. J. Radiat. Oncol. Biol. Phys.* **2005**, *62*, 1405–1411. [CrossRef] [PubMed]
31. Caujolle, J.P.; Mammar, H.; Chamorey, E.; Pinon, F.; Herault, J.; Gastaud, P. Proton beam radiotherapy for uveal melanomas at nice teaching hospital: 16 years' experience. *Int. J. Radiat. Oncol. Biol. Phys.* **2010**, *78*, 98–103. [CrossRef]
32. Macdonald, E.C.A.; Cauchi, P.; Kemp, E.G. Proton beam therapy for the treatment of uveal melanoma in Scotland. *Br. J. Ophthalmol.* **2011**, *95*, 1691–1695. [CrossRef]
33. Tran, E.; Ma, R.; Paton, K.; Blackmore, E.; Pickles, T. Outcomes of Proton Radiation Therapy for Peripapillary Choroidal Melanoma at the BC Cancer Agency. *Int. J. Radiat. Oncol. Biol. Phys.* **2012**, *83*, 1425–1431. [CrossRef]
34. Seibel, I.; Cordini, D.; Rehak, M.; Hager, A.; Riechardt, A.I.; Böker, A.; Heufelder, J.; Weber, A.; Gollrad, J.; Besserer, A.; et al. Local Recurrence After Primary Proton Beam Therapy in Uveal Melanoma: Risk Factors, Retreatment Approaches, and Outcome. *Am. J. Ophthalmol.* **2015**, *160*, 628–636. [CrossRef]
35. Bensoussan, E.; Thariat, J.; Maschi, C.; Delas, J.; Schouver, E.D.; Hérault, J.; Baillif, S.; Caujolle, J.P. Outcomes After Proton Beam Therapy for Large Choroidal Melanomas in 492 Patients. *Am. J. Ophthalmol.* **2016**, *165*, 78–87. [CrossRef] [PubMed]

36. Konstantinidis, L.; Groenewald, C.; Coupland, S.E.; Damato, B. Trans-scleral local resection of toxic choroidal melanoma after proton beam radiotherapy. *Br. J. Ophthalmol.* **2014**, *98*, 775–779. [CrossRef] [PubMed]
37. Damato, B.; Duke, C.; Coupland, S.E.; Hiscott, P.; Smith, P.A.; Campbell, I.; Douglas, A.; Howard, P. Cytogenetics of Uveal Melanoma: A 7-Year Clinical Experience. *Ophthalmology* **2007**, *114*, 1925–1931.e1. [CrossRef]
38. Dogrusöz, M.; Bagger, M.; Van Duinen, S.G.; Kroes, W.G.; Ruivenkamp, C.A.L.; Böhringer, S.; Andersen, K.K.; Luyten, G.P.M.; Kiilgaard, J.F.; Jager, M.J. The prognostic value of AJCC staging in uveal melanoma is enhanced by adding chromosome 3 and 8q status. *Invest. Ophthalmol. Vis. Sci.* **2017**, *58*, 833–842. [CrossRef]
39. Dogrusöz, M.; Jager, M.J. Genetic prognostication in uveal melanoma. *Acta Ophthalmol.* **2018**, *96*, 331–347. [CrossRef]
40. Rodriguez-Vidal, C.; Fernandez-Diaz, D.; Fernandez-Marta, B.; Lago-Baameiro, N.; Pardo, M.; Silva, P.; Paniagua, L.; Blanco-Teijeiro, M.J.; Piñeiro, A.; Bande, M. Treatment of Metastatic Uveal Melanoma: Systematic Review. *Cancers* **2020**, *12*, 2557. [CrossRef] [PubMed]
41. Robertson, A.G.; Shih, J.; Yau, C.; Gibb, E.A.; Oba, J.; Mungall, K.L.; Hess, J.M.; Uzunangelov, V.; Walter, V.; Danilova, L.; et al. Integrative Analysis Identifies Four Molecular and Clinical Subsets in Uveal Melanoma. *Cancer Cell* **2017**, *32*, 204. [CrossRef]
42. Thornton, S.; Coupland, S.E.; Heimann, H.; Hussain, R.; Groenewald, C.; Kacperek, A.; Damato, B.; Taktak, A.; Eleuteri, A.; Kalirai, H. Effects of plaque brachytherapy and proton beam radiotherapy on prognostic testing: A comparison of uveal melanoma genotyped by microsatellite analysis. *Br. J. Ophthalmol.* **2020**, *104*, 1462–1466. [CrossRef]
43. Davis, A.J.; Chen, D.J. Complex DSBs: A need for resection. *Cell Cycle* **2014**, *13*, 3796. [CrossRef]
44. Melia, E.; Parsons, J.L. DNA damage and repair dependencies of ionising radiation modalities. *Biosci. Rep.* **2023**, *43*, BSR20222586. [CrossRef]
45. Collins, A.R.; Ai-guo, M.; Duthie, S.J. The kinetics of repair of oxidative DNA damage (strand breaks and oxidised pyrimidines) in human cells. *Mutat. Res.-DNA Repair* **1995**, *336*, 69–77. [CrossRef]
46. Dianov, G.L.; Hübscher, U. Mammalian Base Excision Repair: The Forgotten Archangel. *Nucleic Acids Res.* **2013**, *41*, 3483. [CrossRef]
47. Caldecott, K.W. Causes and consequences of DNA single-strand breaks. *Trends Biochem. Sci.* **2024**, *49*, 68–78. [CrossRef] [PubMed]
48. Gohil, D.; Sarker, A.H.; Roy, R. Base Excision Repair: Mechanisms and Impact in Biology, Disease, and Medicine. *Int. J. Mol. Sci.* **2023**, *24*, 14186. [CrossRef] [PubMed]
49. Vitti, E.T.; Parsons, J.L. The Radiobiological Effects of Proton Beam Therapy: Impact on DNA Damage and Repair. *Cancers* **2019**, *11*, 946. [CrossRef]
50. Symington, L.S.; Gautier, J. Double-strand break end resection and repair pathway choice. *Annu. Rev. Genet.* **2011**, *45*, 247–271. [CrossRef] [PubMed]
51. Hou, Z.; Yu, T.; Yi, Q.; Du, Y.; Zhou, L.; Zhao, Y.; Wu, Y.; Wu, L.; Wang, T.; Bian, P. High-complexity of DNA double-strand breaks is key for alternative end-joining choice. *Commun. Biol.* **2024**, *7*, 936. [CrossRef] [PubMed]
52. Bétermier, M.; Bertrand, P.; Lopez, B.S. Is Non-Homologous End-Joining Really an Inherently Error-Prone Process? *PLoS Genet.* **2014**, *10*, e1004086. [CrossRef]
53. Sadoughi, F.; Mirsafaei, L.; Dana, P.M.; Hallajzadeh, J.; Asemi, Z.; Mansournia, M.A.; Montazer, M.; Hosseinpour, M.; Yousefi, B. The role of DNA damage response in chemo- and radio-resistance of cancer cells: Can DDR inhibitors sole the problem? *DNA Repair* **2021**, *101*, 103074. [CrossRef]
54. Moynahan, M.E.; Jasin, M. Mitotic homologous recombination maintains genomic stability and suppresses tumorigenesis. *Nat. Rev. Mol. Cell Biol.* **2010**, *11*, 196–207. [CrossRef]
55. Fabbrizi, M.R.; Nickson, C.M.; Hughes, J.R.; Robinson, E.A.; Vaidya, K.; Rubbi, C.P.; Kacperek, A.; Bryant, H.E.; Helleday, T.; Parsons, J.L. Targeting OGG1 and PARG radiosensitises head and neck cancer cells to high-LET protons through complex DNA damage persistence. *Cell Death Dis.* **2024**, *15*, 150. [CrossRef]
56. Carter, R.J.; Nickson, C.M.; Thompson, J.M.; Kacperek, A.; Hill, M.A.; Parsons, J.L. Characterisation of Deubiquitylating Enzymes in the Cellular Response to High-LET Ionizing Radiation and Complex DNA Damage. *Int. J. Radiat. Oncol. Biol. Phys.* **2019**, *104*, 656–665. [CrossRef]
57. Nickoloff, J.A.; Sharma, N.; Taylor, L. Clustered DNA Double-Strand Breaks: Biological Effects and Relevance to Cancer Radiotherapy. *Genes* **2020**, *11*, 99. [CrossRef]
58. Bright, S.J.; Manandhar, M.; Flint, D.B.; Kolachina, R.; Ben Kacem, M.; Martinus, D.K.J.; Turner, B.X.; Qureshi, I.; McFadden, C.H.; Marinello, P.C.; et al. ATR inhibition radiosensitizes cells through augmented DNA damage and G2 cell cycle arrest abrogation. *JCI Insight* **2024**, *9*, e179599. [CrossRef] [PubMed]
59. Gerelchuluun, A.; Zhu, J.; Su, F.; Asaithamby, A.; Chen, D.J.; Tsuboi, K. Homologous recombination pathway may play a major role in high-LET radiation-induced DNA double-strand break repair. *J. Radiat. Res.* **2014**, *55*, i83. [CrossRef]
60. Kashyap, S.; Jha, J.; Singh, M.K.; Singh, L.; Sen, S.; Kaur, J.; Bajaj, M.S.; Pushker, N. DNA damage response proteins and its role in tumor progression of uveal melanoma with patient outcome. *Clin. Transl. Oncol.* **2020**, *22*, 1472–1480. [CrossRef] [PubMed]

61. Dogrusöz, M.; Trasel, A.R.; Cao, J.; Çolak, S.; van Pelt, S.I.; Kroes, W.G.M.; Teunisse, A.F.A.S.; Alsafadi, S.; van Duinen, S.G.; Luyten, G.P.M.; et al. Differential Expression of DNA Repair Genes in Prognostically-Favorable versus Unfavorable Uveal Melanoma. *Cancers* **2019**, *11*, 1104. [CrossRef]
62. Jha, J.; Singh, M.K.; Singh, L.; Pushker, N.; Bajaj, M.S.; Sen, S.; Kashyap, S. Prognostic relevance of ATM protein in uveal melanoma and its association with clinicopathological factors. *Int. J. Clin. Oncol.* **2019**, *24*, 1526–1535. [CrossRef]
63. Hussain, R.N.; Coupland, S.E.; Khzouz, J.; Kalirai, H.; Parsons, J.L. Inhibition of ATM Increases the Radiosensitivity of Uveal Melanoma Cells to Photons and Protons. *Cancers* **2020**, *12*, 1388. [CrossRef]
64. Lühr, A.; von Neubeck, C.; Pawelke, J.; Seidlitz, A.; Peitzsch, C.; Bentzen, S.M.; Bortfeld, T.; Debus, J.; Deutsch, E.; Langendijk, J.A.; et al. "Radiobiology of Proton Therapy": Results of an international expert workshop. *Radiother. Oncol.* **2018**, *128*, 56–67. [CrossRef]
65. Roy, A.; Bera, S.; Saso, L.; Dwarakanath, B.S. Role of autophagy in tumor response to radiation: Implications for improving radiotherapy. *Front. Oncol.* **2022**, *12*, 957373. [CrossRef]
66. Wang, J.Z.; Paulus, P.; Niu, Y.; Zhu, L.; Morisseau, C.; Rawling, T.; Murray, M.; Hammock, B.D.; Zhou, F. The Role of Autophagy in Human Uveal Melanoma and the Development of Potential Disease Biomarkers and Novel Therapeutic Paradigms. *Biomedicines* **2024**, *12*, 462. [CrossRef] [PubMed]
67. Chaurasia, M.; Bhatt, A.N.; Das, A.; Dwarakanath, B.S.; Sharma, K. Radiation-induced autophagy: Mechanisms and consequences. *Free Radic. Res.* **2016**, *50*, 273–290. [CrossRef] [PubMed]
68. Hill, R.M.; Fok, M.; Grundy, G.; Parsons, J.L.; Rocha, S. The Role of Autophagy in Hypoxia-Induced Radioresistance. *Radiother. Oncol.* **2023**, *189*, 109951. [CrossRef] [PubMed]
69. Patel, N.H.; Sohal, S.S.; Manjili, M.H.; Harrell, J.C.; Gewirtz, D.A. The Roles of Autophagy and Senescence in the Tumor Cell Response to Radiation. *Radiat. Res.* **2020**, *194*, 103. [CrossRef]
70. Li, L.; Liu, W.-L.; Su, L.; Lu, Z.-C.; He, X.-S. The Role of Autophagy in Cancer Radiotherapy. *Curr. Mol. Pharmacol.* **2019**, *13*, 31–40. [CrossRef]
71. Liu, S.Z.; Yao, S.J.; Yang, H.; Liu, S.J.; Wang, Y.J. Autophagy: Regulator of cell death. *Cell Death Dis.* **2023**, *14*, 648. [CrossRef] [PubMed]
72. Noguchi, M.; Hirata, N.; Tanaka, T.; Suizu, F.; Nakajima, H.; Chiorini, J.A. Autophagy as a modulator of cell death machinery. *Cell Death Dis.* **2020**, *11*, 517. [CrossRef]
73. Giatromanolaki, A.N.; St Charitoudis, G.; Bechrakis, N.E.; Kozobolis, V.P.; Koukourakis, M.I.; Foerster, M.H.; Sivridis, E.L. Autophagy patterns and prognosis in uveal melanomas. *Mod. Pathol.* **2011**, *24*, 1036–1045. [CrossRef]
74. Truong, A.; Yoo, J.H.; Scherzer, M.T.; Sanchez, J.M.S.; Dale, K.J.; Kinsey, C.G.; Richards, J.R.; Shin, D.; Ghazi, P.C.; Onken, M.D.; et al. Chloroquine sensitizes GNAQ/11-mutated melanoma to MEK1/2 inhibition. *Clin. Cancer Res.* **2020**, *26*, 6374–6386. [CrossRef]
75. Zhao, J.; Yi, Q.; Li, K.; Chen, L.; Dai, L.; Feng, J.; Li, Y.; Zhou, M.; Sun, J. A multi-omics deep learning model for hypoxia phenotype to predict tumor aggressiveness and prognosis in uveal melanoma for rationalized hypoxia-targeted therapy. *Comput. Struct. Biotechnol. J.* **2022**, *20*, 3182–3194. [CrossRef]
76. Beckers, C.; Pruschy, M.; Vetrugno, I. Tumor hypoxia and radiotherapy: A major driver of resistance even for novel radiotherapy modalities. *Semin. Cancer Biol.* **2024**, *98*, 19–30. [CrossRef]
77. Boulefour, W.; Rowinski, E.; Louati, S.; Sotton, S.; Wozny, A.S.; Moreno-Acosta, P.; Mery, B.; Rodriguez-Lafrasse, C.; Magne, N. A Review of the Role of Hypoxia in Radioresistance in Cancer Therapy. *Med. Sci. Monit.* **2021**, *27*, e934116-1. [CrossRef]
78. D-Kondo, N.; Masilela, T.A.M.; Shin, W.G.; Faddegon, B.; LaVerne, J.; Schuemann, J.; Ramos-Mendez, J. Modeling the oxygen effect in DNA strand break induced by gamma-rays with TOPAS-nBio. *Phys. Med. Biol.* **2024**, *69*, 215028. [CrossRef]
79. Sun, J.; Ding, J.; Yue, H.; Xu, B.; Sodhi, A.; Xue, K.; Ren, H.; Qian, J. Hypoxia-induced BNIP3 facilitates the progression and metastasis of uveal melanoma by driving metabolic reprogramming. *Autophagy* **2024**, *21*, 191–209. [CrossRef] [PubMed]
80. Kwon, J.; Lee, D.; Lee, S.A. BAP1 as a guardian of genome stability: Implications in human cancer. *Exp. Mol. Med.* **2023**, *55*, 745–754. [CrossRef]
81. Hu, J.; Li, X.; Yang, L.; Li, H. Hypoxia, a key factor in the immune microenvironment. *Biomed. Pharmacother.* **2022**, *151*, 113068. [CrossRef]
82. Chen, S.; Sang, N. Hypoxia-Inducible Factor-1: A critical player in the survival strategy of stressed cells. *J. Cell Biochem.* **2016**, *117*, 267. [CrossRef]
83. Paraskeva, E.; Haj Zen, A.; Zuheir Bakleh, M.; Al Haj Zen, A. The Distinct Role of HIF-1α and HIF-2α in Hypoxia and Angiogenesis. *Cells* **2025**, *14*, 673. [CrossRef]
84. Asnaghi, L.; Lin, M.H.; Lim, K.S.; Lim, K.J.; Tripathy, A.; Wendeborn, M.; Merbs, S.L.; Handa, J.T.; Sodhi, A.; Bar, E.E.; et al. Hypoxia Promotes Uveal Melanoma Invasion through Enhanced Notch and MAPK Activation. *PLoS ONE* **2014**, *9*, e105372. [CrossRef]

85. Zemba, M.; Dumitrescu, O.M.; Gheorghe, A.G.; Radu, M.; Ionescu, M.A.; Vatafu, A.; Dinu, V. Ocular Complications of Radiotherapy in Uveal Melanoma. *Cancers* **2023**, *15*, 333. [CrossRef]
86. Lane, A.M.; Hartley, C.; Go, A.K.; Wu, F.; Gragoudas, E.S.; Kim, I.K. Survival of patients with recurrent uveal melanoma after treatment with radiation therapy. *Br. J. Ophthalmol.* **2024**, *108*, 729–734. [CrossRef] [PubMed]
87. Huang, R.X.; Zhou, P.K. DNA damage response signaling pathways and targets for radiotherapy sensitization in cancer. *Signal Transduct. Target. Ther.* **2020**, *5*, 60. [CrossRef]
88. Blackford, A.N.; Jackson, S.P. ATM, ATR, and DNA-PK: The Trinity at the Heart of the DNA Damage Response. *Mol. Cell* **2017**, *66*, 801–817. [CrossRef] [PubMed]
89. Doherty, R.E.; Bryant, H.E.; Valluru, M.K.; Rennie, I.G.; Sisley, K. Increased Non-Homologous End Joining Makes DNA-PK a Promising Target for Therapeutic Intervention in Uveal Melanoma. *Cancers* **2019**, *11*, 1278. [CrossRef] [PubMed]
90. Zhang, B.; Wu, H.; Hao, J.; Wu, Y.; Yang, B. Inhibition of DNA-PKcs activity re-sensitizes uveal melanoma cells to radio- and chemotherapy. *Biochem. Biophys. Res. Commun.* **2020**, *522*, 639–646. [CrossRef]
91. Rose, M.; Burgess, J.T.; O'Byrne, K.; Richard, D.J.; Bolderson, E. PARP Inhibitors: Clinical Relevance, Mechanisms of Action and Tumor Resistance. *Front. Cell Dev. Biol.* **2020**, *8*, 564601. [CrossRef]
92. Farmer, H.; McCabe, H.; Lord, C.J.; Tutt, A.H.J.; Johnson, D.A.; Richardson, T.B.; Santarosa, M.; Dillon, K.J.; Hickson, I.; Knights, C.; et al. Targeting the DNA repair defect in BRCA mutant cells as a therapeutic strategy. *Nature* **2005**, *434*, 917–921. [CrossRef]
93. Bryant, H.E.; Schultz, N.; Thomas, H.D.; Parker, K.M.; Flower, D.; Lopez, E.; Kyle, S.; Meuth, M.; Curtin, N.J.; Helleday, T. Specific killing of BRCA2-deficient tumours with inhibitors of poly(ADP-ribose) polymerase. *Nature* **2005**, *434*, 913–917. [CrossRef]
94. Louie, B.H.; Kurzrock, R. BAP1: Not just a BRCA1-associated protein. *Cancer Treat. Rev.* **2020**, *90*, 102091. [CrossRef] [PubMed]
95. de Koning, L.; Decaudin, D.; Botty, R.; Nicolas, A.; Carita, G.; Schuller, M.; Ouine, B.; Cartier, A.; Naguez, A.; Fleury, J.; et al. PARP Inhibition Increases the Response to Chemotherapy in Uveal Melanoma. *Cancers* **2019**, *11*, 751. [CrossRef]
96. Bland, P.; Saville, H.; Wai, P.T.; Curnow, L.; Muirhead, G.; Nieminuszczy, J.; Ravindran, N.; John, M.B.; Hedayat, S.; Barker, H.E.; et al. SF3B1 hotspot mutations confer sensitivity to PARP inhibition by eliciting a defective replication stress response. *Nat. Genet.* **2023**, *55*, 1311–1323. [CrossRef]
97. Zhu, X.; Zou, W.; Meng, X.; Ji, J.; Wang, X.; Shu, H.; Chen, Y.; Pan, D.; Wang, K.; Zhou, F. Elaiophylin Inhibits Tumorigenesis of Human Uveal Melanoma by Suppressing Mitophagy and Inducing Oxidative Stress via Modulating SIRT1/FoxO3a Signaling. *Front. Oncol.* **2022**, *12*, 788496. [CrossRef] [PubMed]
98. Karasic, T.B.; O'Hara, M.H.; Loaiza-Bonilla, A.; Reiss, K.A.; Teitelbaum, U.R.; Borazanci, E.; De Jesus-Acosta, A.; Redlinger, C.; Burrell, J.A.; Laheru, D.A.; et al. Effect of Gemcitabine and nab-Paclitaxel with or Without Hydroxychloroquine on Patients With Advanced Pancreatic Cancer: A Phase 2 Randomized Clinical Trial. *JAMA Oncol.* **2019**, *5*, 993–998. [CrossRef] [PubMed]
99. Anandharaj, A.; Cinghu, S.; Park, W.Y. Rapamycin-mediated mTOR inhibition attenuates survivin and sensitizes glioblastoma cells to radiation therapy. *Acta Biochim. Biophys. Sin.* **2011**, *43*, 292–300. [CrossRef]
100. Kim, E.J.; Jeong, J.H.; Bae, S.; Kang, S.; Kim, C.H.; Lim, Y.B. mTOR inhibitors radiosensitize PTEN-deficient non-small-cell lung cancer cells harboring an EGFR activating mutation by inducing autophagy. *J. Cell Biochem.* **2013**, *114*, 1248–1256. [CrossRef]
101. Li, Q.; Xia, L.; Sun, C.; Zhang, H.; Zheng, M.; Zhang, H.; Lu, H.; Wang, Z. Role of Borneol Induced Autophagy in Enhancing Radiosensitivity of Malignant Glioma. *Front. Oncol.* **2021**, *11*, 749987. [CrossRef] [PubMed]
102. Mendenhall, W.M.; Morris, C.G.; Amdur, R.J.; Mendenhall, N.P.; Siemann, D.W. Radiotherapy alone or combined with carbogen breathing for squamous cell carcinoma of the head and neck. *Cancer* **2005**, *104*, 332–337. [CrossRef]
103. Dong, L.; You, S.; Zhang, Q.; Osuka, S.; Devi, N.S.; Kaluz, S.; Ferguson, J.H.; Yang, H.; Chen, G.; Wang, B.; et al. Arylsulfonamide 64B inhibits hypoxia/HIF-induced expression of c-Met and CXCR4 and reduces primary tumor growth and metastasis of uveal melanoma. *Clin. Cancer Res.* **2018**, *25*, 2206. [CrossRef]
104. Cheng, B.; Ma, X.; Zhou, Y.; Liu, J.; Fei, X.; Pan, W.; Peng, X.; Wang, W.; Chen, J. Recent progress in the development of hypoxia-inducible factor 2α (HIF-2α) modulators: Inhibitors, agonists, and degraders (2009–2024). *Eur. J. Med. Chem.* **2024**, *275*, 116645. [CrossRef]
105. Patel, S.A.; Simon, M.C. Biology of Hypoxia-Inducible Factor-2α in Development and Disease. *Cell Death Differ.* **2008**, *15*, 628. [CrossRef]
106. Nystrom, H.; Jensen, M.F.; Nystrom, P.W. Treatment planning for proton therapy: What is needed in the next 10 years? *Br. J. Radiol.* **2020**, *93*, 20190304. [CrossRef]
107. Parker, T.; Rigney, G.; Kallos, J.; Stefko, S.T.; Kano, H.; Niranjan, A.; Green, A.L.; Aziz, T.; Rath, P.; Lunsford, L.D. Gamma knife radiosurgery for uveal melanomas and metastases: A systematic review and meta-analysis. *Lancet Oncol.* **2020**, *21*, 1526–1536. [CrossRef] [PubMed]
108. Fleury, E.; Pignol, J.P.; Kiliç, E.; Milder, M.; van Rij, C.; Naus, N.; Yavuzyigitoglu, S.; den Toom, W.; Zolnay, A.; Spruijt, K.; et al. Comparison of stereotactic radiotherapy and protons for uveal melanoma patients. *Phys. Imaging Radiat. Oncol.* **2024**, *31*, 100605. [CrossRef] [PubMed]

109. Semeniuk, O.; Yu, E.; Rivard, M.J. Current and Emerging Radiotherapy Options for Uveal Melanoma. *Cancers* **2024**, *16*, 1074. [CrossRef]
110. Hughes, J.R.; Parsons, J.L. FLASH Radiotherapy: Current Knowledge and Future Insights Using Proton-Beam Therapy. *Int. J. Mol. Sci.* **2020**, *21*, 6492. [CrossRef]
111. Di Marco, B.; Sansevero, G.; D'Orsi, B.; De Santis, E.; Salamone, G.; Cavalieri, A.; Masturzo, L.; Celentano, M.; Di Martino, F.; Capaccioli, S.; et al. Unraveling the effects of FLASH and conventional irradiation on retinal pigment epithelial cells: In vitro and in vivo studies. *Sci. Rep.* **2025**, *15*, 22938. [CrossRef] [PubMed]
112. Hrbacek, J.; Kacperek, A.; Beenakker, J.W.M.; Mortimer, L.; Denker, A.; Mazal, A.; Shih, H.A.; Dendale, R.; Slopsema, R.; Heufelder, J.; et al. PTCOG Ocular Statement: Expert Summary of Current Practices and Future Developments in Ocular Proton Therapy. *Int. J. Radiat. Oncol. Biol. Phys.* **2024**, *120*, 1307–1325. [CrossRef] [PubMed]

Disclaimer/Publisher's Note: The statements, opinions and data contained in all publications are solely those of the individual author(s) and contributor(s) and not of MDPI and/or the editor(s). MDPI and/or the editor(s) disclaim responsibility for any injury to people or property resulting from any ideas, methods, instructions or products referred to in the content.

cancers

MDPI

Article

Survival Outcome After Percutaneous Hepatic Perfusion with High-Dose Melphalan for Liver-Dominant Metastatic Uveal Melanoma: A 10-Year Single-Center Experience

Carolin M. Reiner [1,†], Martin A. Schneider [2,†], Hauke Weilert [3,4], Klara Welcker [2], Jochen Hoedtke [5], Andreas H. Mahnken [6], Axel Stang [3,4,*,‡] and Roland Brüning [2,‡]

[1] Asklepios Campus Hamburg, Semmelweis University, 20099 Hamburg, Germany
[2] Department of Diagnostic and Interventional Radiology, Asklepios Hospital Barmbek, 22307 Hamburg, Germany; mar.schneider@asklepios.com (M.A.S.); k.welcker@asklepios.com (K.W.); r.bruening@asklepios.com (R.B.)
[3] Department of Hematology, Oncology and Palliative Care Medicine, Asklepios Hospital Barmbek, 22307 Hamburg, Germany; h.weilert@asklepios.com
[4] Asklepios Tumorzentrum, 22307 Hamburg, Germany
[5] Department of Anesthesiology and Intensive Care Medicine, Asklepios Hospital Barmbek, 22307 Hamburg, Germany; j.hoedtke@asklepios.com
[6] Department of Diagnostic and Interventional Radiology and Nuclear Medicine, St. Josef-Hospital, University Hospital, Ruhr University Bochum, 44791 Bochum, Germany
* Correspondence: a.stang@asklepios.com
† These authors contributed equally to this work.
‡ These authors also contributed equally to this work.

Simple Summary: Melphalan-based percutaneous hepatic perfusion (M-PHP) was approved in 2023 as liver-directed treatment for patients with liver-dominant metastatic uveal melanoma (mUM), which has an overall survival (OS) $\leq$ 12 months. However, the reported M-PHP-related OS benefit varies between 9.6 and 27.4 months and remains poorly defined. Here, we retrospectively assessed the OS outcome in our 10-year experience comprising 99 M-PHP procedures in 38 patients with liver-dominant mUM. The analysis demonstrated a median OS of 29.1 months after first M-PHP treatment; the OS at 1, 2, and 3 years was 79.5%, 53.2%, and 28.5%, respectively. In conclusion, our center's experience demonstrates nearly 2.5-year median OS for M-PHP-treated patients with liver-dominant mUM, which surpasses previously reported OS data. This finding implicates a possible OS benefit from M-PHP treatment in specialized centers, supports the need to account for institutional volume in clinical trials, and provides an OS reference for various novel management strategies for mUM.

Abstract

Background/Objectives: Melphalan-based percutaneous hepatic perfusion (M-PHP) became approved in 2023 for treatment of liver-dominant metastatic uveal melanoma (mUM). Patients with liver-dominant mUM have a poor overall survival (OS) $\leq$ 12 months; however, the reported OS benefit from M-PHP varies in clinical trials from 9.6 to 27.4 months and remains uncertain. Here, we report the OS outcome after 10 years' experience with M-PHP treatment of patients with liver-dominant mUM. Methods: A total of 38 consecutive patients (19 women, median age 57.7 years) with liver-dominant mUM underwent 99 M-PHP procedures (median: 2.6 M-PHP/patient) between April 2014 and March 2024 at our institution. OS outcomes were retrospectively analyzed using Kaplan–Meier methods and Cox proportional hazard models. Results: Median OS was 29.1 months after first M-PHP treatment (median follow-up: 25.8 months). The estimated percentage of patients surviving at 1, 2, and 3 years was 79.5%, 53.2%, and 28.5%, respectively. Each additional M-PHP

cycle was associated with about 40% reduction in the risk of death (hazard ratio = 0.414). Median OS was numerically improved by 8.4 months with ≥3 versus ≤2 cycles of M-PHP administered (29.8 versus 21.4 months, $p = 0.058$). No treatment-related deaths occurred. Conclusions: This study found a clinically meaningful OS benefit in M-PHP-treated patients with liver-dominant mUM, reaching nearly 2.5-year median OS with ≥3 M-PHP cycles administered. This finding supports the need to account for the institutional volume and experience with the M-PHP procedure in both clinical practice and research, and may provide an OS reference for estimating OS gains in the evolving therapeutic landscape for mUM patients.

Keywords: uveal melanoma; liver metastasis; percutaneous hepatic perfusion; melphalan; chemosaturation; survival outcome

1. Introduction

Uveal melanoma (UM) represents 3% of all melanomas and differs profoundly from cutaneous melanoma (CM) in molecular, immunologic, and clinical features [1–5]. Almost 50% of uveal melanoma (UM) patients develop metastatic UM (mUM), usually involving the liver as the prognostically crucial site of disease [6,7]. For those selected patients with resectable mUM, surgery provides a median overall (OS) of ~27 months [8–10]. However, the majority of mUM patients present with unresectable liver metastases, which is usually fatal within 3–12 months due to progressive liver metastases with hepatic failure [11,12]. For mUM patients, hepatic disease control and even slower hepatic progression matters, and therefore OS, rather than response, is the most meaningful endpoint to estimate treatment efficacy in mUM. Until recently, the median OS of mUM patients had been only ~12 months, as consistently assessed in two meta-analyses across all non-surgical treatment modalities [13,14].

While chemotherapy and immune checkpoint inhibitor (ICI) monotherapy have limited efficacy in mUM, dual-ICI regimens with anti-PD-1 and anti-CTLA-4 drugs increase median OS to ~16 months [15–17]. However, considering the risk of ~30–35% serious immune-related adverse events, treatment discontinuation (13.3–28.3%) and treatment-related deaths (0.7–1.0%) associated with the dual-ICI treatment [18,19], the benefit–risk ratio and cost-effectiveness deserve further exploration in mUM [20]. In the subgroup of ~35–45% HLA-A*02:01-positive mUM patients, a phase III study of tebentafusp, a bispecific HLA-directed T-cell engager, showed significantly improved OS compared to chemotherapy or ICI monotherapy (21.6 vs. 16.9 months) [21–23]. However, beyond HLA restriction, the high costs of tebentafusp put considerable financial pressure on the potential beneficiaries and limit clinical access [24].

Given the hepatotropism and limitations of systemic treatments, patients with liver-dominant and liver-only mUM frequently undergo liver-directed therapies (LDT), which have been associated with ~14–16-month median OS across all LDT approaches [13,25,26]. In limited disease, liver lesions can be treated with thermal ablation [27,28] or transarterial chemoembolization (TACE) [29], whereas in cases of multiple liver lesions, selective interstitial radiation therapy (SIRT) [30] and percutaneous hepatic perfusion delivery of high-dose melphalan (M-PHP) [31] are typically employed. M-PHP isolates the hepatic arterial blood flow from the systemic circulation via a double balloon vena cava catheter, saturates the liver with high-dose melphalan, and purifies the venous outflow from residual melphalan by an extracorporeal filtration system [32]. Several phase II trials support the feasibility, safety and efficacy of M-PHP in controlling liver-dominant disease in mUM, but there are

inconsistencies in replicating the same median OS outcome. The reported median OS spans a broad range from 9.6 to 27.4 months [31,33–41], and potential relationships between the number of M-PHP cycles and OS have thus far been poorly investigated.

In the present study, we retrospectively assessed the OS outcome from our 10-year single-center experience using M-PHP as the standard of care (SOC) for patients with liver-dominant mUM. We aimed to correlate our OS estimates to OS efficacy estimates reported in the previous literature to provide information on the potential magnitude of OS benefit from M-PHP in mUM patients for clinical practice and future research.

2. Materials and Methods

2.1. Study Design

This retrospective study included consecutive adult patients (age > 18 years) with histologically confirmed liver-predominant mUM who underwent M-PHP in the radiology department of the Asklepios Hospital Barmbek between April 2014 and March 2024. Patients were allocated for M-PHP treatment based on multidisciplinary tumor board decision; the decision-making for M-PHP treatment was supported by a case-by-case discussion among surgical, radiological, interventional and oncological specialists at our institution. Inclusion criteria and specific thresholds for eligibility of M-PHP treatment were (1) Eastern Cooperative Oncology Group (ECOG) performance status of 0–1, (2) hemoglobin levels $\geq$ 10 g/dL, platelet counts $\geq$ 150,000/µL, and bilirubin levels $\leq$ 2 times the upper limit of normal (ULN), and (3) <70% liver tumor involvement. Patients could have limited extrahepatic disease (EHD). Any number and type of prior treatments were permitted. Patients were excluded if they had (1) extrahepatic metastases larger than 10 mm in lymph nodes (size > 10 mm measured in the short axis) and/or uncontrollable, progressive, and/or predominant EHD at other organ sites, (2) a recent history of transient ischemic attacks or heart failure with a left ventricular ejection fraction < 40%, (3) significant chronic obstructive or restrictive pulmonary disorders, and/or (4) contraindications to general anesthesia.

Baseline imaging was obtained within 6 weeks prior to M-PHP treatment with contrast-enhanced computed tomography (CT) of the chest, abdomen, and pelvis and contrast-enhanced liver magnetic resonance imaging (MRI) to determine vascular anatomy, baseline volume, and distribution of measurable disease; identify extrahepatic disease; and facilitate procedural planning. Patient histories including additional therapies, imaging findings, laboratory tests and values, clinical reports during in-hospital stay and follow-up exams were retrospectively assessed using the institutional medical records, PACS database, and tumor board protocols on e-health platforms. Extracted data were anonymized and transferred into a data sheet for statistical evaluation. The observational follow-up period ended in September 2024, with a recorded date of death or last recorded contact.

2.2. Procedural Details

As described in previous research [42], this approach involved isolating the hepatic circulation using a specialized filtration device, CHEMOSAT® (CHEMOSAT® Second Generation; Delcath Systems Inc., New York, NY, USA), to enable extracorporeal drug removal from the blood. For arterial access, a catheter was inserted into the femoral artery and advanced to the left/right hepatic artery, where a microcatheter administered melphalan at a dose of 3.0 mg/kg ideal body weight, up to a maximum of 220 mg. Venous isolation was achieved using a double-balloon catheter inserted through the contralateral femoral vein, with one balloon positioned below the hepatic veins and the other in the atrium adjacent to the diaphragm portion of the inferior vena cava. The infusion delivered the melphalan solution at a controlled rate, monitored by angiograms to ensure proper flow. This was followed by a 30 min filtration period whereby blood exiting the liver was filtered

extracorporeally to remove the melphalan agent. The filtered blood was then re-infused via the right jugular vein. The procedure, performed under general anesthesia, required close postoperative monitoring, including coagulation status, blood pressure, and laboratory parameters. All patients also received G-CSF to support hematologic recovery and were monitored in intensive care for one night as a precaution.

2.3. Endpoints and Assessments

The primary efficacy endpoint was the median OS after M-PHP treatment. This time-to-event endpoint was defined as the time from the first PHP treatment to date of death for any case, the study cut-off date if still alive in follow-up (30 September 2024), or the last known follow-up date alive; for the latter patients, the OS was assigned censored in the analysis. The secondary exploratory endpoint analysis addressed the impact of the numbers of M-PHP cycles administered on the efficacy endpoint median OS and the risk reduction of patient death by each additional M-PHP cycle administered. For correlation to the efficacy endpoint median OS, patients were stratified in terms of two patient groups who received $\leq$2 or $\geq$3 cycles of M-PHP treatment. Adverse events (AEs) and severe AEs (SAEs) were assessed and graded according to the Clavien–Dindo (CD) [43,44], and Cardiovascular and Interventional Radiological Society of Europe (CIRSE) classification [45].

2.4. Statistical Analysis

Descriptive summary statistics for continuous variables were presented as median and range (minimum/maximum), and categorical variables as frequency, counts and percentages. Time-to-event variables and endpoints were assessed using Kaplan–Meier methods. OS curves and median OS, as well as corresponding 95% confidence intervals (CIs), were generated and estimated with the start date of first M-PHP application. To adjust OS probabilities to each time point, OS data were censored if patients were stated as alive at their last follow-up before the study cut-off follow-up date. The log-rank test was applied to test for significant differences between OS estimates and OS curves; two-sided p values of < 0.05 were considered to indicate statistical significance. Hazard ratios (HRs) from Cox proportional hazard models adjusted to the number M-PHP cycles administered were correlated with efficacy endpoints in terms of risk of death; an HR of <1 indicated a decreased risk of death. Analyses were performed with R 2025 https://r-project.org (accessed on 30 October 2025) and Rstudio IDE 2025 https://posit.co/ (accessed on 30 October 2025). [46,47]

3. Results

3.1. Patient and Study Characteristics

The study included a total of 38 patients (19 [50%] women, median age: 57.5 years; age range: 29–77 years) who underwent a total of 99 M-PHP cycles, with an average of 2.61 M-PHP cycles administered per patient (range 1–6). Exactly half of the cohort (19 patients) received 1 or 2 M-PHP cycles, while the other half (19 patients) underwent $\geq$ 3 cycles (range: 3–6 cycles). At first M-PHP, 34 patients (89.4%) had a liver tumor involvement of $\leq$25%, 6 patients (15.8%) exhibited EHD, and 20 (2.6%) had an elevated (>ULN) LDH level. Before and/or after M-PHP, 21 patients (55.2%) had received additional systemic treatments (chemotherapy, immune checkpoint inhibitors, tebentafusp), and 8 patients (21.0%) had received local liver-directed interventions (transarterial, ablative, or surgical approaches). The demographics and baseline disease characteristics of the patients are described in Table 1.

Table 1. Baseline patient characteristics of patients undergoing melphalan-based percutaneous hepatic perfusion (M-PHP).

Parameters		Entire Cohort
Sample size (n)		38
Age, [1] year		57.5 (29–77)
Male [3]	Count (%)	19 (50)
ECOG-PS, [3] score ≤1	Count (%)	38 (100)
Extent of liver involvement at first M-PHP		
≤10% [3]	Count (%)	29 (76.3)
10–25% [3]	Count (%)	5 (13.2)
25–50%, [3]	Count (%)	3 (7.9)
>50% [3]	Count (%)	1 (2.6)
Extrahepatic disease at first M-PHP		
Yes [3,4]	Count (%)	6 (15.8)
Median time since primary diagnosis to first M-PHP		
Time, [2] years (initial diagnosis uveal melanoma—last contact)	Median (IQR)	3.98
Time, [2] years (initial diagnosis hepatic metastasis/es—last contact)	Median (IQR)	1.95
Lactate dehydrogenase (LDH) before first M-PHP		
>ULN [5] at first M-PHP [3]	Count (%)	20 (52.6)
Additional systemic therapy before/after M-PHP		
Chemotherapy, [3,6]	Count (%)	7 (18.4)
Immune checkpoint inhibitors, [3,7]	Count (%)	11 (28.9)
Tebentafusp only [3]	Count (%)	3 (7.9)
Additional liver-directed therapy before/after M-PHP		
Transarterial approaches, [3,8]	Count (%)	2 (5.26)
Ablative approaches, [3,9]	Count (%)	2 (5.26)
Surgical resection [3]	Count (%)	4 (10.5)
No additional treatments		
Best supportive care (BSC) [3]	Count (%)	17 (44.7)

[1] Mean (standard deviation) [normal data distribution]; [2] median (quartile 1, quartile 3) [outside normal distribution]; [3] count (percentage); [4] lymph node, lung, bone, other visceral, soft tissue, brain; [5] ULN, upper limit of normal; [6] dacarbazine, temozolomide, gemcitabine, platinum, and/or taxane; [7] dual-agent ICI ipilimumab and nivolumab, or monotherapy ipilimumab, nivolumab, or pembrolizumab; [8] transarterial chemoembolization (TACE), or selective internal radiotherapy (SIRT); [9] radiofreqency ablation (RFA), microwave ablation (MWA).

3.2. Survival Outcome

Patient status evaluation at the last study cut-off follow-up date on 30 September 2024 identified 23 (60.5%) patients who had died during the follow-up period. None of the deaths were considered related to M-PHP treatment, device, or procedure. Furthermore, 11 (29%) alive patients were in active follow-up, and 4 patients (10.5%) who were lost to the

last follow-up date were censored as alive. These four patients are international patients who returned to their home countries after completing M-PHP treatment; all four patients were alive at their last known follow-up dates within 6 months after their last M-PHP cycle, and there was no evidence of death. After a median follow-up from the date of first M-PHP treatment of 25.8 months, the estimated median OS for the entire cohort was 29.1 months (95% CI: 18.4–38.9 months), and 1-, 2-, and 3-year OS rates were 79.5% (95% CI: 67.0–94.3%), 53.2% (95% CI: 38.2–74.0%), and 28.5% (95% CI: 15.4–52.8%) (Figure 1).

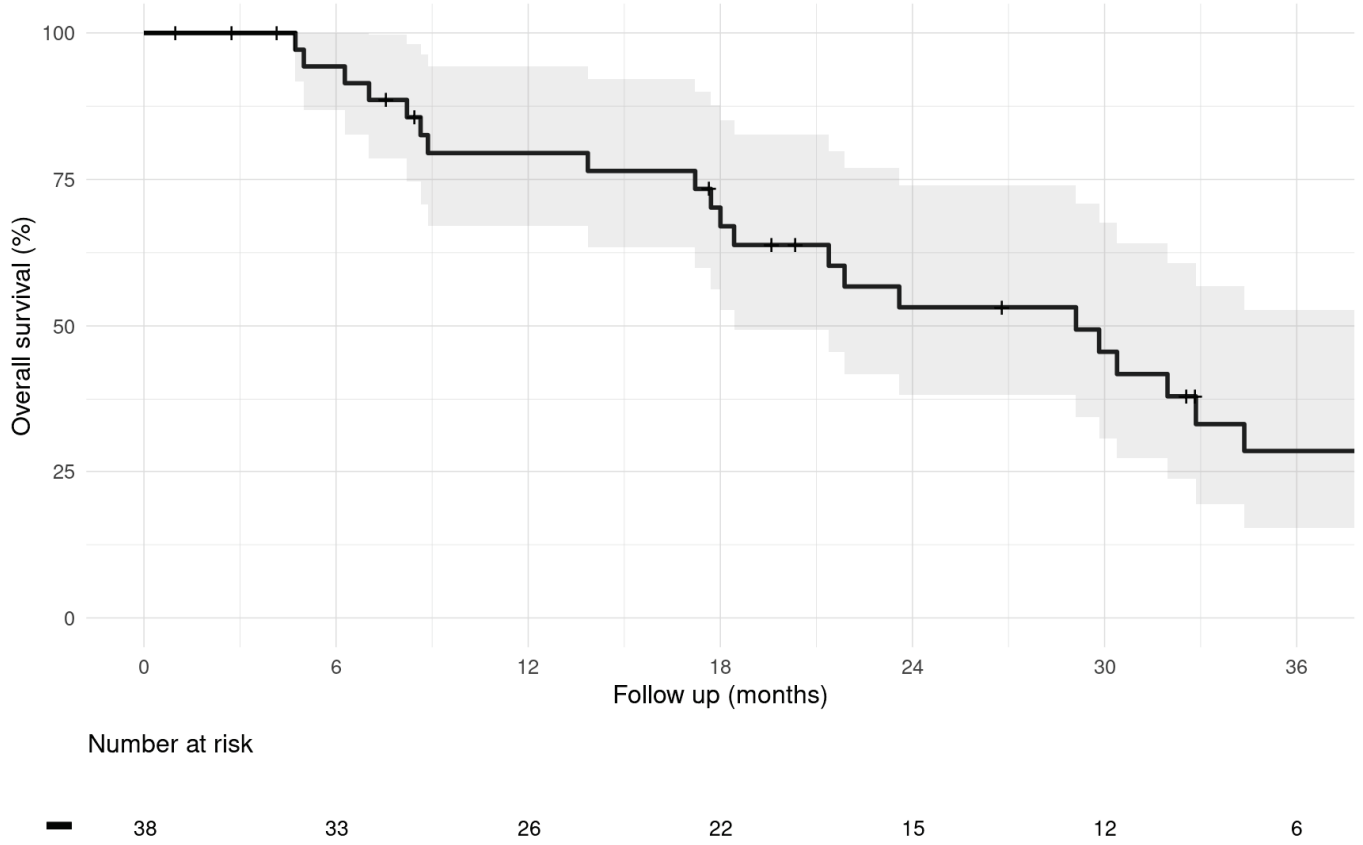


Figure 1. Kaplan–Meier graph of overall survival of the entire study population calculated from first M-PHP treatment. (Median; 95% CI).

3.3. Number of M-PHP Cycles and Survival Outcome

Patients receiving ≥3 M-PHP cycles exhibited a median OS of 29.8 months (95% CI: 21.9–N/A), compared to 21.4 months (95% CI: 8.87–N/A) for those receiving ≤2 cycles of M-PHP; the corresponding 1-, 2-, and 3-year OS rates were 89.5% (95% CI: 76.7–100%), 59.7% (95% CI: 40.3–88.5%), and 28% (95% CI: 11.7–67.1%) versus 66.5% (95% CI: 46.2–95.7%), 44.3% (95% CI: 24.6–79.8%), and 27.7% (95% CI: 11.4–67.5%) (Figure 2). In comparative analysis, the trend towards numerically improved median OS by 8.4 months failed to show statistical significance ($p = 0.058$). Further, especially for the longer-term 3-year OS rates, the 95% CIs were largely overlapping (Figure 2). Cox proportional hazards models showed that each additional M-PHP cycle was associated with about 40% reduction in the risk of death (HR = 0.414), which supports the observed trend towards an improved OS with increasing numbers of M-PHPs administered.

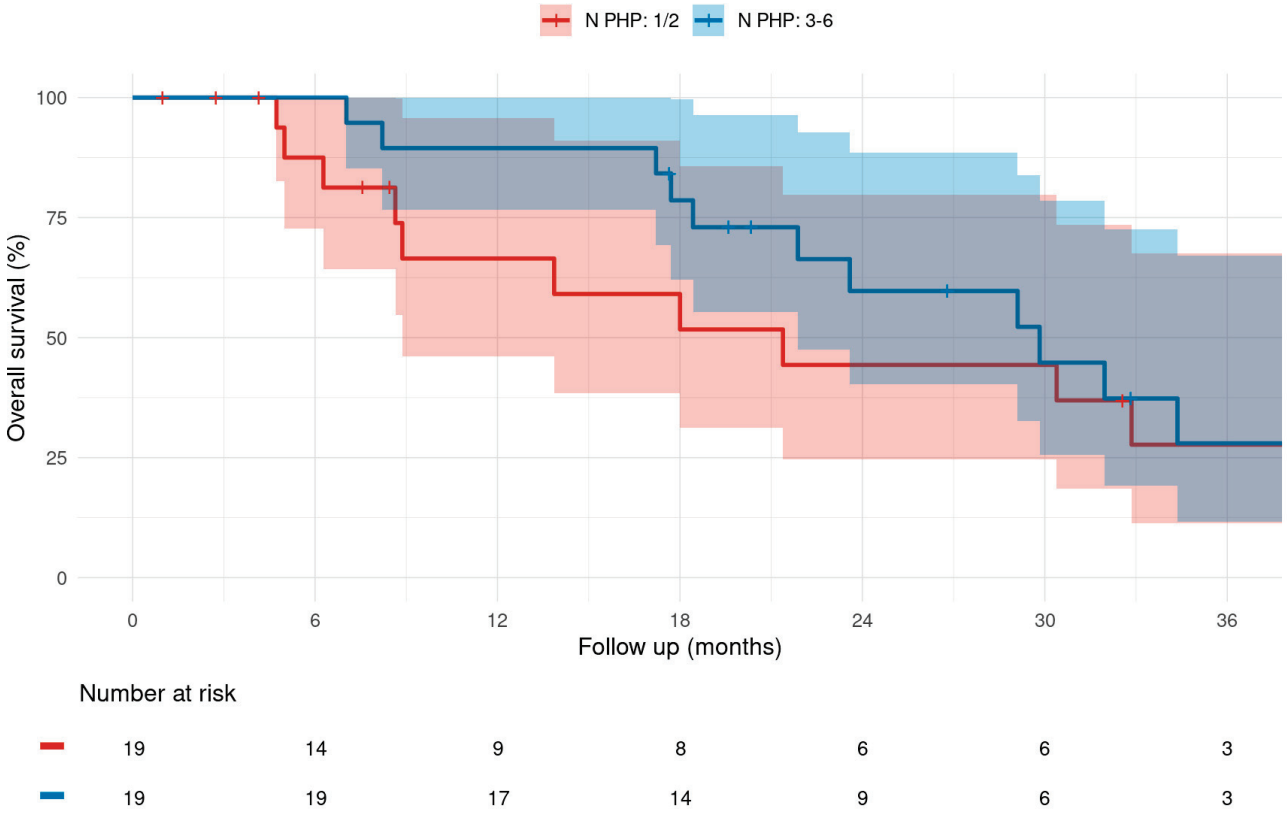


Figure 2. Kaplan–Meier graph of overall survival difference calculated from first M-PHP treatment for a total of 1–2 versus 3–6 M-PHP cycles administered. (Median; 95% CI).

3.4. Safety

Out of the 38 M-PHP-treated patients, 4 patients (10.5%) experienced procedure-related AEs graded ≥ 2 according to CD and CIRSE classification. Post-M-PHP AEs included one heparin-induced thrombocytopenia type II managed appropriately with alternative anticoagulation strategies (CD grade 2, CIRSE grade 2), one pulmonary embolism treated successfully by thrombolytic therapy (CD grade 2, CIRSE grade 3), one non-ST Elevation Myocardial Infarction (NSTEMI) due to an intravasal coronary thrombus treated successfully by coronary stenting and thrombolysis (CD grade 3, CIRSE grade 3), and one cerebral artery basilar embolism in conjunction with bilateral pulmonary embolism requiring interventional neuroradiological thrombectomy and systemic thrombolysis, and leaving the patient with long-term mild sequelea (CD grade 4, CIRSE grade 4). There were no procedure-related deaths. Detailed AE data are summarized in Table 2.

Table 2. Adverse events (AEs) graded ≥ 2 according to the Clavien–Dindo (CD) and Cardiovascular and Interventional Radiological Society of Europe (CIRSE) classification after melphalan-based percutaneous hepatic perfusion (M-PHP) for liver-dominant metastatic uveal melanoma.

Grade	CD	No.	Grade	CIRSE	No
1	Deviation from normal postoperative course without need for pharmacological treatment or surgical, endoscopic and radiological interventions	NA	1	Complication during the procedure which could be solved within the same session; no additional therapy, no post-procedure sequelae	NA

Table 2. *Cont.*

Grade	CD	No.	Grade	CIRSE	No
2	Requiring pharmacological treatment with drugs other than such allowed for grade I	2 [a,b]	2	Prolonged observation including overnight stay as a deviation from the normal post-therapeutic course <48	1 [a]
3	Requiring surgical, endoscopic or radiological intervention	1 [c]	3	Additional post-procedure therapy or prolonged hospital stay (48 h) required; no post-procedure sequelae	2 [b,c]
4	Life-threatening complication (including central nerve system complications) requiring Intensive Unit Care	1 [d]	4	Complication causing a permanent mild sequelae (resuming work and independent living)	1 [d]
5	Death	0	5	Complication causing permanent severe sequelae (requiring ongoing assistance in daily life)	0
			6	Death	0
All	Grades 2–5	4		Grades 2–6	4

[a] Heparin-induced Thrombocytopenia Type II managed appropriately with alternative anticoagulation strategies (CD grade 2, CIRSE grade 2). [b] Pulmonary embolism treated successfully by thrombolytic therapy (CD grade 2, CIRSE grade 3). [c] Non-ST Elevation Myocardial Infarction due to intravasal coronary thrombus treated successfully by coronary stenting and thrombolysis (CD grade 3, CIRSE grade 3). [d] Cerebral artery basilar embolism in conjunction with bilateral pulmonary embolism requiring interventional neuroradiological thrombectomy and systemic thrombolysis, and leaving the patient with long-term mild sequelae (CD grade 4, CIRSE grade 4).

4. Discussion

In the present study, we found a median OS of 29.1 months after first administration of M-PHP in 38 patients with liver-dominant mUM. The estimated percentages of patients' 1-, 2-, and 3-year OS were 79.5%, 53.2%, and 28.5%, respectively. The clinical significance of our study lies in providing long-term outcome data for M-PHP in mUM, supporting the procedure's potential OS benefit. Notably, no treatment-related mortality occurred, and serious procedure-related complications were infrequent (4 out of 38 patients) and manageable, supporting the procedure's safety. However, the OS estimates presented are observational and, as such, are exploratory and intended to provide information on potential M-PHP-related OS benefits for clinical practice and future research.

When estimating potential M-PHP-related OS benefits from our OS data, it seems helpful to refer to OS benchmarks in the evolving therapeutic landscape for mUM. First, until recently, the valid historical median OS of mUM patients was ~12 months, which has been consistently assessed in two meta-analyses across all non-surgical treatment groups [13,14]. Second, dual-ICI, which has become the first-line therapy for a considerable proportion of patients with mUM, was associated with ~16-month median OS in a recent

meta-analysis [17]. Third, the median OS of 21.6 months, and the OS rates at 1, 2, and 3 years of 72%, 45%, and 27%, respectively, for tebentafusp in the landmark approval phase III trial are even slightly lower than those receiving M-PHP in our study [21,22]. Notably, use of tebentafusp is limited to ~35–45% HLA-A*02:01-positive mUM patients, and puts considerable financial pressure (additional 0.47 quality-adjusted life years [QALYs], incremental costs of USD 444.280, and incremental cost-effectiveness ratio of USD 953.230/QUALY) on the OS beneficiaries [24]. Collectively, the median OS found in our observational study (29.1 months) is more than twice as high as the historical OS (~12 months), and nearly 8 months higher than the median OS observed with the currently best pharmacotherapy of mUM (21.6 months). Although cross-trial efficacy comparison is methodically difficult, these OS differences are large enough to be considered clinically meaningful, and they apply to ~90% of mUM patients, as the liver is the primary (~90%), only (~50%) and prognostically crucial site of disease [6,7,11,12]. Notably, M-PHP received approval in 2023 for liver-dominant mUM based on the FOCUS trial, which demonstrated consistent efficacy across patients with exclusively hepatic and limited extrahepatic disease [31].

The multicenter phase III FOCUS (M-PHP) and SCANDIUM trial (M-IHP) evaluated hepatic perfusion with high-dose melphalan in mUM patients compared to a control group receiving best alternative care (BAC) according to investigators' choice (TACE, chemotherapy, ICI monotherapy) [48,49]. Both trials found a clinically meaningful albeit not significantly improved median OS by ~4 months in favor of M-PHP (18.5 vs. 14.5 months) or M-IHP (21.7 vs. 17.6 months). The final results from these two phase III trials, published in 2025, provide the current strongest evidence for a disease-modifying effect and OS gain from hepatic perfusion with high-dose melphalan in mUM patients. Notably, the FOCUS trial closed early due to slow recruitment (85 patients enrolled vs. 240 planned), which illustrates the difficulty to conduct randomized trials aimed at comparing treatments head-to-head in low-prevalence mUM.

There were no M-PHP procedure-related deaths in our study cohort. However, post-M-PHP thromboembolic events were a notable complication in 10.5% of our patients, indicating cautious use of protamine sulfate infusion to reverse heparinization in the post-M-PHP phase. A recent meta-analysis found, on average, a similar OS (17.1 vs. 17.3 month) but higher 30-day-mortality (5.5% vs. 1.8%) for surgical M-IHP compared to minimally invasive M-PHP as loco-regional treatment for liver metastases in mUM [50]. In addition to that, M-PHP has advantages over I-PHP in terms of patient recovery and procedure repeatability. A recent systematic review reported a median OS of 12.3 months for SIRT, an alternative LDT for unresectable liver metastases in mUM [51]. Further, a retrospective single-center study found a significantly longer OS for mUM patients treated with M-PHP than with SIRT (17.2 vs. 10.0 months) [33]. Altogether, these data support M-PHP as the preferred whole-liver LDT to target evident and occult liver metastases in mUM, either for safety (vs. M-IHP) or efficacy (vs. SIRT) reasons.

Over the last decade, published OS data on M-PHP for mUM have been heterogeneous. An earlier phase III trial showed no difference between M-PHP and BAC in mUM patients (10.6 vs. 10.0 months) [34], and non-randomized studies investigating the feasibility, safety, and efficacy of M-PHP in mUM reported different median OS results, ranging between 9.6 and 27.4 months [31,33,35–41]. The inconsistencies in replicating the same OS outcome may come from multiple sources, such as small sample size, differences in study design and/or conduct, variability of patient selection, study cohorts and/or prognostic factors, and technological improvements of the M-PHP procedure over time [26,32,39]. The same between-study variations bias individual cross-trial comparisons, but it is legitimate to compare our median OS (29.1 months) to the aggregated median OS (17.3 months) found in a meta-analysis of M-PHP trials in mUM [50]. Compared to this fairly objective effect

size for M-PHP, and the OS estimate in the approval-relevant FOCUS trial [48], the median OS estimate in our study is even longer. This OS difference may in part be attributed to center experience, case volume, and multidisciplinary patient selection. The impact of such factors on the OS outcome of the demanding M-PHP procedure-related patient care may be underestimated and should receive greater attention in future research.

In this study, a total of 38 patients received 99 M-PHP procedures. While our average number of M-PHP cycles per patient (2.6) is within the range (1.8–4.0) of previous studies [31,33,35–41], we found that each additional M-PHP cycle was associated with ~60% reduced risk of death (HR = 0.414). Moreover, the median OS was numerically 8.4 months higher in patients treated with 3–6 (29.8 months) versus 1–2 M-PHPs (21.4 months). This OS difference showed a trend, but failed to achieve statistical significance ($p = 0.058$), which could in part be attributed to the limited sample size. Otherwise, the almost similar OS rates and overlapping 95% CIs at 3 years (28.0% [11.7–67.1%] vs. 27.7% [11.4–67.5%]) demand caution as to whether the OS trend will persist in the long term. The literature provides little data on the correlation between the number of M-PHPs and OS. Further, there are likely confounding effects from patient management at play, making it difficult to disentangle the M-PHP cycle number as a cause or effect of prolonged OS. For example, the landmark FOCUS trial attempted to complete six M-PHP cycles per protocol (45% of patients completed six cycles) and discontinued M-PHP treatment in case of disease progression [31,48]. In contrast, we personalized the treatment goals and indications before each M-PHP cycle in a multidisciplinary manner, which could also mean continuing M-PHP to slow hepatic disease progression. However, association does not mean causation, and our data do not prove that additional M-PHP cycles cause longer survival. Reverse causation could also be possible, and that slower-progressing patients can receive more M-PHP cycles. However, M-PHP holds an advantage in its repeatability, and our observed trend towards improved OS with higher numbers of M-PHP treatments warrants further investigation in larger, prospective trials.

Our study has limitations. First, major limitations stem from its retrospective design and lack of a control group. Thus, the OS efficacy analyses presented in this study are exploratory. Second, the single-center nature and our strict selection criteria introduce potential selection bias. This could limit the generalizability of our results to a broader mUM population. Third, the sample size is modest, and ~55% of patients received additional therapies before or after M-PHP. This could confound the observed OS outcomes; however, the high diversity of additional periprocedural treatments, along with the small sample and subgroup sizes, limited to produce meaningful data on the effect of additional therapies. Altogether, all efficacy analyses presented in this report are exploratory. Further prospective, larger-scale, multicenter studies in independent patient populations are required to explore the role of additional therapies, to evaluate whether more M-PHP cycles cause longer OS, and to verify the extent to which the findings presented here are generalizable. However, as for its strengths, the OS calculations in our analysis are based on sufficient long-term follow-up, and the magnitude of M-PHP-associated OS effects contributed to the significance of findings. Despite the aforementioned study limitations, we believe that our OS data may provide a source for cross-trial comparison to reported OS efficacy estimates and/or OS advances of various novel management strategies for mUM. In particular, it might be valuable to compare our OS data (median OS: 29.1 months; 2-years OS: 53.2%) with OS data from recent studies on combining M-PHP with immunotherapies and/or targeted therapies [52–54], immunotherapy combinations in tebentafusp-naive and tebentafusp-pretreated mUM cohorts [55], and novel strategies such as (PRAME)-directed T-cell therapy in HLA-A*02+ mUM patients [56].

5. Conclusions

In the challenging treatment of liver-dominant mUM, we found a median OS of 29.1 months after the first M-PHP administration. This OS result is more than twice as high as the historical OS that was valid until 2020 (~12 months), and reaches the OS data for tebentafusp in the approval landmark phase III trial in 2021. Limitations of our analysis include its exploratory character, retrospective design, and the lack of a control group. A prospective evaluation is necessary to confirm our findings. Nevertheless, our long-term outcome results suggest a clinically meaningful OS benefit from M-PHP in the treatment of patients with liver-dominant mUM. Further, our results may also indicate that institutional experience, operators' skills, case volume, and multidisciplinary patient selection will be essential to fully harness the OS benefits of M-PHP in clinical practice and future research.

Author Contributions: Conceptualization, C.M.R., M.A.S. and R.B.; methodology, C.M.R., M.A.S. and R.B.; validation, A.S., H.W., K.W. and J.H.; formal analysis, C.M.R., M.A.S. and R.B.; investigation, M.A.S., A.S., H.W., K.W., J.H. and R.B.; resources, M.A.S. and R.B.; data curation, C.M.R., M.A.S., A.S., K.W. and R.B.; writing—original draft preparation, C.M.R., M.A.S. and A.S.; writing—review and editing, C.M.R., M.A.S., A.S., H.W., R.B. and A.H.M.; visualization, C.M.R. and M.A.S.; supervision, A.S., R.B. and A.H.M.; project administration, M.A.S., A.S., R.B. and A.H.M. All authors have read and agreed to the published version of the manuscript.

Funding: This research received no external funding.

Institutional Review Board Statement: The study was conducted in accordance with the Declaration of Helsinki. Ethical review and approval were waived for this study, due to the retrospective nature of the study.

Informed Consent Statement: Patient consent was waived for this study due to the statement of the Institutional Review Board.

Data Availability Statement: The data presented in this study are available on reasonable request from the corresponding author. The data are not publicly available due to privacy.

Acknowledgments: The authors thank Peter Wohlmuth and Dagmar Pilz for excellent support for the analysis of data.

Conflicts of Interest: The authors declare no conflicts of interest.

Abbreviations

The following abbreviations are used in this manuscript:

M-PHP	Melphalan-based percutaneous hepatic perfusion
mUM	Metastatic uveal melanoma
OS	Overall survival
CM	Cutaneous melanoma
ICI	Immune checkpoint inhibitor
LDT	Liver-directed therapies
SOC	Standard of care
ECOG	Eastern Cooperative Oncology Group
ULN	Upper limit of normal
EHD	Extrahepatic disease
CT	Computed tomography
MRI	Magnetic resonance imaging
AEs	Adverse events
SAEs	Severe adverse events
CD	Clavien–Dindo classification
CIRSE	Cardiovascular and Interventional Radiological Society of Europe classification
CIs	Confidence intervals

HRs	Hazard ratios
NSTEMI	Non-ST elevation myocardial infarction
QUALYs	Quality-adjusted life years
M-IHP	Melphalan-based isolated hepatic perfusion
BAC	Best alternative care
TACE	Transarterial chemoembolization
SIRT	Selective internal radiotherapy

References

1. Hayward, N.K.; Wilmott, J.S.; Waddell, N.; Johansson, P.A.; Field, M.A.; Nones, K.; Patch, A.M.; Kakavand, H.; Alexandrov, L.B.; Burke, H.; et al. Whole-genome landscapes of major melanoma subtypes. *Nature* **2017**, *545*, 175–180. [CrossRef]
2. Wessely, A.; Steeb, T.; Erdmann, M.; Heinzerling, L.; Vera, J.; Schlaak, M.; Berking, C.; Heppt, M.V. The Role of Immune Checkpoint Blockade in Uveal Melanoma. *Int. J. Mol. Sci.* **2020**, *21*, 879. [CrossRef]
3. Javed, A.; Arguello, D.; Johnston, C.; Gatalica, Z.; Terai, M.; Weight, R.M.; Orloff, M.; Mastrangelo, M.J.; Sato, T. PD-L1 expression in tumor metastasis is different between uveal melanoma and cutaneous melanoma. *Immunotherapy* **2017**, *9*, 1323–1330. [CrossRef]
4. Shain, A.H.; Bagger, M.M.; Yu, R.; Chang, D.; Liu, S.; Vemula, S.; Weier, J.F.; Wadt, K.; Heegaard, S.; Bastian, B.C.; et al. The genetic evolution of metastatic uveal melanoma. *Nat. Genet.* **2019**, *51*, 1123–1130. [CrossRef]
5. Rodriguez, D.A.; Sanchez, M.I.; Decatur, C.L.; Correa, Z.M.; Martin, E.R.; Harbour, J.W. Impact of Genetic Ancestry on Prognostic Biomarkers in Uveal Melanoma. *Cancers* **2020**, *12*, 3208. [CrossRef] [PubMed]
6. Bustamante, P.; Piquet, L.; Landreville, S.; Burnier, J.V. Uveal melanoma pathobiology: Metastasis to the liver. *Semin. Cancer Biol.* **2021**, *71*, 65–85. [CrossRef] [PubMed]
7. Carvajal, R.D.; Sacco, J.J.; Jager, M.J.; Eschelman, D.J.; Olofsson Bagge, R.; Harbour, J.W.; Chieng, N.D.; Patel, S.P.; Joshua, A.M.; Piperno-Neumann, S. Advances in the clinical management of uveal melanoma. *Nat. Rev. Clin. Oncol.* **2023**, *20*, 99–115. [CrossRef]
8. Mariani, P.; Piperno-Neumann, S.; Servois, V.; Berry, M.G.; Dorval, T.; Plancher, C.; Couturier, J.; Levy-Gabriel, C.; Lumbroso-Le Rouic, L.; Desjardins, L.; et al. Surgical management of liver metastases from uveal melanoma: 16 years' experience at the Institut Curie. *Eur. J. Surg. Oncol.* **2009**, *35*, 1192–1197. [CrossRef] [PubMed]
9. Trivedi, D.B.; Aldulaimi, N.; Karydis, I.; Wheater, M.; Modi, S.; Stedman, B.; Karavias, D.; Primrose, J.; Pearce, N.; Takhar, A.S. Liver resection for metastatic uveal melanoma: Experience from a supra-regional centre and review of literature. *Melanoma Res.* **2023**, *33*, 71–79. [CrossRef]
10. Maspero, M.; Pezzoli, I.; Di Guardo, L.; Angi, M.; Lo Dico, S.; Sposito, C.; Battiston, C.; Mazzaferro, V. Intention-to-Treat Analysis of Hepatic Resection for Liver Metastases from Uveal Melanoma: A Single-Center Experience. *Ann. Surg. Oncol.* **2025**, *32*, 4989–4996. [CrossRef]
11. Jager, M.J.; Shields, C.L.; Cebulla, C.M.; Abdel-Rahman, M.H.; Grossniklaus, H.E.; Stern, M.H.; Carvajal, R.D.; Belfort, R.N.; Jia, R.; Shields, J.A.; et al. Uveal melanoma. *Nat. Rev. Dis. Primers* **2020**, *6*, 24. [CrossRef] [PubMed]
12. Rantala, E.S.; Hernberg, M.M.; Lundin, M.; Lundin, J.; Kivelä, T.T. Metastatic uveal melanoma managed with best supportive care. *Acta Oncol.* **2021**, *60*, 135–139. [CrossRef]
13. Khoja, L.; Atenafu, E.G.; Suciu, S.; Leyvraz, S.; Sato, T.; Marshall, E.; Keilholz, U.; Zimmer, L.; Patel, S.P.; Piperno-Neumann, S.; et al. Meta-analysis in metastatic uveal melanoma to determine progression free and overall survival benchmarks: An international rare cancers initiative (IRCI) ocular melanoma study. *Ann. Oncol.* **2019**, *30*, 1370–1380. [CrossRef] [PubMed]
14. Rantala, E.S.; Hernberg, M.; Kivelä, T.T. Overall survival after treatment for metastatic uveal melanoma: A systematic review and meta-analysis. *Melanoma Res.* **2019**, *29*, 561–568. [CrossRef]
15. Piulats, J.M.; Espinosa, E.; de la Cruz Merino, L.; Varela, M.; Alonso Carrión, L.; Martín-Algarra, S.; López Castro, R.; Curiel, T.; Rodríguez-Abreu, D.; Redrado, M.; et al. Nivolumab Plus Ipilimumab for Treatment-Naïve Metastatic Uveal Melanoma: An Open-Label, Multicenter, Phase II Trial by the Spanish Multidisciplinary Melanoma Group (GEM-1402). *J. Clin. Oncol.* **2021**, *39*, 586–598. [CrossRef]
16. Pelster, M.S.; Gruschkus, S.K.; Bassett, R.; Gombos, D.S.; Shephard, M.; Posada, L.; Glover, M.S.; Simien, R.; Diab, A.; Hwu, P.; et al. Nivolumab and Ipilimumab in Metastatic Uveal Melanoma: Results From a Single-Arm Phase II Study. *J. Clin. Oncol.* **2021**, *39*, 599–607. [CrossRef]
17. Yamada, K.; Takeuchi, M.; Fukumoto, T.; Suzuki, M.; Kato, A.; Mizuki, Y.; Yamada, N.; Kaneko, T.; Mizuki, N.; Horita, N. Immune checkpoint inhibitors for metastatic uveal melanoma: A meta-analysis. *Sci. Rep.* **2024**, *14*, 7887. [CrossRef]
18. Matsumoto, H.; Somekawa, K.; Horita, N.; Ueda, S.; Kaneko, M.; Kaneko, A.; Fukuda, N.; Izawa, A.; Kamimaki, C.; Tanaka, K.; et al. Adverse events induced by durvalumab and tremelimumab combination regimens: A systematic review and meta-analysis. *Ther. Adv. Med. Oncol.* **2023**, *15*, 17588359231198453. [CrossRef]

19. Somekawa, K.; Horita, N.; Kaneko, A.; Tagami, Y.; Fukuda, N.; Matsumoto, H.; Namkoong, H.; Fujiwara, Y.; Minegishi, K.; Fukumoto, T.; et al. Adverse events induced by nivolumab and ipilimumab combination regimens. *Ther. Adv. Med. Oncol.* **2022**, *14*, 17588359211058393. [CrossRef] [PubMed]
20. Wang, J.; Li, Z.; Yin, H. The Future of Checkpoint Inhibitors in Uveal Melanoma: A Narrative Review. *Ophthalmol. Ther.* **2024**, *13*, 1103–1123. [CrossRef]
21. Nathan, P.; Hassel, J.C.; Rutkowski, P.; Baurain, J.F.; Butler, M.O.; Schlaak, M.; Sullivan, R.J.; Ochsenreither, S.; Dummer, R.; Kirkwood, J.M.; et al. Overall Survival Benefit with Tebentafusp in Metastatic Uveal Melanoma. *N. Engl. J. Med.* **2021**, *385*, 1196–1206. [CrossRef] [PubMed]
22. Hassel, J.C.; Piperno-Neumann, S.; Rutkowski, P.; Baurain, J.F.; Schlaak, M.; Butler, M.O.; Sullivan, R.J.; Dummer, R.; Kirkwood, J.M.; Orloff, M.; et al. Three-Year Overall Survival with Tebentafusp in Metastatic Uveal Melanoma. *N. Engl. J. Med.* **2023**, *389*, 2256–2266. [CrossRef]
23. Piulats, J.M.; Watkins, C.; Costa-García, M.; Del Carpio, L.; Piperno-Neumann, S.; Rutkowski, P.; Hassel, J.C.; Espinosa, E.; de la Cruz-Merino, L.; Ochsenreither, S.; et al. Overall survival from tebentafusp versus nivolumab plus ipilimumab in first-line metastatic uveal melanoma: A propensity score-weighted analysis. *Ann. Oncol.* **2024**, *35*, 317–326. [CrossRef]
24. Luo, S.; Xie, C.; Lin, N.; Lin, D.; Gu, D.; Lin, S.; Huang, X.; Xu, X.; Weng, X. Cost-effectiveness analysis of an orphan drug tebentafusp in patients with metastatic uveal melanoma and a call for value-based pricing. *Melanoma Res.* **2023**, *33*, 525–531. [CrossRef]
25. Ini, C.; Foti, P.V.; Farina, R.; Tiralongo, F.; Castiglione, D.G.; Cannarozzo, M.; Spatola, C.; David, E.; Palmucci, S.; Russo, A.; et al. Percutaneous Locoregional Therapies for the Treatment of Liver Metastases from Uveal Melanoma: A Systematic Review. *Technol. Cancer Res. Treat.* **2025**, *24*, 15330338251343144. [CrossRef]
26. Saldanha, E.F.; Ribeiro, M.F.; Hirsch, I.; Spreafico, A.; Saibil, S.D.; Butler, M.O. How we treat patients with metastatic uveal melanoma. *ESMO Open* **2025**, *10*, 104496. [CrossRef]
27. Mariani, P.; Almubarak, M.M.; Kollen, M.; Wagner, M.; Plancher, C.; Audollent, R.; Piperno-Neumann, S.; Cassoux, N.; Servois, V. Radiofrequency ablation and surgical resection of liver metastases from uveal melanoma. *Eur. J. Surg. Oncol.* **2016**, *42*, 706–712. [CrossRef] [PubMed]
28. Sterbis, E.; Gonsalves, C.; Shaw, C.; Orloff, M.; Sato, T.; Eschelman, D.; Adamo, R. 03: 45 PM Abstract No. 184 Safety and efficacy of microwave ablation for uveal melanoma metastatic to the liver. *J. Vasc. Interv. Radiol.* **2019**, *30*, S84. [CrossRef]
29. Gonsalves, C.F.; Eschelman, D.J.; Thornburg, B.; Frangos, A.; Sato, T. Uveal Melanoma Metastatic to the Liver: Chemoembolization with 1,3-Bis-(2-Chloroethyl)-1-Nitrosourea. *AJR Am. J. Roentgenol.* **2015**, *205*, 429–433. [CrossRef] [PubMed]
30. Gonsalves, C.F.; Eschelman, D.J.; Adamo, R.D.; Anne, P.R.; Orloff, M.M.; Terai, M.; Hage, A.N.; Yi, M.; Chervoneva, I.; Sato, T. A Prospective Phase II Trial of Radioembolization for Treatment of Uveal Melanoma Hepatic Metastasis. *Radiology* **2019**, *293*, 223–231. [CrossRef] [PubMed]
31. Zager, J.S.; Orloff, M.; Ferrucci, P.F.; Choi, J.; Eschelman, D.J.; Glazer, E.S.; Ejaz, A.; Howard, J.H.; Richtig, E.; Ochsenreither, S.; et al. Efficacy and Safety of the Melphalan/Hepatic Delivery System in Patients with Unresectable Metastatic Uveal Melanoma: Results from an Open-Label, Single-Arm, Multicenter Phase 3 Study. *Ann. Surg. Oncol.* **2024**, *31*, 5340–5351. [CrossRef]
32. de Leede, E.M.; Burgmans, M.C.; Meijer, T.S.; Martini, C.H.; Tijl, F.G.J.; Vuyk, J.; van Erkel, A.R.; van der Velde, C.J.H.; Kapiteijn, E.; Vahrmeijer, A.L. Prospective Clinical and Pharmacological Evaluation of the Delcath System's Second-Generation (GEN2) Hemofiltration System in Patients Undergoing Percutaneous Hepatic Perfusion with Melphalan. *Cardiovasc. Intervent Radiol.* **2017**, *40*, 1196–1205. [CrossRef] [PubMed]
33. Kolb, M.; Forschner, A.; Artzner, C.; Grözinger, G.; Said, I.; Dittmann, H.; Seith, F. Selective Internal Radiotherapy (SIRT) and Chemosaturation Percutaneous Hepatic Perfusion (CS-PHP) for Metastasized Uveal Melanoma: A Retrospective Comparative Study. *Cancers* **2023**, *15*, 4942. [CrossRef]
34. Hughes, M.S.; Zager, J.; Faries, M.; Alexander, H.R.; Royal, R.E.; Wood, B.; Choi, J.; McCluskey, K.; Whitman, E.; Agarwala, S.; et al. Results of a Randomized Controlled Multicenter Phase III Trial of Percutaneous Hepatic Perfusion Compared with Best Available Care for Patients with Melanoma Liver Metastases. *Ann. Surg. Oncol.* **2016**, *23*, 1309–1319. [CrossRef]
35. Modi, S.; Gibson, T.; Vigneswaran, G.; Patel, S.; Wheater, M.; Karydis, I.; Gupta, S.; Takhar, A.; Pearce, N.; Ottensmeier, C.; et al. Chemosaturation with percutaneous hepatic perfusion of melphalan for metastatic uveal melanoma. *Melanoma Res.* **2022**, *32*, 103–111. [CrossRef]
36. Karydis, I.; Gangi, A.; Wheater, M.J.; Choi, J.; Wilson, I.; Thomas, K.; Pearce, N.; Takhar, A.; Gupta, S.; Hardman, D.; et al. Percutaneous hepatic perfusion with melphalan in uveal melanoma: A safe and effective treatment modality in an orphan disease. *J. Surg. Oncol.* **2018**, *117*, 1170–1178. [CrossRef]
37. Dewald, C.L.A.; Warnke, M.M.; Brüning, R.; Schneider, M.A.; Wohlmuth, P.; Hinrichs, J.B.; Saborowski, A.; Vogel, A.; Wacker, F.K. Percutaneous Hepatic Perfusion (PHP) with Melphalan in Liver-Dominant Metastatic Uveal Melanoma: The German Experience. *Cancers* **2021**, *14*, 118. [CrossRef]

38. Meijer, T.S.; Burgmans, M.C.; de Leede, E.M.; de Geus-Oei, L.F.; Boekestijn, B.; Handgraaf, H.J.M.; Hilling, D.E.; Lutjeboer, J.; Vuijk, J.; Martini, C.H.; et al. Percutaneous Hepatic Perfusion with Melphalan in Patients with Unresectable Ocular Melanoma Metastases Confined to the Liver: A Prospective Phase II Study. *Ann. Surg. Oncol.* **2021**, *28*, 1130–1141. [CrossRef] [PubMed]
39. Tong, T.M.L.; Samim, M.; Kapiteijn, E.; Meijer, T.S.; Speetjens, F.M.; Brüning, R.; Schroeder, T.H.; El-Sanosy, S.; Maschke, H.; Wacker, F.K.; et al. Predictive Parameters in Patients Undergoing Percutaneous Hepatic Perfusion with Melphalan for Unresectable Liver Metastases from Uveal Melanoma: A Retrospective Pooled Analysis. *Cardiovasc. Intervent Radiol.* **2022**, *45*, 1304–1313. [CrossRef] [PubMed]
40. Artzner, C.; Mossakowski, O.; Hefferman, G.; Grosse, U.; Hoffmann, R.; Forschner, A.; Eigentler, T.; Syha, R.; Grözinger, G. Chemosaturation with percutaneous hepatic perfusion of melphalan for liver-dominant metastatic uveal melanoma: A single center experience. *Cancer Imaging* **2019**, *19*, 31. [CrossRef]
41. Vogl, T.J.; Koch, S.A.; Lotz, G.; Gebauer, B.; Willinek, W.; Engelke, C.; Brüning, R.; Zeile, M.; Wacker, F.; Vogel, A.; et al. Percutaneous Isolated Hepatic Perfusion as a Treatment for Isolated Hepatic Metastases of Uveal Melanoma: Patient Outcome and Safety in a Multi-centre Study. *Cardiovasc. Intervent Radiol.* **2017**, *40*, 864–872. [CrossRef]
42. Marquardt, S.; Kirstein, M.M.; Brüning, R.; Zeile, M.; Ferrucci, P.F.; Prevoo, W.; Radeleff, B.; Trillaud, H.; Tselikas, L.; Vicente, E.; et al. Percutaneous hepatic perfusion (chemosaturation) with melphalan in patients with intrahepatic cholangiocarcinoma: European multicentre study on safety, short-term effects and survival. *Eur. Radiol.* **2019**, *29*, 1882–1892. [CrossRef]
43. Dindo, D.; Demartines, N.; Clavien, P.A. Classification of surgical complications: A new proposal with evaluation in a cohort of 6336 patients and results of a survey. *Ann. Surg.* **2004**, *240*, 205–213. [CrossRef]
44. Clavien, P.A.; Barkun, J.; de Oliveira, M.L.; Vauthey, J.N.; Dindo, D.; Schulick, R.D.; de Santibañes, E.; Pekolj, J.; Slankamenac, K.; Bassi, C.; et al. The Clavien-Dindo classification of surgical complications: Five-year experience. *Ann. Surg.* **2009**, *250*, 187–196. [CrossRef]
45. Filippiadis, D.K.; Binkert, C.; Pellerin, O.; Hoffmann, R.T.; Krajina, A.; Pereira, P.L. Cirse Quality Assurance Document and Standards for Classification of Complications: The Cirse Classification System. *Cardiovasc. Intervent Radiol.* **2017**, *40*, 1141–1146. [CrossRef] [PubMed]
46. Cox, D.R.; Oakes, D.O. *Analysis of Survival Data*; Chapman and Hall: London, UK, 1984.
47. Kalbfleisch, J.D.; Prentice, R.L. *The Statistical Analysis of Failure Time Data*; Wiley: New York, NY, USA, 1980.
48. Zager, J.S.; Orloff, M.; Ferrucci, P.F.; Choi, J.; Eschelman, D.J.; Glazer, E.S.; Ejaz, A.; Howard, J.H.; Richtig, E.; Ochsenreither, S.; et al. An Open-label, Randomized Study of Melphalan/Hepatic Delivery System Versus Best Alternative Care in Patients with Unresectable Metastatic Uveal Melanoma. *Ann. Surg. Oncol.* **2025**, *32*, 4976–4988. [CrossRef] [PubMed]
49. Olofsson Bagge, R.; Nelson, A.; Shafazand, A.; All-Eriksson, C.; Cahlin, C.; Elander, N.; Gustavsson, A.; Helgadottir, H.; Kiilgaard, J.F.; Kinhult, S.; et al. Survival and Quality of Life After Isolated Hepatic Perfusion with Melphalan as a Treatment for Uveal Melanoma Liver Metastases: Final Results From the Phase III Randomized Controlled Trial SCANDIUM. *Ann. Surg.* **2025**, *282*, 100–107. [CrossRef] [PubMed]
50. Bethlehem, M.S.; Katsarelias, D.; Olofsson Bagge, R. Meta-Analysis of Isolated Hepatic Perfusion and Percutaneous Hepatic Perfusion as a Treatment for Uveal Melanoma Liver Metastases. *Cancers* **2021**, *13*, 4726. [CrossRef]
51. Alexander, H.; Wen, D.; Chu, M.; Han, C.; Hadden, P.; Thomas, R.; Bartlett, A. Selective internal radiation therapy for hepatic metastases of uveal melanoma: A systematic review. *Br. J. Radiol.* **2022**, *95*, 20210200. [CrossRef]
52. Tong, T.M.L.; van der Kooij, M.K.; Speetjens, F.M.; van Erkel, A.R.; van der Meer, R.W.; Lutjeboer, J.; van Persijn van Meerten, E.L.; Martini, C.H.; Zoethout, R.W.M.; Tijl, F.G.J.; et al. Combining Hepatic Percutaneous Perfusion with Ipilimumab plus Nivolumab in advanced uveal melanoma (CHOPIN): Study protocol for a phase Ib/randomized phase II trial. *Trials* **2022**, *23*, 137. [CrossRef]
53. Cao, L.; Chen, S.; Sun, R.; Ashby, C.R., Jr.; Wei, L.; Huang, Z.; Chen, Z.S. Darovasertib, a novel treatment for metastatic uveal melanoma. *Front. Pharmacol.* **2023**, *14*, 1232787. [CrossRef] [PubMed]
54. Koch, E.A.T.; Heppt, M.V.; Berking, C. The Current State of Systemic Therapy of Metastatic Uveal Melanoma. *Am. J. Clin. Dermatol.* **2024**, *25*, 691–700. [CrossRef]
55. Dimitriou, F.; Orloff, M.M.; Koch Hein, E.C.; Cheng, P.F.; Hughes, I.F.; Simeone, E.; Montazeri, K.; Grover, P.; Mehmi, I.; Gerard, C.L.; et al. Treatment sequence with tebentafusp and immune checkpoint inhibitors in patients with metastatic uveal melanoma and metastatic GNA11/GNAQ mutant melanocytic tumors. *Eur. J. Cancer* **2025**, *214*, 115161. [CrossRef] [PubMed]
56. Wermke, M.; Araujo, D.M.; Chatterjee, M.; Tsimberidou, A.M.; Holderried, T.A.W.; Jazaeri, A.A.; Reshef, R.; Bokemeyer, C.; Alsdorf, W.; Wetzko, K.; et al. Autologous T cell therapy for PRAME(+) advanced solid tumors in HLA-A*02(+) patients: A phase 1 trial. *Nat. Med.* **2025**, *31*, 2365–2374. [CrossRef] [PubMed]

Disclaimer/Publisher's Note: The statements, opinions and data contained in all publications are solely those of the individual author(s) and contributor(s) and not of MDPI and/or the editor(s). MDPI and/or the editor(s) disclaim responsibility for any injury to people or property resulting from any ideas, methods, instructions or products referred to in the content.

cancers

MDPI

Communication

Unraveling Resistance Mechanisms to Gαq Pathway Inhibition in Uveal Melanoma: Insights from Signaling-Activation Library Screening

Simone Lubrano [1,2,†], Rodolfo Daniel Cervantes-Villagrana [1,2,†], Nadia Arang [1,3], Elena Sofia Cardenas-Alcoser [1,2], Kuniaki Sato [1,2], Gabriela Cuesta-Margolles [1,2], Justine S. Paradis [1], Monica Acosta [1] and J. Silvio Gutkind [1,2,*]

[1] Moores Cancer Center, University of California San Diego, La Jolla, CA 92093, USA; rcervantesvillagrana@health.ucsd.edu (R.D.C.-V.); nadia.arang@ucsf.edu (N.A.); ecardenasalcoser@health.ucsd.edu (E.S.C.-A.); gcuestamargolles@health.ucsd.edu (G.C.-M.)
[2] Department of Pharmacology, School of Medicine, University of California San Diego, La Jolla, CA 92093, USA
[3] Quantitative Biosciences Institute (QBI), University of California San Francisco, San Francisco, CA 94158, USA
* Correspondence: sgutkind@health.ucsd.edu
† These authors contributed equally to this work.

Simple Summary

Uveal melanoma is an aggressive ocular malignancy with high mortality rates. Although localized interventions such as surgical resection or radiotherapy effectively control the primary tumor, many patients ultimately develop metastatic disease. Current therapies targeting principal oncogenic drivers often fail to provide durable responses, underscoring the need to elucidate alternative survival pathways that confer resistance. In this study, we systematically evaluated gene function in laboratory models of uveal melanoma, identifying critical contributions from signaling pathways including JAK/STAT, BCL2/BCL-XL, PI3K/mTOR, and Hippo. These results highlight novel molecular mechanisms underpinning therapeutic resistance and support the development of combinatorial treatment strategies. Such approaches may offer improved clinical outcomes for patients with advanced uveal melanoma by effectively targeting both primary oncogenic drivers and resistance mechanisms.

Abstract

Background/Objectives: Uveal melanoma (UVM), the leading primary intraocular cancer in adults, is driven by *GNAQ*/*GNA11* mutations, encoding the active forms of Gαq proteins. While local treatments like surgery or radiation can control primary tumors, nearly half of patients die from metastasis. Our aim was identifying potential pathways involved in resistance to targeted therapy in UVM. Methods: Here, we screened 100 pathway-activating mutant complementary DNAs by lentiviral overexpression to identify those that enhance the survival of cancer cells in the presence of clinically relevant targeted therapies, using *BAP1* wild-type UVM cells and validated the most significant results in *BAP1*-mutant cells. Results: This revealed JAK/STAT activation, overexpression of anti-apoptotic BCL2/BCL-XL, and dysregulated PI3K/mTOR or Hippo pathways as escape routes under MEK-ERK or FAK inhibition. Bioinformatic analysis of UVM transcriptome in TCGA further showed that high expression of the hallmark PI3K/AKT/mTOR pathway and IL6/JAK/STAT signaling correlates with poor prognosis. A similar correlation was shown by YAP and anti-apoptotic signatures. The analysis of individual representative genes from these signatures revealed that *MTOR*, *BCL2L1* (BCL-XL), and *TEAD4* gene expression are linked to poorer survival, underscoring the potential clinical impact of these adaptive pathways.

Proliferation and apoptosis assay demonstrated that aberrant activation of AKT and YAP promotes resistance to FAK and MEK inhibitors. Conclusions: These findings support the adaptability of UVM lesions and suggest rational combination therapies targeting both primary *GNAQ*/*GNA11*-driven oncogenic signals and their compensatory networks as a more effective, personalized treatment approach for advanced UVM.

Keywords: uveal melanoma; resistance; MEK; FAK; AKT; mTOR; BCL-XL; YAP/TEAD; hippo pathway

1. Introduction

Uveal melanoma (UVM) originates from melanocytes within the uveal tract (choroid, ciliary body, and iris), and it is the most common primary intraocular malignancy in adults [1], with an incidence of approximately 5 cases per million per year [2]. Despite modern surgical, laser, and radiotherapeutic modalities achieving satisfactory local tumor control, nearly half of patients eventually develop metastatic disease, most notably in the liver, where survival typically drops to less than 12 months from the time of diagnosis [3]. Current systemic therapies offer only limited benefit in the metastatic setting [4,5], highlighting an urgent need for strategies to overcome intrinsic and acquired therapy resistance mechanisms, and thereby improve patient treatment outcomes.

In contrast to cutaneous melanoma, which frequently harbors UV-induced mutations in *BRAF* and *NRAS* [6,7], UVM is driven by distinct oncogenic events that reflect a different pathophysiological profile. The majority of UVM cases (over 90%) harbor mutations in *GNAQ* or *GNA11*, which encode Gαq subunits that instigate constitutive signaling through downstream pathways such as MEK-ERK and YAP [8–10]. These alterations create a tumor microenvironment and signaling architecture distinct from other melanoma subtypes, emphasizing the need for specialized therapeutic approaches. A particularly notable genetic event involves the inactivation of the tumor suppressor BAP1 in nearly 50% of patients, which strongly correlates with a high-risk, metastatic phenotype [11]. This leads to dysregulated DNA damage responses, driving tumor aggressiveness and disease progression; however, how these changes integrate with or modulate critical survival pathways remains only partially understood. Recent studies have highlighted the centrality of focal adhesion kinase (FAK) [12] in the context of oncogenic *GNAQ*/*GNA11* alterations, which converge on FAK, AKT, and YAP activation concomitant with components of the MEK-ERK axis to initiate proliferative signals, maintain cell viability, and promote resistance to targeted therapies. Nonetheless, the intricate interplay among these nodal pathways and how they collectively establish a dynamic, adaptive signaling circuit capable of evading single-agent therapies remains poorly defined.

Targeted therapies have revolutionized cancer treatment by selectively inhibiting oncogenic drivers. However, a persistent and difficult challenge is the ability of tumor cells to engage compensatory bypass pathways that neutralize or circumvent the inhibitory effects of these agents. Specifically, the prolonged blockade of signaling hubs, such as EGFR, PI3K, or BRAF, has been shown to activate intricate feedback loops that disrupt or rewire signal transduction, ultimately conferring therapeutic resistance and promoting disease progression [13–17]. In response, there is a growing consensus that combinatorial strategies targeting both the principal oncogenic node and its critical compensatory pathways are necessary to achieve sustained clinical benefit [18]. Yet major questions remain unanswered regarding which Gαq–regulated routes underlie resistance to canonical (e.g., MEK inhibitors, MEKi [19–21]) and non-canonical (e.g., FAKi [8,12,22]) targeting agents,

https://doi.org/10.3390/cancers18010074

and which feedback mechanisms should be precisely co-targeted to optimize therapeutic efficacy. Specifically, despite preclinical evidence that MEKi and FAKi may reduce UVM cell proliferation, these interventions often yield cytostatic rather than cytotoxic responses. Over time, the surviving tumor cells acquire or exploit alternative molecular programs, rendering the tumor refractory and enabling tumor progression or relapse after an initial favorable response. In the present study, we used a recently described "signaling toolkit" strategy to identify mechanisms of resistance to MEKi or FAKi, and explored the status of activation of the emerging adaptive resistance pathways by transcriptome analysis of large RNA sequencing datasets from UVM lesions.

2. Materials and Methods

2.1. Cell Lines, Culture Procedures and Chemicals

HEK293 cells were maintained in DMEM (D6429, Sigma-Aldrich Inc., St. Louis, MO, USA) supplemented with 10% FBS (F2442, Sigma-Aldrich Inc., St. Louis, MO, USA), 1X antibiotic-antimycotic solution (A5955, Sigma-Aldrich Inc., St. Louis, MO, USA), and 1X Plasmocin prophylactic (ant-mpp, InvivoGen, San Diego, CA, USA). Uveal melanoma cell line 92.1 was maintained in RPMI-1640 medium (R8758, Sigma-Aldrich Inc., St. Louis, MO, USA) supplemented with 10% FBS, 1X antibiotic/antimycotic solution, and 1X Plasmocin prophylactic. Uveal melanoma cell line MP46 was cultured in RPMI-1640 medium (R8758, Sigma-Aldrich Inc., St. Louis, MO, USA) supplemented with 20% FBS,1X antibiotic/antimycotic solution, and 1X Plasmocin prophylactic. All the uveal melanoma cell lines were provided by Dr. Andrew Aplin (Thomas Jefferson University, Philadelphia, PA, USA).

Trametinib (GSK1120212) #S2673 and VS-4718 (PND-1186) #S7653 were obtained from SelleckChem (Houston, TX, USA).

2.2. Library and Transfections

Lentiviral cDNA library containing 100 distinct both gain-of-function and loss-of-function (dominant-negative) mutants was generously provided by Dr. Wood [23]. All pathway-activating constructs were generated in lentiviral format, and the viruses were produced in HEK293 cells. All 100 distinct lentiviruses were aliquoted and stored at -80 °C. As negative controls, we used the lentiviral HCRed (Addgene, Watertown, MA, USA, 25892) and luciferase (Addgene, Watertown, MA, USA, 25894). To generate cell populations overexpressing each cDNA construct, 92.1 cells were seeded at a density of 500,000 cells per well in a 6-well plate, with one well designated for each lentivirus to be transduced. After 24 h, each well was infected with a single virus from the library at a multiplicity of infection (MOI) of 0.3, ensuring that most infected cells contained only one viral integration. The lentivirus was added directly to the cells in the presence of polybrene (7.5 μg/mL), and the plates were centrifuged at $1200\times g$ for 1 h at 37 °C. Twenty-four hours post-infection, the medium was replaced with fresh medium containing puromycin (2 μg/mL) to initiate the selection process. After 48 h of puromycin selection, the cells were split into approximately six equal portions to be frozen at -80 °C and to prepare the viability experiments.

2.3. Concentration–Response Curves in Viability Assays

Cells (8000 per well) were plated in 96-well white plates in supplemented medium. For viability screening, cells expressing oncogenic mutants and controls were seeded in parallel. The next day, the cells were treated with increasing inhibitor concentrations. Each inhibitor was tested in seven serial dilutions, with technical triplicates, for 72 h. For trametinib (MEKi), we used 0.003, 0.01, 0.03, 0.1, 0.3, 1, and 10 nM, and for VS-4718 (FAKi), 0.003, 0.01, 0.03, 0.1, 0.3, 1, and 10 μM concentrations in supplemented medium. Cell

https://doi.org/10.3390/cancers18010074

viability was assessed using the AquaBluer Cell Viability Reagent and measured with a Spark microplate reader (Tecan). Briefly, after 72 h of incubation, the supernatant was aspirated, and supplemental media was added with Aqua Bluer at a 1:100 dilution and incubated for at least 3 h at 37 °C in a 5% CO_2 atmosphere. GI_{50} values were calculated with GraphPad Prism (v10.4.1, GraphPad Software, Inc., Boston, MA, USA) using a nonlinear regression model (log[inhibitor] vs. response, three-parameter variable slope).

2.4. Acridine Orange/Ethidium Bromide Apoptosis Staining

Uveal melanoma cells (92.1 parental, and YAP-5SA and myr-Flag-AKT expressing cells) were seeded in 12-well plates to ~80% confluence and then treated with FAK or MEK inhibitors for 24 h. Cells were washed with 1X PBS and stained with acridine orange/ethidium bromide (50 μg/mL each in PBS). Acridine orange (cat. A3568) and ethidium bromide (cat. 15585011) were obtained from Invitrogen (Carlsbad, CA, USA). Fluorescent images were captured using an inverted microscope (10×) (Echo Revolve, BICO Company, San Diego, CA, USA). Two fields per condition (≥100 cells/field) were imaged in triplicate. Finally, the cells were manually classified as live (green fluorescence) and apoptotic (red and green fluorescence). Acridine orange is permeable in live cells, and ethidium bromide only influxes dying cells.

2.5. Proliferation

Cells (10,000 per well) were plated in 96-well clear plates in supplemented medium; parental 92.1 cells and myr-AKT or YAP-5SA expressing cells were seeded in parallel. The next day, the cells were treated in 200 μL supplemented medium with vehicle, FAK inhibitor (0.3 μM, VS-4718), or MEK inhibitor (3 nM, trametinib). Cell confluency was measured using the Cellcyte 3 microscope (Echo, BICO, San Diego, CA, USA) in live cells in real-time during 72 hrs. The analysis of confluency was performed using the Cellcyte 3 software, and the normalized data were plotted.

2.6. Western Blot

Cells were seeded in 6-well plates at a density of 300,000 cells (parental cells and myr-AKT or YAP-5SA cells). When they reach an appropriate confluency, cells were serum starved and treated with the FAK inhibitor (1 μM, VS-4718), MEK inhibitor (10 nM, trametinib) for 24 h. For cell lysates, cells were washed with cold 1X PBS and then lysed using Pierce™ RIPA buffer (Thermo Scientific, Waltham, MA, USA, catalog #89900) supplemented with HaltTM Protease and Phosphatase Inhibitor Cocktail (ThermoFisher Scientific, Waltham, MA, USA, 78440) and 1mM sodium orthovanadate (New England Biolabs, Ipswich, MA, USA, P0758S). The lysates were centrifuged at maximum speed at 4 °C, and protein concentrations were determined using DC Protein Assay (BioRad Laboratories, Hercules, CA, USA, catalog #5000111). Finally, lysates were mixed with 4× Laemmli Sample Buffer (BioRad Laboratories, Hercules, CA, USA, 1610747) containing β-mercaptoethanol and boiled for 5 min at 98 °C. The protein samples were resolved by SDS-PAGE gels at 20–30 mAmps and transferred to PVDF membranes (Immobilon-P membranes, Millipore, St. Louis, MO, USA, catalog no. IPV00010) at 25 V overnight. The membranes were blocked with 5% (*w*/*v*) skim milk in 1X TBS-T for 1 hr, and after washing with TBS-T, incubated with the corresponding primary antibodies from Cell Signaling Technologies. Antibodies were used at a 1:1000 dilution: cl-PARP (#5625), ERK1/2 (#9102), pT202/Y204-ERK1/2 (#9101), AKT (#9272), YAP (#14074), and GAPDH (#5174). HRP-conjugated goat anti-rabbit and anti-mouse IgG (Southern Biotech, Birmingham, AL, USA) were applied at a 1:10,000 dilution. Chemiluminescence was detected using Immobilon Western Chemiluminescent HRP substrate (Millipore, St. Louis, MO, USA) and with the

https://doi.org/10.3390/cancers18010074

ChemiDoc imaging system (Bio-Rad, Hercules, CA, USA). All representative Western blots were conducted in at least 3 independent experiments.

2.7. Caspase Activity

We performed CaspaseGlo3/7 assays to measure caspase activity. 92.1 cells were plated at a density of 10,000 cells/well in 96-well white plates one day before the treatments. After 24 h incubation in supplemented 10% FBS medium, the cells were starved and treated with FAK inhibitor (1 μM, VS-4718), MEK inhibitor (10 nM, trametinib), or vehicle control in 100 μL per well. Apoptosis was evaluated 24 h after treatment using the Caspase-Glo 3/7 Assay System (Promega G8090) according to the manufacturer's guidelines. Briefly, reagents were added to each well with a final dilution of 1:8, and the plates were maintained in darkness at room temperature for 1 hr. Finally, we read the fluorescence in the Spark microplate reader (Tecan, San Jose, CA, USA).

2.8. Wound Closure

Cells were seeded on 0.02% gelatin (pre-coated for 1 h) in 12-well plates. After 24 h, the confluent cell monolayers were wounded in the middle with a pipette tip, the cells were washed with 1X PBS to remove the debris on the wound and stimulated with serum-free or supplemental medium (10% FBS). Inhibitors for FAK (1 μM, VS-4718), or MEK (10 nM, trametinib) were incubated for 2 h before wounding and during cell migration. After 18 h, cells were fixed with 4% PFA, stained with crystal violet, washed with PBS, and photographed.

2.9. Survival Analysis in TCGA Uveal Melanoma (UVM) Data

RNA-seq and clinical data for the TCGA-UVM dataset were downloaded from the National Cancer Institute Genomic Data Commons using the TCGAbiolinks R package, Release 3.22. Gene signature scores for each patient sample were calculated using the YAP target genes described previously [24] or curated gene sets in MSigDB (https://www.gsea-msigdb.org/gsea/msigdb, accessed 12 December 2025) by single-sample gene set enrichment analysis (ssGSEA) implemented in GenePattern (www.genepattern.org, accessed 12 December 2025). For survival analysis, we first modeled the pathway activity as a continuous variable in Cox proportional hazards regression, utilizing ssGSEA scores generated above. For visualization (Kaplan–Meier plots), patients were divided into "high" and "low" groups, using maximally selected rank statistics as implemented in the survminer R package. This method identifies the optimal cut-off point for a continuous variable, while formally correcting for the multiple testing inherent in scanning all possible thresholds. Unlike naïve repeated log-rank testing, this approach provides adjusted *p*-values and controls type I error. For survival analysis in (see below), the same approach was applied to determine the cutoff for "high" or "low" patient groups utilizing individual gene expression values (Transcripts Per Million; TPM) from TCGA-UVM dataset. All statistical analyses were performed in R version 4.4.1.

2.10. Statistical Analysis

All experiments were repeated at least three times. Data are presented as mean ± standard deviation (SD). Multiple comparisons were assessed by one-way or two-way ANOVA following Tukey post hoc, as indicated. Statistical significance in survival curves (Kaplan–Meier plots) was evaluated by the log-rank test. Hazard ratios were computed where relevant. A p-value < 0.05 was considered statistically significant. All analyses were performed in GraphPad Prism (Version 10.4.1, GraphPad Software, Boston, MA, USA, www.graphpad.com).

https://doi.org/10.3390/cancers18010074

3. Results

3.1. Unbiased Lentiviral Signaling Pathway Activation Screen in UVM Cells

To address the urgent need for a systematic map of resistance-mediating pathways, we first employed an unbiased lentiviral signaling pathway activation screen in 92.1 UVM cells (BAP1 wild-type). This screen was designed to capture a broad spectrum of signaling architecture commonly implicated in oncogenic processes [23]. Specifically, we took advantage of a library of 100 constructs (puromycin-selectable), primarily encoding constitutively active variants of key nodes for signaling pathways known to be pivotal in tumorigenesis (e.g., Ras/MAPK, PI3K/AKT/mTOR, STAT3, Wnt, Notch, TGFβ, Hippo, and oncogenic transcription factors). The library also included a small number of loss-of-function or dominant-negative constructs (e.g., LATS-K697R), whose net effect likewise drives signaling activation. The use of constitutively active mutants, dominant active mutants for pathway repressors, or chimeric fusion active proteins ensured robust and durable signaling output from each node (Figure 1, Table 1).

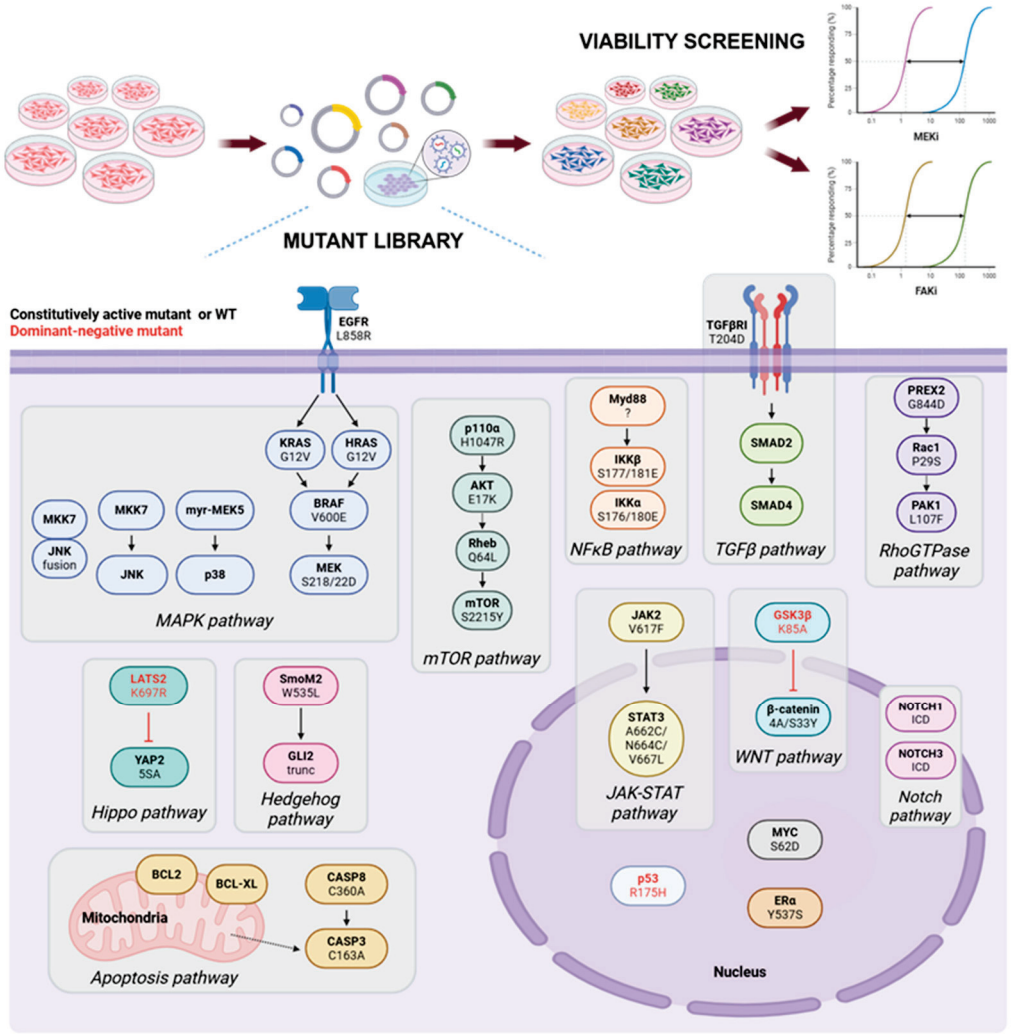


Figure 1. Schematic depicting for mutant library screening to identify resistance mechanisms to MEK or FAK inhibitors. Black, activation (constitutive active mutant or wild type); red, inhibition (dominant negative mutant).

https://doi.org/10.3390/cancers18010074

Table 1. List of genes included in the mutant library screen, grouped by pathways involved in resistance mechanisms, including PI3K/AKT/mTOR, RAS/MAPK, TGF-β/SMAD, NF-κB, and apoptosis pathways.

Pathway	Genes and Expression Constructs
PI3K/AKT/mTOR Pathway	*AKT1*, *MTOR*, *PTEN*, *PIK3CA*, *PIK3CG*, *PIK3R1*, myr-FLAG-PI3K, myr-FLAG-Akt, FLAG-Rheb (Q64L)
RAS/MAPK Pathway	*BRAF*, *KRAS*, *NRAS*, *MAP2K1*, *MEK1*, *MAP2K4*, *MEK1* (S218D/S222D), HRas (G12V), Kras (G12V), JNK2 WT O/E (MAPK9), p38 WT O/E (MAPK14), MKK6(S207E/T211E), Mkk7-JNK2 fusion
Cell Cycle Regulation	*CCND1*, *CDKN1A*, *CDKN1B*, *RB1*, *STAG2*
Receptor Tyrosine Kinases	*EGFR*, *FGFR2*, *FGFR3*, *FLT3*, *PDGFRA*, *RET*, *HGF*
WNT/β-catenin Pathway	*CTNNB1*, β-catenin (S33A, S37A, T41A), β-catenin (S33Y), GSK3b(K85A)
Notch Signaling	Notch1 intracell.domain, Notch3 intracell.domain
TGF-β/SMAD Pathway	*SMAD2*, *SMAD4*, *ACVR1B*, *TGFBR1* (T204D)
Epigenetic Regulation	*EZH2*, *HIST1H1C*, *H3F3B*, *KLF4*, *BAP1*, *TET2*
DNA Damage Response	*CHEK2*, *MLH1*, *MSH2*
Oxidative Stress Response	*NFE2L2*, *KEAP1*
Apoptosis	*BCL2*, *BCL-XL*, Caspase-8 (C360A), Caspase-3 (C163A)
Transcription Factors	*FOXA1*, *ELF3*, *GATA2*, *GATA3*, *RUNX1*, *VHL*
NF-κB Pathway	IKKa (S176E/S180E), FLAG-IKKb (S177E/S181E), *CYLD*, *MYD88*
RNA Splicing Pathway	*U2AF1*
Jak/Stat Pathway	JAK2 (V617F), C-term-FLAG-Stat3(A661C/N663C)
JNK Pathway	JNK2 WT O/E (*MAPK9*), Mkk7-JNK2 fusion
ERK5 Pathway	MEK5 DD, myr-MEK5
p38 MAPK Pathway	p38 WT O/E (*MAPK14*), MKK6(S207E/T211E)
Hedgehog Pathway	Gli2 truncation, 4x myc Gli2 truncation, SmoM2
Estrogen Receptor Pathway	ERα (Y537S mutant)
Hippo Pathway	YAP2 5SA, LATS2(K697R) kinase dead
P53 Pathway	p53 (R175H mutant DN)
Ral-GEF Pathway	H-Ras (G12V, E37G), Rgl2-CAAX, RalA(G23V)(two forms—full and mature peptide), *MEK1*

Each lentivirus was introduced into UVM cells to generate 100 unique lines, each stably overexpressing a single construct. Following puromycin selection, the lines were subjected to full dose–response curves for both MEK (trametinib) and FAK (VS-4718) inhibitors. We derived independent IC_{50} values for each inhibitor and measured cell viability at maximal inhibitory doses (C_{max}) (Figure 1). This approach enabled us to capture shifts in

https://doi.org/10.3390/cancers18010074

dose–response kinetics (i.e., increased IC_{50} values) and any changes in maximal achievable cytostatic or cytotoxic effects.

3.2. Emerging Pathways Driving Resistance to MEK and FAK Inhibition

As anticipated, constructs that augment MAPK signaling emerged prominently in our screens. For example, overexpression of HRAS-G12V or BRAF-V600E, well-established oncoproteins driving ERK hyperactivation, provided robust rescue from MEKi (Figure 2A and Supplementary Table S1). These same constructs also partially conferred protection against FAKi (Figure 3A and Supplementary Table S2). In line with our prior work demonstrating synergy between MEK and FAK dual inhibition in UVM [25], these observations highlight ERK reactivation as a recurrent and potent escape route for *GNAQ*-driven tumor cells, and also reveal that the constitutively active FAK-Y180I/M183A mutant can preserve cellular viability when MEK activity is pharmacologically suppressed (Figure 2A–C).

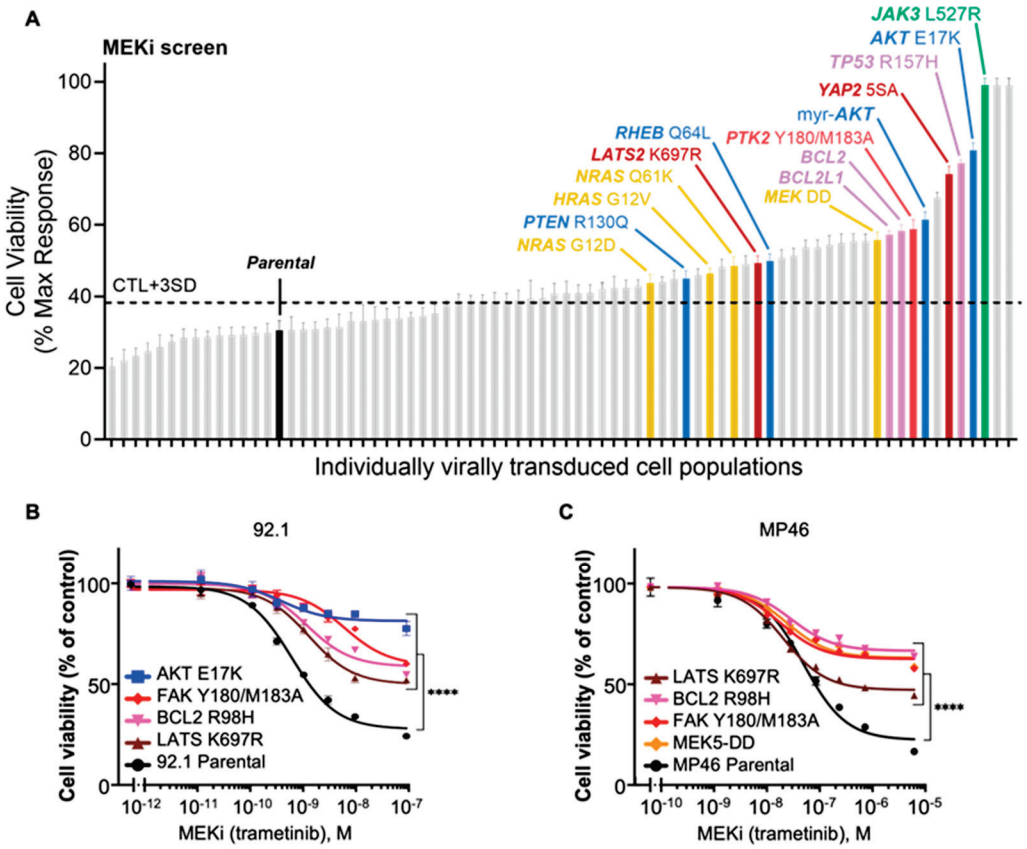


Figure 2. Signaling library toolkit screening reveals candidates as resistance-promoting pathways for MEK inhibition. (**A**) MEKi screen shows cell viability responses of individually virally transduced cell populations in 92.1 cells. Notable resistance mutations include AKT E17K, HRAS G12V, BCL2, and FAK Y180/M183A, which exceed the control threshold. CTL + 3SD: mean viability of control samples plus three times the standard deviation used as a cut-off for resistance. (**B**) Dose–response curves for MEKi (trametinib) in 92.1 cells demonstrate enhanced resistance in populations expressing AKT E17K, BCL2 R98H, LATS K697R, and FAK Y180/M183A compared to parental cells. (**C**) Dose–response curves for MEKi (trametinib) in MP46 cells validate resistance phenotypes driven by LATS K697R, BCL2, FAK Y180/M183A, and MEK5-DD compared to parental MP46 cells. Two-way ANOVA followed by Tukey post hoc, **** $p < 0.0001$.

https://doi.org/10.3390/cancers18010074

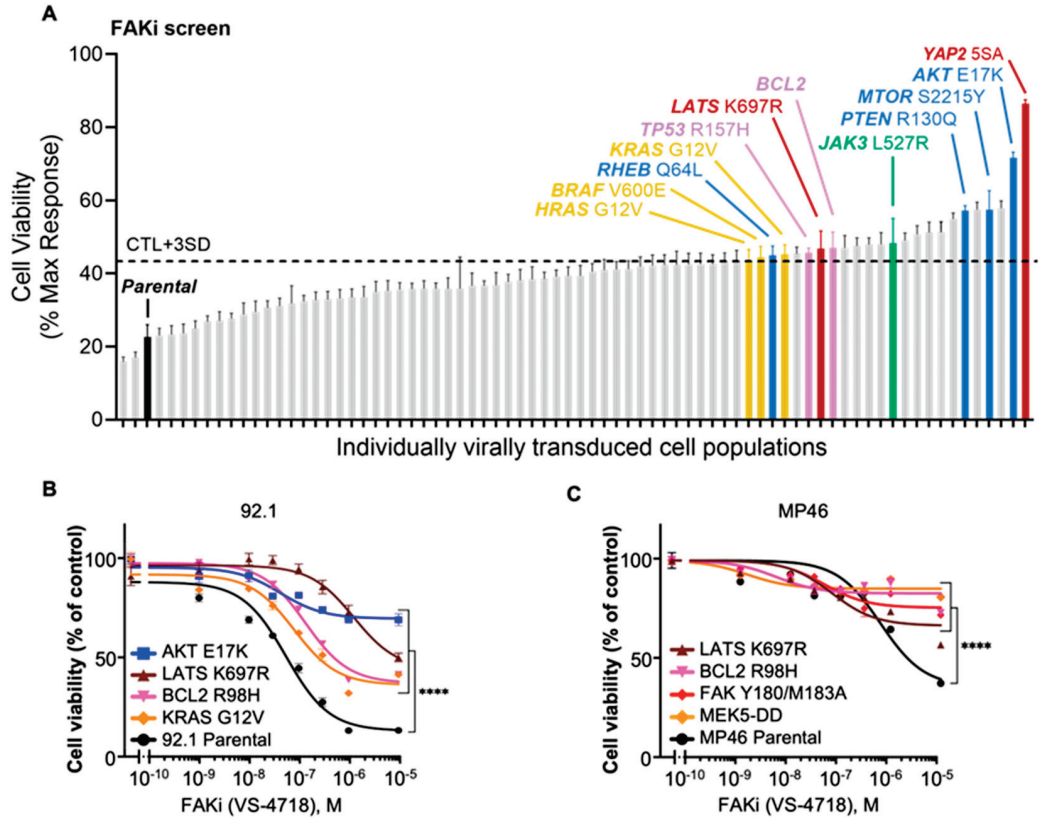


Figure 3. Signaling activation library screening reveals candidates as resistance-promoting pathways for FAK inhibition. (**A**) FAKi screen shows cell viability responses of individually virally transduced cell populations in 92.1 cells. Resistance mutations identified include AKT E17K, mTOR S2215Y, PTEN R130Q, JAK3 L527R, p53 R157H, BCL2, and KRAS G12V, exceeding the control threshold. CTL + 3SD: mean viability of control samples plus three times the standard deviation used as a cutoff for resistance. (**B**) Dose–response curves for FAKi (VS-4718) in 92.1 cells demonstrate resistance phenotypes driven by AKT E17K, BCL2 R98H, LATS K697R, and KRAS G12V compared to parental cells. (**C**) Dose–response curves for FAKi (VS-4718) in MP46 cells confirm resistance driven by LATS K697R, BCL2, FAK Y180/M183A, and MEK5-DD compared to parental MP46 cells. Two-way ANOVA followed by Tukey post hoc, **** $p < 0.0001$.

Beyond the canonical and FAK-centric mechanisms, our unbiased approach identified additional molecular events that can override MEKi or FAKi growth suppression. Overexpression of BCL2 or BCL-XL (also known as BCL2L1) profoundly bypassed the cytostatic effects of either inhibitor. Similarly, the oncogenic gain-of-function mutant p53-R175H decreased sensitivity to both MEKi and FAKi, indicating that the acquisition of p53 alterations (as p53 is rarely mutated in UVM) might be relevant for tailoring therapy and predicting resistance (Figure 3A–C).

We found that PI3K/AKT/mTOR-activating constructs were among the top hits that were rescued from FAKi (Figure 3A–C). For instance, myr-AKT, AKT E17K and mTOR S2215Y, suggest a central and yet underexplored role for PI3K pathway regulation by *GNAQ* via FAK in UVM, which we have recently described based on genome-wide CRISPR-Cas9 screens using FAKi in UVM cells [26]. Interestingly, constitutively active JAK3-L527R and kinase-dead LATS-K697R also emerged as resistance nodes. The LATS-K697R construct, part of the Hippo tumor suppressor pathway, abolishes the LATS kinase function by disrupting the ATP-binding site (lysine-to-arginine mutation), preventing it from phosphorylating and inactivating YAP/TAZ. This loss of LATS activity, in turn, promotes hyperactive YAP/TAZ signaling, offsetting the growth-inhibitory signals triggered by MEK

https://doi.org/10.3390/cancers18010074

or FAK blockade. Aligned with these results, constitutively active YAP (YAP2-5SA) was also among the top resistance hits.

These findings collectively extend our mechanistic scope, highlighting potential targets that could be explored to optimize therapeutic response. We then validated the most significant hits in MP46 cells (BAP1-mutated), rather than performing a full screen, to confirm that these top resistance mechanisms could similarly emerge despite their distinct genetic background (Figures 2C and 3C).

3.3. Gene Set Enrichment Analysis Identifies Key Oncogenic Pathways Correlating with Poor Survival in Uveal Melanoma

Based on the resistance mechanisms identified in our in vitro models under FAK or MEK inhibition, we next sought to determine whether these same pathways are clinically relevant in UVM. To that end, we queried the TCGA UVM cohort (n = 80) and performed Gene Set Enrichment Analysis (GSEA) focusing on curated pathway signatures encompassing Hippo/YAP, PI3K/AKT/mTOR, and IL6/JAK/STAT and anti-apoptosis signaling. Specifically, we used publicly available Hallmark and Reactome gene sets from the Molecular Signatures Database (MSigDB) that capture the core components and downstream targets of each pathway [27,28].

Our GSEA revealed that high expression of the Hallmark PI3K/AKT/mTOR pathway (Figure 4A) or Hallmark mTORC1 signaling (Figure 4B) correlated with significantly worse overall survival (p = 0.0051 and p = 0.0021, respectively), aligned with our in vitro data that mTOR pathway activation drives therapeutic resistance. Moreover, tumors with a high anti-apoptosis gene signature (Figure 4C) showed markedly reduced survival (p = 0.0076), in line with our identification of BCL2/BCL-XL upregulation as a key resistance mechanism. High IL6/JAK/STAT signaling (Figure 4D) was even more strongly associated with adverse outcomes ($p < 0.0001$), further underscoring that JAK/STAT blockade may represent an important complementary strategy in UVM therapy. Notably, a high YAP signature (e.g., CTGF, CYR61, and other canonical YAP targets) (Figure 4E) also tracked with significantly inferior survival (p = 0.0019), highlighting the clinical importance of Hippo pathway dysregulation in UVM.

Collectively, these results underscore that the same pathways identified in our mechanistic screen, PI3K/AKT/mTOR, anti-apoptosis (BCL2 family), IL6/JAK/STAT and Hippo/YAP, are not only active in primary UVM tumors but are also associated with worse survival profiles in large patient cohorts (n = 80).

3.4. Correlating Key Resistance-Associated Genes with Patient Survival in Uveal Melanoma

To investigate the translational implications of these observations, we next assessed whether expression levels of key resistance-associated genes correlated with patient outcomes in a cohort of 80 individuals diagnosed with UVM. Focusing on MTOR, BCL2, and TEAD, each patient was categorized as having "high" or "low" transcript levels (TPM). The Kaplan–Meier survival curves uncovered distinct patterns among the three genes (Figure 5). High MTOR expression was associated with a steep decline in overall survival (OS) between 20 and 60 months (log-rank p = 0.044). By five years, survival in the high-MTOR group approached 20%, whereas the low-MTOR cohort exceeded 60%. These data highlight a potential role for upregulated mTOR signaling in aggressive disease phenotypes and underscore the plausibility of integrating mTOR inhibitors with MEKi or FAKi to counteract emergent resistance (Figure 5A).

https://doi.org/10.3390/cancers18010074

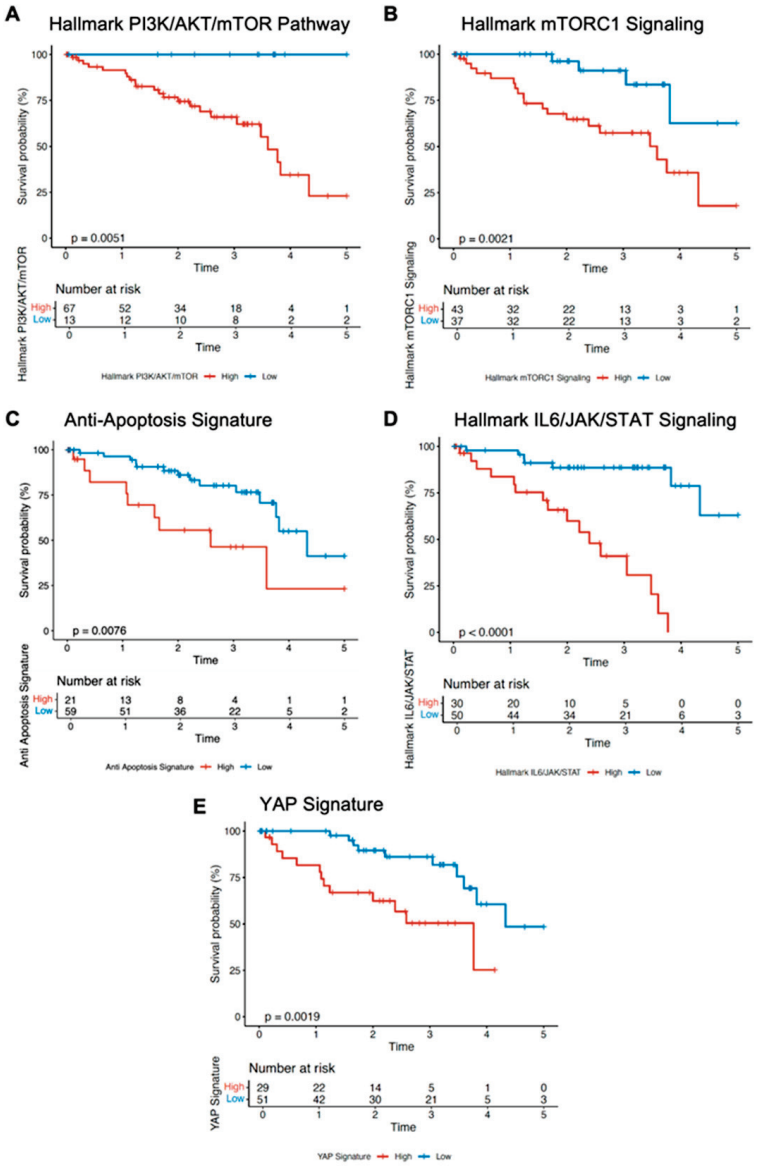


Figure 4. Pathway activity impacts overall survival in uveal melanoma. Gene Set Enrichment Analysis (GSEA) of the TCGA UVM cohort (n = 80) using Hallmark and Reactome gene sets from MSigDB reveals clinical relevance of key pathways identified in resistance mechanisms under FAK or MEK inhibition. (**A**) High activity of the PI3K/AKT/mTOR pathway is associated with significantly worse overall survival ($p = 0.0051$). (**B**) Elevated mTORC1 signaling correlates with poor survival outcomes ($p = 0.0021$). (**C**) High anti-apoptosis pathway activity is linked to reduced survival ($p = 0.0076$). (**D**) Increased IL6/JAK/STAT signaling is associated with worse survival ($p < 0.0001$). (**E**) High YAP signature activity predicts poorer survival outcomes ($p = 0.0019$).

Analysis of BCL2L1, a key anti-apoptotic gene, showed elevated transcript levels were linked with significantly worse survival ($p = 0.04$), suggesting that tumors with heightened anti-apoptotic capacity may rapidly evade cancer therapies (Figure 5B). Targeting BCL-XL (e.g., via BH3 mimetics) combined with existing inhibitors could disrupt this powerful survival shield. Notably, high TEAD4 expression was associated with a pronounced risk of mortality (log-rank $p = 0.00087$), with a hazard ratio of 4.8 ($p = 0.0025$), highlighting the critical involvement of Hippo pathway effectors in driving UVM aggressiveness and potential therapy escape (Figure 5C).

https://doi.org/10.3390/cancers18010074

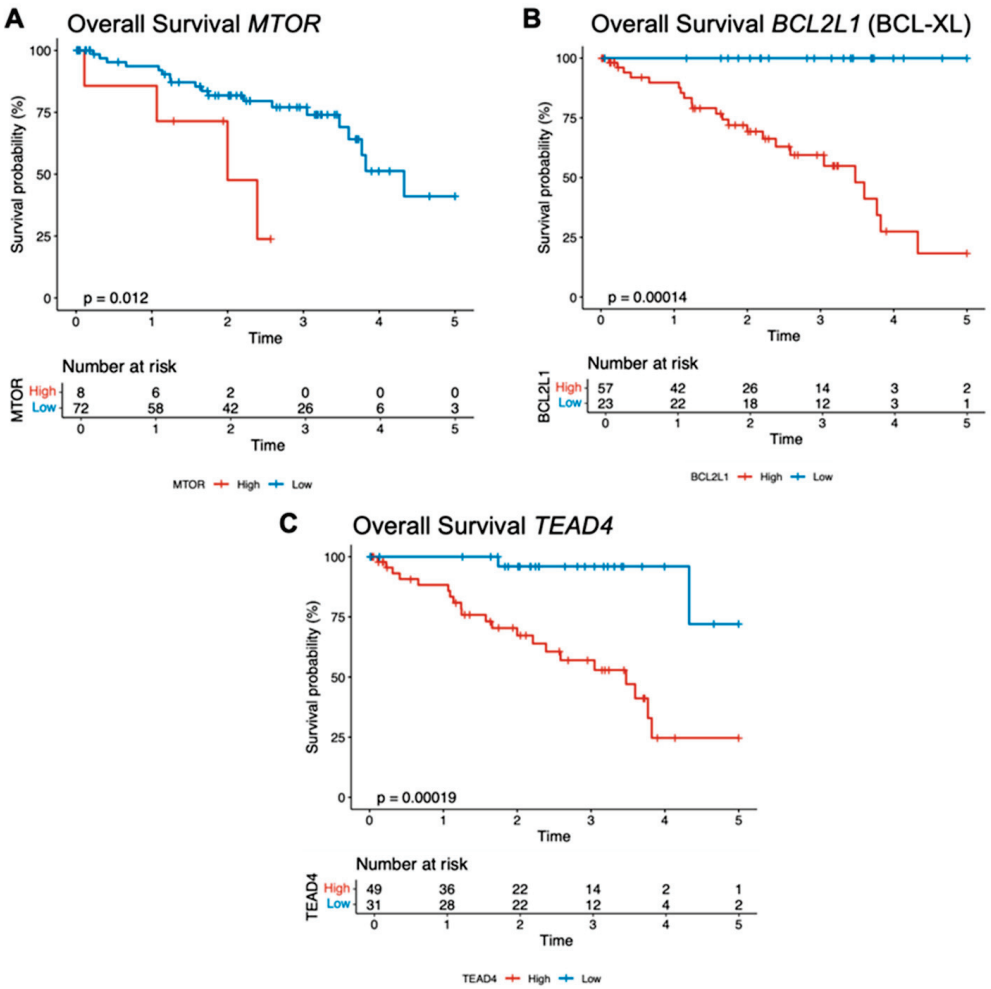


Figure 5. Elevated expression of mTOR, BCL2L1 (BCL-XL), and TEAD4 correlates with worse overall survival. Kaplan–Meier survival curves illustrate the difference in patient outcomes in the TCGA Uveal Melanoma cohort (n = 80) when classified into high (red) versus low (blue) transcript expression groups for each gene. (**A**) High mTOR expression is associated with reduced overall survival (log-rank $p = 0.012$). (**B**) High BCL2L1 expression (anti-apoptotic BCL-XL) significantly predicts poorer survival (log-rank $p = 0.00014$). (**C**) High TEAD4 expression, reflecting active Hippo–YAP/TEAD signaling, correlates with inferior patient outcomes (log-rank $p = 0.00019$). Numbers at risk for each subgroup are shown below the *x*-axis.

Although UVM is predominantly driven by GNAQ/GNA11 mutations, these data illuminate an additional, non-mutational layer of plasticity that may arise during therapy. Taken together, our screen and correlative analyses delineate potential biomarkers for patient selection or exclusion (based on high expression of MTOR or BCL2L1), real-time monitoring of therapeutic response (assessing upregulation of PI3K/mTOR or BCL2-family members), and design of next-generation combination strategies aimed at delaying or preventing resistance. Indeed, prior work in other malignancies supports that concurrent PI3K/mTOR inhibition can enhance the efficacy of MEK blockade [29,30]. Our findings now extend these insights to UVM and underscore the translational relevance of targeting these pathways (e.g., with PI3K/mTOR inhibitors, BH3 mimetics, or JAK inhibitors) alongside MEK or FAK blockade to prevent or delay resistance.

https://doi.org/10.3390/cancers18010074

3.5. Aberrant Activation of the AKT and YAP Pathways Induces Resistance to the Antiproliferative Effects of MEKi and FAKi

Building on our results, we selected the two most representative candidate oncogenic mechanisms to explore the effect of aberrant PI3K/AKT (myr-AKT) and YAP/TEAD (YAP-5SA) pathway activation on resistance to the cytotoxic effects of FAKi and MEKi. We initially analyzed the proliferation of parental 92.1 cells and myr-AKT and YAP-5SA-expressing cells treated with FAKi or MEKi (Figure 6A–D) (see Western blots below, Figure 7). We observed that myr-AKT and YAP-5SA-expressing cells resist FAKi and MEKi treatment, proliferating efficiently in contrast to parental cells, where proliferation was inhibited by these treatments. Interestingly, the proliferation of myr-AKT cells was significantly greater than that of parental cells (Figure 6B). Aligned with these findings, cell migration in wound-closure assays showed that the oncoproteins myr-AKT and YAP-5SA also increase cell motility in serum-containing medium (Supporting Figure S1). At the same time, FAKi decreased cell migration and MEKi increased cell motility, consistent with the previously reported increased FAK activation in response to MEK inhibitors in uveal [25] and cutaneous melanoma [31]. The AKT and YAP pathways did not affect the effect of FAKi and MEKi on cell migration, in contrast to promoting resistance to the anti-proliferative effects of these treatments (Supporting Figure S1).

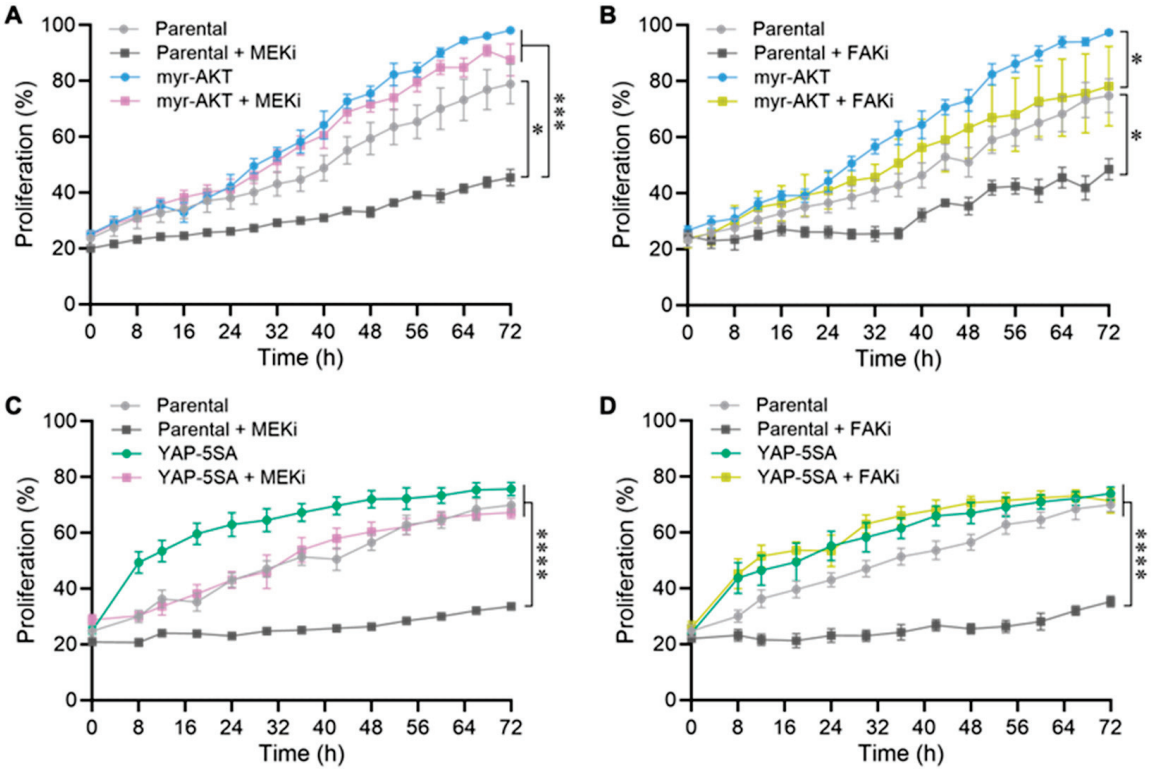


Figure 6. Expression of myr-AKT and YAP-5SA oncoproteins promotes resistance to MEKi and FAKi. (**A**) Proliferation assays of parental cells and myr-AKT with or without treatment with MEKi (3 nM, trametinib) or (**B**) with FAKi (0.3 μM, VS-4718). Two-way repeated measures ANOVA followed by Tukey post hoc, * $p < 0.05$, *** $p < 0.001$. (**C**) proliferation of parental and YAP-5SA cells treated with MEKi (3 nM, trametinib) or (**D**) with FAKi (0.3 μM, VS-4718). Two-way repeated measures ANOVA followed by Tukey post hoc, **** $p < 0.001$.

https://doi.org/10.3390/cancers18010074

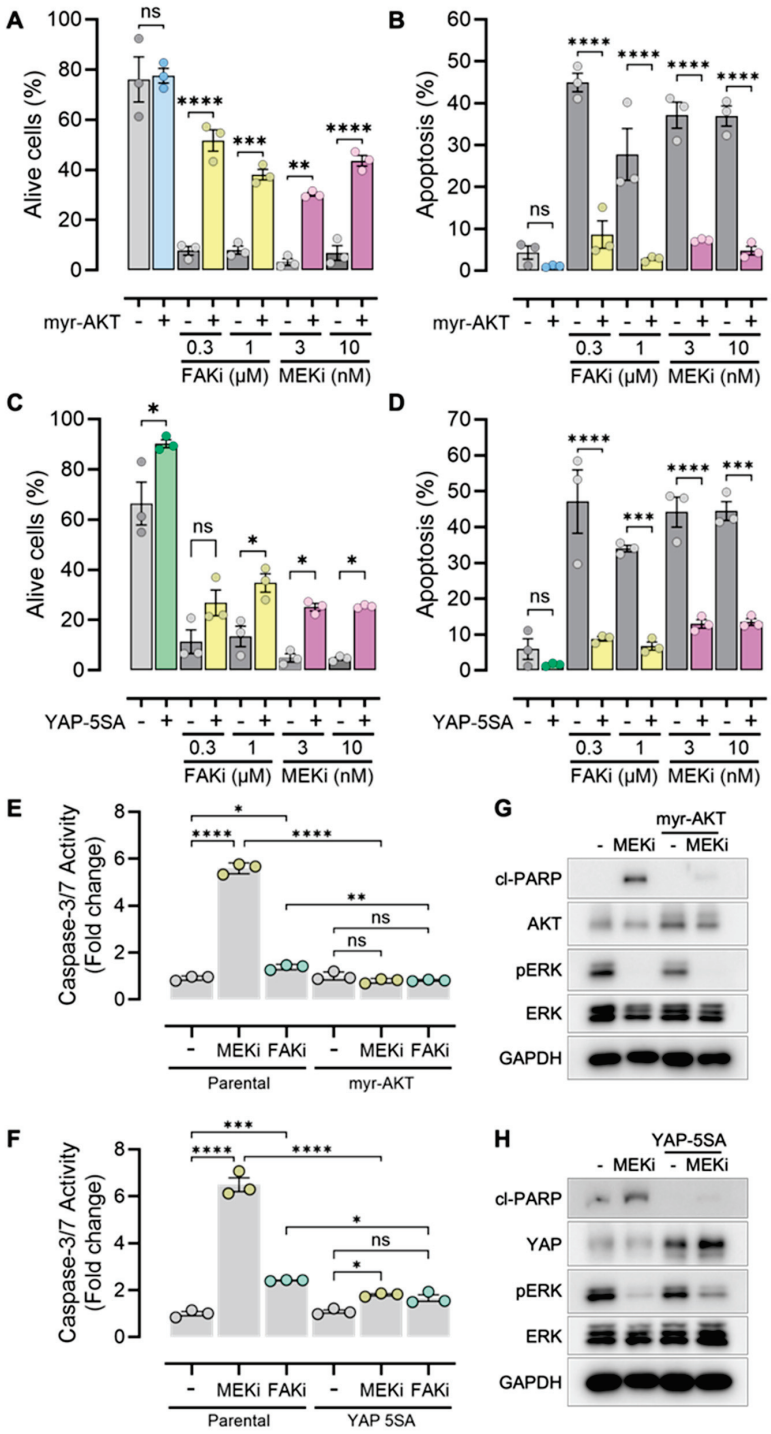


Figure 7. Activation of YAP and AKT pathways promotes resistance to apoptosis induced by MEK and FAK inhibitors. (**A**) Quantification of live cells and (**B**) apoptotic cells treated with FAKi or MEKi in parental cells and myr-AKT cells. FAKi (VS-4718) 0.3 and 1 μM; MEKi (trametinib) 3 and 10 nM. One-way ANOVA followed by Tukey post hoc; ns, not significant, ** $p < 0.01$, *** $p < 0.001$, **** $p < 0.0001$. (**C**). Quantification of live cells, (**D**) apoptotic cells treated with FAKi or MEKi in parental cells and YAP-5SA cells. FAKi (VS-4718) 0.3 and 1 μM; MEKi (trametinib) 3 and 10 nM. One-way ANOVA followed by Tukey post hoc; ns, not significant, * $p < 0.05$, *** $p < 0.001$, **** $p < 0.0001$. (**E**) Caspase-3/7 activity assays in parental, myr-AKT, and (**F**) YAP-5SA cells treated with MEKi (10 nM, trametinib) and FAKi (1 μM, VS-4718). One-way ANOVA followed by Tukey post hoc; ns, not significant, * $p < 0.05$, ** $p < 0.01$, *** $p < 0.001$, **** $p < 0.001$. (**G**) Western blot of cl-PARP in myr-AKT and (**H**) YAP-5SA expressing cells treated with MEKi (10 nM, trametinib) by 24 h. The uncropped blots are shown in Figure S3.

https://doi.org/10.3390/cancers18010074

3.6. Myr-AKT and YAP-5SA Protect UVM Cells from FAKi- or MEKi-Induced Apoptosis

We hypothesized that the protective effects of myr-AKT and YAP-5SA in UVM cells against the cytotoxicity of FAKi and MEKi may result from counteracting their effectiveness in promoting cell death. We evaluated the impact of FAKi and MEKi on apoptotic cell death using ethidium bromide and acridine orange fluorescence staining of cells, where the live cells stain only the nucleus with green fluorescence (acridine orange), in contrast the apoptotic cells have green and red fluorescence (acridine + ethidium bromide) because the integrity of the plasma and nuclear membrane was compromised (Supporting Figure S2). FAKi and MEKi drastically decreased the percentage of parental 92.1 live cells, with the majority of cells showing membrane permeability for ethidium bromide influx (Figure 7A,C, Supporting Figure S2). When cells express myr-AKT or YAP-5SA and are treated with FAKi and MEKi, the apoptotic cells decreased significantly (Figure 7B,D). Subsequently, we also analyzed caspase 3/7 activity. MEKi increased caspase activity in the treated parental cells, while FAKi, as a single agent, was less effective. UVM cells expressing myr-AKT (Figure 7E) and YAP-5SA (Figure 7F) were resistant to the induction of caspase by MEKi, suggesting that the oncoproteins promote pro-survival pathways resulting in reduced caspase activation. Consistently, when analyzing cleaved-PARP, we confirmed that myr-AKT (Figure 7G) and YAP-5SA (Figure 7H) reduce cell death, without considerably altering the effect of MEKi on reducing pERK; therefore, the AKT and YAP pathways induce resistance mechanisms independent of ERK reactivation.

4. Discussion

Targeted therapies are essential in precision oncology, but their success in uveal melanoma is limited by the rapid emergence of adaptive resistance. By screening 100 active or dominant-negative mutants resulting in persistent activation of cancer-associated signaling nodes in a BAP1 wild-type UVM model (92.1) and validating the top hits in a BAP1-mutated cellular model (MP46), we characterized potential signaling mechanisms that modulate sensitivity to GNAQ-pathway inhibition. While the use of ectopic gene expression in UVM cells may have some limitations with respect to the activation of endogenous signaling events; nonetheless, this approach, this approach allowed for the identification of pathways whose activation is sufficient to attenuate drug response under these defined experimental conditions.

Earlier clinical trials with MEK inhibitors have shown limited benefit [19–21]. Accumulating evidence suggests that adaptive compensatory signaling may contribute to the insufficient therapeutic effect. Our study highlights several canonical and non-canonical signaling pathways that, when experimentally activated, are capable of modulating sensitivity to MEK and FAK inhibition, outlining a network of potential adaptive signaling responses in uveal melanoma cells.

Among the pathways identified, the Hippo/YAP pathway appeared as a notable modulator of drug sensitivity. The oncogenic role of YAP in UVM is well established [8,32]. In the context of our in vitro models, we observed that YAP hyperactivation, either through loss of upstream Hippo pathway regulator LATS or directly activated by expression of a phosphorylation-defective YAP mutant, was associated with reduced sensitivity to FAK and MEK inhibition. These findings are consistent with YAP/TEAD-mediated transcription acting as a downstream transcriptional output for multiple signaling inputs associated with reduced drug sensitivity in our experimental models.

Our results also highlight the PI3K/AKT/mTOR axis in the modulation of response to both MEK and FAK inhibition. Previous studies suggested a role for AKT/mTOR reactivation in limiting the activity of MEK inhibitors [33], but which component within this pathway could restore survival signaling functionally remained unclear. Through an

https://doi.org/10.3390/cancers18010074

unbiased screen, we observed that constitutive activation of this pathway (e.g., by myr-AKT and mTOR variants) is sufficient to partially restore cell viability under combined inhibition in both BAP1-wildtype and BAP1-mutant cell lines. These findings provide a mechanistic rationale for further investigating combination strategies that concurrently target MEK, FAK, and mTOR and may help clarify the synergy reported in previous in vivo studies [33].

In addition to signaling pathways regulating proliferation and survival, our data indicate that modulation of apoptotic thresholds can influence drug response. Specifically, overexpression of BCL2 or BCL-XL protected UVM cells from therapy-induced cell death in our assays. This is consistent with the sensitivity of UVM patient-derived xenograft (PDX) models to BH3 mimetics in [34]. In addition, our data demonstrate that BCL-2 family upregulation is not only associated with resistance but also a functional determinant of cancer cell survival in vitro that can be pharmacologically reversed. In this regard, we have recently demonstrated the increase in BCL-XL, BCL2, and MCL1 during the treatment with MEK and FAK inhibitors [35]. Specifically, we observed that BCL2 promotes resistance to MEKi and FAKi combination, which can be exploited pharmacologically using BCL2 inhibitors (venetoclax) that act synergistically to promote UVM cell death [35]. Therefore, BCL-2 inhibition represents a promising strategy to convert the cytostatic effect of current therapies into a cytotoxic response. In addition, emerging data suggest that BCL-XL expression may contribute to resistance to FAKi and MEKi, in conjunction with BCL2.

Limitations and future directions: In summary, this study examines the signaling plasticity of uveal melanoma cells by systematically mapping pathways that allow cells to evade growth suppression and cell death upon MEK and FAK inhibition in controlled in vitro experimental settings. We report multiple resistance mechanisms (including activation of PI3K/mTOR, BCL-2 family proteins, YAP/TEAD, and potentially JAK/STAT) within a coherent framework, and delineate specific signaling nodes that modulate cellular responses to pathway inhibition.

The concordance between our findings and the adaptive mechanisms reported across multiple UVM models supports the biological relevance of the pathways identified in our screen, yet we acknowledge that the present analyses were performed in a limited number of cell lines and relied on ectopic expression levels that may exceed physiological thresholds. In addition, our experimental approach relied exclusively on in vitro models and did not include in vivo or patient-derived systems, which will be important to further evaluate the relevance of these findings in more complex biological contexts

Going forward, it will be crucial to validate our findings across additional UVM models and expanded patient cohorts to prioritize the most tractable molecular targets and develop multimodal therapeutic strategies that aim to prevent resistance before it emerges.

5. Conclusions

These insights pave the way for the development of customized therapeutic regimens that anticipate and minimize resistance, creating an opportunity for deeper and more durable responses and potentially curative outcomes in patients with advanced UVM. Notably, by focusing on validating the most significant results in MP46 (BAP1-mutated) UVM cells, we observed consistent mechanisms of resistance, reinforcing the notion that targeting shared compensatory pathways (e.g., BCL-2 family, PI3K/mTOR, YAP/TEAD) alongside *GNAQ*/*GNA11*-driven signaling networks represent a critical strategy for advancing UVM therapy.

Supplementary Materials: The following supporting information can be downloaded at https://www.mdpi.com/article/10.3390/cancers18010074/s1, Table S1: MEKi screen shows Cell Viability Max Response of individually virally transduced cell populations with mutant library in 92.1 cells; Table S2: FAKi screen shows Cell Viability Max Response of individually virally transduced cell

https://doi.org/10.3390/cancers18010074

populations with mutant library in 92.1 cells. Figure S1: The myr-AKT and YAP5SA oncoproteins increase cell migration in wound closure assay; Figure S2: Cytotoxicity of FAKi and MEKi in myr-AKT and YAP-5SA 92.1 cells; Figure S3: Uncropped Western blot images corresponding to the blots shown in Figure 7.

Author Contributions: Conceptualization, S.L., R.D.C.-V. and J.S.G.; methodology, S.L., R.D.C.-V., N.A. and E.S.C.-A.; validation, J.S.P., M.A., K.S., E.S.C.-A. and G.C.-M.; formal analysis, R.D.C.-V. and K.S.; investigation, S.L., R.D.C.-V., N.A. and E.S.C.-A.; resources, J.S.G.; data curation, S.L., R.D.C.-V. and K.S.; writing—original draft preparation, S.L. and R.D.C.-V.; writing—review and editing, S.L., R.D.C.-V. and J.S.G.; visualization, S.L., R.D.C.-V. and J.S.G.; supervision, J.S.G.; project administration, S.L., R.D.C.-V. and J.S.G.; funding acquisition, S.L., N.A. and J.S.G. All authors have read and agreed to the published version of the manuscript.

Funding: This work was supported by grants European Union Horizon 2020 Marie Sk1ødowska-Curie no. 101027731 (to S.L.), AIRC and the European Union's Horizon 2020 Marie Sklødowska-Curie no. 800924 (to S.L.), DGE-1650112 (to N.A.), NIH T32GM007752 (to N.A), NIH R01 CA257505 (to J.S.G), National Institutes of Health (NCI U54 CA274502) (to J.S.G.), and Melanoma Research Alliance MRA827624 (to J.S.G.).

Data Availability Statement: The data generated and analyzed during the current study are available from the corresponding author upon reasonable request.

Acknowledgments: Cartoons created with https://BioRender.com.

Conflicts of Interest: J. Silvio Gutkind reports consulting fees from Radionetics Oncology, BTB Therapeutics, Pangea Therapeutics, and Acurion, and is the founder of Kadima Pharmaceuticals, all unrelated to the current study. Other authors declare no competing financial interests.

Abbreviations

The following abbreviations are used in this manuscript:

UVM	Uveal melanoma
FAK	Focal adhesion kinase
GSEA	Gene Set Enrichment Analysis
MSigDB	Molecular Signatures Database

References

1. Helgadottir, H.; Hoiom, V. The genetics of uveal melanoma: Current insights. *Appl. Clin. Genet.* **2016**, *9*, 147–155. [CrossRef] [PubMed]
2. Singh, A.D.; Turell, M.E.; Topham, A.K. Uveal melanoma: Trends in incidence, treatment, and survival. *Ophthalmology* **2011**, *118*, 1881–1885. [CrossRef] [PubMed]
3. Luke, J.J.; Triozzi, P.L.; McKenna, K.C.; Van Meir, E.G.; Gershenwald, J.E.; Bastian, B.C.; Gutkind, J.S.; Bowcock, A.M.; Streicher, H.Z.; Patel, P.M.; et al. Biology of advanced uveal melanoma and next steps for clinical therapeutics. *Pigment. Cell Melanoma Res.* **2015**, *28*, 135–147. [CrossRef]
4. Rantala, E.S.; Hernberg, M.; Kivela, T.T. Overall survival after treatment for metastatic uveal melanoma: A systematic review and meta-analysis. *Melanoma Res.* **2019**, *29*, 561–568. [CrossRef]
5. Khoja, L.; Atenafu, E.G.; Suciu, S.; Leyvraz, S.; Sato, T.; Marshall, E.; Keilholz, U.; Zimmer, L.; Patel, S.P.; Piperno-Neumann, S.; et al. Meta-analysis in metastatic uveal melanoma to determine progression free and overall survival benchmarks: An international rare cancers initiative (IRCI) ocular melanoma study. *Ann. Oncol.* **2019**, *30*, 1370–1380. [CrossRef]
6. Davies, H.; Bignell, G.R.; Cox, C.; Stephens, P.; Edkins, S.; Clegg, S.; Teague, J.; Woffendin, H.; Garnett, M.J.; Bottomley, W.; et al. Mutations of the BRAF gene in human cancer. *Nature* **2002**, *417*, 949–954. [CrossRef]
7. Curtin, J.A.; Fridlyand, J.; Kageshita, T.; Patel, H.N.; Busam, K.J.; Kutzner, H.; Cho, K.H.; Aiba, S.; Brocker, E.B.; LeBoit, P.E.; et al. Distinct sets of genetic alterations in melanoma. *N. Engl. J. Med.* **2005**, *353*, 2135–2147. [CrossRef] [PubMed]
8. Feng, X.; Degese, M.S.; Iglesias-Bartolome, R.; Vaque, J.P.; Molinolo, A.A.; Rodrigues, M.; Zaidi, M.R.; Ksander, B.R.; Merlino, G.; Sodhi, A.; et al. Hippo-independent activation of YAP by the GNAQ uveal melanoma oncogene through a trio-regulated rho GTPase signaling circuitry. *Cancer Cell* **2014**, *25*, 831–845. [CrossRef]

https://doi.org/10.3390/cancers18010074

9. Van Raamsdonk, C.D.; Bezrookove, V.; Green, G.; Bauer, J.; Gaugler, L.; O'Brien, J.M.; Simpson, E.M.; Barsh, G.S.; Bastian, B.C. Frequent somatic mutations of GNAQ in uveal melanoma and blue naevi. *Nature* **2009**, *457*, 599–602. [CrossRef]
10. Van Raamsdonk, C.D.; Griewank, K.G.; Crosby, M.B.; Garrido, M.C.; Vemula, S.; Wiesner, T.; Obenauf, A.C.; Wackernagel, W.; Green, G.; Bouvier, N.; et al. Mutations in GNA11 in uveal melanoma. *N. Engl. J. Med.* **2010**, *363*, 2191–2199. [CrossRef]
11. Harbour, J.W.; Onken, M.D.; Roberson, E.D.; Duan, S.; Cao, L.; Worley, L.A.; Council, M.L.; Matatall, K.A.; Helms, C.; Bowcock, A.M. Frequent mutation of BAP1 in metastasizing uveal melanomas. *Science* **2010**, *330*, 1410–1413. [CrossRef] [PubMed]
12. Feng, X.; Arang, N.; Rigiracciolo, D.C.; Lee, J.S.; Yeerna, H.; Wang, Z.; Lubrano, S.; Kishore, A.; Pachter, J.A.; Konig, G.M.; et al. A Platform of Synthetic Lethal Gene Interaction Networks Reveals that the GNAQ Uveal Melanoma Oncogene Controls the Hippo Pathway through FAK. *Cancer Cell* **2019**, *35*, 457–472 e455. [CrossRef]
13. Wang, Z.; Martin, D.; Molinolo, A.A.; Patel, V.; Iglesias-Bartolome, R.; Degese, M.S.; Vitale-Cross, L.; Chen, Q.; Gutkind, J.S. mTor co-targeting in cetuximab resistance in head and neck cancers harboring PIK3CA and RAS mutations. *J. Natl. Cancer Inst.* **2014**, *106*, dju215. [CrossRef]
14. Lui, V.W.Y.; Hedberg, M.L.; Li, H.; Vangara, B.S.; Pendleton, K.; Zeng, Y.; Lu, Y.; Zhang, Q.; Du, Y.; Gilbert, B.; et al. Frequent mutation of the PI3K pathway in head and neck cancer defines predictive biomarkers. *Cancer Discov.* **2013**, *3*, 761–769. [CrossRef] [PubMed]
15. Quesnelle, K.M.; Grandis, J.R. Dual kinase inhibition of EGFR and HER2 overcomes resistance to cetuximab in a novel in vivo model of acquired cetuximab resistance. *Clin. Cancer Res.* **2011**, *17*, 5935–5944. [CrossRef]
16. Stabile, L.P.; He, G.; Lui, V.W.; Thomas, S.; Henry, C.; Gubish, C.T.; Joyce, S.; Quesnelle, K.M.; Siegfried, J.M.; Grandis, J.R. c-Src activation mediates erlotinib resistance in head and neck cancer by stimulating c-Met. *Clin. Cancer Res.* **2013**, *19*, 380–392. [CrossRef]
17. Yamaguchi, K.; Iglesias-Bartolome, R.; Wang, Z.; Callejas-Valera, J.L.; Amornphimoltham, P.; Molinolo, A.A.; Cohen, E.E.; Califano, J.A.; Lippman, S.M.; Luo, J.; et al. A synthetic-lethality RNAi screen reveals an ERK-mTOR co-targeting pro-apoptotic switch in PIK3CA+ oral cancers. *Oncotarget* **2016**, *7*, 10696–10709. [CrossRef]
18. Anderson, G.R.; Winter, P.S.; Lin, K.H.; Nussbaum, D.P.; Cakir, M.; Stein, E.M.; Soderquist, R.S.; Crawford, L.; Leeds, J.C.; Newcomb, R.; et al. A Landscape of Therapeutic Cooperativity in KRAS Mutant Cancers Reveals Principles for Controlling Tumor Evolution. *Cell Rep.* **2017**, *20*, 999–1015. [CrossRef]
19. Falchook, G.S.; Lewis, K.D.; Infante, J.R.; Gordon, M.S.; Vogelzang, N.J.; DeMarini, D.J.; Sun, P.; Moy, C.; Szabo, S.A.; Roadcap, L.T.; et al. Activity of the oral MEK inhibitor trametinib in patients with advanced melanoma: A phase 1 dose-escalation trial. *Lancet Oncol.* **2012**, *13*, 782–789. [CrossRef]
20. Carvajal, R.D.; Sosman, J.A.; Quevedo, J.F.; Milhem, M.M.; Joshua, A.M.; Kudchadkar, R.R.; Linette, G.P.; Gajewski, T.F.; Lutzky, J.; Lawson, D.H.; et al. Effect of selumetinib vs chemotherapy on progression-free survival in uveal melanoma: A randomized clinical trial. *JAMA* **2014**, *311*, 2397–2405. [CrossRef] [PubMed]
21. Carvajal, R.D.; Piperno-Neumann, S.; Kapiteijn, E.; Chapman, P.B.; Frank, S.; Joshua, A.M.; Piulats, J.M.; Wolter, P.; Cocquyt, V.; Chmielowski, B.; et al. Selumetinib in Combination With Dacarbazine in Patients With Metastatic Uveal Melanoma: A Phase III, Multicenter, Randomized Trial (SUMIT). *J. Clin. Oncol.* **2018**, *36*, 1232–1239. [CrossRef]
22. Vaque, J.P.; Dorsam, R.T.; Feng, X.; Iglesias-Bartolome, R.; Forsthoefel, D.J.; Chen, Q.; Debant, A.; Seeger, M.A.; Ksander, B.R.; Teramoto, H.; et al. A genome-wide RNAi screen reveals a Trio-regulated Rho GTPase circuitry transducing mitogenic signals initiated by G protein-coupled receptors. *Mol. Cell* **2013**, *49*, 94–108. [CrossRef]
23. Martz, C.A.; Ottina, K.A.; Singleton, K.R.; Jasper, J.S.; Wardell, S.E.; Peraza-Penton, A.; Anderson, G.R.; Winter, P.S.; Wang, T.; Alley, H.M.; et al. Systematic identification of signaling pathways with potential to confer anticancer drug resistance. *Sci. Signal* **2014**, *7*, ra121. [CrossRef]
24. Zanconato, F.; Forcato, M.; Battilana, G.; Azzolin, L.; Quaranta, E.; Bodega, B.; Rosato, A.; Bicciato, S.; Cordenonsi, M.; Piccolo, S. Genome-wide association between YAP/TAZ/TEAD and AP-1 at enhancers drives oncogenic growth. *Nat. Cell Biol.* **2015**, *17*, 1218–1227. [CrossRef]
25. Paradis, J.S.; Acosta, M.; Saddawi-Konefka, R.; Kishore, A.; Gomes, F.; Arang, N.; Tiago, M.; Coma, S.; Lubrano, S.; Wu, X.; et al. Synthetic Lethal Screens Reveal Cotargeting FAK and MEK as a Multimodal Precision Therapy for GNAQ-Driven Uveal Melanoma. *Clin. Cancer Res.* **2021**, *27*, 3190–3200, Correction in *Clin. Cancer Res.* **2021**, *27*, 4664. https://doi.org/10.1158/1078-0432.CCR-21-2433. [CrossRef] [PubMed]
26. Arang, N.; Lubrano, S.; Rigiracciolo, D.C.; Nachmanson, D.; Lippman, S.M.; Mali, P.; Harismendy, O.; Gutkind, J.S. Whole-genome CRISPR screening identifies PI3K/AKT as a downstream component of the oncogenic GNAQ-focal adhesion kinase signaling circuitry. *J. Biol. Chem.* **2023**, *299*, 102866. [CrossRef] [PubMed]
27. Subramanian, A.; Tamayo, P.; Mootha, V.K.; Mukherjee, S.; Ebert, B.L.; Gillette, M.A.; Paulovich, A.; Pomeroy, S.L.; Golub, T.R.; Lander, E.S.; et al. Gene set enrichment analysis: A knowledge-based approach for interpreting genome-wide expression profiles. *Proc. Natl. Acad. Sci. USA* **2005**, *102*, 15545–15550. [CrossRef] [PubMed]

https://doi.org/10.3390/cancers18010074

28. Liberzon, A.; Birger, C.; Thorvaldsdottir, H.; Ghandi, M.; Mesirov, J.P.; Tamayo, P. The Molecular Signatures Database (MSigDB) hallmark gene set collection. *Cell Syst.* **2015**, *1*, 417–425. [CrossRef]
29. Posch, C.; Moslehi, H.; Feeney, L.; Green, G.A.; Ebaee, A.; Feichtenschlager, V.; Chong, K.; Peng, L.; Dimon, M.T.; Phillips, T.; et al. Combined targeting of MEK and PI3K/mTOR effector pathways is necessary to effectively inhibit NRAS mutant melanoma in vitro and in vivo. *Proc. Natl. Acad. Sci. USA* **2013**, *110*, 4015–4020. [CrossRef]
30. McNeill, R.S.; Canoutas, D.A.; Stuhlmiller, T.J.; Dhruv, H.D.; Irvin, D.M.; Bash, R.E.; Angus, S.P.; Herring, L.E.; Simon, J.M.; Skinner, K.R.; et al. Combination therapy with potent PI3K and MAPK inhibitors overcomes adaptive kinome resistance to single agents in preclinical models of glioblastoma. *Neuro Oncol.* **2017**, *19*, 1469–1480. [CrossRef]
31. Lubrano, S.; Cervantes-Villagrana, R.D.; Faraji, F.; Ramirez, S.; Sato, K.; Adame-Garcia, S.R.; Officer, A.; Arang, N.; Rigiracciolo, D.C.; Anguiano Quiroz, P.Y.; et al. FAK inhibition combined with the RAF-MEK clamp avutometinib overcomes resistance to targeted and immune therapies in BRAF V600E melanoma. *Cancer Cell* **2025**, *43*, 428–445.e6. [CrossRef]
32. Yu, F.X.; Luo, J.; Mo, J.S.; Liu, G.; Kim, Y.C.; Meng, Z.; Zhao, L.; Peyman, G.; Ouyang, H.; Jiang, W.; et al. Mutant Gq/11 promote uveal melanoma tumorigenesis by activating YAP. *Cancer Cell* **2014**, *25*, 822–830. [CrossRef] [PubMed]
33. Ho, A.L.; Musi, E.; Ambrosini, G.; Nair, J.S.; Deraje Vasudeva, S.; de Stanchina, E.; Schwartz, G.K. Impact of combined mTOR and MEK inhibition in uveal melanoma is driven by tumor genotype. *PLoS ONE* **2012**, *7*, e40439. [CrossRef] [PubMed]
34. Nemati, F.; de Montrion, C.; Lang, G.; Kraus-Berthier, L.; Carita, G.; Sastre-Garau, X.; Berniard, A.; Vallerand, D.; Geneste, O.; de Plater, L.; et al. Targeting Bcl-2/Bcl-XL induces antitumor activity in uveal melanoma patient-derived xenografts. *PLoS ONE* **2014**, *9*, e80836. [CrossRef] [PubMed]
35. Lubrano, S.; Cervantes-Villagrana, R.D.; Arang, N.; Officer, A.; Adame-Garcia, S.R.; Cuesta-Margolles, G.; Aplin, A.E.; Gutkind, J.S. Inhibition of anti-apoptotic BCL2 overcomes adaptive resistance to co-targeting of the protein kinase FAK and MEK in GNAQ-driven uveal melanoma. *J. Biol. Chem.* **2025**, *301*, 110712. [CrossRef]

Disclaimer/Publisher's Note: The statements, opinions and data contained in all publications are solely those of the individual author(s) and contributor(s) and not of MDPI and/or the editor(s). MDPI and/or the editor(s) disclaim responsibility for any injury to people or property resulting from any ideas, methods, instructions or products referred to in the content.

https://doi.org/10.3390/cancers18010074

cancers

MDPI

Article

Cancer Vaccine Targeting Mutated GNAQ-Expressing Uveal Melanoma

Vitali Alexeev [1,*], Mizue Terai [1], Sergei Koshkin [1], Olga Igoucheva [2] and Takami Sato [1]

[1] Department of Medical Oncology, Sidney Kimmel Cancer Center, Thomas Jefferson University, 1015 Walnut Street, Philadelphia, PA 19107, USA; mizue.terai@jefferson.edu (M.T.); sergei.koshkin@jefferson.edu (S.K.); takami.sato@jefferson.edu (T.S.)
[2] Department of Dermatology and Cutaneous Biology, Sidney Kimmel Medical College, Thomas Jefferson University, 233 S. 10th Street, Philadelphia, PA 19107, USA
* Correspondence: vitali.alexeev@jefferson.edu; Tel.: +1-215-503-1042

Simple Summary

Most effective immunotherapeutics rely on activation of a patient's immune system to fight cancer; however, they are only somewhat effective against metastatic uveal melanoma (MUM). This study explored DNA vaccination as a way to teach the immune system to recognize tumors and prevent the progression of metastatic lesions from dormant malignant cells and tumor seeds. Our findings indicate that cancer-fighting immune cells activated by DNA vaccines in animals and human cells can recognize and attack tumor cells characterized by the common UM-associated cancer-driving mutation. An enhanced form of this vaccine containing multiple parts and improved structure was even more effective in activating cancer-fighting immune cells. These data suggest that such a vaccine could be further improved toward the design of a novel MUM-preventive strategy.

Abstract

Background/Objectives: Uveal melanoma (UM) is the most common intraocular malignancy in adults. Although brachytherapy of the primary tumor provides an approximate 80% five-year survival, with time, nearly half of patients experience predominant liver metastases. It was proposed that malignant cells migrate early and stay dormant as they adapt to the liver microenvironment. We propose that cancer vaccine-mediated activation of UM-targeted immunity in primary UM patients could prevent progression of metastatic disease from dormant cells or malignant seeds. Thus, this study explored DNA vaccination as a measure to educate the immune system to recognize the most common UM-associated Q209L tumor driver mutation in GNAQ and GNA11 G-alpha proteins. **Methods:** Several DNA constructs encoding mutated GNAQ were developed and tested for activation of UM-reactive T cells in HLA-A2/Hd transgenic mice and human T cells ex vivo. **Results:** Constructs containing immune-enhancing PADRE and VP22-derived epitopes boosted T cell responses against mutant GNAQ, which correlated with reduced experimental lung metastases. Ex vivo dendritic cell-mediated T cell activation with vaccine constructs containing optimized structure produced cytolytic T cells that secreted IFN gamma and killed mutated GNAQ-expressing UM cells in vitro. **Conclusions:** These findings propose the utility of the fusion DNA vaccines in eliciting T cell immunity against UM cells bearing the Q209L mutation in GNAQ/GNA11 protein to prevent the establishment and progression of metastatic disease.

Keywords: DNA vaccine; uveal melanoma; fusion antigen; VP22; PADRE; protective immunity; mutated GNAQ

1. Introduction

Uveal melanoma (UM) is the most common intraocular malignancy in adults, accounting for 3.1% of all recorded cases of melanoma [1,2]. Although treatment of the primary intraocular lesions provides a favorable outcome for most of the patients [3], up to 50% of patients subsequently develop metastatic UM (MUM), most commonly in the liver, and succumb to the disease [4] even with the most advanced immunotherapies. The overall response rate in immune checkpoint inhibitors (ICIs) was low (3–18%), and median overall survival (OS) and progression-free survival (PFS) were reported to be 12–16 months and 2.7–3.0 months, respectively. Objective response rate to a novel T cell engager, Tebentafusp, was also low (9%) with a median PFS of 3.3 months and a median OS of 21.7 months in treatment-naïve MUM patients [5–7]. Low response to ICI and Tebentafusp therapies could be caused by the lack or paucity of the naturally occurring MUM-recognizing T cells and by the lack of T cell recruitment to MUM and quiescent/exhausted phenotype of the intratumoral T cells. These findings suggest that new modalities are needed to activate UM-specific T cell response or educate the immune system to recognize UM-associated antigens. Most primary UM and MUM share a tumor driver activating point mutation in highly homologous GNAQ and GNA11 Gα proteins, a substitution of glutamine at position 209 with leucine (Q209L) [8,9]. In our clinic, 62.5% of MUM cases are characterized by Q209L mutation in Gα proteins [10]. Given that branched amino acids, such as leucine, enhance binding of the peptides to HLA-A*02:01, we aimed this proof-of-concept study at evaluating immunogenicity of the Q209L-harboring GNAQ and at the potential to elicit T cell-mediated immunity using the deoxyribonucleic acid (DNA) vaccine platform. Multiple clinical studies highlight the advantages of DNA vaccines over other cancer vaccine platforms (reviewed in [11]). They elicit systemic, antigen-specific immune responses and durable immunologic memory while remaining safe, well-tolerated, and suitable for repeated administration. Unlike viral vaccines, they pose no risk of pathogenic infection or neutralizing antibody induction, and unlike RNA vaccines, they are stable and easily scalable. Moreover, DNA vaccines could be customized using standard molecular techniques for personalized therapies. Combining different immune-enhancing epitopes and mutated GNAQ (mtGNAQ), we optimized vaccine composition and assessed vaccine-mediated activation of UM-recognizing T cells ex vivo and in vivo. Despite the limitations (listed in the Section 4), our findings support mtGNAQ as a promising target for tumor-directed immunity.

2. Materials and Methods

2.1. DNA Vaccine Construction and Vaccination

To generate the mtGNAQ-specific DNA vaccine, full-length mouse GNAQ cDNA was amplified from total RNA isolated from Melan-a mouse melanocytes [12] using the Superscript III RT kit (Thermo Fisher, Waltham, MA, USA, #18080051) and PfuUltra II DNA polymerase (Agilent, Santa Clara, CA, USA, # 600670). There is 99.9% homology between mouse and human GNAQ protein sequences with exception of the hydrophobic alanine (A171) in human GNAQ that changes to polar serine in the mouse protein (Figure S1); therefore, a DNA vaccine targeting Q209L mutation could be used in both humans and mice. The cDNA was ligated into the pEF6/V5-His TOPO vector (Thermo Fisher, # K961020). Q209L and anchoring substitutions were introduced into the cDNA using a

https://doi.org/10.3390/cancers18030480

Phusion site-directed mutagenesis system (Thermo Fisher, #F541). Four vaccine vectors containing full-length wild-type and mutant GNAQ (mtGNAQ) cDNA alone or fused in-frame with PADRE (mtGNAQ-PADRE) with and without VP22 cDNA at the 5′ end (VP22-mtGNAQ-PADRE) were constructed (Figure 1a) using standard molecular cloning techniques. PADRE- and VP22-encoding sequences have been used to enhance the activation of T helper cells and cytotoxic T cells [13,14]. In vivo DNA vaccination was performed using the BTX ECM 830 system as described in our prior studies [15].

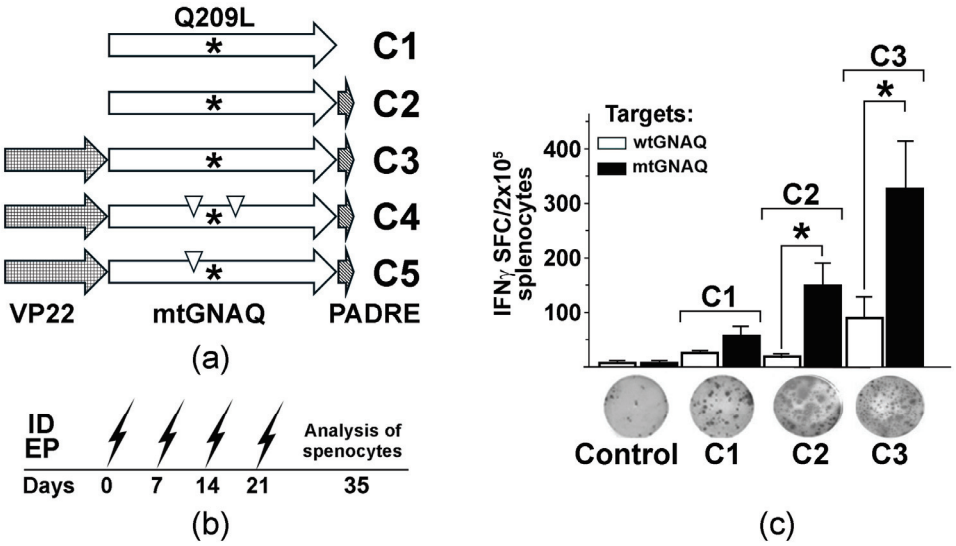


Figure 1. Design and testing of mtGNAQ DNA vaccine-induced T cell activation in vivo. (**a**) Diagram illustrating designs of the fusion vaccines containing VP22 and mtGNAQ ORFs and PADRE. Asterisks and down triangles indicate the position of the Q209L mutation and anchoring substitutions, respectively. (**b**) Timeline of DNA vaccinations via intradermal electroporation (ID EP, zigzag arrows) and collection of the splenocytes. (**c**) Column chart illustrating enumeration of IFNγ spot forming cells in differently vaccinated mice. Data are presented as an average of five independent measurements ± SD. Images of representative ELISpot wells corresponding to respective treatments are shown below the columns. In panels, statistical significance ($p < 0.05$) is indicated by asterisk.

2.2. Cells

HLA-A*02:01-positive human periferal blood mononucleated cells (PBMC) were isolated from human whole periferal blood (StemCell Technologies, Vancouver, BC, Canada, Leukopack, Cat#200-0043). Primary monocytes and T cells were isolated from PBMC by negative selection using cell type-specific negative selection kits (StemCell Technologies, Cat# 19359 (CD14+ monocytes) and Cat#19359 17961 (naïve pan-T cells)).

HLA-A*02:01-positive UM002 cells were isolated in the laboratory from uveal melanoma metastasis; 92.1 cell line was purchased from Millipore Sigma (Cat.# 13012458, Burlington, MA, USA); primary human melanocytes 1801c were kindly provided by Dr. Zalfa Abdel-Malek (University of Cincinnati, Cincinnati, OH, USA). CM006 cutaneous melanoma cells were isolated from cutaneous melanoma metastasis in the laboratory.

2.3. IFNγ ELISpot Assay

Mouse and human T cell activation was evaluated by IFNγ ELISpot assays using species-specific kits (eBioscience Santa Clara, CA, USA, #88-7384-88; ImmunoSpot, Rutesheim, Germany, #hIFNg), as devised by the manufacturers. Mouse or human melanocytic cells expressing mutated or wild-type GNAQ were used as targets.

https://doi.org/10.3390/cancers18030480

2.4. mtGNAQ Model for In Vivo Animal Studies

To generate a suitable mouse cell model, spontaneously immortalized non-tumorigenic mouse melanocytes, Melan-a, were stably transduced with expression vectors encoding HLA-A2/K^b (Addgene, Watertown, MA, USA, #14906, a gift from L. Sherman [16]) and full-length mtGNAQ via nucleofection. After selection, the cells acquired TPA-independent growth in vitro and the ability to produce blue nevus-like lesions in the skin (Figure S2). The resultant cells were used in all animal experiments. All animal studies were approved by the Institutional Animal Care and Use Committee. To establish pulmonary metastases, mtGNAQ-expressing cells (5×10^5 cells per mouse) were injected into HLA-A2/Hd transgenic mice via tail vein. Once lesions were established (2 weeks), animals were vaccinated via intradermal (ID) electroporation (EP), as described previously [15]. Five mice per cohort were used in all experiments.

2.5. Ex Vivo T Cell Activation and Analysis

Ex vivo activation of HLA-A*0201-positive T cells with autologous dendritic cells (DCs) was performed as previously described [17], with modifications. Briefly, $CD14^+$ monocytes and $CD3^+$ pan-T cells were isolated from PBMC of healthy donors. Monocytes were differentiated into DCs using a DC differentiation kit (StemCell Technologies), and immature DCs were transduced with DNA vaccines via nucleofection (#VPA-1004; Lonza, Basel, Switzerland). DC maturation was induced by adding 50 ng/mL TNFα, and DCs were exposed to autologous T cells at DC:T ratio of 1:40. After 24 h, DC maturation markers CD80 and CD86 as well as vaccine products were assessed by fluorescence activated cell sorting (FACS) and Western blot, respectively (Figure S2). After the initial activation and two re-stimulations with vaccine-transduced DCs, pooled polyclonal T cells were exposed to wtGNAQ and mtGNAQ targets. T cell activation was assessed using the IFNγ ELISpot assays. DCs and T cells from the three donors were tested. All kits, reagents, and culture media used for DC and T cell isolation, preparation, and culture were purchased from StemCell Technologies (Supplementary Materials S1). The cytotoxic activity of activated T cells was assessed using a FACS-based cell toxicity assay (Millipore, Burlington, MA, USA, #4500-0230) and the GuavaEasyCyte FACS system. Data were analyzed using GuavaSoft 2.7 software.

2.6. Immuno-Sequencing and Analysis of T Cell Repertoire

Evaluation and analysis of the T cell repertoire of the UM-recognizing vaccine-activated T cells were performed on RNA samples isolated from activated T cells using services provided by Creative Biolabs (Shirley, NY, USA).

2.7. Statistical Analysis

One-way analysis of variance (ANOVA) and paired *t*-test were performed using the GraphPad Prism 10.1.1 software. All experiments, except for RNA sequencing, were performed with at least three biological replicates. Statistical significance was set at $p < 0.05$.

3. Results

3.1. Fusion DNA Vaccine Enhance Q209L-Specific T Cell Immunity In Vivo

To evaluate whether the presence of the mutant leucine in Q209L enhances presentation of the mutated peptides by the MHC molecules, we completed an in silico analysis of the Q209L-harboring peptides (Table S1). This analysis predicts that the presence of mutant L in P7, P9, and P8 positions of the nonamers increases the binding of the peptides to HLA-A*01:01, A*02:01 and A*03:01, respectively, converting these peptides to potential weak binders (Table S1).

https://doi.org/10.3390/cancers18030480

To assess the immunogenicity of mtGNAQ, we created three DNA vaccine constructs encoding mutated GNAQ (mtGNAQ) (GNAQ are highly conservative among species. Amino acid sequences of mouse and human GNAQ are 99.9% identical with only one amino acid difference (A/S) at position 170 (Figure S1)) alone (construct C1) or fused in-frame with Pan DR-binding epitope (PADRE) on 3′ end (construct C2) and herpes simplex virus VP22 encoding sequence on 5′ end of mtGNAQ (construct C3) (Figure 1a). To define whether these constructs could activate mtGNAQ-specific immunity, naïve HLA-A2/Hd mice were vaccinated via intradermal (ID) electroporation (EP). This method provides efficient vaccine expression in mouse skin (Figure S2a). Vaccine administration sites were pre-treated with CCL21. Our previous studies demonstrated that such pre-treatment significantly enhances recruitment leukocytes, including $CCR7^+$ dendritic cells and T cells, and improves DNA vaccine efficacy [15]. Two weeks after four consecutive once-a-week vaccinations (Figure 1b), the activation of mtGNAQ-specific T cells was assessed by IFNγ ELISpot assay. Melan-a cells engineered to express mtGNAQ and HLA-A2/Kb hybrid MHC (MelanQ-A2) (Figure S2b–e) were used as targets. When injected intradermally into mouse skin, these cells produce blue nevus-like lesions (Figure S2f). Parental Melan-a mouse melanocytic cells [12] were used as control. This assay showed that vaccination with mtGNAQ alone (construct C1) produced a small number of IFNγ spot-forming cells (SFCs). The fusion of mtGNAQ with PADRE (construct C2) led to a marginal increase in SFCs, whereas VP22-mtGNAQ-PADRE (construct C3) provided the highest number of activated T cells when exposed to mtGNAQ targets (Figure 1c). Insignificant T cell activation after exposure to Melan-a cells suggested that T cells from C3-vaccinated mice specifically recognize targets expressing mtGNAQ.

3.2. Fusion DNA Vaccine Potentiates Cellular Immunity Sufficient to Prevent Metastatic Lesions

To develop a MUM-like experimental metastatic model, tumor-like cells (MelanoQ-A2) were inoculated intravenously (iv) into HLA-A2/Hd mice. Formation of multiple small pulmonary lesions confirmed the suitability of this cell model (Figure 2a). Then, experimental and control mice were iv inoculated with MelanQ-A2 cells and vaccinated via ID EP with Mock and mtGNAQ-encoding constructs four times once a week. Mock-, C1-, and C2-vaccinated animals develop respiratory distress within 6, 7, and 12 weeks after tumor inoculation, respectively. C3-vaccinated mice did not show signs of pulmonary distress for 15 weeks (Figure 2b). Evaluation of lung metastases showed that vaccination with C3 construct substantially reduced progression of pulmonary lesions (Figure 2b) and enhanced survival of the tumor-bearing mice beyond 7 weeks (Figure 2c). Reduction of tumor burden coincided with T cell activation quantified by IFNγ ELISpot (Figure 2d). Splenocytes from C3-vaccinated mice showed a significantly higher number of IFNγ SFCs than splenocytes from other vaccinated and control cohorts (Figure 2d). Considering that HLA-A2/Hd mice can generate T cells that recognize HLA-A2-bound epitopes [18], HLA-A2-restricted T cell response was differentiated using IFNγ ELISpot assay by exposure of splenocytes to mutated peptides bound to human T2 ($HLA\text{-}A^*0201^+$) cells. It showed the presence of T cells recognizing HLA-A*02:01-bound mutant GNAQ peptides (Figure 2e).

https://doi.org/10.3390/cancers18030480

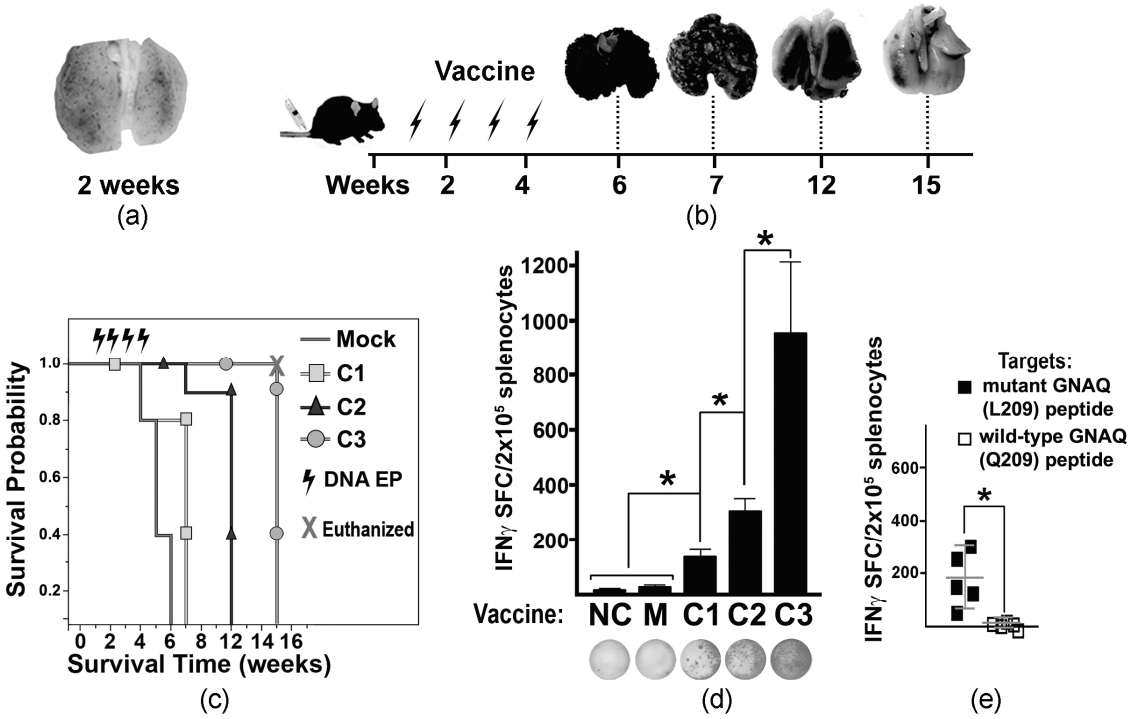


Figure 2. Tumor progression and vaccine-mediated T cell activation in tumor-bearing mice. (**a**) A2. cells. (**b**) Diagram illustrating the experimental timeline of vaccine administration and collection of tumor-affected lungs (representative images are shown above the timeline). Arrows indicate the times of ID EP. (**c**) Kaplan–Meier viability plot illustrating survival probability of tumor-bearing mice (weeks) vaccinated with different DNA constructs (as indicated in the key). Mice in the C3-vaccinated cohort were euthanized at week 15 to terminate the experiment with hazard ratio (HR) = 0.04 compared to the Mock-treated cohort. (**d**) Column chart illustrating the IFNγ ELISpot assay defining T cell activation in differently vaccinated mice. MelanQ-A2 cells were used at targets. The DNA vaccine constructs (C1, C2, and C3) are indicated below the columns. NC—negative control (splenocytes from naïve non-tumor-bearing mice); M—Mock-treated tumor-bearing mice. Data are presented as average SFCs from splenocytes collected from four animals per cohort ± SD. Representative photographs of ELISpot wells are shown below respective columns. (**e**) Scatter plot chart illustrates the specificity of T cell activation (IFNγ ELISpot assay) toward mutant GNAQ peptides loaded onto human T2 (HLA-A*0201) cells. The averages ± SD are shown in the charts. Splenocytes isolated from the C3-vaccinated mice were used. Statistical significance ($p < 0.05$) is indicated by an asterisk.

3.3. Anchor Modifications of mtGNAQ Enhance Human T Cell Activation Ex Vivo

To evaluate whether mtGNAQ-encoding fusion antigens could potentiate human T cell-mediated immunity toward mtGNAQ, we established a DNA vaccine-based ex vivo T cell activation protocol using donor-derived autologous DC and T cells. With the goal to improve mtGNAQ peptide-HLA-A*02:01 binding, predicted R202L or D205L and E212V anchoring substitutions (Table S1) were introduced into the mtGNAQ cDNA of the C3 construct. The resultant vectors were designated as C4 (R202L) and C5 (D205L and E212V) (Table S1, Figure 1a). $CD14^+$ monocytes from two different donors were differentiated into immature DC (Figure S3a,b) and nucleofected with C3 and anchor-modified constructs. Then DC maturation was induced and the expression of the fusion construct was validated by Western blot (Figure S3c). Vaccine-traduced mature $CD80^+$ $CD86^+$ DC (Figure S3e) were exposed to autologous pan-T cells. After the initial T cell priming, two re-stimulations with vaccine-transduced DC and low-dose IL-2 were performed at 1-week intervals. Then, T cell activation was evaluated by IFNγ ELISpot assay using UM-derived mtGNAQ and control, wild-type GNAQ-expressing melanocytic cells as targets. Quantitation of SFCs showed

https://doi.org/10.3390/cancers18030480

that C4 and C5 constructs provided, on average, five times greater T cell activation than the C3 construct (Figure 3a,b). T cell activity toward wild-type GNAQ-expressing melanocytes (1801c) and cutaneous melanoma cells (CM006) was not detected, although some response to one of the tested targets (CM006) was seen in C5-activated T cells (Figure 3a,b). FACS-based cytotoxicity assay showed that all three constructs produced specific cytolytic T cells recognizing mtGNAQ-expressing UM cells (92.1). The cytolytic activity of C5-activated T cells was the greatest, although there was no significant difference between CTL activity elicited by C5 and C4 constructs (Figure 3c). CTL activity toward UM was also confirmed by the xCELLigence real-time cytotoxicity assay, which showed progressive elimination of UM targets by differently activated T cells within 2 and 5 h (Figure S3e). Significantly higher Granzyme B activity of the C5 and C4-activaed T cells confirmed a greater response toward mtGNAQ UM targets (Figure 3d). Aggregation of DiO-labeled C5 and C4 ex vivo activated T cells on clusters of mtGNAQ UM targets within 1 h and the lack of accumulation of these T cells on control targets (CM006) also support the specificity of the T cell response toward mtGNAQ-expressing cells (Figure 3e).

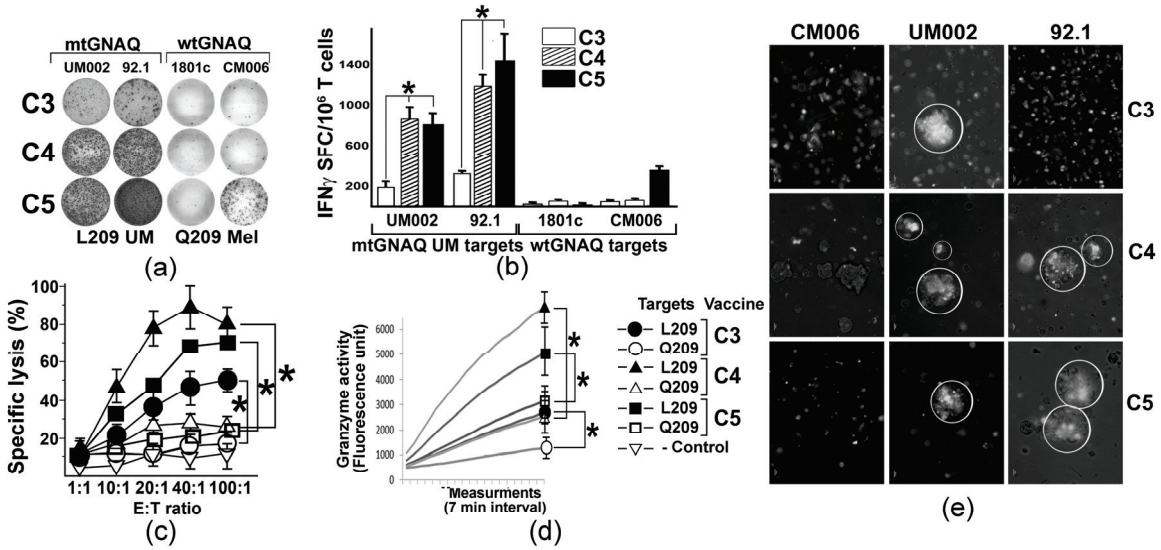


Figure 3. T cell activation by unmodified and anchor-modified DNA vaccines ex vivo. (**a**) Representative images illustrating the presence of IFNγ SFC in human T cells activated by different vaccine constructs (shown to the left) ex vivo; mtGNAQ-expressing UM cells and wtGNAQ-expressing melanocytic cells (indicated above the columns) were used as targets. (**b**) Column charts illustrating quantitation of IFNγ positive spots produced by T cells activated by different constructs (indicated in the key). Mutant and wild-type mtGNAQ targets are shown below the columns. Data are presented as averages of IFNγ SFC collected from three independent experiments ± SD. Assays were conducted in technical duplicates. (**c**,**d**) Charts illustrating cytotoxicity (**c**) and granzyme B activity (**d**) of vaccine-activated T cells (constructs indicated in the key to the right of the charts). In (**c**), Effector/Target (E:T) ratio is shown on the *x*-axis; specific lysis of target cells is shown on the *y*-axis. Data are collected from three independent experiments with technical duplicates and presented as an average ± SD. In (**d**), representative Granzyme B activity was measured in lysates of T cells exposed to wild-type and mutant GNAQ targets for 2 h. Activity was measured for 2 h with 7 min intervals using fluorescence-based Granzyme B activity assay. SDs at the endpoint were calculated from three independent measurements. CM006 and 92.1 cells were used as wtGNAQ and mtGNAQ targets, respectively. (**e**) Representative micrograph illustrating aggregation of Vybrant DiO-labeled ex vivo activated human T cells (white) on clusters of mtGNAQ UM cell (nonfluorescent; 92.1 and UM002) and lack of aggregation on the wild-type GNAQ-expressing cells (unlabeled, CM006). C3, C4, and C5 T cell-activating vaccine constructs are indicated to the right of the panels. Scale bar—10 μm. In all panels, statistical significance ($p < 0.05$) is indicated by asterisks.

https://doi.org/10.3390/cancers18030480

3.4. TCR Repertoire Suggests a Predominant Expansion of a Specific T Cell Clones in DNA Vaccine-Activated T Cell Population

To explore the diversity of the TCR repertoire in a pool of C5-activated T cells, we employed an RNA-based immuno-sequencing platform. The complementarity-determining region 3 (CDR3) length distribution (Figure 4a) and multiple sequence alignment indicated on shared CDR3 sequences with five fully conserved and three partly conserved residues are denoted with asterisk and octothorp, respectively (Figure 4b). Analysis of V-J pairing usage showed predominant pairing of TRBV6-2 with TRBJ2-5 (Figure 4c). Distribution analysis showed that approximately 30% of the top 100 TRB sequences expressed a specific TRB, suggesting expansion of specific T cells in the analyzed polyclonal population (Figure 4d). Saturation evaluation confirmed that the amount of sequencing data was reasonable, and that it accounted for most TCR sequences (Figure 4e).

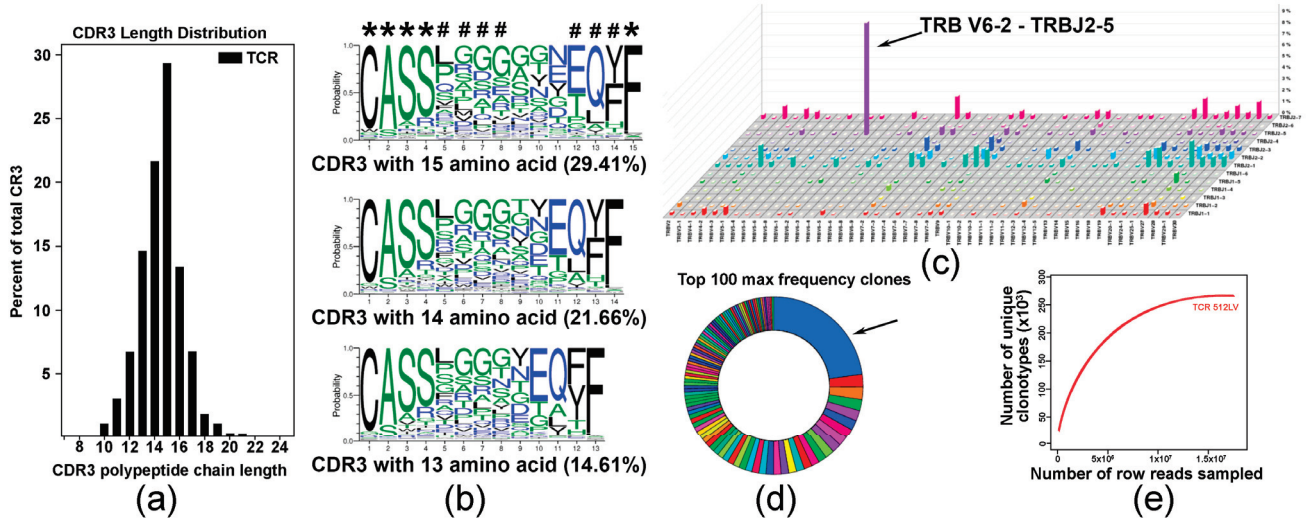


Figure 4. Analysis of T cell repertoire in C4-activated T cells. (**a**) Analysis of CDR3 length distribution in C4-activated T cell sample. Data are presented as percent of specific polypeptide chain length. (**b**) Analysis of amino acid conservation of the top three sequences with the largest CDR3 length distribution. Five fully conserved and three partly conserved residues are denoted with asterisk and octothorp, respectively. (**c**) V-J pairing usage analysis in TCR assembly showing preferential TRB V6-2 and J2-5 pairing in a pool of vaccine-activated T cells. (**d**) Diagram illustrating TRB distribution statistics showing that more than 30% of vaccine-activated T cells express specific TCRB (arrow). (**e**) Saturation evaluation showing that the amount of sequencing data used was sufficient and reached saturation.

4. Discussion

Clinical experience of the past decade has demonstrated that primary intraocular melanoma could be successfully managed by brachytherapy, which provides about an 80% five-year survival rate [19]. However, with time, nearly half of patients experience predominant liver metastases [2]. Despite recent advancements in immunotherapy for cutaneous melanoma, MUM remains intractable to this therapy, owing to the low frequency of UM-associated somatic mutations [20] and poor recruitment or quiescence of immune effectors to the hepatic MUM lesions [21]. The timing of UM metastasis to the liver is not well established, but it is believed that malignant cells migrate early and stay dormant as they adapt to the liver microenvironment. With the ultimate goal to target MUM cells and tumor seeds early and prevent MUM progression, in this study, we explored whether active vaccination could elicit UM-specific immunity. Previously, several attempts were made to target mutated tumor drivers (e.g., mutated BRAF, RAS) by immunotherapy. Some studies have shown that T cell response toward these proteins could be elicited by different

https://doi.org/10.3390/cancers18030480

vaccination approaches and enhanced by varying vaccine composition [22–24]. Using the flexibility of DNA vaccination platform that allows manipulation of vaccine structure and composition, we tested whether different vaccine designs could activate T cell-mediated immunity toward Q209L mutant GNAQ/GNA11, the most frequent tumor driver mutation in UM. GNAQ/GNA11 polypeptide sequence spanning the Q209L mutation site does not contain strong HLA-A*02:01 binders. Yet, we predicted that leucine, being a branched amino acid, stabilizes the HLA-A:02*01—peptide complex [25] and provides weak MHC-binding, making mutated peptide "visible" for the immune system. As naturally occurring mtGNAQ-specific T cells have not been isolated, it is plausible that mtGNAQ peptide–MHC complexes are not stable enough to produce strong T cell responses.

To improve the efficacy of mtGNAQ-specific vaccines, we employed several strategies including (i) VP22 and PADRE DNA vaccine fusion partners to enhance T cell activation, (ii) CCL21-enhanced DNA vaccination protocol [15], and (iii) introduction of HLA-A*02:01 anchoring substitutions to the putative immunogenic peptide [26–29]. Our data demonstrated that in-frame fusion of VP22 cDNA with antigen-encoding cDNA provided four times greater in vivo T cell activation than the construct lacking VP22 (Figures 1 and 2). Despite prior research [13], the mechanisms of VP22-mediated immune response enhancement remain undefined [30]. Our in silico analysis showed that VP22 contains three regions enriched with human HLA-A*0101, -A*0201, and -A*0301 putative binding epitopes (Figure S4). It is plausible that the binding of these VP22 epitopes to MHC I increases clustering of the co-stimulatory molecules on the surface of vaccine-transduced DC and enhances the activation of tumor antigen-specific T cells. Although further investigation is required, our observations suggest that these regions can be independently used for the design of HLA-specific vaccines.

In the past, we have shown that the addition of CCL21 to vaccine composition enhances recruitment of $CCR7^+$ T cells and mature DC to the vaccine administration site and facilitates T cell activation [15]. Introduction of anchoring amino acids into the antigenic epitope was successfully used in the past [26–29]. Our data showing that anchor-modified constructs (C4, C5) enhance UM-specific T cell immunity support this notion. Besides functional assays (IFNγ ELISpot, CTL and granzyme B activity), clonal expansion of vaccine-induced T cells was also supported by immuno-sequencing data showing the predominant expansion of specific T cell clones in a population of ex vivo activated T cells (Figure 4). Our in silico analysis also predicted that the Q209L mutation could create putative HLA-DR1, HLA-DR2, and HLA-DR5 binding epitopes (Table S2) that could be processed in an MHC II-dependent manner after lysis of the UM cells by vaccine-activated CTL and enhanced activation of T helper cells and antibody response [31]. These predictions have yet to be validated.

Our studies are limited to a rather small sample size used in the in vivo experimentation, yet the LaMorter power calculation on the obtained results (Figure 2d) showed that employed cohorts of animals provide 95% power to detect difference with alpha 0.01. This study is also limited by the lack of extended tumor monitoring in animals responding to vaccine by the inhibition of tumor progression. Yet, the timeframe was sufficient to compare different vaccine constructs for the ability to activate T cells and inhibit tumor progression. Due to the lack of immunocompetent animal models recapitulating human UM, this study is limited to the use of mouse melanocytic cells engineered to mimic human UM. Although artificial, this model allowed us to validate vaccine-mediated activation of mtGNAQ-specific immunity in vivo. Being a proof of concept, this study did not differentiate CD4- and CD8-mediated response, acquisition of immunologic memory, or durability of immune response. Our ex vivo findings provide proof-of-concept data demonstrating that optimization of the vaccine could enhance its efficacy. It is acknowledged that these

https://doi.org/10.3390/cancers18030480

data obtained with human leukocytes isolated from blood of a healthy donor may not be generalizable to UM patients. An important area for future studies will include further optimization of vaccine composition, broader investigation of the therapeutic capacity of vaccine-activated human T cells in animal models recapitulating human MUM, evaluation of ex vivo T cell activation protocol with UM patient-derived leukocytes, and testing of vaccine efficacy in humanized animal models.

5. Conclusions

Collectively, our findings demonstrate that mtGNAQ/GNA11 peptides harboring the Q209L substitution can be recognized by T cells activated by DNA vaccines in vivo and ex vivo. The data showed that anchoring modification(s) of the mtGNAQ epitope in the vaccine sequence could further enhance human T cell activity toward UM cells. These findings suggest that the established ex vivo protocol is suitable for activating UM-specific T cells suitable for MUM treatment. Although further studies with UM patient-derived cells are required to validate the production of functionally active T cells ex vivo, our data suggest that nucleic acid-based vaccination could be further improved to elicit protective immunity toward MUM.

Supplementary Materials: The following supporting information can be downloaded at: https://www.mdpi.com/article/10.3390/cancers18030480/s1, Table S1. In silico analysis of GNAQ peptide binding to HLA-A* molecules. Table S2. In silico prediction of Q209L GNAQ peptide binding to HLA-DR* molecules. Figure S1. Alignment of mouse and human GNAQ sequences. Figure S2. Vaccine expression and development of mtGNAQ mouse cells. Figure S3. Ex vivo DC differentiation, vaccine expression, and real-time cytotoxicity. Figure S4. Analysis of VP22 putative MHC I-binding sites.

Author Contributions: V.A.: Conceptualization, methodology development, project administration, supervision, acquisition of experimental data, writing—review and editing, validation. M.T.: Experimentation, formal analysis of the data, review and editing of the manuscript. S.K.: Acquisition of experimental data, formal analysis, review and editing of the manuscript. O.I.: Formal analysis, visualization of the data, writing—review and editing. T.S.: Conceptualization, methodology development, supervision, acquisition of funding, review and editing. All authors have read and agreed to the published version of the manuscript.

Funding: This work was supported in part by the Jill and Kevin Plancher Research Funds, the Hasumi International Research Foundation for VA and MT, and the Jefferson Institute of Molecular Medicine for OI and VA.

Institutional Review Board Statement: All animal studies were approved by the Institutional Animal Care and Use Committee of Thomas Jefferson University. Protocol 21-08-422 approved on 8 January 2024. Ammended protocol approved on 28 May 2025.

Informed Consent Statement: Human subjects were not involved in this study.

Data Availability Statement: Data generated by the authors are included in this article. The raw data generated by the authors and T cell receptor (TCR) sequencing raw data files are available upon request.

Acknowledgments: We would like to acknowledge the support from Melanoma Research Institute of Excellence (TJU), technical support from the institutional Laboratory Animal Service (TJU), and technical support from the former Sidney Kimmel Medical School students Sarah Ahmed and Toby Mathew.

Conflicts of Interest: Authors declare no conflict of interest.

https://doi.org/10.3390/cancers18030480

Abbreviations

The following abbreviations are used in this manuscript:

UM	Uveal melanoma
MUM	Metastatic uveal melanoma
HLA	Human lymphocyte antigen
PADRE	Pan-DR-binding epitope
ICI	immune checkpoint inhibitors
PFS	Progression-free survival
OS	Overall survival
mt	Mutant
wt	Wild-type
DNA	Deoxyribonucleic acid
RNA	Ribonucleic acid
RT	Reverse transcription
VP22	Viral protein 22
TPA	12-O-tetradecanoylphorbol-13-acetate
CD	Cluster differentiation
DC	Dendritic cells
FACS	Fluorescence activated cell sorting
IFN	Interferon
ANOVA	analysis of variance
TCR	T cell receptor
CDR3	Complementarity-determining region 3
CCL21	-C-motif chemokine 21; Secondary lymphoid chemokine 21
CCR7	-C-motif chemokine receptor 7
ELISpot	Enzyme-Linked Immunosorbent Spot
CTL	Cytotoxic T lymphocyte

References

1. Singh, A.D.; Turell, M.E.; Topham, A.K. Uveal melanoma: Trends in incidence, treatment, and survival. *Ophthalmology* **2011**, *118*, 1881–1885. [CrossRef]
2. Weinberger, Y.; Bena, J.; Singh, A.D. Uveal Melanoma: 5-Year Update on Incidence, Treatment, and Survival (SEER 1975–2020). *Ocul. Oncol. Pathol.* **2025**, *11*, 30–36. [CrossRef]
3. Diener-West, M.; Earle, J.D.; Fine, S.L.; Hawkins, B.S.; Moy, C.S.; Reynolds, S.M.; Schachat, A.P.; Straatsma, B.R.; Collaborative Ocular Melanoma Study Group. The COMS randomized trial of iodine 125 brachytherapy for choroidal melanoma, II: Characteristics of patients enrolled and not enrolled. COMS Report No. 17. *Arch. Ophthalmol.* **2001**, *119*, 951–965.
4. Collaborative Ocular Melanoma Study Group. Assessment of metastatic disease status at death in 435 patients with large choroidal melanoma in the Collaborative Ocular Melanoma Study (COMS): COMS report no. 15. *Arch. Ophthalmol.* **2001**, *119*, 670–676. [CrossRef]
5. Carvajal, R.D.; Butler, M.O.; Shoushtari, A.N.; Hassel, J.C.; Ikeguchi, A.; Hernandez-Aya, L.; Nathan, P.; Hamid, O.; Piulats, J.M.; Rioth, M.; et al. Clinical and molecular response to tebentafusp in previously treated patients with metastatic uveal melanoma: A phase 2 trial. *Nat. Med.* **2022**, *28*, 2364–2373. [CrossRef] [PubMed]
6. Carvajal, R.D.; Nathan, P.; Sacco, J.J.; Orloff, M.; Hernandez-Aya, L.F.; Yang, J.; Luke, J.J.; Butler, M.O.; Stanhope, S.; Collins, L.; et al. Phase I Study of Safety, Tolerability, and Efficacy of Tebentafusp Using a Step-Up Dosing Regimen and Expansion in Patients With Metastatic Uveal Melanoma. *J. Clin. Oncol.* **2022**, *40*, 1939–1948. [CrossRef] [PubMed]
7. Pelster, M.S.; Gruschkus, S.K.; Bassett, R.; Gombos, D.S.; Shephard, M.; Posada, L.; Glover, M.S.; Simien, R.; Diab, A.; Hwu, P.; et al. Nivolumab and Ipilimumab in Metastatic Uveal Melanoma: Results From a Single-Arm Phase II Study. *J. Clin. Oncol.* **2021**, *39*, 599–607. [CrossRef]
8. Van Raamsdonk, C.D.; Bezrookove, V.; Green, G.; Bauer, J.; Gaugler, L.; O'Brien, J.M.; Simpson, E.M.; Barsh, G.S.; Bastian, B.C. Frequent somatic mutations of GNAQ in uveal melanoma and blue naevi. *Nature* **2009**, *457*, 599–602. [CrossRef]
9. Van Raamsdonk, C.D.; Griewank, K.G.; Crosby, M.B.; Garrido, M.C.; Vemula, S.; Wiesner, T.; Obenauf, A.C.; Wackernagel, W.; Green, G.; Bouvier, N.; et al. Mutations in GNA11 in uveal melanoma. *N. Engl. J. Med.* **2010**, *363*, 2191–2199. [CrossRef] [PubMed]

https://doi.org/10.3390/cancers18030480

10. Terai, M.; Shimada, A.; Chervoneva, I.; Hulse, L.; Danielson, M.; Swensen, J.; Orloff, M.; Wedegaertner, P.B.; Benovic, J.L.; Aplin, A.E.; et al. Prognostic Values of G-Protein Mutations in Metastatic Uveal Melanoma. *Cancers* **2021**, *13*, 5749. [CrossRef]
11. Shariati, A.; Khezrpour, A.; Shariati, F.; Afkhami, H.; Yarahmadi, A.; Alavimanesh, S.; Kamrani, S.; Modarressi, M.H.; Khani, P. DNA vaccines as promising immuno-therapeutics against cancer: A new insight. *Front. Immunol.* **2024**, *15*, 1498431. [CrossRef]
12. Bennett, D.C.; Cooper, P.J.; Hart, I.R. A line of non-tumorigenic mouse melanocytes, syngeneic with the B16 melanoma and requiring a tumour promoter for growth. *Int. J. Cancer* **1987**, *39*, 414–418. [CrossRef]
13. Engelhorn, M.E.; Guevara-Patino, J.A.; Merghoub, T.; Liu, C.; Ferrone, C.R.; Rizzuto, G.A.; Cymerman, D.H.; Posnett, D.N.; Houghton, A.N.; Wolchok, J.D. Mechanisms of immunization against cancer using chimeric antigens. *Mol. Ther.* **2008**, *16*, 773–781. [CrossRef]
14. Park, J.Y.; Jin, D.H.; Lee, C.M.; Jang, M.J.; Lee, S.Y.; Shin, H.S.; Chung, Y.H.; Kim, K.Y.; Kim, S.S.; Lee, W.B.; et al. $CD4^+$ TH1 cells generated by Ii-PADRE DNA at prime phase are important to induce effectors and memory $CD8^+$ T cells. *J. Immunother.* **2010**, *33*, 510–522. [CrossRef]
15. Igoucheva, O.; Grazzini, M.; Pidich, A.; Kemp, D.M.; Larijani, M.; Farber, M.; Lorton, J.; Rodeck, U.; Alexeev, V. Immunotargeting and eradication of orthotopic melanoma using a chemokine-enhanced DNA vaccine. *Gene Ther.* **2013**, *20*, 939–948. [CrossRef] [PubMed]
16. Irwin, M.J.; Heath, W.R.; Sherman, L.A. Species-restricted interactions between CD8 and the alpha 3 domain of class I influence the magnitude of the xenogeneic response. *J. Exp. Med.* **1989**, *170*, 1091–1101. [CrossRef]
17. Santegoets, S.J.; Schreurs, M.W.; Masterson, A.J.; Liu, Y.P.; Goletz, S.; Baumeister, H.; Kueter, E.W.; Lougheed, S.M.; van den Eertwegh, A.J.; Scheper, R.J.; et al. In vitro priming of tumor-specific cytotoxic T lymphocytes using allogeneic dendritic cells derived from the human MUTZ-3 cell line. *Cancer Immunol. Immunother.* **2006**, *55*, 1480–1490. [CrossRef] [PubMed]
18. Escobar, P.; Yu, Z.; Terskikh, A.; Holmes, N.; Corradin, G.; Mach, J.P.; Healy, F. Induction in transgenic mice of HLA-A2.1-restricted cytotoxic T cells specific for a peptide sequence from a mutated p21ras protein. *Clin. Exp. Immunol.* **1999**, *116*, 214–219. [CrossRef]
19. Rivas, A.; Samlowski, W.; McCannel, T.A. Unexpectedly Low Rate of Metastasis and Death Among Patients Treated for Uveal Melanoma with Brachytherapy, Vitrectomy, and Silicone Oil. *Cancers* **2025**, *17*, 2683. [CrossRef]
20. Royer-Bertrand, B.; Torsello, M.; Rimoldi, D.; El Zaoui, I.; Cisarova, K.; Pescini-Gobert, R.; Raynaud, F.; Zografos, L.; Schalenbourg, A.; Speiser, D.; et al. Comprehensive Genetic Landscape of Uveal Melanoma by Whole-Genome Sequencing. *Am. J. Hum. Genet.* **2016**, *99*, 1190–1198. [CrossRef] [PubMed]
21. Leonard-Murali, S.; Bhaskarla, C.; Yadav, G.S.; Maurya, S.K.; Galiveti, C.R.; Tobin, J.A.; Kann, R.J.; Ashwat, E.; Murphy, P.S.; Chakka, A.B.; et al. Uveal melanoma immunogenomics predict immunotherapy resistance and susceptibility. *Nat. Commun.* **2024**, *15*, 2863. [CrossRef]
22. Cintolo, J.A.; Datta, J.; Xu, S.; Gupta, M.; Somasundaram, R.; Czerniecki, B.J. Type I-polarized BRAF-pulsed dendritic cells induce antigen-specific $CD8^+$ T cells that impact BRAF-mutant murine melanoma. *Melanoma Res.* **2016**, *26*, 1–11. [CrossRef]
23. Rahma, O.E.; Hamilton, J.M.; Wojtowicz, M.; Dakheel, O.; Bernstein, S.; Liewehr, D.J.; Steinberg, S.M.; Khleif, S.N. The immunological and clinical effects of mutated ras peptide vaccine in combination with IL-2, GM-CSF, or both in patients with solid tumors. *J. Transl. Med.* **2014**, *12*, 55. [CrossRef]
24. Wainberg, Z.A.; Weekes, C.D.; Furqan, M.; Kasi, P.M.; Devoe, C.E.; Leal, A.D.; Chung, V.; Perry, J.R.; Kheoh, T.; McNeil, L.K.; et al. Lymph node-targeted, mKRAS-specific amphiphile vaccine in pancreatic and colorectal cancer: Phase 1 AMPLIFY-201 trial final results. *Nat. Med.* **2025**, *31*, 3648–3653. [CrossRef]
25. Hopkins, J.R.; MacLachlan, B.J.; Harper, S.; Sewell, A.K.; Cole, D.K. Unconventional modes of peptide-HLA-I presentation change the rules of TCR engagement. *Discov. Immunol.* **2022**, *1*, kyac001. [CrossRef]
26. Baleeiro, R.B.; Dunmall, L.S.C.; Liu, P.; Lu, S.; Lone, Y.; Lemoine, N.R.; Wang, Y. Optimized Anchor-Modified Peptides Targeting Mutated RAS Are Promising Candidates for Immunotherapy. *Front. Immunol.* **2022**, *13*, 902709. [CrossRef] [PubMed]
27. Borbulevych, O.Y.; Baxter, T.K.; Yu, Z.; Restifo, N.P.; Baker, B.M. Increased immunogenicity of an anchor-modified tumor-associated antigen is due to the enhanced stability of the peptide/MHC complex: Implications for vaccine design. *J. Immunol.* **2005**, *174*, 4812–4820. [CrossRef]
28. Cole, D.K.; Edwards, E.S.; Wynn, K.K.; Clement, M.; Miles, J.J.; Ladell, K.; Ekeruche, J.; Gostick, E.; Adams, K.J.; Skowera, A.; et al. Modification of MHC anchor residues generates heteroclitic peptides that alter TCR binding and T cell recognition. *J. Immunol.* **2010**, *185*, 2600–2610. [CrossRef]
29. Irvine, K.R.; Parkhurst, M.R.; Shulman, E.P.; Tupesis, J.P.; Custer, M.; Touloukian, C.E.; Robbins, P.F.; Yafal, A.G.; Greenhalgh, P.; Sutmuller, R.P.; et al. Recombinant virus vaccination against "self" antigens using anchor-fixed immunogens. *Cancer Res.* **1999**, *59*, 2536–2540. [PubMed]

https://doi.org/10.3390/cancers18030480

30. Posnett, D.N.; Engelhorn, M.E.; Lin, Y.; Merghoub, T.; Duan, F.; Wolchok, J.D.; Houghton, A.N. Development of effective vaccines for old mice in a tumor model. *Vaccine* **2009**, *27*, 1093–1100. [CrossRef] [PubMed]
31. Tegeler, C.M.; Scheid, J.; Rammensee, H.G.; Salih, H.R.; Walz, J.S.; Heitmann, J.S.; Nelde, A. HLA-DR Presentation of the Tumor Antigen MSLN Associates with Clinical Outcome of Ovarian Cancer Patients. *Cancers* **2022**, *14*, 2260. [CrossRef] [PubMed]

Disclaimer/Publisher's Note: The statements, opinions and data contained in all publications are solely those of the individual author(s) and contributor(s) and not of MDPI and/or the editor(s). MDPI and/or the editor(s) disclaim responsibility for any injury to people or property resulting from any ideas, methods, instructions or products referred to in the content.

https://doi.org/10.3390/cancers18030480

cancers

MDPI

Article

Clinicopathological Characteristics and BAP1 Expression in an Enucleation-Based Uveal Melanoma Cohort: A Single-Center Croatian Experience with Long-Term Follow-Up

Domagoj Vlašić [1,*], Mira Knežić Zagorec [2,*], Antonia Jakovčević [3], Dina Lešin Gaćina [4], Marijana Ćorić [5,6] and Tomislav Jukić [4,6]

1 Department of Ophthalmology, Dubrovnik General Hospital, 20000 Dubrovnik, Croatia
2 Department of Ophthalmology, University Hospital "Sveti Duh", 10000 Zagreb, Croatia
3 Department of Pathology and Cytology "Ljudevit Jurak", University Hospital Centre "Sestre milosrdnice", 10000 Zagreb, Croatia
4 Department of Ophthalmology, University Hospital Centre Zagreb, 10000 Zagreb, Croatia
5 Department of Pathology and Cytology, University Hospital Centre Zagreb, 10000 Zagreb, Croatia; marijana.coric@kbc-zagreb.hr
6 School of Medicine, University of Zagreb, 10000 Zagreb, Croatia
* Correspondence: domagojv@bolnica-du.hr or domagojvlasic@yahoo.com (D.V.); mkneziczagorec@kbsd.hr or mira.knezic94@gmail.com (M.K.Z.)

Simple Summary

Uveal melanoma is the most common primary eye cancer in adults and spreads to the liver in about half of patients, leading to poor outcomes. The protein BAP1, which normally suppresses tumor growth, is frequently lost in aggressive uveal melanomas. However, data on BAP1 loss in Central and Southeastern European populations are scarce. In this descriptive study, we analyzed BAP1 protein expression in tumor tissue from 58 Croatian patients who underwent surgical removal of the eye for uveal melanoma and were followed for a median follow-up of over 11 years—one of the longest follow-up periods reported. We found BAP1 loss in 91.4% of patients, substantially higher than typical literature values of 43–56%, which we attribute to the advanced nature of tumors requiring eye removal. The severely imbalanced distribution of BAP1 status (53 versus 5 patients) precluded meaningful prognostic analysis. These findings provide the first comprehensive BAP1 immunohistochemical data from Croatia and highlight the critical impact of study design on the reported prevalence of BAP1 loss.

Abstract

Background/Objectives: Loss of nuclear BAP1 (BRCA1-associated protein 1) expression is a well-established adverse prognostic marker in uveal melanoma (UM). However, data from Central and Southeastern European populations are limited. This descriptive study aimed to evaluate BAP1 immunohistochemical expression in a Croatian enucleation-based UM cohort, characterize its associations with clinicopathological parameters, and contextualize the findings within the published literature. Methods: Formalin-fixed, paraffin-embedded tumor tissue from 58 consecutive patients with primary choroidal and ciliary body melanoma treated with enucleation at University Hospital Centre Zagreb (2006–2016) was analyzed immunohistochemically for BAP1 nuclear expression. Associations with clinicopathological parameters were assessed using chi-square and Fisher's exact tests. Survival analysis was performed using Kaplan–Meier estimation, log-rank tests, and Cox proportional hazards regression with a median follow-up of 11.2 years. Results: Loss of nuclear BAP1 expression was observed in 53/58 (91.4%) specimens, resulting in a severely imbalanced distribution (53 versus 5 patients) precluding meaningful comparative survival analysis. Five-year

and 10-year overall survival rates were 72.4% and 51.7%, respectively, with a median overall survival of 14.5 years. BAP1 loss was associated with longer disease-free survival (log-rank $p = 0.020$); however, this finding likely reflects a statistical artifact attributable to the extremely small BAP1-retained group ($n = 5$) harboring concurrent adverse features and should not be interpreted biologically. The study was underpowered to draw prognostic inferences regarding BAP1 status. Exploratory survival analyses are presented for transparency but should not be interpreted inferentially. Conclusions: The exceptionally high prevalence of BAP1 loss reflects the selection bias inherent in enucleation-based cohorts, which are enriched for large, molecularly high-risk tumors. This study provides the first comprehensive BAP1 immunohistochemical data from Croatia, contributing to the growing evidence that enucleation cohorts represent a distinct, biologically high-risk subgroup in which BAP1 immunohistochemistry offers limited discriminatory value. The extended follow-up of 11.2 years confirms the prolonged natural history of UM. Future multi-center studies incorporating molecular validation and diverse treatment modalities are needed to establish the prognostic utility of BAP1 across the full spectrum of UM disease.

Keywords: uveal melanoma; BAP1; immunohistochemistry; enucleation; survival; Croatia; selection bias; choroidal melanoma; tumor suppressor; descriptive study

1. Introduction

Uveal melanoma (UM) is the most common primary intraocular malignancy in adults, with an annual incidence of 5–7 cases per million in Western populations [1,2]. Despite high rates of local tumor control exceeding 95% with contemporary treatment modalities, the 10-year metastatic rate remains approximately 34–50%, with the liver as the predominant site of dissemination [3,4]. Once metastatic disease develops, the prognosis is poor, with a median survival of 6–12 months and limited response to currently available systemic therapies [5]. The recent approval of tebentafusp for HLA-A*02:01-positive patients represents the first significant advance in metastatic UM, yet the overall survival benefit remains modest (median 21.7 vs. 16.0 months) [6].

The identification of inactivating mutations in the *BAP1* gene (BRCA1-associated protein 1, chromosome 3p21.1) by Harbour et al. in 2010 represented a paradigm shift in our understanding of UM biology [7]. *BAP1* encodes a nuclear deubiquitinase that removes monoubiquitin from histone H2A at lysine 119 (H2AK119ub1) as the catalytic subunit of the Polycomb repressive deubiquitinase (PR-DUB) complex [8]. This activity maintains open chromatin configurations at promoters of melanocyte differentiation genes, including *MITF*, *TYR*, and *DCT*, thereby preserving a differentiated, non-metastatic phenotype [9]. Loss of BAP1 function, occurring through biallelic inactivation (typically monosomy 3 combined with a point mutation on the remaining allele), results in chromatin compaction, transcriptional silencing of differentiation programs, and acquisition of a primitive, stem cell-like phenotype associated with metastatic competence [10].

Immunohistochemical (IHC) detection of BAP1 loss has emerged as a practical and cost-effective prognostic tool for routine paraffin-embedded specimens [11–14]. Multiple studies have demonstrated that loss of nuclear BAP1 staining correlates strongly with monosomy 3, a gene expression class 2 (metastatic) phenotype, and adverse clinical outcomes [11–17]. The Liverpool group reported that BAP1 loss was present in 43% of their series of enucleation specimens and was independently associated with increased metastatic risk [11]. Koopmans et al. observed *BAP1* loss in 51% of a mixed cohort of 74 patients [12]. Most recently, Kennedy et al. analyzed 308 consecutive enucleations from

https://doi.org/10.3390/cancers18081211

Dublin and demonstrated that BAP1 loss outperformed AJCC staging, monosomy 3 status, and TCGA molecular classification in predicting survival [17].

Despite this extensive literature, data on BAP1 expression in UM from Central and Southeastern European populations remain scarce. Although a recent comprehensive analysis of 1140 primary UM tumors has characterized the molecular landscape across tumor sizes [18], most BAP1 IHC studies are based on enucleation cohorts, which are systematically enriched for large, advanced tumors with unfavorable molecular profiles. This selection bias is a critical consideration when evaluating the prevalence of BAP1 loss and its prognostic value. Epidemiological data on UM in Croatia are limited to a single retrospective analysis from Split-Dalmatia County, which reports an incidence of 4.4 per million [19,20].

This study aimed to: (1) determine the prevalence of BAP1 loss by IHC in a well-characterized Croatian UM cohort treated with enucleation; (2) assess associations between BAP1 status and clinicopathological parameters; (3) describe overall survival (OS) and disease-free survival (DFS) in this cohort and perform exploratory analyses of BAP1 status in relation to outcomes; and (4) contextualize our findings within the published literature, with particular attention to the influence of cohort selection on the reported prevalence of BAP1 loss.

2. Materials and Methods

2.1. Study Design and Patient Selection

This retrospective, single-center cohort study was conducted on archived formalin-fixed, paraffin-embedded (FFPE) tumor tissue specimens stored at the Department of Pathology and Cytology at the University Hospital Centre (UHC) Zagreb. A search of the institutional database of the Department of Ophthalmology identified 62 consecutive patients who underwent primary enucleation for histopathologically confirmed UM of the choroid and/or ciliary body between 1 January 2006 and 31 December 2016.

Inclusion criteria were: (i) histopathologically confirmed primary choroidal and/or ciliary body melanoma; (ii) adequate tumor tissue available in archived FFPE blocks; (iii) largest tumor diameter (LTD) measured before fixation; (iv) complete clinical data, including demographics and outcome; and (v) minimum follow-up of 5 years or documented death within the follow-up period.

Exclusion criteria were: (i) prior radiotherapy, chemotherapy, or any oncological treatment before enucleation; (ii) primary iris melanoma; (iii) inadequate tissue for IHC analysis (e.g., poor fixation, insufficient tumor volume); (iv) extensive tumor necrosis precluding evaluation; and (v) dense pigmentation interfering with IHC visualization.

After applying these criteria, four patients were excluded (two for inadequate fixation and two for extensive necrosis), yielding in a final study cohort of 58 patients.

Clinical and histopathological data were extracted from medical records at UHC Zagreb. Mortality data were obtained from the Croatian National Cancer Registry. OS was defined as the interval from enucleation to death from any cause or last follow-up. DFS was defined as the interval from enucleation to the first documented metastasis, death from UM, or last follow-up. The study was censored on 31 December 2023. The study protocol was approved by the Ethics Committee of UHC Zagreb (protocol no. 8.1-21/248-2, 02/21 AG; approved 29 November 2021) and conducted in accordance with the Declaration of Helsinki. Given the retrospective nature of the study, which used archived tissue, the Ethics Committee waived the requirement for individual informed consent.

https://doi.org/10.3390/cancers18081211

2.2. Histopathological Evaluation

All hematoxylin and eosin-stained slides were reviewed by an experienced ophthalmic pathologist. Tumors were classified according to the 2025 World Health Organization (WHO) Classification of Tumours of the Eye as follows: (a) spindle cell melanoma—composed exclusively of spindle cells; (b) mixed cell melanoma—containing both spindle and epithelioid cells; and (c) epithelioid melanoma—comprising >50% epithelioid cells. The following parameters were recorded: LTD (mm), ciliary body involvement (present/absent), mitotic count (per mm^2), lymphocytic infiltration (present/absent), scleral involvement (present/absent), extraocular extension (present/absent), and vascular invasion (present/absent).

2.3. Immunohistochemistry

Serial sections (4 μm) were cut from representative FFPE tumor blocks. Antigen retrieval was performed using DAKO PT Link (Agilent Technologies, Santa Clara, CA, USA) at 97 °C for 20 min in citrate buffer (pH 6.0). Automated staining was performed on a DAKO Autostainer Link 48 platform (Agilent Technologies, Santa Clara, CA, USA) using a mouse monoclonal anti-BAP1 antibody (clone C-4, 1:50, Santa Cruz Biotechnology, Santa Cruz, CA, USA) with 60 min incubation at room temperature. Endogenous peroxidase activity was blocked with 0.3% hydrogen peroxide for 10 min. The DAKO EnVision Flex Plus detection system (Agilent Technologies, Santa Clara, CA, USA) was used for visualization. Both 3-amino-9-ethylcarbazole (AEC) and 3,3′-diaminobenzidine (DAB) chromogens were employed in parallel to address the well-documented challenge of distinguishing chromogen signal from endogenous melanin pigment in pigmented tumors [21]. The AEC chromogen produces a red reaction product that is easily distinguished from the brown/black melanin pigment commonly present in UM tissue. In contrast, the brown DAB chromogen can be difficult to distinguish from melanin, especially in heavily pigmented tumors. Thus, the AEC-stained sections provide clearer visualization of BAP1-positive and -negative cells in pigmented specimens. Tissue bleaching was not performed to preserve antigenic epitopes. Hematoxylin counterstaining was applied. Appropriate positive (non-neoplastic hepatic tissue) and negative (primary antibody omission) controls were included in each run.

2.4. Assessment of BAP1 Expression

BAP1 nuclear expression was evaluated by light microscopy (Olympus BX-41, Olympus Corporation, Tokyo, Japan) independently by the investigator under the supervision of a senior pathologist. Expression was graded semiquantitatively as follows: (−) absent—complete loss of nuclear staining in tumor cells; (+) weak—nuclear staining in <10% of tumor cells; (++) moderate—nuclear staining in 10–50% of tumor cells; (+++) strong—nuclear staining in >50% of tumor cells.

Complete loss of nuclear BAP1 expression in tumor cells, with preserved expression in adjacent non-neoplastic stromal cells and vascular endothelium (serving as an internal positive control), was classified as BAP1 loss. For the primary statistical analysis, expression was dichotomized: BAP1 loss (categories −, +, and ++, i.e., ≤50% positive tumor cells) versus BAP1 retained (category +++ only, i.e., >50% positive tumor cells). This cutoff was selected based on the established principle that strong, diffuse nuclear staining (>50%) most reliably indicates functional BAP1 protein expression. A sensitivity analysis using an alternative cutoff (BAP1 loss defined as categories − and + only, i.e., <10% positive tumor cells, versus BAP1 retained defined as categories ++ and +++, i.e., ≥10%) was also performed to assess the robustness of findings across different thresholds.

https://doi.org/10.3390/cancers18081211

2.5. Statistical Analysis

Statistical analysis was performed using IBM SPSS Statistics version 21.0 (IBM Corporation, Armonk, NY, USA). Continuous variables were described as mean ± standard deviation (SD) or median with range/interquartile range (IQR), depending on the normality of the distribution (Shapiro–Wilk test). Categorical variables were expressed as frequencies and percentages. Associations between BAP1 status and categorical clinicopathological variables were assessed using Pearson's chi-square test or Fisher's exact test when expected cell frequencies were <5. Continuous variables were compared between BAP1 groups using the Mann–Whitney U test.

Survival analysis was performed using the Kaplan–Meier method with log-rank (Mantel–Cox) test comparisons. Univariate and multivariate prognostic analyses were conducted using Cox proportional hazards regression, with results expressed as hazard ratios (HR) and 95% confidence intervals (CI). The proportional hazards assumption was assessed using Schoenfeld residual tests and log-log plots. Variables with $p < 0.20$ in univariate analysis were included in the multivariate model.

A priori power analysis using G*Power 3.1 (Heinrich-Heine University, Düsseldorf, Germany) confirmed >80% power for detecting large effect sizes (Cohen's w = 0.5) with the available sample of 58 patients for overall cohort comparisons. However, due to severely imbalanced BAP1 distribution (53 versus 5 patients), the study was underpowered for meaningful comparative survival analyses between BAP1 groups, and these analyses should be considered exploratory rather than inferential. The limited number of events relative to the number of covariates constrained the use of multivariate models. No correction for multiple testing was applied due to the exploratory nature of the subgroup analyses. All tests were two-sided, with $p < 0.05$ considered statistically significant.

3. Results

3.1. Patient Demographics and Tumor Characteristics

The study cohort comprised 58 patients (30 men [51.7%] and 28 women [48.3%]) with a median age at diagnosis of 62 years (range 31–87; mean 59.8 ± 14.2 years). The most common histological type was mixed cell melanoma (36/58, 62.1%), followed by spindle cell (13/58, 22.4%) and epithelioid (9/58, 15.5%) melanoma. The mean LTD was 15.8 ± 3.72 mm (median 15.5 mm, range 10–24 mm). Ciliary body involvement was present in 8 (13.8%) tumors. Scleral involvement was observed in 49 (84.5%) cases, extraocular extension in 7 (12.1%), and vascular invasion in 25 (43.1%). The median mitotic count was 3 per mm^2 (range 0–25). Lymphocytic infiltration was present in 11 (19.0%) specimens.

The median follow-up was 11.2 years (range 0.3–21.3; mean 10.8 ± 4.1 years). During the follow-up period, 32 (55.2%) patients died: 26 (81.3% of deaths) from metastatic UM and 6 (18.7%) from other causes. Metastatic disease occurred in 26 (44.8%) patients, with a median time to metastasis of 3.8 years (range 0.5–12.4; mean 4.2 ± 3.1 years). Comprehensive demographic and clinicopathological data are presented in Table 1.

Table 1. Patient Demographics and Clinicopathological Characteristics (n = 58).

Parameter	Value
Sex	
Male	30 (51.7%)
Female	28 (48.3%)
Age at diagnosis (years)	
Mean ± SD	59.8 ± 14.2
Median (range)	62 (31–87)

https://doi.org/10.3390/cancers18081211

Table 1. *Cont.*

Parameter	Value
Histological type	
Spindle cell	13 (22.4%)
Mixed cell	36 (62.1%)
Epithelioid	9 (15.5%)
Largest tumor diameter (mm)	
Mean ± SD	15.8 ± 3.72
Median (range)	15.5 (10–24)
Ciliary body involvement	8 (13.8%)
Scleral involvement	49 (84.5%)
Extraocular extension	7 (12.1%)
Vascular invasion	25 (43.1%)
Mitotic count (/mm^2)	
Median (range)	3 (0–25)
Lymphocytic infiltration	11 (19.0%)
Follow-up (years)	
Median (range)	11.2 (0.3–21.3)
Mean ± SD	10.8 ± 4.1
Outcome	
Alive	26 (44.8%)
Dead—uveal melanoma	26 (44.8%)
Dead—other causes	6 (10.3%)
Metastatic disease	26 (44.8%)
Time to metastasis (years)	
Median (range)	3.8 (0.5–12.4)
Mean ± SD	4.2 ± 3.1

SD, standard deviation. Bold text and blue color are used to emphasize key values within the table.

3.2. BAP1 Immunohistochemical Expression

Representative examples of retained and lost BAP1 expression are shown in Figure 1, with parallel DAB (panels A–C) and AEC (panels D–F) chromogen staining demonstrating the advantage of AEC in distinguishing immunoreactivity from endogenous melanin pigment. Loss of nuclear BAP1 expression was identified in 53/58 (91.4%) tumors. Only 5 (8.6%) tumors retained nuclear BAP1 expression (Figure 2A). Semiquantitative analysis revealed the following distribution: absent expression (−) in 43 specimens (74.1%), weak (+) in 6 specimens (10.3%), moderate (++) in 4 specimens (6.9%), and strong (+++) in 5 specimens (8.6%) (Figure 2B). In all positive cases, strong nuclear staining in tumor cells was accompanied by internal positive controls (stromal fibroblasts and endothelial cells).

3.3. Associations Between BAP1 Status and Clinicopathological Parameters

A trend toward an association was observed between BAP1 loss and vascular invasion (Fisher's exact test, $p = 0.063$): all 25 tumors (100%) with vascular invasion showed BAP1 loss, compared with 84.8% of tumors without vascular invasion. No significant associations were found between BAP1 status and sex ($p = 0.678$), age at diagnosis ($p = 0.739$), histological type ($p = 0.871$), tumor size (LTD, $p = 0.582$), ciliary body involvement ($p = 0.136$), lymphocytic infiltration ($p = 0.562$), scleral involvement ($p = 0.291$), extraocular extension ($p = 1.000$), or mitotic count ($p = 0.412$). BAP1 loss was present in 84.6% of patients

https://doi.org/10.3390/cancers18081211

who developed metastases, compared with 96.9% of those who remained metastasis-free ($p = 0.163$). Detailed results are presented in Table 2 and Figure 3.

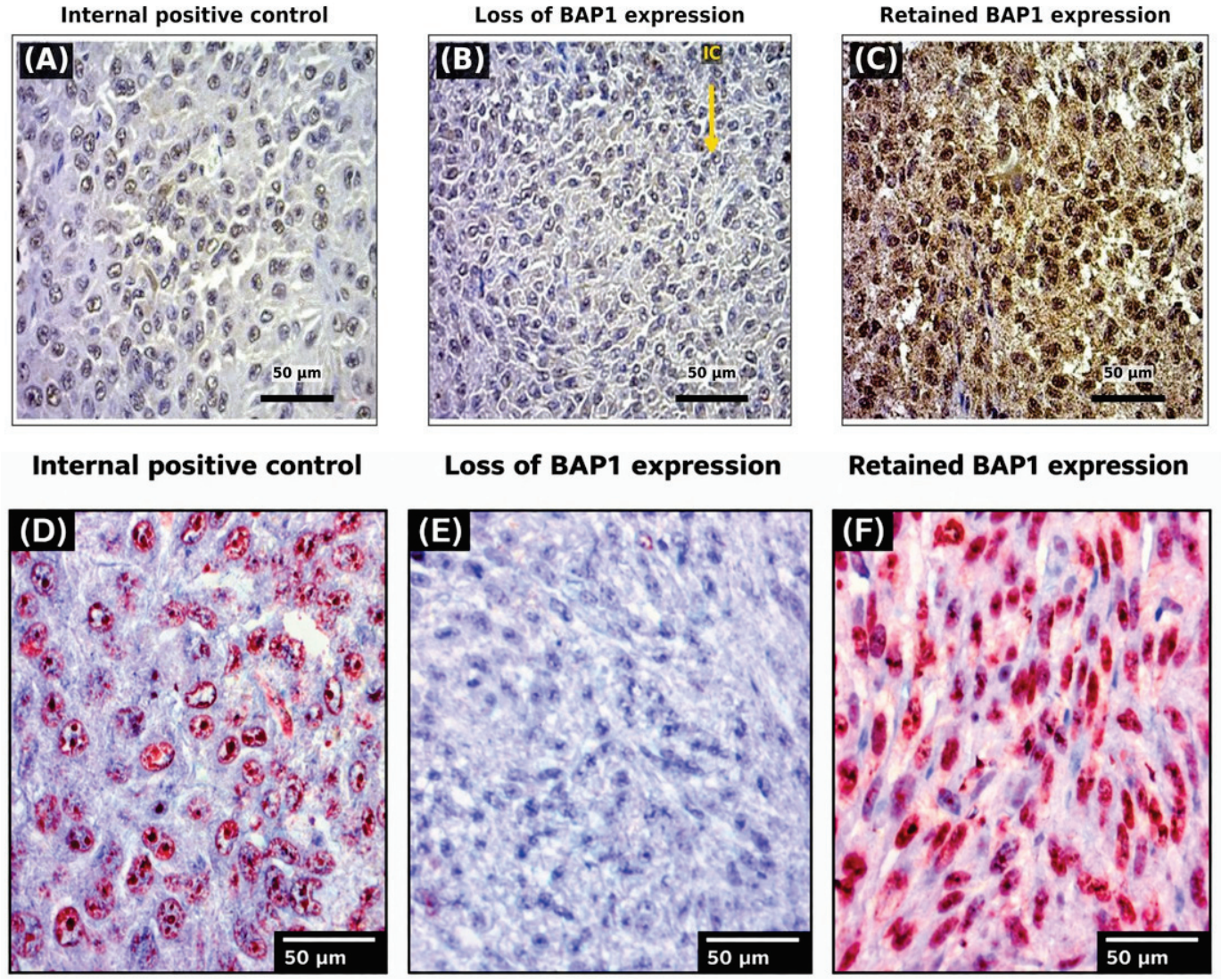


Figure 1. Representative immunohistochemical staining for BAP1 in uveal melanoma using DAB (panels (**A**–**C**), upper row) and AEC (panels (**D**–**F**), lower row) chromogens, with hematoxylin counterstain (scale bars = 50 µm). The brown DAB chromogen can be difficult to distinguish from endogenous melanin pigment in pigmented tumors; therefore, parallel AEC staining was performed, as the red AEC reaction product is easily distinguishable from brown/black melanin. (**A**) Internal positive control (DAB): non-neoplastic hepatic tissue showing preserved nuclear BAP1 immunoreactivity (brown). (**B**) Loss of BAP1 expression (DAB): complete absence of nuclear staining in tumor cells. The yellow arrow (IC) indicates an interspersed non-neoplastic stromal cell with preserved BAP1 nuclear staining, serving as an internal positive control. (**C**) Retained BAP1 expression (DAB): strong, diffuse nuclear immunoreactivity (brown) in tumor cells, classified as category +++ (>50% positive tumor cells). (**D**) Internal positive control (AEC): non-neoplastic hepatic tissue with preserved nuclear BAP1 immunoreactivity (red), confirming adequate antibody reactivity with the AEC detection system. (**E**) Loss of BAP1 expression (AEC): complete absence of red nuclear staining in tumor cells, showing only hematoxylin-stained nuclei visible (blue/purple), confirming true loss of BAP1. (**F**) Retained BAP1 expression (AEC): strong, diffuse red nuclear staining in tumor cells, clearly distinguishable from endogenous melanin pigment (brown/black), illustrating the advantage of AEC over DAB in pigmented uveal melanoma specimens.

https://doi.org/10.3390/cancers18081211

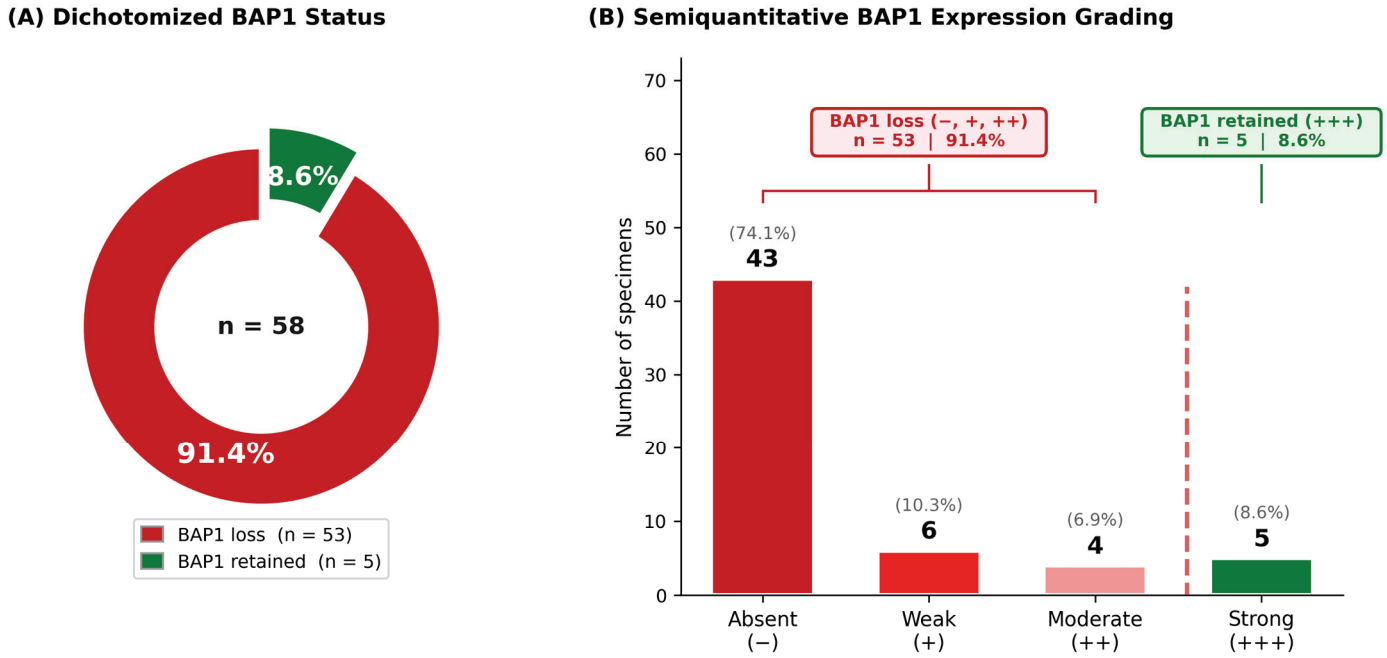


Figure 2. Distribution of BAP1 nuclear expression in uveal melanoma specimens (n = 58). (**A**) Dichotomized BAP1 status: BAP1 loss (red; n = 53, 91.4%) versus BAP1 retained (green; n = 5, 8.6%). (**B**) Semiquantitative BAP1 expression grading: absent (−) in 43 (74.1%), weak (+) in 6 (10.3%), moderate (++) in 4 (6.9%), and strong (+++) in 5 (8.6%). The red dashed line demarcates the BAP1 loss category (−, +, and ++, comprising 91.4%) from the BAP1 retained category (category +++ only, 8.6%).

Table 2. Associations of BAP1 Status with Clinicopathological Parameters.

Parameter	BAP1 Loss (n = 53)	BAP1 Retained (n = 5)	p-Value
Sex			0.678 [a]
Male	28 (52.8%)	2 (40.0%)	
Female	25 (47.2%)	3 (60.0%)	
Age at diagnosis (years), median (range)	62 (31–87)	58 (42–78)	0.739 [b]
Histological type			0.871 [a]
Spindle cell	12 (22.6%)	1 (20.0%)	
Mixed cell	33 (62.3%)	3 (60.0%)	
Epithelioid	8 (15.1%)	1 (20.0%)	
LTD (mm), mean ± SD	15.9 ± 3.8	15.0 ± 3.2	0.582 [b]
Ciliary body involvement	6 (11.3%)	2 (40.0%)	0.136 [a]
Scleral involvement	45 (84.9%)	4 (80.0%)	0.291 [a]
Extraocular extension	6 (11.3%)	1 (20.0%)	1.000 [a]
Vascular invasion	25 (47.2%)	0 (0.0%)	**0.063** [a]
Mitotic count (/mm^2), median (range)	3 (0–25)	2 (0–8)	0.412 [b]
Lymphocytic infiltration	10 (18.9%)	1 (20.0%)	0.562 [a]
Metastatic disease	22 (41.5%)	4 (80.0%)	0.163 [a]

LTD, largest tumor diameter; SD, standard deviation. [a] Fisher's exact test; [b] Mann–Whitney U test. Red bold indicates $p < 0.10$. Bold text and blue color are used to emphasize key values within the table.

https://doi.org/10.3390/cancers18081211

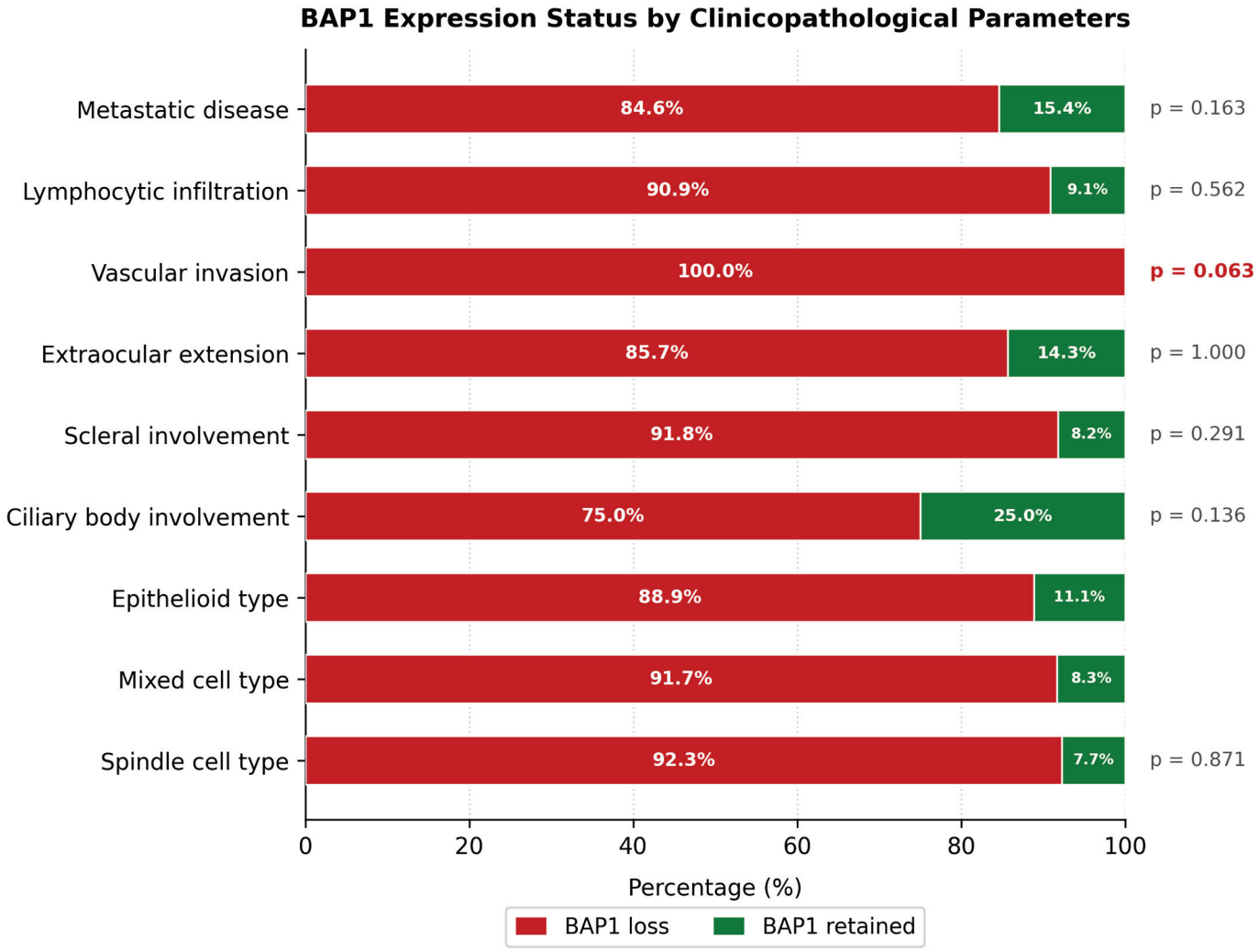


Figure 3. BAP1 expression status by clinicopathological parameters. Horizontal stacked bars show the proportion of patients with BAP1 loss (red) versus BAP1 retained (green). A trend toward an association was observed between BAP1 loss and vascular invasion ($p = 0.063$). No significant associations were found with histological type ($p = 0.871$), ciliary body involvement ($p = 0.136$), or metastatic status ($p = 0.163$).

3.4. Survival Analysis

3.4.1. Overall Cohort Survival

Kaplan–Meier analysis of the entire cohort demonstrated 5-year and 10-year OS rates of 72.4% (95% CI: 58.9–82.3%) and 51.7% (95% CI: 37.8–64.0%), respectively, with a median OS of 14.5 years (95% CI: 10.3–18.7). DFS rates at 5 and 10 were 65.5% (95% CI: 51.6–76.4%) and 48.3% (95% CI: 34.5–60.8%), respectively (Figure 4).

3.4.2. Survival by BAP1 Status

BAP1 loss was not significantly associated with OS (log-rank test, $p = 0.215$). The median OS was 14.5 years in the BAP1-loss group and 12.3 years in the BAP1-retained group. In an exploratory analysis, BAP1 loss was nominally associated with longer DFS (log-rank $p = 0.020$): the BAP1-retained group ($n = 5$) had a median DFS of 2.3 years, while the BAP1-loss group ($n = 53$) did not reach median DFS during follow-up (Figure 5). However, this counterintuitive finding reflects a statistical artifact driven by the extremely small and unrepresentative BAP1-retained group ($n = 5$), all of whom had concurrent adverse features, and should not be interpreted biologically (see Section 4).

https://doi.org/10.3390/cancers18081211

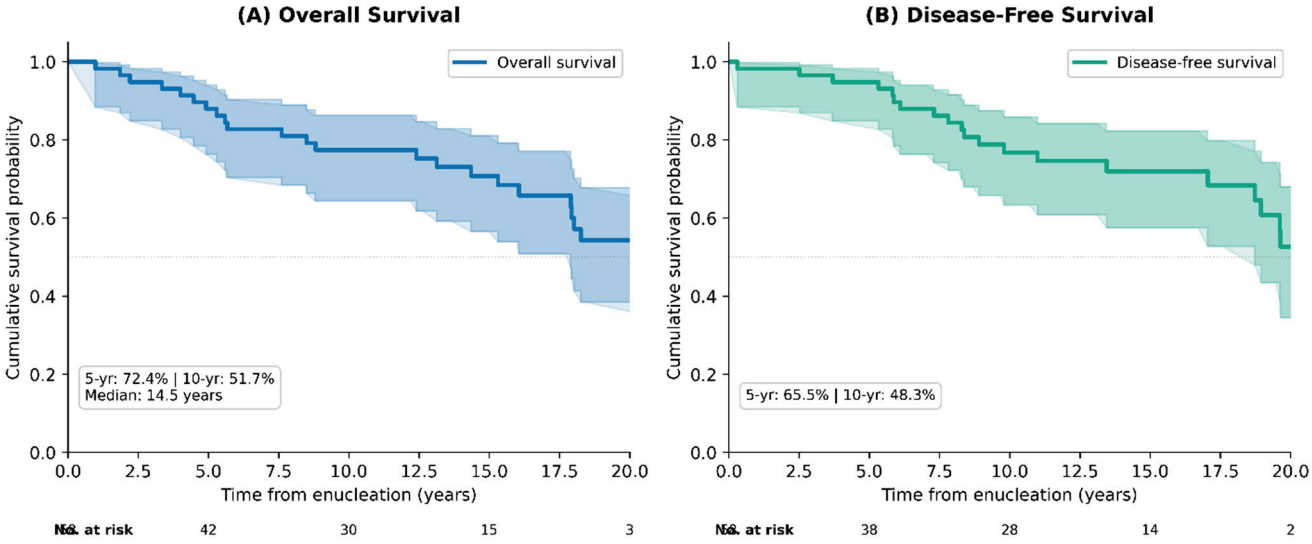


Figure 4. Kaplan–Meier survival curves for the entire cohort (n = 58). (**A**) Overall survival (OS): 5-year OS 72.4%, 10-year OS 51.7%, median OS 14.5 years. (**B**) Disease-free survival (DFS): 5-year DFS 65.5%, 10-year DFS 48.3%. Shaded areas represent 95% confidence intervals. Numbers at risk are shown below each panel.

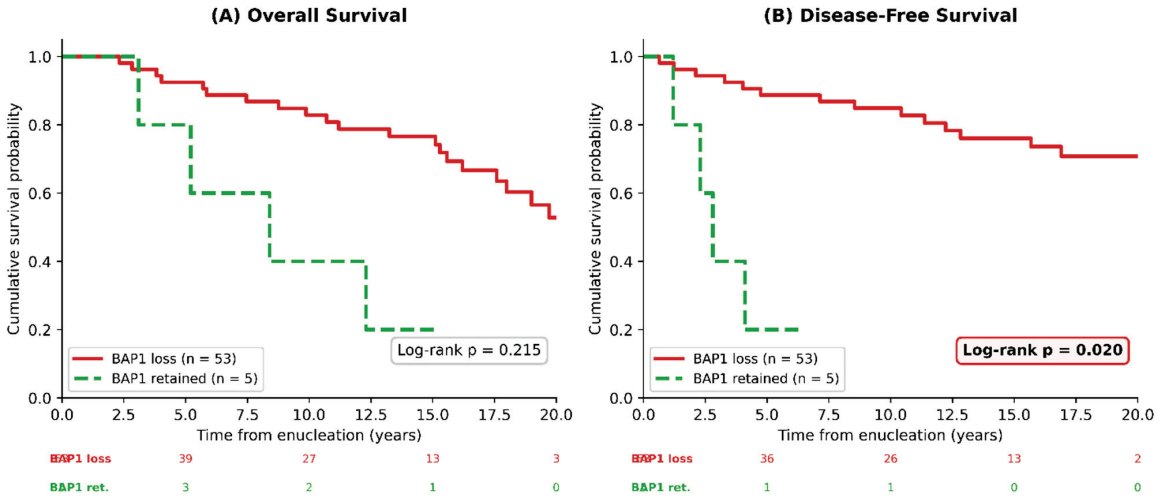


Figure 5. Kaplan–Meier survival curves stratified by BAP1 status. (**A**) Overall survival (OS, log-rank p = 0.215): no significant difference was observed between BAP1 loss (red, n = 53) and BAP1 retained (green dashed, n = 5). (**B**) Disease-free survival (DFS, log-rank p = 0.020): the BAP1-retained group showed a shorter DFS; this counterintuitive finding reflects a statistical artifact attributable to concurrent adverse features and the extremely small subgroup size (n = 5). Numbers at risk are shown below each panel.

3.4.3. Exploratory Univariate and Multivariate Analysis

The following survival analyses should be interpreted with caution due to severely imbalanced BAP1 groups (53 versus 5 patients) and the limited number of events, which render the study underpowered for prognostic inference. In univariate Cox regression for OS, epithelioid histological type showed a non-significant trend toward worse survival (HR = 2.87; 95% CI: 0.86–9.55; p = 0.086), whereas BAP1 loss was not significant for OS (HR = 0.58; 95% CI: 0.22–1.51; p = 0.264).

In multivariate analysis for OS, including BAP1 status, histological type, LTD, age, and vascular invasion, no variable reached independent significance (Table 3, Figure 6A). Of note, the inclusion of five covariates for 32 events exceeds the recommended ratio of

https://doi.org/10.3390/cancers18081211

approximately 10 events per variable, and these results should be interpreted with caution. Epithelioid histology tended to be associated with worse OS (HR = 4.03; 95% CI: 0.80–20.24; $p = 0.090$).

Table 3. Exploratory Univariate and Multivariate Cox Proportional Hazards Regression Analysis.

Variable	Univariate HR (95% CI)	*p*-Value	Multivariate HR (95% CI)	*p*-Value
Overall Survival				
BAP1 loss (vs. retained)	0.58 (0.22–1.51)	0.264	0.64 (0.20–2.04)	0.448
Epithelioid type (vs. spindle/mixed)	2.87 (0.86–9.55)	0.086	4.03 (0.80–20.24)	0.090
LTD (per mm)	1.05 (0.95–1.16)	0.332	1.03 (0.91–1.17)	0.616
Age (per year)	1.02 (0.99–1.05)	0.185	1.02 (0.98–1.06)	0.294
Vascular invasion	1.48 (0.72–3.04)	0.286	1.25 (0.55–2.85)	0.596
Disease-Free Survival				
BAP1 loss (vs. retained)	0.27 (0.09–0.82)	**0.020**	0.18 (0.03–1.05)	0.056
Age (per year)	1.03 (1.00–1.06)	0.088	**1.04 (1.00–1.09)**	**0.048**
Ciliary body involvement	1.96 (0.74–5.17)	0.175	1.73 (0.56–5.39)	0.342
Epithelioid type (vs. spindle/mixed)	1.68 (0.58–4.87)	0.340	1.52 (0.42–5.54)	0.523
LTD (per mm)	1.04 (0.93–1.15)	0.506	1.01 (0.88–1.15)	0.927
Vascular invasion	1.62 (0.75–3.49)	0.221	1.34 (0.55–3.28)	0.524

HR, hazard ratio; CI, confidence interval; LTD, largest tumor diameter. Red bold indicates $p < 0.05$. Variables with $p < 0.20$ in univariate analysis were included in the multivariate model.

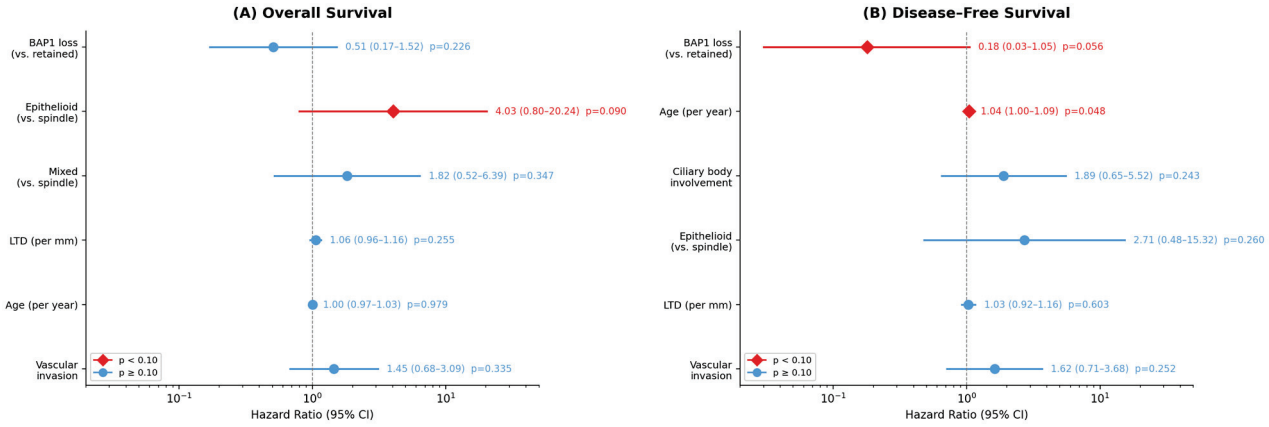


Figure 6. Forest plots of multivariate Cox proportional hazards regression. (**A**) Overall survival: epithelioid histology showed a trend toward significance (HR = 4.03; 95% CI: 0.80–20.24; $p = 0.090$). (**B**) Disease-free survival: patient age was the only independent predictor (HR = 1.04; 95% CI: 1.00–1.09; $p = 0.048$). BAP1 loss showed a non-significant protective association (HR = 0.18; 95% CI: 0.03–1.05; $p = 0.056$). Red diamonds indicate $p < 0.10$; blue circles indicate $p \geq 0.10$.

For DFS, the multivariate model including BAP1 status, age, ciliary body involvement, histological type, LTD, and vascular invasion identified patient age as the only statistically significant independent predictor (HR = 1.04; 95% CI: 1.00–1.09; $p = 0.048$), indicating a 4% increase in metastatic risk per year of age at diagnosis. BAP1 loss showed a nominally protective association (HR = 0.18; 95% CI: 0.03–1.05; $p = 0.056$); however, this reflects a statistical artifact due to the extremely small BAP1-retained group ($n = 5$) and unstable hazard ratio estimates and should not be interpreted as evidence of a true biological effect (Table 3, Figure 6B). The proportional hazards assumption was satisfied for all variables (Schoenfeld test, all $p > 0.05$). Given the inclusion of six covariates in 26 DFS events,

https://doi.org/10.3390/cancers18081211

the model exceeds the recommended events-per-variable ratio, and the results should be regarded as exploratory.

3.5. Comparison with Published Literature

To contextualize the exceptionally high prevalence of BAP1 loss (91.4%) observed in our cohort, we compiled data from six major published BAP1 IHC studies in UM (Table 4, Figure 7). Reported BAP1 loss rates ranged from 43% to 56%, with a weighted average of approximately 50%. Thus, our observed prevalence exceeds these values by 35–48 percentage points.

Table 4. Comparison of BAP1 Loss Prevalence Across Published Uveal Melanoma IHC Studies.

Study	Year	*n*	Cohort Type	BAP1 Loss *n* (%)	Median FU (Years)
Kalirai et al. [11]	2014	120	Enucleation	52 (43%)	3.7
Koopmans et al. [12]	2014	74	Mixed (enucl. + biopsy)	38 (51%)	5.4
Szalai et al. [13]	2020	62	Enucleation	31 (50%)	4.2
Farquhar et al. [14]	2018	69	Enucleation	35 (51%)	3.5
Stålhammar et al. [15]	2021	54	Enucleation	30 (56%)	6.3
Kennedy et al. [17]	2024	308	Enucleation	148 (48%)	5.8
Present study	**2025**	**58**	**Enucleation**	**53 (91.4%)**	**11.2**

IHC, immunohistochemistry; FU, follow-up; enucl., enucleation. The present study is highlighted.

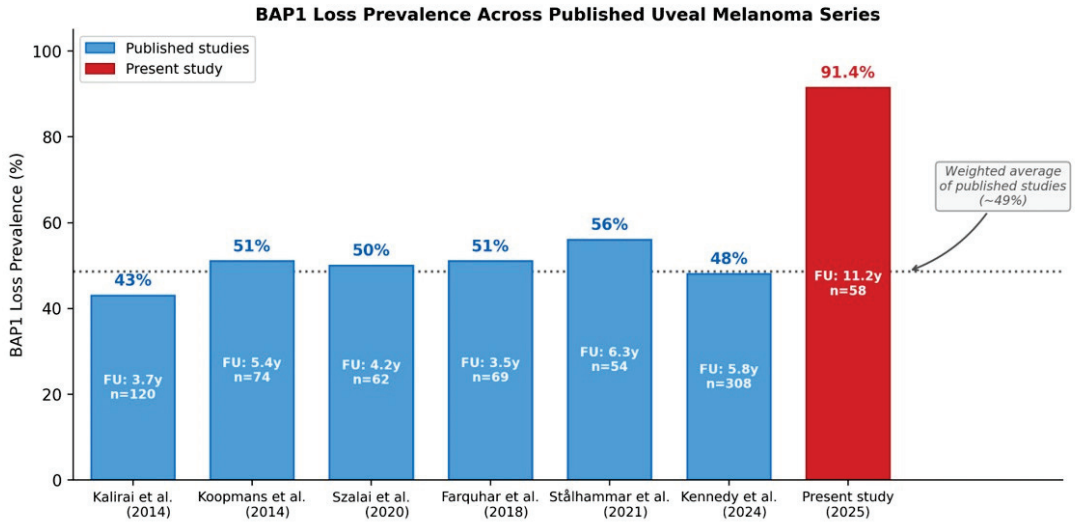


Figure 7. BAP1 loss prevalence across published uveal melanoma series. Bar chart comparing BAP1 loss rates from six major published IHC studies (blue) with the present study (red). Published rates ranged from 43% to 56% (weighted average ~50%, dotted line), while the present study reports 91.4%. The difference reflects the enucleation-enriched, high-risk composition of our cohort and methodological approach. Median follow-up duration for each study is indicated by the bars [11–15,17].

4. Discussion

This descriptive study provides the first comprehensive IHC analysis of BAP1 expression in UM from a Croatian institution, with a median follow-up of 11.2 years–substantially longer than that of most published series. Three principal findings emerge: (1) the exceptionally high prevalence of BAP1 loss, attributable to the enucleation-based study design; (2) the severely imbalanced BAP1 distribution, which precludes meaningful prognostic analysis; and (3) the confirmation of a prolonged natural history, highlighting the need for extended patient surveillance.

https://doi.org/10.3390/cancers18081211

4.1. BAP1 Loss Prevalence in the Context of Cohort Selection

The 91.4% prevalence of BAP1 loss in our cohort is the highest reported in any primary UM series and warrants careful interpretation. Published studies report BAP1 loss rates of 43–56% in primary UM specimens [11–17], while rates of 81–84% have been documented in metastatic lesions [22]. Our finding falls between these ranges, approaching the prevalence observed in metastatic tissue.

Several factors may contribute to this exceptionally high prevalence. While the enucleation-based study design is enriched for advanced tumors, this alone cannot fully account for the discrepancy: the Dublin series by Kennedy et al. [17] also evaluated exclusively enucleation specimens and reported only 48% BAP1 loss, while the Liverpool cohort [11] had a comparable mean LTD (16.5 mm versus 15.8 mm in our series). Additional methodological factors likely play a role. First, differences in BAP1 staining protocols, antibody clones, and scoring thresholds across institutions may significantly influence reported prevalence. In our study, we employed a threshold of >50% positive tumor cells to define BAP1 retention (category +++ only), which is more stringent than the $\geq$10% cutoff used in some published series. This stricter cutoff reclassifies moderate expressors (10–50%) as BAP1 loss, which accounts for a substantial portion of the observed discrepancy. Second, true geographic or population-specific differences in BAP1 loss frequency among Croatian UM patients cannot be excluded, although this hypothesis requires validation in larger cohorts. Third, our cohort characteristics—85% scleral involvement and 43% vascular invasion—indicate a particularly advanced subset even within the enucleation population.

Stålhammar et al. [23] reported that 69% of tumors in their enucleation series were AJCC stage IIb or higher, and BAP1-lost tumors had significantly greater mean volumes (2109 vs. 1552 mm^3, $p = 0.025$). Ewens et al. [24] directly compared enucleation specimens with fine-needle aspiration biopsies and found that metastases developed in 70% of enucleated eyes versus 36% of biopsied tumors ($p = 0.006$), while the frequency of BAP1 mutations was comparable between the two groups ($p = 0.79$). These findings suggest that survival differences are primarily driven by tumor size and stage rather than BAP1 status per se, highlighting that enucleation cohorts represent a biologically distinct patient population.

A critical implication for clinical practice is that BAP1 IHC results must be interpreted in the context of the tissue acquisition method. The prognostic utility of BAP1 loss—demonstrated convincingly in large, balanced cohorts by Kennedy et al. [17] and Kalirai et al. [11]—is diminished when the reference group (BAP1-retained) is extremely small, as in our cohort ($n = 5$). This underscores the need for multi-center collaborative studies that include both enucleation and biopsy specimens to establish generalizable prognostic models.

4.2. The Counterintuitive Survival Finding: A Statistical Artifact

The nominally significant association between BAP1 loss and longer DFS (log-rank $p = 0.020$) directly contradicts the extensive literature establishing BAP1 loss as an adverse prognostic marker [11–17]. Several studies with adequately powered reference groups have consistently reported the opposite: Stålhammar et al. reported a median metastasis-free survival of 2.4 years for BAP1-lost versus 16.0 years for BAP1-retained tumors ($p < 0.0001$) [16], Koopmans et al. observed DFS of 32 versus 133 months ($p < 0.001$) [12], and Liu-Smith and Lu calculated a hazard ratio of 9.57 (95% CI: 2.82–32.5) for overall mortality with low BAP1 expression [22].

This finding represents a statistical artifact driven by three compounding factors. First, the extremely small BAP1-retained group ($n = 5$) produces unstable survival estimates with wide confidence intervals. Second, all five patients with retained BAP1 harbored independent adverse features: large tumors (4/5 with LTD > 15 mm), ciliary body involvement

https://doi.org/10.3390/cancers18081211

(2/5), and epithelioid morphology (1/5). Third, the likelihood of confounding is high when the reference group represents <10% of the total cohort. This interpretation aligns with that of Shields et al. [25], who noted that Kaplan–Meier curves in small subgroups can appear similar yet fail to reach statistical significance.

4.3. Extended Follow-Up and Natural History

The median follow-up of 11.2 years in our cohort provides valuable insights into the natural history of UM. Notably, metastatic events continued to occur beyond 10 years post-enucleation, with the latest metastasis documented at 12.4 years. This extended latency is consistent with the concept of tumor dormancy in UM and carries important clinical implications: current AJCC staging models and surveillance guidelines, which primarily focus on the first five years, may inadequately capture late-onset metastases. Although definitive surveillance recommendations are beyond the scope of this study, our findings suggest that follow-up limited to five years may miss a subset of metastatic events.

The 5-year and 10-year OS rates of 72.4% and 51.7% in our cohort are broadly consistent with those reported in historical enucleation series. For comparison, the COMS study reported 5-year and 10-year melanoma-specific mortality rates of approximately 16% and 34%, respectively, for medium-sized tumors [26], whereas the European EUMC multicenter study reported 5-year OS of 62% for large tumors [27]. Our intermediate outcomes likely reflect the mixed tumor-size distribution in our cohort.

4.4. Clinical Implications and Future Directions

The near-universal BAP1 loss in our cohort (91.4%) has important clinical implications. First, it reinforces the concept that patients requiring enucleation represent a uniformly high-risk population, for whom enrollment in adjuvant therapy trials should be prioritized. Second, it highlights that, specifically for enucleation specimens, BAP1 IHC alone offers limited discriminative value. As demonstrated in a recent comprehensive analysis of 1140 primary UM tumors across all sizes [18], molecular characterization beyond BAP1 IHC is essential for accurate prognostic stratification. Complementary prognostic markers, including chromosome 8q status, gene expression profiling, and PRAME expression [28], may further refine risk assessment in this already high-risk group [29].

The therapeutic landscape for metastatic UM is evolving rapidly. Beyond tebentafusp [6], the combination of darovasertib and crizotinib has shown promising results in the OptimUM-01 trial [30], and HDAC inhibitors targeting the BAP1–HDAC4 epigenetic axis [31] represent a biologically rational approach validated in preclinical models [32,33]. Characterization of BAP1 status in treatment-naive primary tumors, as performed in this study, provides the essential baseline data to inform future biomarker-guided therapeutic strategies.

4.5. Strengths and Limitations

Strengths of this study include the extended follow-up (median 11.2 years), comprehensive clinicopathological characterization, mortality data from the Croatian National Cancer Registry, and the novelty of providing the first BAP1 IHC data from a Croatian UM cohort. The use of dual chromogen systems (AEC and DAB) effectively addresses the technical challenge of melanin interference.

Limitations include the retrospective design, relatively small sample size (n = 58), and the highly unbalanced BAP1 distribution (91.4% loss), which precludes reliable prognostic assessment. A major limitation is the exclusive reliance on IHC without molecular validation. The absence of BAP1 mutation analysis, assessment of chromosome 3 status (e.g., monosomy 3 by FISH or other methods), and gene expression profiling classification limits both biological interpretation and comparison with genomic data. Potential discor-

https://doi.org/10.3390/cancers18081211

dance between IHC and molecular findings is a recognized concern: IHC detects protein loss but may not capture all functionally relevant mutations, and conversely, some mutations may not result in detectable protein loss. These molecular data were not available for the study period (2006–2016) at our institution. Additionally, the single-center design and exclusive reliance on enucleation specimens limit generalizability. Future multi-center studies incorporating both enucleation and biopsy specimens, with concurrent molecular profiling, are needed to fully characterize the prognostic utility of BAP1 across the spectrum of UM disease.

5. Conclusions

This descriptive study provides the first comprehensive BAP1 IHC analysis in a Croatian UM cohort, revealing an exceptionally high prevalence of BAP1 loss (91.4%) that reflects both the systematic enrichment for advanced tumors inherent in enucleation-based study designs and the stringent IHC scoring threshold employed. The severely imbalanced BAP1 distribution (53 versus 5 patients) rendered the study underpowered for prognostic inference, and the counterintuitive survival association observed is a statistical artifact that should not be interpreted biologically. The extended median follow-up of 11.2 years confirms the prolonged natural history of UM, with metastatic events occurring beyond 10 years from primary treatment. These findings underscore the critical importance of adequately sized reference groups in biomarker studies and the need for molecular validation beyond IHC alone. Future multi-center studies integrating BAP1 IHC with chromosome 3 status, gene expression profiling, and diverse treatment modalities are warranted to establish the prognostic utility of BAP1 across the full spectrum of UM disease.

Author Contributions: Conceptualization, D.V., M.Ć. and A.J.; Methodology, D.V. and M.K.Z.; Formal Analysis, D.V.; Investigation, D.V. and A.J.; Resources, M.Ć. and T.J.; Data Curation, D.V. and A.J.; Writing—Original Draft Preparation, D.V., D.L.G., and M.K.Z.; Writing—Review and Editing, M.Ć.; Visualization, D.V. and A.J.; Supervision, M.Ć. and A.J.; Project Administration. M.Ć. and M.K.Z. All authors have read and agreed to the published version of the manuscript.

Funding: This research received no external funding.

Institutional Review Board Statement: The study was conducted in accordance with the Declaration of Helsinki and approved by the Ethics Committee of University Hospital Centre Zagreb (protocol code: 8.1-21/248-2, 02/21 AG; date of approval: 29 November 2021).

Informed Consent Statement: Patient consent was waived by the Ethics Committee due to the retrospective nature of the study, which used archived pathological specimens with anonymized data.

Data Availability Statement: The data presented in this study are available upon reasonable request from the corresponding author. Data are not publicly available due to patient privacy considerations.

Acknowledgments: The authors thank the staff of the Department of Pathology and Cytology at UHC Zagreb for technical assistance with immunohistochemical staining and the Croatian National Cancer Registry for providing mortality data.

Conflicts of Interest: The authors declare no conflicts of interest.

References

1. Jager, M.J.; Shields, C.L.; Cebulla, C.M.; Abdel-Rahman, M.H.; Grossniklaus, H.E.; Stern, M.H.; Carvajal, R.D.; Belfort, R.N.; Jia, R.; Shields, J.A.; et al. Uveal melanoma. *Nat. Rev. Dis. Primers* **2020**, *6*, 24. [CrossRef]
2. Krantz, B.A.; Dave, N.; Komatsubara, K.M.; Marr, B.P.; Carvajal, R.D. Uveal melanoma: Epidemiology, etiology, and treatment of primary disease. *Clin. Ophthalmol.* **2017**, *11*, 279–289. [CrossRef]
3. Carvajal, R.D.; Sacco, J.J.; Jager, M.J.; Eschelman, D.J.; Olofsson Bagge, R.; Harbour, J.W.; Chieng, N.D.; Patel, S.P.; Joshua, A.M.; Piperno-Neumann, S. Advances in the clinical management of uveal melanoma. *Nat. Rev. Clin. Oncol.* **2023**, *20*, 99–115. [CrossRef]

https://doi.org/10.3390/cancers18081211

4. Collaborative Ocular Melanoma Study Group. The COMS randomized trial of iodine 125 brachytherapy for choroidal melanoma: V. Twelve-year mortality rates and prognostic factors: COMS report No. 28. *Arch. Ophthalmol.* **2006**, *124*, 1684–1693. [CrossRef]
5. Pelster, M.S.; Gruschkus, S.K.; Bassett, R.; Gombos, D.S.; Shephard, M.; Posada, L.; Cuellar, S.; Marcott, V.; Patel, S.P. Nivolumab and ipilimumab in metastatic uveal melanoma: Results from a single-arm phase II study. *J. Clin. Oncol.* **2021**, *39*, 599–607. [CrossRef] [PubMed]
6. Nathan, P.; Hassel, J.C.; Rutkowski, P.; Baurain, J.F.; Butler, M.O.; Schlaak, M.; Sullivan, R.J.; Ochsenreither, S.; Dummer, R.; Kirkwood, J.M.; et al. Overall survival benefit with tebentafusp in metastatic uveal melanoma. *N. Engl. J. Med.* **2021**, *385*, 1196–1206. [CrossRef] [PubMed]
7. Harbour, J.W.; Onken, M.D.; Roberson, E.D.; Doshi, S.; Worley, L.; Tuscan, R.; Pressey, J.G. Frequent mutation of BAP1 in metastasizing uveal melanomas. *Science* **2010**, *330*, 1410–1413. [CrossRef]
8. Scheuermann, J.C.; de Ayala Alonso, A.G.; Oktaba, K.; Ly-Hartig, N.; McGinty, R.K.; Fraterman, S.; Wilm, M.; Muir, T.W.; Müller, J. Histone H2A deubiquitinase activity of the Polycomb repressive complex PR-DUB. *Nature* **2010**, *465*, 243–247. [CrossRef]
9. Kuznetsov, J.N.; Aguero, T.H.; Owens, D.A.; Kurtenbach, S.; Field, M.G.; Durante, M.A.; Rodriguez, D.A.; King, M.L.; Harbour, J.W. BAP1 regulates epigenetic switch from pluripotency to differentiation in developmental lineages, giving rise to BAP1-mutant cancers. *Sci. Adv.* **2019**, *5*, eaax1738. [CrossRef]
10. Robertson, A.G.; Shih, J.; Yau, C.; Gibb, E.A.; Oba, J.; Mungall, K.L.; Cherniack, A.D.; Akbani, R.; Hoadley, K.A.; Mungall, A.J.; et al. Integrative analysis identifies four molecular and clinical subsets in uveal melanoma. *Cancer Cell* **2017**, *32*, 204–220. [CrossRef] [PubMed]
11. Kalirai, H.; Dodson, A.; Fajber, S.; Coupland, S.E. Lack of BAP1 protein expression in uveal melanoma is associated with increased metastatic risk and has utility in routine prognostic testing. *Br. J. Cancer* **2014**, *111*, 1373–1380. [CrossRef] [PubMed]
12. Koopmans, A.E.; Verdijk, R.M.; Brouwer, R.W.W.; van den Bosch, T.P.P.; van den Berg, M.M.P.; Vaarwater, J.; de Klein, A.; Kilic, E. Clinical significance of immunohistochemistry for detection of BAP1 mutations in uveal melanoma. *Mod. Pathol.* **2014**, *27*, 1321–1330. [CrossRef]
13. See, R.T.; Stålhammar, G.; Phillips, S.; Grossniklaus, H.E. BAP1 immunoreactivity correlates with gene expression class in uveal melanoma. *Ocul. Oncol. Pathol.* **2020**, *6*, 129–137. [CrossRef]
14. Farquhar, N.; Thornton, S.; Coupland, S.E.; Coulson, J.M.; Sacco, J.J.; Krishna, Y.; Heimann, H.; Taktak, A.; Cebulla, C.M.; Abdel-Rahman, M.H.; et al. Patterns of BAP1 protein expression provide insights into prognostic significance and the biology of uveal melanoma. *J. Pathol. Clin. Res.* **2017**, *4*, 26–38. [CrossRef]
15. Stålhammar, G.; See, T.R.O.; Phillips, S.; Grossniklaus, H.E. Intratumor heterogeneity in uveal melanoma BAP-1 expression. *Cancers* **2021**, *13*, 1143. [CrossRef]
16. Stålhammar, G.; See, T.R.O.; Phillips, S.S.; Grossniklaus, H.E. Density of PAS positive patterns in uveal melanoma: Correlation with vasculogenic mimicry, gene expression class, BAP-1 expression, macrophage infiltration, and risk for metastasis. *Mol. Vis.* **2019**, *25*, 502–516.
17. Kennedy, S.; Owens, S.; Ivers, L.; Hegarty, C.; O'Neill, V.; Berenguer-Pina, J.J.; Horgan, N.; Crown, J.; Walsh, N. Prognostic value of BAP1 protein expression in uveal melanoma. *Am. J. Surg. Pathol.* **2024**, *48*, 329–336. [CrossRef]
18. Dollar, J.J.; Decatur, C.L.; Weis, E.; Schefler, A.C.; Materin, M.A.; Fuller, T.S.; Skalet, A.H.; Reichstein, D.A.; Kim, I.K.; Piggott, K.D.; et al. Early genetic evolution of driver mutations in uveal melanoma. *Nat. Commun.* **2025**, *16*, 11322. [CrossRef]
19. Ivanišević, P.; Bojić, L.; Tomić, S.; Bućan, K.; Ivanišević, M.; Lešin, M.; Pleština-Borjan, I.; Stanić, R. Clinico-epidemiological analysis of choroidal melanoma in Split Area, Croatia. *Acta Med. Croat.* **2011**, *65*, 257–261.
20. Pašalić, D.; Nikuševa-Martić, T.; Sekovanić, A.; Kaštelan, S. Genetic and epigenetic features of uveal melanoma—An overview and clinical implications. *Int. J. Mol. Sci.* **2023**, *24*, 12807. [CrossRef]
21. Mudhar, H.S.; Parsons, M.A.; Sisley, K.; Rundle, P.; Singh, A.; Rennie, I.G. A critical appraisal of the prognostic and predictive factors for uveal malignant melanoma. *Histopathology* **2004**, *45*, 1–12. [CrossRef]
22. Liu-Smith, F.; Lu, Y. Opposite roles of BAP1 in overall survival of uveal melanoma and cutaneous melanoma. *J. Clin. Med.* **2020**, *9*, 411. [CrossRef]
23. Uner, O.E.; See, T.R.O.; Szalai, E.; Grossniklaus, H.E.; Stålhammar, G. Estimation of the timing of BAP1 mutation in uveal melanoma progression. *Sci. Rep.* **2021**, *11*, 8923. [CrossRef]
24. Ewens, K.G.; Kanetsky, P.A.; Richards-Yutz, J.; Purrazzella, J.; Shields, C.L.; Ganguly, T.; Ganguly, A. Genomic profile of 320 uveal melanoma cases: Chromosome 8p-loss and metastatic outcome. *Investig. Ophthalmol. Vis. Sci.* **2013**, *54*, 5721–5729. [CrossRef] [PubMed]
25. Shields, C.L.; Mayro, E.L.; Bas, Z.; Dockery, P.W.; Yaghy, A.; Lally, S.E.; Ganguly, A.; Shields, J.A. Ten-year outcomes of uveal melanoma based on The Cancer Genome Atlas (TCGA) classification in 1001 cases. *Indian J. Ophthalmol.* **2021**, *69*, 1839–1845. [CrossRef] [PubMed]
26. The Collaborative Ocular Melanoma Study (COMS) randomized trial of pre-enucleation radiation of large choroidal melanoma II: Initial mortality findings. COMS report no. 10. *Am. J. Ophthalmol.* **1998**, *125*, 779–796. [CrossRef] [PubMed]

https://doi.org/10.3390/cancers18081211

27. Fallico, M.; Raciti, G.; Longo, A.; Reibaldi, M.; Bonfiglio, V.; Russo, A.; Caltabiano, R.; Gattuso, G.; Falzone, L.; Avitabile, T. Current molecular and clinical insights into uveal melanoma (Review). *Int. J. Oncol.* **2021**, *58*, 10. [CrossRef]
28. Han, L.M.; Lee, K.W.; Uludag, G.; Seider, M.I.; Afshar, A.R.; Bloomer, M.M.; Pekmezci, M. Prognostic value of BAP1 and preferentially expressed antigen in melanoma (PRAME) immunohistochemistry in uveal melanomas. *Mod. Pathol.* **2023**, *36*, 100081. [CrossRef]
29. Dogrusöz, M.; Jager, M.J.; Damato, B. Uveal Melanoma Treatment and Prognostication. *Asia Pac. J. Ophthalmol.* **2017**, *6*, 186–196.
30. Piperno-Neumann, S.; Carlino, M.S.; Boni, V.; Loirat, D.; Speetjens, F.M.; Park, J.J.; Calvo, E.; Carvajal, R.D.; Nyakas, M.; Gonzalez-Maffe, J.; et al. A phase I trial of LXS196, a protein kinase C (PKC) inhibitor, for metastatic uveal melanoma. *Br. J. Cancer* **2023**, *128*, 1040–1051. [CrossRef]
31. Bakhoum, M.F.; Curtis, E.J.; Goldbaum, M.H.; Mischel, P.S. BAP1 methylation: A prognostic marker of uveal melanoma metastasis. *npj Precis. Oncol.* **2021**, *5*, 89. [CrossRef] [PubMed]
32. Kuznetsoff, J.N.; Owens, D.A.; Lopez, A.; Rodriguez, D.A.; St Laurent, G.; Bhatt, T.; Durante, M.A.; Kurtenbach, S.; Harbour, J.W. Dual screen for efficacy and toxicity identifies HDAC inhibitor with distinctive activity spectrum for BAP1-mutant uveal melanoma. *Mol. Cancer Res.* **2021**, *19*, 215–226. [CrossRef] [PubMed]
33. Ny, L.; Jespersen, H.; Karlsson, J.; Alsén, S.; Filges, S.; All-Eriksson, C.; Andersson, B.; Carneiro, A.; Helgadottir, H.; Levin, M.; et al. The PEMDAC phase 2 study of pembrolizumab and entinostat in patients with metastatic uveal melanoma. *Nat. Commun.* **2021**, *12*, 5155. [CrossRef] [PubMed]

Disclaimer/Publisher's Note: The statements, opinions and data contained in all publications are solely those of the individual author(s) and contributor(s) and not of MDPI and/or the editor(s). MDPI and/or the editor(s) disclaim responsibility for any injury to people or property resulting from any ideas, methods, instructions or products referred to in the content.

https://doi.org/10.3390/cancers18081211

cancers

MDPI

Article

A Phase II Trial of Defactinib Combined with Avutometinib in Patients with Metastatic Uveal Melanoma

Rino S. Seedor [1,*], Mizue Terai [1], Sergei Koshkin [1], Andrew E. Aplin [2], Marlana Orloff [1], Erin Sharpe-Mills [1], Madeleine Naccarato [1], Aurora Mills [1], Alfredo A. Molinolo [3], J. Silvio Gutkind [3] and Takami Sato [1]

[1] Department of Medical Oncology, Sidney Kimmel Comprehensive Cancer Center, Thomas Jefferson University, Philadelphia, PA 19107, USA; mizue.terai@jefferson.edu (M.T.); sergei.koshkin@jefferson.edu (S.K.); marlana.orloff@jefferson.edu (M.O.); erin.sharpe-mills@jefferson.edu (E.S.-M.); madeleine.naccarato@jefferson.edu (M.N.); takami.sato@jefferson.edu (T.S.)
[2] Department of Pharmacology, Physiology and Cancer Biology, Thomas Jefferson University, Philadelphia, PA 19107, USA; andrew.aplin@jefferson.edu
[3] Moores Cancer Center, University of California San Diego, San Diego, CA 92093, USA; amolinolo@health.ucsd.edu (A.A.M.); sgutkind@health.ucsd.edu (J.S.G.)
* Correspondence: rino.seedor@jefferson.edu; Tel.: +1-215-955-4687; Fax: +1-215-503-2715

Simple Summary

Although significant improvements in survival have been achieved in cutaneous melanoma, metastatic uveal melanoma (MUM) remains a deadly disease with limited treatment options. This study is a phase II study evaluating the combination of an FAK inhibitor (defactinib) with a RAF/MEK inhibitor (avutometinib) for the treatment of MUM. Twelve patients with a median of two prior therapies were treated in the study, with a disease control rate of 50%. Patients who achieved stabilization of their disease were on treatment for an average of 5.6 months. The combination was quite tolerable for patients, with no patients requiring dose reduction or discontinuation. This is the first study reporting on the use of an FAK inhibitor combination in MUM.

Abstract

Background: Treatment options are limited, and outcomes remain poor for patients with metastatic uveal melanoma (MUM). We conducted an investigator-initiated, prospective, single-arm, single-institution, phase II study evaluating the combination of an FAK inhibitor (defactinib) with a RAF/MEK inhibitor (avutometinib) for the treatment of MUM. **Methods:** From February 2021 through January 2023, 12 patients with MUM were treated with the combination of defactinib and avutometinib. Defactinib was given 200 mg twice daily, and avutometinib was given 3.2 mg twice a week. Both drugs were given for 3 weeks on and 1 week off (28-day cycle). Disease control rate was the primary endpoint of this study. **Results:** Median lines of prior therapies for the patients were two. After two cycles, six patients achieved stable disease while six patients developed progressive disease (disease control rate of 50%). With a median follow-up of 20.0 months, the median progression-free survival was 3.0 months and the median overall survival was 20.0 months. The combination was quite tolerable for patients, with no patients requiring dose reduction or discontinuation. Trial enrollment was stopped early by study sponsors before the anticipated accrual of 18 patients due to no patients having a significant reduction in disease. **Conclusions:** This is the first study reporting on the use of an FAK inhibitor combination in MUM. Further research should seek to elucidate an optimal combination treatment strategy for MUM, such as FAK and PKC inhibitors, for improved blockade of the signaling pathways downstream of GNAQ/GNA11 driver mutations.

Keywords: uveal melanoma; metastatic uveal melanoma; targeted therapy; FAK inhibitor; defactinib; avutometinib

1. Introduction

Uveal melanoma (UM) is the most common intraocular malignant tumor in adults. Primary UMs are effectively treated by plaque radiotherapy or enucleation; however, up to 50% of UM patients who are treated for their primary tumors ultimately succumb to advanced disease [1,2]. The liver is the organ of metastasis in approximately 90% of advanced-stage disease [3,4]. Standard chemotherapies rarely induce clinical responses in patients with macro-metastasis [5–7] and 1-year survival of metastatic UM (MUM) patients is less than 30% [8,9]. UM tumors have a low mutational burden [10,11], which is thought to contribute to their low immunogenicity and poor responses to immunotherapy. Objective response rates (ORR) appear low, ranging from 5% with the cytotoxic T-lymphocyte-associated protein 4 (CTLA-4) antibody ipilimumab, 3.6% with anti-programmed cell death 1 (PD-1) antibodies (e.g., nivolumab), 10–21% with combination ipilimumab and nivolumab, and 7.7% with the combination of the lymphocyte activation gene-3 (LAG-3) antibody relatlimab and nivolumab [12–18]. Tebentafusp was approved for the treatment of MUM as it led to an improvement in overall survival (OS), but it is restricted to patients with HLA-A*02:01, and the ORR was only 9% [19]. Percutaneous hepatic perfusion was also recently approved for the treatment of MUM, but it is limited to patients with less than 50% hepatic involvement and limited extrahepatic metastasis [20]. There is still an urgent need to develop effective therapeutic strategies for MUM patients.

Activating mutations (typically Q209) in genes encoding alpha subunits of the heterotrimeric G proteins, GNAQ and GNA11, are found in 80–90% of UM [21–24]. Mutant GNAQ and GNA11 signal to several pathways, including MEK-ERK1/2, which are required for tumor cell growth [22,23,25,26]. Unfortunately, inhibition of the MEK/ERK pathway has failed to provide clinical benefits in MUM patients. In a phase II trial of the MEK inhibitor selumetinib (NCT01143402), the partial response rate was 15%, and median progression-free survival (PFS) was improved compared to standard chemotherapy (temozolomide/dacarbazine) (15.9 versus 7.0 weeks, respectively); however, OS improvement did not reach statistical significance, possibly due to the cross-over design of the trial [27]. The SUMIT phase III trial [28] analyzing selumetinib in combination with dacarbazine was terminated early since it showed a poor response rate and only a one-month improvement of median PFS, compared to dacarbazine alone. This suggests that, although MEK/MAPK networks activated by PLC-β may contribute to UM initiation, they may not be critical for the maintenance of tumorigenic potential in UM.

Using a synthetic biology approach and a genome-wide RNAi screen, it was discovered that Gαq activates a highly conserved Rho-GEF, TRIO, and the consequent stimulation of Rho-regulated pathways leading to the activation of YAP, independently of PLC-β, the best-known target of Gαq [29]. The tyrosine kinase FAK was found to provide a direct link between Gαq and tyrosine phosphorylation networks controlling YAP and promotes UM growth [30]. FAK is a cytosolic protein kinase that has multiple effects on a cancer cell and its environment. It is associated with drug resistance, as it can be activated in cancer cells when it is exposed to other signal tyrosine kinase inhibitors. FAK can also be activated by cellular stress and receptor tyrosine kinase inhibitors and signals through critical nodes in the signal transduction pathway such as MEK [31]. Nuclear FAK drives the transcription of chemokines and cytokines, including Ccl5 and TGFβ2, which promote the formation of an immunosuppressive, pro-tumorigenic microenvironment [32]. The

https://doi.org/10.3390/cancers18142232

kinase activity of nuclear-targeted FAK in squamous cell carcinoma cells has been shown to drive exhaustion of CD8+ T cells and recruitment of regulatory T cells in the tumor microenvironment by regulating chemokine/cytokine and ligand-receptor networks [32]. These changes inhibit antigen-primed cytotoxic CD8+ T cell activity, permitting growth of FAK-expressing tumors. These findings suggest that FAK may have a significant impact on tumor stroma, restoring anti-tumor immunity [32].

Interestingly, UM represents the human cancer harboring the highest level of FAK overexpression [30]. Furthermore, *PTK2* expression (the gene that encodes for FAK) has been significantly correlated with reduced overall survival in UM patients, aligning with its potential biological role in UM [30]. FAK knockdown or CRISPR/Cas9 genome editing reduced UM cell proliferation and tumorigenesis [30]. FAK inhibitors had limited effects in cutaneous melanoma harboring *BRAF* oncogenes, but inhibited FAK (and YAP), and reduced cell proliferation and tumor growth in vivo in UM [31], thereby establishing FAK as a druggable target in UM.

Building on this, a kinome-wide CRISPR-Cas9 sgRNA screen was performed to identify synthetic lethal gene interactions that can be exploited therapeutically [33]. sgRNAs targeting the PKC and MEK-ERK signaling pathways were significantly depleted after FAK inhibition, with ERK activation representing a predominant resistance mechanism. Furthermore, pharmacological inhibition of MEK and FAK showed remarkable synergistic growth-inhibitory effects in UM cells and exerted cytotoxic effects leading to tumor collapse in UM xenograft and liver MUM models in vivo [33].

Defactinib is a small-molecule, orally available selective inhibitor of FAK. Avutometinib is a small-molecule, orally available first-in-class oral RAF/MEK clamp that potently inhibits MEK1/2 kinase activities and induces inactive complexes of MEK with ARAF, BRAF, and CRAF, potentially creating a more complete and durable anti-tumor response through maximal RAS/MAPK pathway inhibition [34–36]. In contrast to currently available MEK-only inhibitors, avutometinib blocks both MEK kinase activity and the ability of RAF to phosphorylate MEK. This unique mechanism allows avutometinib to block MEK signaling without the compensatory activation of MEK that appears to limit the efficacy of the MEK-only inhibitors.

Together, avutometinib and defactinib have the potential to offer more complete blockade of the signaling that drives the growth of RAS/MAPK pathway-dependent tumors with the objective of deeper and more durable responses [37]. The combination of defactinib and avutometinib is being evaluated in several clinical trials, and has been recently approved by the FDA for KRAS-mutated recurrent low-grade serous ovarian cancer (LGSOC) [38]. The FRAME study was a phase 1 study investigating the combination in patients with advanced solid tumors including LGSOC, KRAS wild-type or mutant, and non-small cell lung cancer (NSCLC) with KRAS mutations (NCT03875820) [39]. The response rate in subjects with KRAS-mutated LGSOC was 58.3% (7 of 12 subjects with partial response (PR)), and 42.3% (11 of 26 subjects with PR) for all subjects with LGSOC (KRAS wild-type or mutant). The FRAME study led to the development of several tumor specific clinical trials with the combination, including the phase 1/2 RAMP 205 trial evaluating the combination with gemcitabine and nab-paclitaxel in first-line metastatic pancreatic cancer (NCT05669482), the Phase 1/2 RAMP 203 study of KRAS G12C-mutated NSCLC combined with sotorasib (NCT05074810), and the phase 2 RAMP 201 (NCT04625270) and phase 3 RAMP 301 (NCT06072781) trials evaluating the combination in patients with recurrent LGSOC. The phase 2 RAMP 201 trial of defactinib and avutometinib in recurrent LGSOC was notable for a confirmed ORR of 31% with a median duration of response of 31.1 months [39]. Median PFS was 12.9 months. In KRAS-mutated patients, the ORR was even better at 44% and median PFS of 22 months. The combination was generally well-tolerated, with a 10%

https://doi.org/10.3390/cancers18142232

discontinuation rate due to AEs. The most frequent grade ≥3 treatment-related adverse events (AEs) were elevated creatine phosphokinase (24%), diarrhea (8%), and anemia (5%). Accelerated FDA approval of defactinib and avutometinib for the treatment of adults with KRAS-mutated recurrent LGSOC was obtained on May 8, 2025, based on the phase 2 RAMP 201 trial analysis.

Given the preclinical data demonstrating synergistic efficacy of FAK and RAF/MEK inhibition for UM, and the safety and efficacy demonstrated in other trials, we designed a clinical trial evaluating defactinib and avutometinib in metastatic uveal melanoma.

2. Materials and Methods

2.1. Study Design

This was an investigator-initiated, prospective, single-arm, single-institution, phase 2 trial evaluating the combination of an FAK inhibitor (defactinib) with a RAF/MEK inhibitor (avutometinib) for the treatment of patients with MUM (ClinicalTrials.gov number, NCT04720417). Patients were eligible if they were ≥18 years with confirmed metastatic UM. Patients could be treatment-naïve or have received prior treatment (4-week washout period required). Defactinib was given 200 mg twice daily, and avutometinib was given 3.2 mg twice a week (e.g., Monday/Thursday or Tuesday/Friday). Both drugs were given for 3 weeks on and 1 week off (28-day cycle). Treatment continued for up to 2 years until disease progression, death, unacceptable toxicity, or withdrawal of consent occurred. Post-treatment, patients were followed for survival until their death or up to 5 years after the last patient was enrolled. Scans were performed every 2 cycles/8 weeks on study with a CT scan of the chest and pelvis and MRI of the abdomen, which were assessed locally. Additional details are provided in the study protocol (Supplementary File S1).

All patients provided written informed consent prior to enrollment into this study. The original protocol and all amendments were approved by the Institutional Review Board at Thomas Jefferson University (IRB#20P.1113). The study was conducted in accordance with the Declaration of Helsinki and Good Clinical Practice guidelines.

2.2. End Points and Assessments

The primary objective of the study was to investigate the potential efficacy of the combination of defactinib and avutometinib in patients with MUM. No medication was approved for MUM by the US FDA at the time of the study design, and it was felt that potential clinical benefit could be obtained if MUM patients achieved stable disease (SD); therefore, we considered disease control rate (DCR) of 50% as a meaningful primary endpoint for this early phase clinical study. DCR included complete response (CR), partial response (PR), and stable disease (SD) as determined by RECIST criteria version 1.1 after two cycles. This was considered to be an appropriate goal since the overall response rate (ORR) (CR+PR) and disease control rate (DCR) (CR+PR+SD) of combination treatments using the FDA-approved medications, ipilimumab and nivolumab, were reported to be 11.8–16.7% and 29.4–64%, respectively [15]. The ORR and DCR for tebentafusp were 9% and 46%, respectively [19]. The ORR in MUM is historically quite low across systemic therapies, even with therapies demonstrating overall survival benefit. Even with a low response rate, tebentafusp demonstrated significant overall survival benefit, likely in part driven by patients achieving SD. To avoid premature termination based on low ORR, we decided to use DCR as the primary endpoint of this clinical study. DCR represents a clinically meaningful and statistically feasible primary endpoint and is being considered a valid endpoint in many recent clinical trials [40].

The secondary endpoints of the study were PFS, OS, and safety. PFS was defined as the time from start of first study treatment until confirmed progression of metastasis or

https://doi.org/10.3390/cancers18142232

death from any cause, or censored at the date of last follow-up visit. OS was defined as the time from start of first study treatment until death from any cause, or censored at the date last known alive. Adverse events were scored with the use of the National Cancer Institute Common Terminology Criteria for Adverse Events, version 5.0.

2.3. Biomarker Studies

Although clearly exploratory, we included a couple of biomarker studies to investigate the response and potential resistance mechanisms to study drugs.

2.4. ERK Phosphorylation

As part of an exploratory analysis, we studied the ERK activity in blinded pre-treatment and post-treatment tumor biopsies in sections of formalin-fixed, paraffin-embedded tissues. Coded tissue slides were stained without quenching the pigmentation, as the cytoplasmic background did not interfere with the assessment of nuclear immunoreactivity of the phosphorylated, activated form of ERK (pERK). The percentage of cells with nuclear pERK signals was quantified in several areas of interest that covered the entire tumor. Positive nuclear staining was further confirmed using QuPath [41].

2.5. RNA-Seq Profiling of Paired Tumor Specimens

We also examined whether any biomarkers were associated with therapeutic sensitivity or disease progression. To explore this, we analyzed RNA gene expression profiles in patient-derived xenograft (PDX) models established from biopsy specimens from patients. The deidentified tumor tissues obtained from patients pre- and post-treatment were implanted into the livers of NSG mice (NOD.Cg-Prkdc scid Il2rg tm1Wjl/SzJ; Jackson Laboratory, Bar Harbor, ME) to establish PDX models (n = 2–3 from each tumor tissue) [42]. The animal protocol (ID#01587) was approved by the Institutional Animal Care and Use Committee at Thomas Jefferson University. Mice were housed in a specific pathogen-free facility. The mice were euthanized at 6–7 months post-tumor implantation, and tumor tissues were harvested for subsequent analyses. Two tumor fragments harvested from PDX were processed for RNA extraction using the RNA Mini Kit (Qiagen, Hilden, Germany). RNA-seq was performed by Azenta (Burlington, MA, USA). Raw reads underwent adapter trimming and quality control, followed by a standard pipeline for bulk RNA-seq differential expression analysis. To remove murine contamination inherent to liver PDX samples, trimmed reads were aligned in parallel with STAR to the human GRCh38 reference genome (GENCODE v42) and the mouse GRCm39 genome (GENCODE vM32). Human-specific reads were identified using the Disambiguate tool. Transcript-level abundances were quantified with Salmon in alignment-based mode using GENCODE v42 transcript annotations. Differential expression analysis was performed with DESeq2, and results were visualized with volcano plots generated using the Enhanced Volcano package v1.28.2. Technical replicates, represented by tumor fragments collected from the same PDX tumor, were collapsed prior to differential expression analysis.

2.6. Reverse-Phase Protein Array (RPPA)

Reverse-phase protein array (RPPA) profiling was performed by the MD Anderson Cancer Center Functional Proteomics Core Facility using validated antibodies and standardized procedures as previously described [43]. Protein and phosphoprotein abundance levels were quantified using the RPPASPACE algorithm. Level 4 (L4) log2-transformed RPPA data, normalized for sample loading and batch effects, were used for downstream analyses. The RPPA panel included 401 validated antibodies recognizing total and phosphoproteins involved in major signaling pathways. Because RPPA measures a defined antibody panel rather than the full proteome, pathway assignment was restricted to key functional

https://doi.org/10.3390/cancers18142232

protein and phosphoprotein nodes represented in the RPPA dataset. Pathway-related antibody groups were initially defined using MSigDB pathway annotations and then filtered to include only antibodies available in the RPPA panel. Eight signaling modules were evaluated for their relevance, including FAK/MEK pathway inhibition, inflammatory responses, apoptosis, and potential adaptive resistance mechanisms:

- BCL2 anti-apoptotic pathway (BCL2, BCL-xL, MCL1): reflects pro-survival signaling and resistance to apoptosis.
- Apoptotic priming (BIM, PUMA, BAX, BAK): represents the readiness of cells to undergo apoptosis.
- Apoptosis execution (cleaved caspase-3, caspase-7): indicates active apoptotic cell death.
- MAPK/ERK pathway (pERK, pMEK, p90RSK): reflects canonical downstream signaling of MEK inhibition and potential reactivation.
- FAK/Src signaling (pFAK, pSRC, pPYK2): represents the direct target axis of FAK inhibition.
- JAK/STAT pathway (IL-6, JAK2, STAT3, PD-L1): reflects cytokine-mediated inflammatory signaling, STAT3-dependent survival programs, and immune checkpoint regulation.
- mTORC1 output (pS6K, pS6, p4E-BP1): captures translational and metabolic signaling downstream of growth pathways.
- SGK/mTORC2 pathway (SGK1, SGK3, pNDRG1, pRICTOR): represents an AKT-independent survival axis implicated in resistance.

For visualization, RPPA L4 log2-normalized values were displayed as a descriptive heatmap to provide an overview of pathway-related protein and phosphoprotein abundance patterns. Antibodies were grouped by signaling module, while samples were displayed without unsupervised clustering. No statistical testing was applied to this visualization.

2.7. Immunohistochemical Staining of Aldehyde Dehydrogenase 1 Family Member A3 (ALDH1A3)

For immunohistochemistry (IHC), tumor biopsy specimens from patients and PDX specimens were fixed in 10% neutral-buffered formalin overnight at room temperature, embedded in paraffin, and sectioned. Paraffin-embedded tissue sections with 4 μm were deparaffinized, and antigen retrieval was accomplished using TE buffer pH 9.0 with a steamer for 20 min. Sections were incubated with Bioxall blocking solution (Vector Laboratories, Burlingame, CA, USA) followed by rabbit anti-human ALDH1A3 (Proteintech, 25167-1-AP) antibody (1/400) at 4 °C overnight. The following day, sections were incubated for 60 min at room temperature in ImmPRESS AP anti-Rabbit IgG Reagent (Vector Laboratories) and for 7 min in ImmPact Vector Red (Vector Laboratories). Sections were counterstained with hematoxylin (Vector Laboratories) for 30 s at room temperature.

2.8. Statistical Analysis

In order to characterize the efficacy of the combination of defactinib and avutometinib in MUM patients, Simon's Optimal two-stage design was used for conducting this clinical trial [44]. The best response during study treatment in individual patients was used for efficacy analysis. The null hypothesis was that the true response rate is 20%, and the alternative hypothesis was that the true response rate is 50%. Simon's Optimal two-stage design was selected with a maximum of 18 patients and a target alpha level of 0.05 and power of 80%. The cohort escalation design was guided by a desire to stop the trial early if the actual stabilization rate is 20% or less.

The trial was carried out in two stages. In stage I, a total number of 8 patients would be accrued. If there were 2 or fewer overall responses (CR+PR+SD) among these 8 patients, further enrollment of patients would be stopped with the conclusion that the DCR cannot

https://doi.org/10.3390/cancers18142232

be 50% or greater. Otherwise, an additional 10 patients would be accrued in stage II, resulting in a total sample size of 18. If there were 7 or more responses among these 18 patients, we would reject the null hypothesis and claim that the treatment is promising [Optimal Design]. With this design, we had no more than a 5% chance of concluding effective ($\geq$50% stabilization rate) when the success rate was at most 20%. Similarly, we had no more than a 20% chance of concluding ineffective ($\leq$20% stabilization rate) when it was effective (50% stabilization rate). If the actual response rate was 20% or worse, we had at least a 0.79 probability that the trial would stop after the first 14 subjects. The overall power of this design was 80.0%.

Documenting anti-tumor activity was the primary objective of this trial. Patients must have received at least one cycle of the trial medication and have had at least one post-baseline RECIST assessment (or have progressed prior to this assessment) to be evaluable for response. To visualize the overall response time, we plotted the response from on-treatment time in swimmer's plots. Waterfall plots were used to visualize the tumor reduction or increase in size after 2 cycles. Kaplan–Meier curves were constructed to estimate the median PFS and OS.

For the exploratory ERK activity analysis, differences between pre- and post-treatment values were analyzed for each case using the paired *t*-test (GraphPad Prism version 10.0.0 for Windows, GraphPad Software, Boston, MA, USA, www.graphpad.com).

3. Results

From February 2021 through January 2023, a total of 13 subjects were enrolled in the study. The study terminated enrollment in April 2023. Trial enrollment was stopped early by study sponsors before the anticipated accrual of 18 patients due to no patients having a significant reduction in disease (only SD, no CR or PR). Stage I enrollment was complete, and the continuation rule was met, but only 4 of the planned 10 patients were enrolled in stage II.

Of the 13 enrolled patients, one subject did not complete screening due to rapid disease progression. 12 total patients received treatment. In stage I, eight subjects were treated, and DCR was 50% (four patients with SD, four patients with PD), meeting criteria to move on to stage II. In stage II, four additional subjects were treated before the study terminated enrollment. DCR for the 12 patients was 50% (6 patients with SD, 6 patients with PD). All 12 patients have died from UM. The CONSORT diagram can be found in Figure 1.

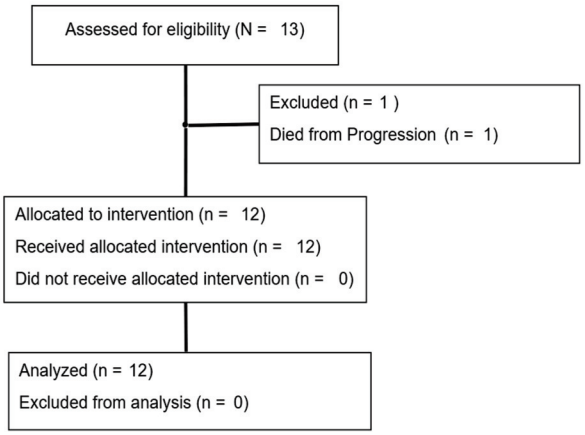


Figure 1. CONSORT diagram.

Patient baseline demographic and clinical information can be found in Table 1. The median age of the patients was 52 years, and 50% were male. Aside from the one patient with a known *SF3B1* mutation that recurred 8 years after her primary eye diagnosis, all other

https://doi.org/10.3390/cancers18142232

patients developed metastasis within 3 years of their primary eye diagnosis. All patients had hepatic metastases, while eight of the patients had both hepatic and extrahepatic metastases at the time of study enrollment. Eight patients (66.7%) had M1a disease, three patients (25%) had M1b, and only one patient (8.3%) had M1c disease. Median lines of prior therapy were 2 (range 0–6), with three patients (25%) being treatment-naïve. For the nine patients who had prior therapy, median time on the treatment immediately before this trial was 5 months. The time to systemic recurrence from initial eye treatment was 28 months, 36 months, and 12 months in the 3 treatment-naïve patients. The breakdown of each patient's clinical and demographic information, response to therapy, and treatment pre- and post- progression can be found in Table 2. All but one patient received at least one subsequent treatment prior to death, which varied from liver-directed therapy such as immunoembolization, radioembolization, chemoembolization, to systemic therapy such as tebentafusp, checkpoint inhibitor therapy, and a clinical trial.

Table 1. Baseline demographic and clinical characteristics.

Demographic Characteristics	***n* = 12**
Age (median, age)—years	52 (27–72)
Gender, male	6 (50.0%)
Race, white	12 (100.0%)
Primary eye tumor size (mean, range)	Diameter—11.6 mm (8.0–20.0) Thickness—4.1 mm (2.7–20.0)
High-risk molecular features of primary uveal melanoma	Monosomy 3—1 (8.3%) 8q amplification—1 (8.3%) Monosomy 3+8q amplification—6 (50.0%) Class 2—2 (16.7%) Monosomy 3+8q amplification & Class 2—1 (8.3%) Unknown—1 (8.3%)
HLA type	HLA-A*02:01—5 (41.7%) Other HLA—7 (58.3%)
Metastasis stage	M1a (largest $\leq$ 3 cm)—8 (66.7%) M1b (3.1–8 cm)—3 (25.0%) M1c (>8 cm)—1 (8.3%)
Metastatic organ involvement	Liver—12 (100.0%) Bone—4 (33.3%) Lung—6 (50.0%) Others—6 (50.0%)
Liver tumor burden	<20% involvement—9 (75.0%) 20–50% involvement—3 (25.0%) >50% involvement—0 (0%)
Line of therapy (median, range) Treatment naïve	2 (0–6) 3 (25.0%)

As shown in Table 2, after two cycles, six patients achieved SD (50%) while the other six patients developed PD. No patients achieved CR or PR. Of the three patients who were treatment-naïve, two achieved SD while one patient had PD. Tumor shrinkage was experienced in 58% of patients, or 7 of 12 patients (Figure 2). Patient 2 had a −1% change in the target liver lesions but experienced non-target bone and nodal progression after two cycles, so she had PD at first scans. Best overall response (BOR) was achieved in the first two cycles in most patients, although two patients achieved BOR after four cycles

https://doi.org/10.3390/cancers18142232

and one patient achieved BOR after four cycles (Table 2). Median duration of treatment was 2.6 months for all patients, and 5.6 months for patients with SD. Median duration of stabilization (time from scan showing SD to scan showing PD) in the six patients who achieved SD was 3.8 months. The three patients with more than 20% liver involvement were all PD. Swimmer's Plot is shown in Figure 3.

Table 2. Detailed patient characteristics.

ID	Age	Mutation *	Stage	% Liver Involved	Extrahepatic Met	Tx Duration (Months)	RECIST Response	BOR	Hepatic PD	Extrahepatic PD	# of Prior Met Tx	Prior Met Tx	Post PD Tx
1	30	GNA11 Q209L	M1c	20–50%	Y	2.1	PD	26% after 2 cycles	Y	Y	6	IE+ipi+VPA, tebe, ipi/nivo, CE, Sys, Sys	CE, Sys Trial, Sys
2	27	BAP1, no GNAQ/11	M1b	20–50%	Y	2.5	PD	−1% after 2 cycles	N	Y	4	IE, RE, CE, Sys	None
3	54	N/A	M1a	<20%	N	1.9	PD	28% after 2 cycles	Y	N/A	1	IE	RE, Tebe, opdualag, Sys
4	60	N/A	M1a	<20%	N	1.8	PD	37% after 2 cycles	Y	N/A	0	None	IE, CE, opdualag
5	40	GNAQ Q209L, SF3B1 R625H	M1a	<20%	Y	6.1	SD	−10% after 6 cycles	Y	N	1	RE+ipi/nivo on trial	IE, CE, Sys
6	72	N/A	M1a	<20%	N	5.9	SD	−7% after 2 cycles	Y	N/A	0	None	IE, tebe, CE, ipi/nivo, opdualag, Sys
7	72	N/A	M1b	<20%	Y	9.3	SD	−14% after 2 cycles	Y	Y	6	Sys Trial, MWA, Tebe, ipi/nivo, Sys, Sys	Sys
9	60	N/A	M1a	<20%	N	5.5	SD	−9% after 4 cycles	Y	N/A	0	None	IE, CE, tebe, nivo, ipi/nivo
10	52	N/A	M1b	20–50%	Y	2.1	PD	2% after 2 cycles	Y	Y	6	IE, RE, CE, Sys, ipi/nivo, Sys	Sys
11	51	N/A	M1a	<20%	Y	2.0	PD	−1% after 2 cycles	N	Y	2	IE, RE	Ipi/nivo, CE
12	51	GNAQ Q209P, BAP1	M1a	<20%	Y	3.6	SD	2% after 2 cycles	N	Y	1	PHP	Sys, Sys, IE, ipi/nivo
13	59	GNA11 Q209L, BAP1	M1a	<20%	Y	9.0	SD	−16% after 4 cycles	N	Y	2	IE, RE	ipi/nivo, opdualag

* Molecular mutational testing was performed on metastatic samples. BOR = best overall response; CE = chemoembolization; IE = immunoembolization; ipi = ipilimumab; Met = metastatic; MWA = microwave ablation; N/A = not available; nivo = nivolumab; PD = progressive disease; PHP = percutaneous hepatic perfusion; RE = radioembolization; SD = stable disease; Sys = systemic therapy clinical trial; tebe = tebentafusp; Tx = treatment; VPA = valproic acid.

https://doi.org/10.3390/cancers18142232

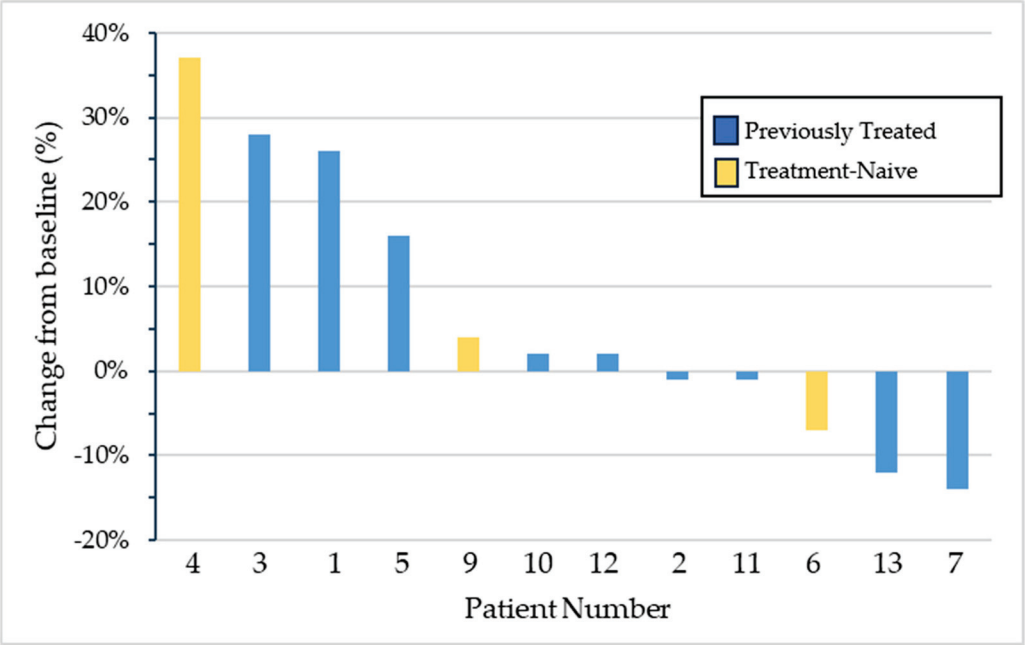


Figure 2. Waterfall plot of best tumor response (n = 12).

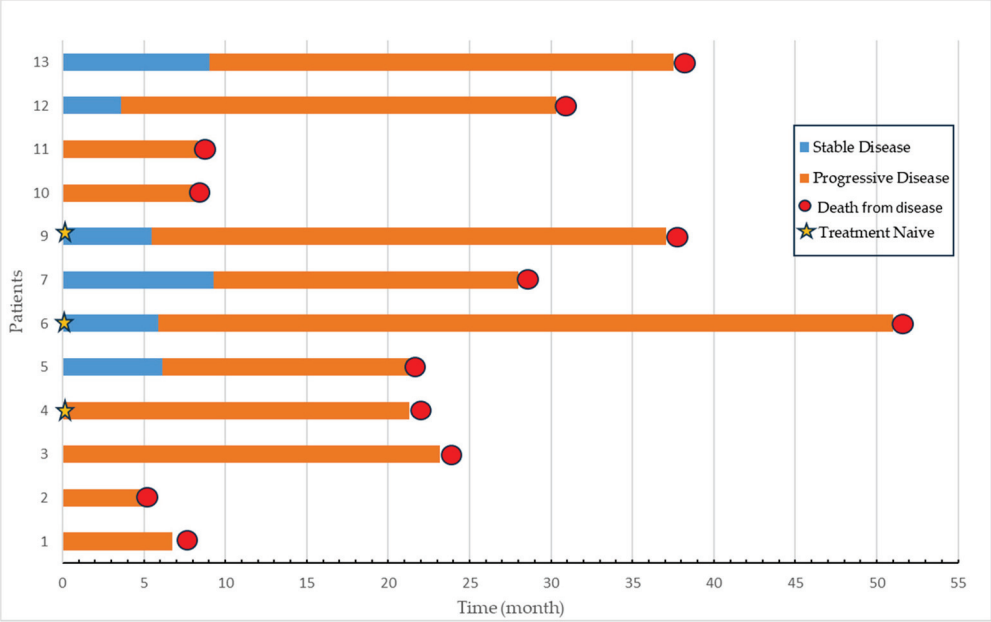


Figure 3. Swimmer's plot (n = 12).

With a median follow-up of 20.0 months, the median PFS was 3.0 months (95% CI 2.1–6.0 months) and median OS was 20.0 months (95% CI 8.3–28.1 months). The Kaplan–Meier curves of PFS and OS are shown in Figure 4. Median PFS and OS were longer for treatment-naïve patients (n = 3) vs. the previously treated patients (n = 9). Treatment-naïve patients had a median PFS of 5.5 months and median OS of 31.5 months. Previously treated patients had a median PFS of 2.5 months and median OS of 15.3 months. The prolonged OS of the treatment-naïve group may have been driven by post-progression therapy, since the median number of post-progression therapies received before death was 3 for the entire group, 5 for treatment-naïve patients, and 2 for the previously treated patients.

https://doi.org/10.3390/cancers18142232

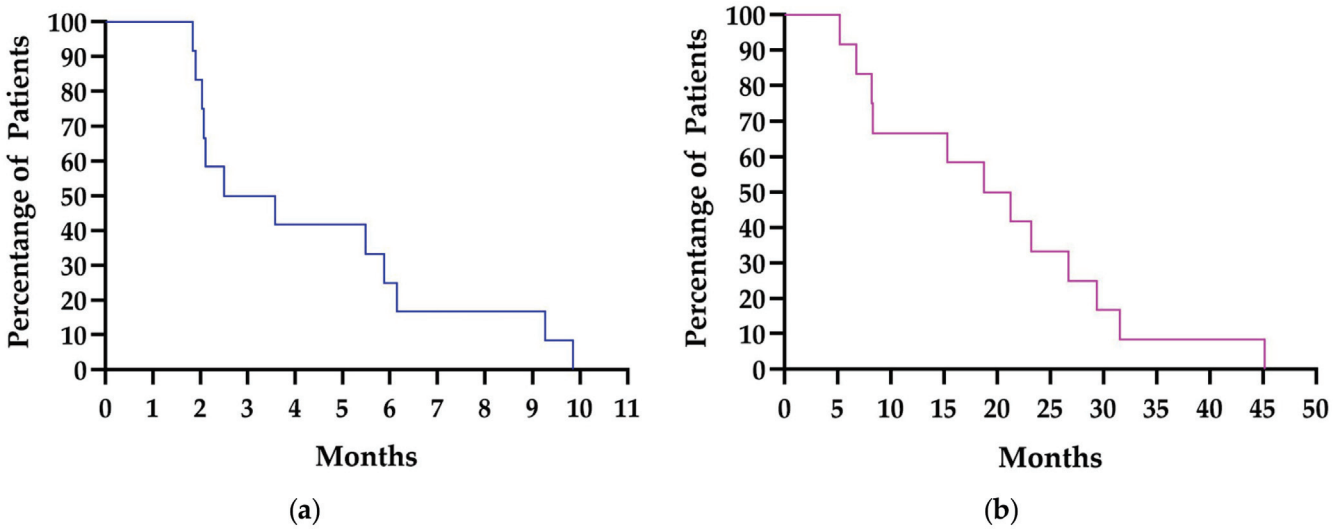


Figure 4. Progression-free survival and overall survival (n = 12). (**a**) Progression-free survival; (**b**) Overall survival.

3.1. Safety

All treatment-related adverse events (AEs) were Grade 1–2 except one Grade 3 AE of asymptomatic elevated creatine phosphokinase levels (CPK) that resolved with holding treatment and did not recur upon restarting (Table 3). There were no Grade 4 AEs. Patient 13 developed Grade 3 CPK elevation on cycle 1 day 13, which resolved to Grade 1 twelve days later, and treatment was resumed without any dose adjustments. Most frequently reported treatment-related AEs included rash (12/12, 100.0%), diarrhea (8/12, 66.7%), edema (6/12, 50.0%), nausea (6/12, 50%), fatigue (6/12, 50.0%), and blurry vision (6/12, 50.0%).

Because avutometinib is known to cause visual changes, all patients underwent detailed ophthalmological examination at multiple time points (at screening, cycle 2 day 1, cycle 3 day 1, cycle 5 day 1, every 3rd cycle after, and end of treatment). All visual changes on trial were Grade 1, transient, and self-resolved. Four of the patients experienced blurry vision that lasted 24 h or less. Patient 5 had three periods of Grade 1 blurry vision, each lasting 6–15 days, during the first three cycles (none during subsequent cycles). There were no changes in the ophthalmologic examination for patient 5. Patient 13 experienced two episodes of blurry vision during the first two cycles, lasting 8 days and 24 h, respectively. By cycle 3, the blurry vision had completely resolved, but ophthalmologic examination on cycle 3 day 1 was notable for a new small focus of subfoveal fluid in the affected eye on optical coherence tomography scan. Treatment was continued, and on the next ophthalmologic examination the subfoveal fluid had resolved without intervention.

No dose reductions or discontinuations were required for any patients. All side effects resolved after discontinuing trial medications. No treatment-related serious AEs or deaths occurred.

https://doi.org/10.3390/cancers18142232

Table 3. Treatment-related adverse events (n = 12).

AE Description	Any Grade	Grade 1	Grade 2	Grade 3	Grade 4
	Number of patients with an event (percent)				
Any adverse event	12 (100.0)	12 (100.0)	9 (75.0)	3 (25.0)	0
Treatment-related adverse events *					
Any	12 (100.0)	12 (100.0)	6 (50.0)	1 (8.3)	0
Rash	12 (100.0)	12 (100.0)	4 (33.3)	0	0
Diarrhea	8 (66.7)	8 (66.7)	1 (8.3)	0	0
Nausea	6 (50.0)	6 (50.0)	0	0	0
Fatigue	6 (50.0)	6 (50.0)	1 (8.3)	0	0
Edema	6 (50.0)	6 (50.0)	1 (8.3)	0	0
Visual impairment	6 (50.0)	6 (50.0)	0	0	0
Pruritis	4 (33.3)	4 (33.3)	0	0	0
Mucositis	4 (33.3)	3 (25.0)	1 (8.3)		
Abdominal pain	3 (25.0)	3 (25.0)	0	0	0
Dysgeusia	3 (25.0)	3 (25.0)	0	0	0
Dizziness	2 (16.7)	2 (16.7)	0	0	0
Anorexia	2 (16.7)	2 (16.7)	0	0	0
Dry skin	2 (16.7)	2 (16.7)	0	0	0
CPK elevation	1 (8.3)	1 (8.3)	1 (8.3)	1 (8.3)	0
Dry Mouth	2 (16.7)	2 (16.7)	0	0	0
Fever	2 (16.7)	1 (8.3)	1 (8.3)	0	0
Alopecia	1 (8.3)	1 (8.3)	1 (8.3)	0	0
Vomiting	1 (8.3)	1 (8.3)	0	0	0
Reflux	1 (8.3)	1 (8.3)	0	0	0
Thrombocytopenia	1 (8.3)	1 (8.3)	0	0	0
Constipation	1 (8.3)	1 (8.3)	0	0	0
Concentration impairment	1 (8.3)	1 (8.3)	0	0	0

* The investigators determined whether adverse events were related to a trial agent. Patients may have had more than one event.

3.2. Investigation on Biomarkers Linked to Therapeutic Sensitivity

During this clinical study, biopsy specimens were collected before and after completion of one cycle of combination therapy if clinically feasible. Four biopsy specimens from SD patients (patients 5, 7, 12, 13) and three from PD patients (patients 1, 4, 10) were analyzed for biomarker studies. Additionally, PDX were established from seven metastatic biopsy specimens and used for analysis: four PDX from SD (patients 7, 9, 12, 13) and three PDX from PD (patients 1, 4, 10). Due to the limited amounts of available tissue from individual patients, fewer specimens were used for individual tests, and not all exploratory translational endpoints were able to be evaluated.

3.3. Phosphorylation of ERK

We speculated that if a combination of FAK and RAF/MEK inhibitors works, the downstream activation of the Mitogen-Activated Protein Kinase (MAPK) pathway should be inhibited. We tested four patients whose pre- and post-treatment biopsy samples were available for ERK activity analysis. Reduction in active ERK (pERK) was observed in two

https://doi.org/10.3390/cancers18142232

patients who achieved SD (patients 7 and 12), but not in two patients who had PD (patients 4 and 10) (Figure 5). This result indicates the presence of alternative pathways to activate ERK despite upstream RAF/MEK inhibition.

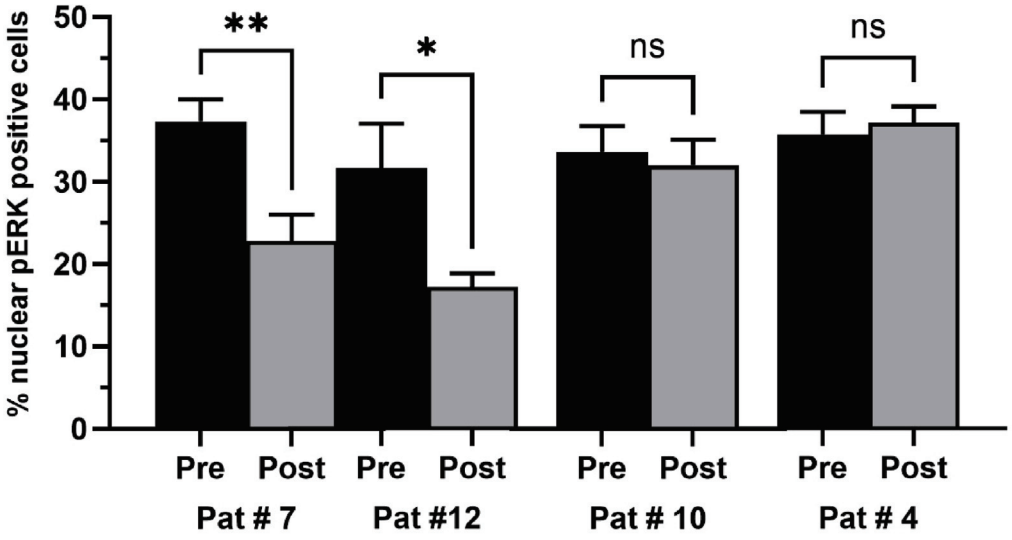


Figure 5. Pre- and post-treatment pERK nuclear staining. ns = not significant. *p* values **: 0.0192; *: 0.0371.

3.4. RNA Gene Expression Profiles in Patient-Derived Xenograft (PDX)

To obtain sufficient tissue for RNA sequencing and to identify potential biomarkers associated with treatment response or disease progression, we established PDX models using pre- and post-treatment biopsy specimens. RNA-seq analysis of matched pre- and post-treatment PDX samples from two patients with PD (patients 1 and 10) showed increased Aldehyde Dehydrogenase 1 Family Member A3 (ALDH1A3) mRNA expression in post-treatment PDX tumors (Figure 6a).

To validate this finding at the protein level, IHC analysis for ALDH1A3 was performed on patient biopsy specimens (Figure 6b) and PDX tumors (Supplemental Figure S1). The percentage of positive tumor cells was quantified in up to 10 non-overlapping high-power fields per sample using Celleste 4.1. The percentage of ALDH1A3-positive cells significantly increased after treatment in two out of the three patients who experienced PD (patients 1 and 4), whereas patients who achieved SD (patients 5, 7, and 12) tended to show a decrease in ALDH1A3 expression in their post-treatment biopsy specimens (Figure 6c). One patient with PD showed no significant change (patient 10). However, in the pre-treatment biopsy, this patient exhibited nearly 100% ALDH1A3-positive cells, which did not change after treatment. In contrast to biopsy specimens, PDX tumors developed from biopsy specimens of patient 10 showed areas of positive and negative tumor cell staining, indicating heterogeneity among the original uveal melanoma cells (Supplement Figure S1). These observations should be considered exploratory because of the limited number of matched PDX specimens.

https://doi.org/10.3390/cancers18142232

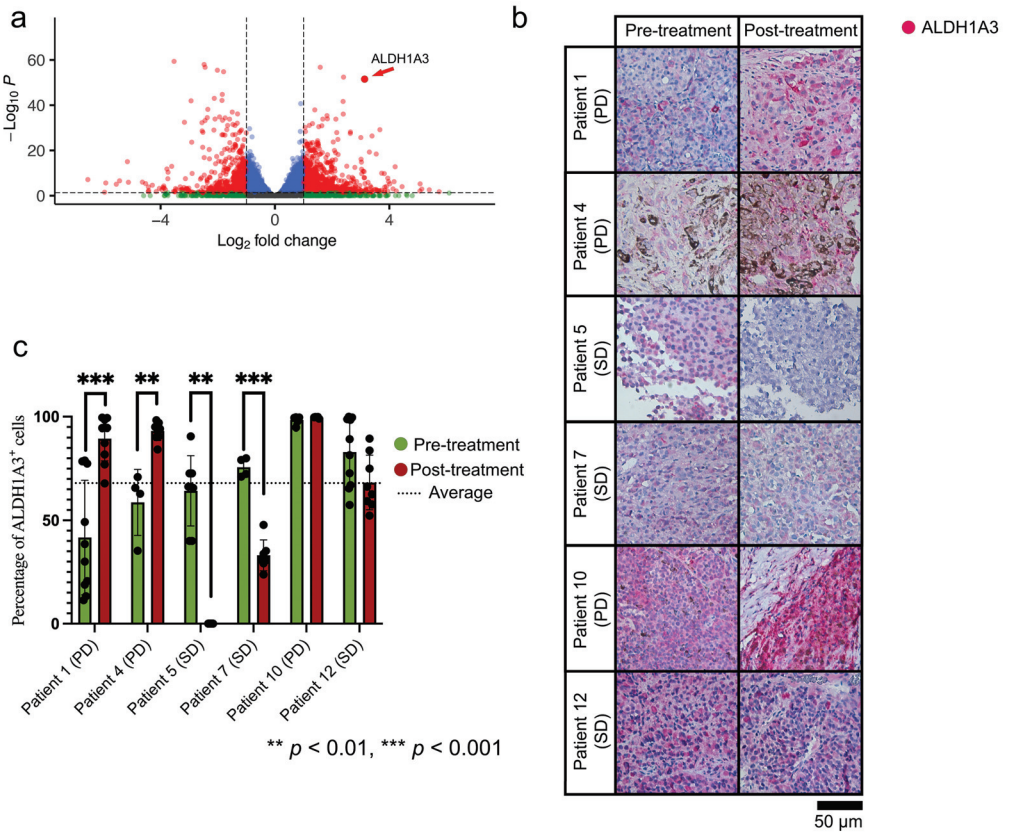


Figure 6. Expression of the ALDH1A3 gene and protein in PDX specimens and biopsy specimens obtained from pre- and post-treatment. (**a**) Volcano plot of RNA-seq data comparing post- and pre-treatment obtained from patient-derived xenograft (PDX) specimens. Dashed lines mark log2FC = 1 and FDR = 0.05. (**b**) Immunohistochemical staining for ALDH1A3 protein in biopsy specimens from MUM patients. ALDH1A3 protein was visualized using an antibody conjugated to alkaline phosphatase. Representative 200× fields are shown; scale bar, 50 μm. (**c**) Quantification of ALDH1A3-positive cells in biopsy specimens from MUM patients. Green bar: pre-treatment, red bar: post-treatment. The dotted line indicates the average level across all samples.

3.5. Investigation on Signaling Modules That Capture the Potential Adaptive Resistance Mechanisms

Since the sample size was very small, this analysis was explorative and performed to obtain baseline data for future investigation on the FAK and MEK inhibitor combination.

As shown in Figure 7, we observed a trend towards persistent pro-survival signaling, especially through mTORC1 and mTORC2 pathways. In particular, the elevated SGK-mTORC2 signaling suggests an AKT-independent survival mechanism of UM cancer cells. Although the results are highly speculative with a small sample size, there was also a trend towards increased BCL2 anti-apoptotic pathway activity in PD tumors, particularly after treatment. Together, these data suggest that resistance to combined FAK/MEK inhibition in UM might be associated with persistent pro-survival signaling, particularly in the mTORC1 and mTORC2 pathways, and with BCL2 expression.

Notably, these features were consistently observed across both patient-derived tumor samples and matched PDX models in our MUM omics database in patients who did not receive FAK and MEK inhibitor treatment (Supplemental Figures S2 and S3), supporting the biological relevance of the observed phenomena in this clinical trial.

https://doi.org/10.3390/cancers18142232

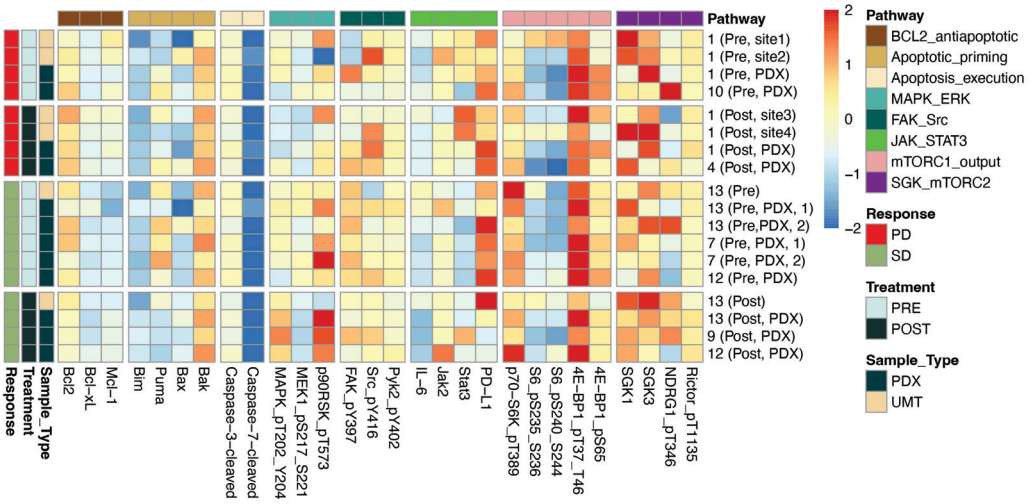


Figure 7. Descriptive heatmap of protein and phosphoprotein abundance across pathway-related RPPA markers. RPPA values are shown as L4 log2-normalized protein and phosphoprotein abundance, where 0 represents the cohort median, +1 indicates approximately 2-fold higher abundance, and −1 indicates approximately 2-fold lower abundance of a given protein or phosphoprotein relative to the cohort. Positive values indicate higher protein abundance and/or phosphorylation (consistent with increased pathway output), whereas negative values indicate lower abundance and/or phosphorylation compared with the typical tumor in the dataset. Antibodies were grouped by signaling module, while samples were displayed without unsupervised clustering. No statistical testing was applied to this visualization. The heatmap should be interpreted as a descriptive overview of pathway-related RPPA patterns. Treatment annotation indicates pre-treatment (Pre) and post-treatment (Post) specimens. Response annotation indicates progressive disease (PD) or stable disease (SD). Sample type annotation indicates metastatic uveal melanoma biopsy specimens (UMT) or patient-derived xenograft tumors (PDX).

4. Discussion

We conducted a phase 2, single-arm, single-institution study of the combination of defactinib, an FAK inhibitor, and avutometinib, an RAF/MEK inhibitor, in patients with metastatic uveal melanoma. We treated 12 patients with the combination and achieved SD in 50% of the patients. The median PFS was 3.0 months, and the median OS was 20.0 months with the combination. The combination was quite tolerable for patients, with only one transient and asymptomatic Grade 3 AE of elevated CPK. No patients required dose reduction or discontinuation.

Patients who were treatment naïve had a longer median PFS and OS in comparison to patients who had previous treatment, although the numbers are quite small to make a definitive comparison. Patients who were treatment-naïve received more post-progression therapies, which could have driven the improvement in OS but would not explain the improvement in PFS. Because of the heterogeneity of pre- and post-trial treatments, it is difficult to comment on the influence of specific therapies on the outcomes.

No benefit relative to other available therapies was observed with the combination of avutometinib and defactinib, highlighting the difference in the biology of MUM relative to other cancer types, such as KRAS-mutated LGSOC, in which avutometinib and defactinib have been shown to be effective. There were no CR or PRs seen after 2 cycles in our trial. A DCR of 50% is in line with other systemic therapies for MUM, and our median PFS and OS also are similar to the results of published tebentafusp and ipilimumab/nivolumab studies. Tebentafusp achieved an objective response of 11% compared to 5% in the control group, with a DCR of 46% [45]. Patients who received tebentafusp had a median PFS of 3.4 months and OS of 21.6 months [45]. Similarly, ipilimumab with nivolumab achieved

https://doi.org/10.3390/cancers18142232

an ORR of 11.5–18%, DCR of 51–63.5%, median PFS of 3.0–5.5 months, and median OS of 12.7–19.1 months [46,47]. Despite strong growth suppression in in vitro experiments with MEK inhibitors, results of other MEK-targeted therapies have also been disappointing, with a systematic review of six clinical trials of MEK inhibitors in MUM showing a median PFS of 3.1 weeks to 16 weeks and overall response rate of 0 to 14% [48]. This discrepancy might indicate the presence of resistance mechanisms or alternative pathways for downstream ERK activation in the tumor microenvironment of patients.

Increasing ALDH1A3 mRNA expression was identified by RNA-seq analysis of PDX specimens and validated at the protein level in patient biopsy specimens, particularly after disease progression. Since PDXs are passaged only in vivo, they avoid the selective culture pressures associated with in vitro. ALDH1A3, an aldehyde-metabolizing enzyme associated with metabolic and oxidative stress, has been reported to exhibit stem cell-like properties. A previous study has shown that ALDH1A3 contributes to therapy resistance in various cancers and is associated with poor survival as well as tumor regrowth post-therapy [49]. Consistent with the literature, increased ALDH1A3 was also observed in MUM patients who experienced PD. ALDH-high tumor subpopulations have been proposed as potential targets for ALDH-directed or ALDH-activated prodrug strategies, including metronidazole-based approaches [50,51]. Although successful PDX engraftment may enrich for biologically aggressive tumor populations and potentially introduce selection bias, the association of ALD1H3 expression was independently confirmed in patient original biopsy specimens, supporting the translational relevance of our finding. However, due to the limited sample size, the findings should be considered exploratory and interpreted with caution. Further investigation with larger patient samples is required to confirm this observation.

Given a lack of tumor response with the combination, other combination strategies are likely necessary to achieve clinical benefit for patients with MUM. A high-throughput chemogenetic drug screen in four genetically distinct *GNAQ*-mutant UM cell lines using a collection of ~2500 mechanistically annotated, oncology-focused agents identified PKC-targeting drugs among the top hits [52]. Among them, darovasertib, a PKC inhibitor under current clinical investigation for the treatment of UM [53], exhibited the most differential Z-AUC score and lowest IC50 across all PKC inhibitors tested. Darovasertib concomitantly inhibits both canonical and non-canonical Gαq-driven signaling pathways (e.g., PKC and PKN/FAK, respectively) [52]. While the blockade of PKC/PKN by darovasertib disrupts Gαq-driven signaling axes, darovasertib alone is insufficient to promote a sustained inhibition of YAP activity downstream of FAK. The partial reduction in FAK activation by darovasertib may sensitize FAK for its further inhibition by direct ATP-competitive kinase inhibitors, thus reinforcing a multipronged pharmacology paradigm that ultimately requires co-targeting both Gαq-regulated signaling axes to achieve a durable clinical benefit. In fact, the combination of darovasertib and an FAK inhibitor has been found to have efficacy in complementary UM PDX models, further supporting the potential combination in MUM [54]. Currently, darovasertib is being evaluated with crizotinib in MUM, and this combination has shown impressive clinical efficacy, with 92% of patients having tumor shrinkage in 68 patients treated in the phase 1/2 dose-escalation trial [53,55]. However, darovasertib with crizotinib has common drug-related AEs that can be challenging for patients. It would be worth investigating whether defactinib in combination with darovasertib could be a more tolerable, efficacious alternative relative to darovasertib with crizotinib.

It is of note that Lubrano et al. recently identified multiple resistance mechanisms by screening 100 pathway-activating mutant complementary DNAs by lentiviral overexpression in *BAP1* wild-type and *BAP-1* mutant UM cells [56]. Using a "signaling toolkit" strategy, their study revealed JAK-STAT activation, overexpression of anti-apoptotic

https://doi.org/10.3390/cancers18142232

BCL2/BCLXL, and dysregulated PI3K/mTOR or Hippo pathways as escape routes under MEK-ERK or FAK inhibition. In fact, our institutional omics data indicate upregulation of key signaling components in JAK-STAT3 and SGK-mTORC2 pathways in MUM tissue specimens. SGK1 is functionally associated with the PI3K/AKT signaling pathway [57]. However, SGK1 is not a direct component of AKT, but they are parallel downstream effectors of PI3K signaling. As HGF/MET-mediated PI3K/AKT signaling is commonly activated in hepatic UM metastases [58], the increased SGK1 expression observed in tumors may not simply indicate the constitutional pathway activation, but rather may reflect a shift toward SGK1-mediated adaptive and compensatory survival signaling in the liver microenvironment. These data might partly explain the lack of response to treatment with FAK and MEK inhibitors in this clinical trial. Lubrano et al. further demonstrated improved efficacy by adding a BCL2 inhibitor to FAK and MEK [56]. These findings provide a mechanistic rationale for investigating combination strategies with inhibitors targeting compensatory networks of FAK and MEK inhibition, such as mTOR inhibitors and BCL-inhibitors, to overcome resistance mechanisms. Although a 3-drug combination treatment might be clinically challenging, the above in vitro and omics data of MUM suggest directions for improvement.

Our study has several limitations. Our statistical design was based on Simon's two-stage design, with a planned enrollment of 18 patients during two stages. Although our primary endpoint was DCR of 50% and the DCR of the enrolled 12 patients was 50%, the lack of any CR or PR was disappointing, and thus trial enrollment was stopped early by study sponsors. Therefore, although our data met the goal for the first stage, we were not able to complete the second stage and reject the null hypothesis. As only 12 patients were treated, the limited sample size limits the strength of our conclusions about efficacy. Furthermore, our study is a single-institution small study with significant variation in treatments before and after our trial medication; this may introduce selection bias and also limit generalizability. Molecular information was only available for five of the patients. Further studies with integrated molecular profiling could help identify patients who are more likely to benefit from the combination treatment. Finally, due to limited amounts of available tissue from individual patients, not all exploratory translational endpoints were able to be evaluated. FAK inhibitors have recognized immunomodulatory effects, so future evaluation of the tumor immune microenvironment, such as CD8-positive lymphocytes, macrophage populations, PD-L1 expression, or spatial immune profiling, could also be helpful in better understanding the impact of FAK inhibitors on MUM tumors.

Although the data from this study are preliminary and mostly exploratory, our results suggest that the combination treatment with FAK and MEK inhibitors would not be clinically useful in metastatic uveal melanoma. An improved design for future clinical studies needs to be developed.

5. Conclusions

In conclusion, in this phase 2 study of the combination regimen of defactinib and avutometinib, stable disease was achieved in half of patients with MUM. Treatment was well tolerated with only one transient asymptomatic Grade 3 CPK elevation. Although our trial was small and stopped early, it provides important insights into non-canonical targeting of Gαq-driven signaling pathways, including FAK and potential resistance mechanisms. Further research should seek to elucidate an optimal combination treatment strategy for MUM, such as FAK and PKC inhibitors, for a clinically tolerable and efficacious treatment, targeting the signaling pathways downstream of GNAQ/GNA11 driver mutations.

https://doi.org/10.3390/cancers18142232

Supplementary Materials: The following supporting information can be downloaded at: https://www.mdpi.com/article/10.3390/cancers18142232/s1, Figure S1: Immunohistochemical staining for the ALDH1A3 protein in matched pre- and post-treatment PDX specimens from MUM patients; Figures S2: Descriptive boxplot of TPM-normalized expression of selected pathway-related genes in an independent institutional cohort of metastatic uveal melanoma biopsy specimens; Figure S3: Descriptive heatmap of pathway-related protein and phosphoprotein abundance measured by RPPA in metastatic biopsy specimens; File S1: Protocol.

Author Contributions: Conceptualization, R.S.S., J.S.G. and T.S.; methodology, R.S.S., J.S.G. and T.S.; formal analysis, R.S.S., M.T., S.K., A.M., J.S.G. and T.S.; investigation, R.S.S., M.T., S.K., M.O., E.S.-M., M.N. and T.S.; writing—original draft preparation, R.S.S.; writing—review and editing, R.S.S., M.T., S.K., A.E.A., M.O., E.S.-M., M.N., A.M., A.A.M., J.S.G. and T.S.; supervision, T.S.; funding acquisition, R.S.S. and T.S. All authors have read and agreed to the published version of the manuscript.

Funding: This research was funded by Verastem Oncology, Inc. The sponsor or funding organization had no role in the conduct of this research. Support for the PDX experiment was through the Plancher Fund at Thomas Jefferson University.

Institutional Review Board Statement: The study was conducted in accordance with the Declaration of Helsinki, and approved by the Institutional Review Board of Thomas Jefferson University (IRB#20P.1113, 11/12/2020).

Informed Consent Statement: Informed consent was obtained from all subjects involved in the study.

Data Availability Statement: The original contributions presented in this study are included in the article/Supplementary Material. Further inquiries can be directed to the corresponding author.

Conflicts of Interest: R.S.S. served on the advisory board for Bristol Myers Squibb and Immunocore. M.O. is a consultant for Immunocore, Ideaya, and Delcath and serves on the Scientific Advisory Board of Trisalus. T.S. is a consultant for Immunocore and Castle Biosciences, and reports honoraria and travel support from Castle Biosciences. J.S.G. reports consulting fees from Radionetics Oncology, BTB Therapeutics, and Acurion and is the founder of Kadima Pharmaceuticals, all of which are unrelated to the current study. The remaining authors declare no competing interests. The funders had no role in the design of the study; in the collection, analyses, or interpretation of data; in the writing of the manuscript; or in the decision to publish the results.

Abbreviations

The following abbreviations are used in this manuscript:

UM	Uveal Melanoma
MUM	Metastatic Uveal Melanoma
ORR	Overall response rate
CTLA-4	Cytotoxic T-lymphocyte-associated protein 4
PD-1	Programmed cell death 1
LAG-3	Lymphocyte activation gene-3
OS	Overall survival
PFS	Progression-free survival
LGSOC	Low-grade serous ovarian cancer
NSCLC	Non-small cell lung cancer
PR	Partial response
CR	Complete Response
SD	Stable Disease
DCR	Disease control rate
AE	Adverse events
pERK	Phosphorylated ERK
PDX	Patient-derived xenograft
RPPA	Reverse-phase protein array

https://doi.org/10.3390/cancers18142232

IHC	Immunohistochemical
BOR	Best overall response
CPK	Creatine phosphokinase

References

1. Singh, A.D.; Turell, M.E.; Topham, A.K. Uveal melanoma: Trends in incidence, treatment, and survival. *Ophthalmology* **2011**, *118*, 1881–1885. [CrossRef] [PubMed]
2. Diener-West, M.; Reynolds, S.M.; Agugliaro, D.J.; Caldwell, R.; Cumming, K.; Earle, J.D.; Hawkins, B.S.; Hayman, J.A.; Jaiyesimi, I.; Jampol, L.M.; et al. Development of metastatic disease after enrollment in the COMS trials for treatment of choroidal melanoma: Collaborative Ocular Melanoma Study Group Report No. 26. *Arch. Ophthalmol.* **2005**, *123*, 1639–1643. [CrossRef] [PubMed]
3. Kujala, E.; Mäkitie, T.; Kivelaä, T. Very Long-Term Prognosis of Patients with Malignant Uveal Melanoma. *Investig. Ophthalmol. Vis. Sci.* **2003**, *44*, 4651–4659. [CrossRef] [PubMed]
4. Economou, M.A.; All-Ericsson, C.; Bykov, V.; Girnita, L.; Bartolazzi, A.; Larsson, O.; Seregard, S. Receptors for the liver synthesized growth factors IGF-1 and HGF/SF in uveal melanoma: Intercorrelation and prognostic implications. *Acta Ophthalmol.* **2008**, *86*, 20–25. [CrossRef] [PubMed]
5. Bedikian, A.Y. Metastatic uveal melanoma therapy: Current options. *Int. Ophthalmol. Clin.* **2006**, *46*, 151–166. [CrossRef] [PubMed]
6. Albert, D.M.; Ryan, L.M.; Borden, E.C. Metastatic Ocular and Cutaneous Melanoma: A Comparison of Patient Characteristics and Prognosis. *Arch. Ophthalmol.* **1996**, *114*, 107–108. [CrossRef]
7. Bedikian, A.Y.; Legha, S.S.; Mavligit, G.; Carrasco, C.H.; Khorana, S.; Plager, C.; Papadopoulos, N.; Benjamin, R.S. Treatment of uveal melanoma metastatic to the liver: A review of the M. D. Anderson Cancer Center experience and prognostic factors. *Cancer* **1995**, *76*, 1665–1670. [CrossRef]
8. Kath, R.; Hayungs, J.; Bornfeld, N.; Sauerwein, W.; Höffken, K.; Seeber, S. Prognosis and treatment of disseminated uveal melanoma. *Cancer* **1993**, *72*, 2219–2223. [CrossRef]
9. Gragoudas, E.S.; Egan, K.M.; Seddon, J.M.; Glynn, R.J.; Walsh, S.M.; Finn, S.M.; Munzenrider, J.E.; Spar, M.D. Survival of patients with metastases from uveal melanoma. *Ophthalmology* **1991**, *98*, 383–389. [CrossRef] [PubMed]
10. Krauthammer, M.; Kong, Y.; Ha, B.H.; Evans, P.; Bacchiocchi, A.; McCusker, J.P.; Cheng, E.; Davis, M.J.; Goh, G.; Choi, M.; et al. Exome sequencing identifies recurrent somatic RAC1 mutations in melanoma. *Nat. Genet.* **2012**, *44*, 1006–1014. [CrossRef] [PubMed]
11. Furney, S.J.; Pedersen, M.; Gentien, D.; Dumont, A.G.; Rapinat, A.; Desjardins, L.; Turajlic, S.; Piperno-Neumann, S.; de la Grange, P.; Roman-Roman, S.; et al. SF3B1 mutations are associated with alternative splicing in uveal melanoma. *Cancer Discov.* **2013**, *3*, 1122–1129. [CrossRef] [PubMed]
12. Yang, J.; Manson, D.K.; Marr, B.P.; Carvajal, R.D. Treatment of uveal melanoma: Where are we now? *Ther. Adv. Med. Oncol.* **2018**, *10*, 1758834018757175. [CrossRef] [PubMed]
13. Johnson, D.B.; Daniels, A.B. Continued Poor Survival in Metastatic Uveal Melanoma: Implications for Molecular Prognostication, Surveillance Imaging, Adjuvant Therapy, and Clinical Trials. *JAMA Ophthalmol.* **2018**, *136*, 986–988. [CrossRef] [PubMed]
14. Algazi, A.P.; Tsai, K.K.; Shoushtari, A.N.; Munhoz, R.R.; Eroglu, Z.; Piulats, J.M.; Ott, P.A.; Johnson, D.B.; Hwang, J.; Daud, A.I.; et al. Clinical outcomes in metastatic uveal melanoma treated with PD-1 and PD-L1 antibodies. *Cancer* **2016**, *122*, 3344–3353. [CrossRef] [PubMed]
15. Schank, T.E.; Hassel, J.C. Immunotherapies for the Treatment of Uveal Melanoma-History and Future. *Cancers* **2019**, *11*, 1048. [CrossRef] [PubMed]
16. Bol, K.F.; Ellebaek, E.; Hoejberg, L.; Bagger, M.M.; Larsen, M.S.; Klausen, T.W.; Kohler, U.H.; Schmidt, H.; Bastholt, L.; Kiilgaard, J.F.; et al. Real-World Impact of Immune Checkpoint Inhibitors in Metastatic Uveal Melanoma. *Cancers* **2019**, *11*, 1489. [CrossRef] [PubMed]
17. Heppt, M.V.; Amaral, T.; Kahler, K.C.; Heinzerling, L.; Hassel, J.C.; Meissner, M.; Kreuzberg, N.; Loquai, C.; Reinhardt, L.; Utikal, J.; et al. Combined immune checkpoint blockade for metastatic uveal melanoma: A retrospective, multi-center study. *J. Immunother. Cancer* **2019**, *7*, 299. [CrossRef] [PubMed]
18. Lutzky, J.; Hernandez-Aya, L.; Feun, L.; Correa, Z.; King, J.; Estevez, C.; Decatur, C.; Dollar, J.J.; Reis, I.; Harbour, J.W. 1126P A phase II study of nivolumab/relatlimab in metastatic uveal melanoma. *Ann. Oncol.* **2024**, *35*, S741. [CrossRef]
19. Nathan, P.; Hassel, J.C.; Rutkowski, P.; Baurain, J.-F.; Butler, M.O.; Schlaak, M.; Sullivan, R.J.; Ochsenreither, S.; Dummer, R.; Kirkwood, J.M.; et al. Overall Survival Benefit with Tebentafusp in Metastatic Uveal Melanoma. *N. Engl. J. Med.* **2021**, *385*, 1196–1206. [CrossRef] [PubMed]
20. Zager, J.S.; Orloff, M.M.; Ferrucci, P.F.; Glazer, E.S.; Ejaz, A.; Richtig, E.; Ochsenreither, S.; Lowe, M.C.; Reddy, S.A.; Beasley, G.; et al. FOCUS phase 3 trial results: Percutaneous hepatic perfusion (PHP) with melphalan for patients with ocular melanoma liver metastases (PHP-OCM-301/301A). *J. Clin. Oncol.* **2022**, *40*, 9510. [CrossRef]

https://doi.org/10.3390/cancers18142232

21. Harbour, J.W. The genetics of uveal melanoma: An emerging framework for targeted therapy. *Pigment. Cell Melanoma Res.* **2012**, *25*, 171–181. [CrossRef] [PubMed]
22. Van Raamsdonk, C.D.; Bezrookove, V.; Green, G.; Bauer, J.; Gaugler, L.; O'Brien, J.M.; Simpson, E.M.; Barsh, G.S.; Bastian, B.C. Frequent somatic mutations of GNAQ in uveal melanoma and blue naevi. *Nature* **2009**, *457*, 599–602. [CrossRef]
23. Van Raamsdonk, C.D.; Griewank, K.G.; Crosby, M.B.; Garrido, M.C.; Vemula, S.; Wiesner, T.; Obenauf, A.C.; Wackernagel, W.; Green, G.; Bouvier, N.; et al. Mutations in GNA11 in uveal melanoma. *N. Engl. J. Med.* **2010**, *363*, 2191–2199. [CrossRef]
24. Onken, M.D.; Worley, L.A.; Long, M.D.; Duan, S.; Council, M.L.; Bowcock, A.M.; Harbour, J.W. Oncogenic mutations in GNAQ occur early in uveal melanoma. *Invest. Opthal Vis. Sci.* **2008**, *49*, 5230–5234. [CrossRef] [PubMed]
25. Vaque, J.P.; Dorsam, R.T.; Feng, X.; Iglesias-Bartolome, R.; Forsthoefel, D.J.; Chen, Q.; Debant, A.; Seeger, M.A.; Ksander, B.R.; Teramoto, H.; et al. A genome-wide RNAi screen reveals a Trio-regulated Rho GTPase circuitry transducing mitogenic signals initiated by G protein-coupled receptors. *Mol. Cell* **2013**, *49*, 94–108. [CrossRef] [PubMed]
26. Khalili, J.S.; Yu, X.; Wang, J.; Hayes, B.C.; Davies, M.A.; Lizee, G.; Esmaeli, B.; Woodman, S.E. Combination small molecule MEK and PI3K inhibition enhances uveal melanoma cell death in a mutant GNAQ- and GNA11-dependent manner. *Clin. Cancer Res.* **2012**, *18*, 4345–4355. [CrossRef] [PubMed]
27. Carvajal, R.D.; Sosman, J.A.; Quevedo, J.F.; Milhem, M.M.; Joshua, A.M.; Kudchadkar, R.R.; Linette, G.P.; Gajewski, T.F.; Lutzky, J.; Lawson, D.H.; et al. Effect of selumetinib vs chemotherapy on progression-free survival in uveal melanoma: A randomized clinical trial. *JAMA* **2014**, *311*, 2397–2405. [CrossRef] [PubMed]
28. Carvajal, R.D.; Schwartz, G.K.; Mann, H.; Smith, I.; Nathan, P.D. Study design and rationale for a randomised, placebo-controlled, double-blind study to assess the efficacy of selumetinib (AZD6244; ARRY-142886) in combination with dacarbazine in patients with metastatic uveal melanoma (SUMIT). *BMC Cancer* **2015**, *15*, 467. [CrossRef] [PubMed]
29. Feng, X.; Degese, M.S.; Iglesias-Bartolome, R.; Vaque, J.P.; Molinolo, A.A.; Rodrigues, M.; Zaidi, M.R.; Ksander, B.R.; Merlino, G.; Sodhi, A.; et al. Hippo-independent activation of YAP by the GNAQ uveal melanoma oncogene through a trio-regulated rho GTPase signaling circuitry. *Cancer Cell* **2014**, *25*, 831–845. [CrossRef] [PubMed]
30. Feng, X.; Arang, N.; Rigiracciolo, D.C.; Lee, J.S.; Yeerna, H.; Wang, Z.; Lubrano, S.; Kishore, A.; Pachter, J.A.; Konig, G.M.; et al. A Platform of Synthetic Lethal Gene Interaction Networks Reveals that the GNAQ Uveal Melanoma Oncogene Controls the Hippo Pathway through FAK. *Cancer Cell* **2019**, *35*, 457–472 e455. [CrossRef] [PubMed]
31. Sulzmaier, F.J.; Jean, C.; Schlaepfer, D.D. FAK in cancer: Mechanistic findings and clinical applications. *Nat. Rev. Cancer* **2014**, *14*, 598–610. [CrossRef] [PubMed]
32. Serrels, A.; Lund, T.; Serrels, B.; Byron, A.; McPherson, R.C.; von Kriegsheim, A.; Gomez-Cuadrado, L.; Canel, M.; Muir, M.; Ring, J.E.; et al. Nuclear FAK controls chemokine transcription, Tregs, and evasion of anti-tumor immunity. *Cell* **2015**, *163*, 160–173. [CrossRef] [PubMed]
33. Paradis, J.S.; Acosta, M.; Saddawi-Konefka, R.; Kishore, A.; Lubrano, S.; Gomes, F.G.; Arang, N.; Tiago, M.; Coma, S.; Wu, X.; et al. Synthetic Lethal Screens Reveal Co-Targeting FAK and MEK as a Multimodal Precision Therapy for *GNAQ*-Driven Uveal Melanoma. *Clin. Cancer Res.* **2021**, *27*, 3190–3200. [CrossRef] [PubMed]
34. Coma, S.; Chowdhury, S.; Dilly, J.; Musteanu, M.; Barbacid, M.; Aguirre, A.J.; Pachter, J.A. Abstract 402: Dual RAF/MEK inhibitor VS-6766 enhances antitumor efficacy of KRAS G12C inhibitors through vertical inhibition of RAS, RAF and MEK. *Cancer Res.* **2022**, *82*. [CrossRef]
35. Ishii, N.; Harada, N.; Joseph, E.W.; Ohara, K.; Miura, T.; Sakamoto, H.; Matsuda, Y.; Tomii, Y.; Tachibana-Kondo, Y.; Iikura, H.; et al. Enhanced inhibition of ERK signaling by a novel allosteric MEK inhibitor, CH5126766, that suppresses feedback reactivation of RAF activity. *Cancer Res.* **2013**, *73*, 4050–4060. [CrossRef] [PubMed]
36. Lito, P.; Saborowski, A.; Yue, J.; Solomon, M.; Joseph, E.; Gadal, S.; Saborowski, M.; Kastenhuber, E.; Fellmann, C.; Ohara, K.; et al. Disruption of CRAF-mediated MEK activation is required for effective MEK inhibition in KRAS mutant tumors. *Cancer Cell* **2014**, *25*, 697–710. [CrossRef] [PubMed]
37. Lubrano, S.; Faraji, F.; Cervantes-Villagrana, R.D.; Ramirez, S.; Arang, N.; Officer, A.; Rigiracciolo, D.C.; Quiroz, P.Y.A.; Bacchiocchi, A.; Halaban, R.; et al. Abstract 4745: A novel combination therapy targeting RAF, MEK and FAK to overcome skin cutaneous melanoma treatment resistance. *Cancer Res.* **2024**, *84*. [CrossRef]
38. FDA. FDA Grants Accelerated Approval to the Combination of Avutometinib and Defactinib for KRAS-Mutated Recurrent Low-Grade Serous Ovarian Cancer. Available online: https://www.fda.gov/drugs/resources-information-approved-drugs/fda-grants-accelerated-approval-combination-avutometinib-and-defactinib-kras-mutated-recurrent-low (accessed on 1 June 2026).
39. Banerjee, S.; Krebs, M.G.; Greystoke, A.; Garces, A.I.; Perez, V.S.; Terbuch, A.; Shinde, R.; Caldwell, R.; Grochot, R.; Rouhifard, M.; et al. Defactinib with avutometinib in patients with solid tumors: The phase 1 FRAME trial. *Nat. Med.* **2025**, *31*, 3074–3080. [CrossRef] [PubMed]
40. Tolcher, A.W. Stable disease is a valid end point in clinical trials. *Cancer J.* **2009**, *15*, 374–378. [CrossRef] [PubMed]

https://doi.org/10.3390/cancers18142232

41. Bankhead, P.; Loughrey, M.B.; Fernández, J.A.; Dombrowski, Y.; McArt, D.G.; Dunne, P.D.; McQuaid, S.; Gray, R.T.; Murray, L.J.; Coleman, H.G.; et al. QuPath: Open source software for digital pathology image analysis. *Sci. Rep.* **2017**, *7*, 16878. [CrossRef] [PubMed]
42. Kageyama, K.; Ohara, M.; Saito, K.; Ozaki, S.; Terai, M.; Mastrangelo, M.J.; Fortina, P.; Aplin, A.E.; Sato, T. Establishment of an orthotopic patient-derived xenograft mouse model using uveal melanoma hepatic metastasis. *J. Transl. Med.* **2017**, *15*, 145. [CrossRef] [PubMed]
43. Taylor, I.W.; Linding, R.; Warde-Farley, D.; Liu, Y.; Pesquita, C.; Faria, D.; Bull, S.; Pawson, T.; Morris, Q.; Wrana, J.L. Dynamic modularity in protein interaction networks predicts breast cancer outcome. *Nat. Biotechnol.* **2009**, *27*, 199–204. [CrossRef] [PubMed]
44. Simon, R. Optimal two-stage designs for phase II clinical trials. *Control Clin. Trials* **1989**, *10*, 1–10. [CrossRef] [PubMed]
45. Hassel, J.C.; Piperno-Neumann, S.; Rutkowski, P.; Baurain, J.F.; Schlaak, M.; Butler, M.O.; Sullivan, R.J.; Dummer, R.; Kirkwood, J.M.; Orloff, M.; et al. Three-Year Overall Survival with Tebentafusp in Metastatic Uveal Melanoma. *N. Engl. J. Med.* **2023**, *389*, 2256–2266. [CrossRef] [PubMed]
46. Pelster, M.S.; Gruschkus, S.K.; Bassett, R.; Gombos, D.S.; Shephard, M.; Posada, L.; Glover, M.S.; Simien, R.; Diab, A.; Hwu, P.; et al. Nivolumab and Ipilimumab in Metastatic Uveal Melanoma: Results from a Single-Arm Phase II Study. *J. Clin. Oncol.* **2021**, *39*, 599–607. [CrossRef] [PubMed]
47. Piulats, J.M.; Espinosa, E.; de la Cruz Merino, L.; Varela, M.; Alonso Carrion, L.; Martin-Algarra, S.; Lopez Castro, R.; Curiel, T.; Rodriguez-Abreu, D.; Redrado, M.; et al. Nivolumab Plus Ipilimumab for Treatment-Naive Metastatic Uveal Melanoma: An Open-Label, Multicenter, Phase II Trial by the Spanish Multidisciplinary Melanoma Group (GEM-1402). *J. Clin. Oncol.* **2021**, *39*, 586–598. [CrossRef] [PubMed]
48. Steeb, T.; Wessely, A.; Ruzicka, T.; Heppt, M.V.; Berking, C. How to MEK the best of uveal melanoma: A systematic review on the efficacy and safety of MEK inhibitors in metastatic or unresectable uveal melanoma. *Eur. J. Cancer* **2018**, *103*, 41–51. [CrossRef] [PubMed]
49. Duan, J.J.; Cai, J.; Guo, Y.F.; Bian, X.W.; Yu, S.C. ALDH1A3, a metabolic target for cancer diagnosis and therapy. *Int. J. Cancer* **2016**, *139*, 965–975. [CrossRef] [PubMed]
50. Croker, A.K.; Rodriguez-Torres, M.; Xia, Y.; Pardhan, S.; Leong, H.S.; Lewis, J.D.; Allan, A.L. Differential Functional Roles of ALDH1A1 and ALDH1A3 in Mediating Metastatic Behavior and Therapy Resistance of Human Breast Cancer Cells. *Int. J. Mol. Sci.* **2017**, *18*, 2039. [CrossRef] [PubMed]
51. Kawamoto, M.; Umebayashi, M.; Tanaka, H.; Koya, N.; Nakagawa, S.; Kawabe, K.; Onishi, H.; Nakamura, M.; Morisaki, T. Combined Gemcitabine and Metronidazole Is a Promising Therapeutic Strategy for Cancer Stem-like Cholangiocarcinoma. *Anticancer. Res.* **2018**, *38*, 2739–2748. [CrossRef] [PubMed]
52. Arang, N.; Lubrano, S.; Ceribelli, M.; Rigiracciolo, D.C.; Saddawi-Konefka, R.; Faraji, F.; Ramirez, S.I.; Kim, D.; Tosto, F.A.; Stevenson, E.; et al. High-throughput chemogenetic drug screening reveals PKC-RhoA/PKN as a targetable signaling vulnerability in GNAQ-driven uveal melanoma. *Cell Rep. Med.* **2023**, *4*, 101244. [CrossRef] [PubMed]
53. McKean, M.; Chmielowski, B.; Butler, M.O.; Carvajal, R.; Rodon, J.; Carlino, M.; Kim, K.B.; Wise-draper, T.; Khan, S.; Salama, A.K.S.; et al. 1081O ctDNA reduction and clinical efficacy of the darovasertib + crizotinib (daro + crizo) combination in metastatic uveal melanoma (MUM). *Ann. Oncol.* **2023**, *34*, S651. [CrossRef]
54. Tarin, M.; Némati, F.; Decaudin, D.; Canbezdi, C.; Marande, B.; Silva, L.; Derrien, H.; Jochemsen, A.G.; Gardrat, S.; Piperno-Neumann, S.; et al. FAK Inhibitor-Based Combinations with MEK or PKC Inhibitors Trigger Synergistic Antitumor Effects in Uveal Melanoma. *Cancers* **2023**, *15*, 2280. [CrossRef] [PubMed]
55. Orloff, M.M.; Ramelyte, E.; Butler, M.O.; Rutkowski, P.; Guardo, L.D.; Carlino, M.S.; Chmielowski, B.; Kennedy, L.B.; Montazeri, K.; Sacco, J.J.; et al. Darovasertib plus crizotinib vs investigator's choice as first-line treatment for patients with HLA-A2 negative metastatic uveal melanoma: Primary results from the OptimUM-02 trial. *J. Clin. Oncol.* **2026**, *44*, LBA9503. [CrossRef]
56. Lubrano, S.; Cervantes-Villagrana, R.D.; Arang, N.; Cardenas-Alcoser, E.S.; Sato, K.; Cuesta-Margolles, G.; Paradis, J.S.; Acosta, M.; Gutkind, J.S. Unraveling Resistance Mechanisms to Gαq Pathway Inhibition in Uveal Melanoma: Insights from Signaling-Activation Library Screening. *Cancers* **2025**, *18*, 74. [CrossRef] [PubMed]
57. Bruhn, M.A.; Pearson, R.B.; Hannan, R.D.; Sheppard, K.E. Second AKT: The rise of SGK in cancer signalling. *Growth Factors* **2010**, *28*, 394–408. [CrossRef] [PubMed]
58. Tanaka, R.; Terai, M.; Londin, E.; Sato, T. The Role of HGF/MET Signaling in Metastatic Uveal Melanoma. *Cancers* **2021**, *13*, 5457. [CrossRef] [PubMed]

Disclaimer/Publisher's Note: The statements, opinions and data contained in all publications are solely those of the individual author(s) and contributor(s) and not of MDPI and/or the editor(s). MDPI and/or the editor(s) disclaim responsibility for any injury to people or property resulting from any ideas, methods, instructions or products referred to in the content.

https://doi.org/10.3390/cancers18142232

MDPI AG
Grosspeteranlage 5
4052 Basel
Switzerland
Tel.: +41 61 683 77 34

Cancers Editorial Office
E-mail: cancers@mdpi.com
www.mdpi.com/journal/cancers



Disclaimer/Publisher's Note: The title and front matter of this reprint are at the discretion of the Guest Editors. The publisher is not responsible for their content or any associated concerns. The statements, opinions and data contained in all individual articles are solely those of the individual Editors and contributors and not of MDPI. MDPI disclaims responsibility for any injury to people or property resulting from any ideas, methods, instructions or products referred to in the content.





Academic Open
Access Publishing

mdpi.com

ISBN 978-3-7258-9050-7